Universitat Politècnica de València

Departamento de Comunicaciones

Doctoral Thesis

Development of New Tunable Passive Microwave Components in Waveguide Technology

Javier Ossorio García

Marzo 2021

Director

Dr. Vicente E. Boria Esbert (Universitat Politècnica de València)

Tesis Doctoral presentada al Departamento de Comunicaciones,
en el cumplimiento parcial de los requisitos para obtener:
Título de Doctor en Ingeniería de Telecomunicación
por la Universitat Politècnica de València.
10 de Marzo de 2021, Valencia

Esta Tesis Doctoral ha contado con la inestimable ayuda y asesoramiento externo del **Dr. Marco Guglielmi (Retired Engineer, ESA)**, sin el cual, el desarrollo y presentación de la misma no hubiera sido posible, y al que se le agradece su ayuda, consejos y asesoramiento continuado durante todos estos años.

Agradecimientos

Querría utilizar esta página para agradecer y dedicar unas palabras a todos aquellos que en algún grado, y de forma consciente o inconsciente, han ayudado a que este documento haya sido concluido.

Al comenzar esta aventura hace cinco años nunca hubiera imaginado cómo lo terminaría, ni el camino recorrido hasta este momento. Y es que, mirando la vista atrás, es difícil imaginar todo el esfuerzo necesario para sacar adelante algo como una tesis doctoral. Cientos de horas de lectura de papers, días delante del ordenador con simulaciones interminables y otras tantas aprendiendo a medir los dispositivos que se fabricaban, todo esto mientras había que redactar papers con el querido LateX, para defender y justificar ante expertos del campo de las microondas el trabajo realizado. Y es que, cualquiera que haya escrito en LateX sabe que al final, incluso, se le coge un poco de cariño a ese programa que sólo saca errores en el registro.

Por supuesto, nada de esto hubiera sido posible sin la confianza, maestría, paciencia y talento de mis dos tutores de la tesis. Vicente y Marco, sin duda, para vosotros es mi primer agradecimiento. Y es que no solo me habéis aportado todas las herramientas necesarias para hacer la tesis, sino que, con paciencia y confianza me habéis guiado para enfrentarme al mundo laboral, para entender el mundo que rodea a nuestro trabajo de investigación y enseñado valiosas lecciones, para aportar contenido científico de calidad que ayude a mejorar el mundo. Muchas gracias por todo.

Mi segundo agradecimiento, como no podía ser de otra manera, es a mi madre y mi padre. Sin vosotros nunca hubiera sido posible estudiar la carrera que quería. Nunca dudasteis de mi y de mi determinación, y gracias a eso, desde mucho antes de comenzar la carrera, ya sabía que estaríais allí, apoyándome. Algo que habéis hecho día tras día, muchas veces sin entender ni lo que hacía, ni como lo hacía. Vuestro ha sido el empuje que necesitaba para tomar las decisiones que me han llevado hasta terminar este trabajo.

También me gustaría agradecer a todas las personas del GAM y VSC su ayuda, y por tratarme como uno más del grupo desde el primer día. Ya sea por esas charlas a la hora de comer, o por todo el material e instalaciones que habéis puesto a mi disposición para aprender y desarrollar mis habilidades prácticas en el laboratorio.

Por último, me gustaría agradecer a mis imprescindibles amigas y amigos, mi segunda familia, todo el apoyo durante estos años. Y es que el descanso y la diversión también han sido una parte importante para poder llevar la tesis hasta buen puerto. Pero también habéis sido mi inspiración, un modelo a seguir, y las ganas de mejorar día tras día, tanto profesional como personalmente.

Me dejaré a mucha gente sin nombrar, así que para todos ellos, muchas gracias.

Resumen

La presente tesis doctoral tiene como objetivo principal el estudio, desarrollo, diseño y fabricación de nuevos componentes pasivos de microondas, tales como filtros y multiplexores que operen en las bandas de alta frecuencia de los actuales y futuros satélites de telecomunicación (bandas Ku, K y Ka) entre 12 y 40 GHz. Dichos componentes deben ser capaces de ofrecer tanto respuestas clásicas sencillas como avanzadas (elípticas), y presentar una capacidad de resintonización (tanto en términos de frecuencia central como de ancho de banda). Estos componentes darán solución a las necesidades actuales de los sistemas de comunicaciones espaciales, que requieren de mayores tasas de transmisión de datos (señales de mayor ancho de banda), así como de mayor flexibilidad en las frecuencias de operación, para ofrecer con un mismo dispositivo distintos servicios y prestaciones.

Para ello, se proponen tanto modificaciones a las estructuras de filtros clásicos de microondas actuales, como la introducción de nuevas estructuras. Asimismo, también se investigará el uso de los tornillos de ajuste post-fabricación de los filtros como tornillos de sintonía metálicos, así como la posible introducción de tornillos de sintonía realizados con distintos materiales dieléctricos. Se pretende, de esta forma, mejorar las respuestas de los dispositivos actuales; reduciendo su tamaño y costes de producción (debido a la relajación de las tolerancias de fabricación), abaratando de esta forma la fabricación y futura operación de los mismos.

Aprovechando estos nuevos dispositivos, se abordará también el diseño, fabricación y medida de componentes más complejos, como pueden ser los los diplexores de canal o los conmutadores con respuesta selectiva en frecuencia, todos ellos necesarios en los sistemas de comunicaciones espaciales y en íntima relación con los filtros previamente mencionados.

Por último, el desarrollo de todos estos nuevos dispositivos vendrá acompañado de una metodología de diseño basado en el uso del Mapeo Espacial Agresivo (Aggressive Space Mapping, ASM) especialmente adaptado a los filtros en guía de onda.

Resum

La present tesis doctoral té com a objectiu el estudi, desenvolupament, diseny i fabricació de nous components pasius de microones, tals com els filtres i multiplexors que operen en les bandes d'alta freqüencia dels actuals i futurs satèl·lits de telecomunicació (bandes Ku, K i Ka) entre 12 i 40 GHz, Aquests components han de ser capaços d'oferir tant, respostes clàsiques sencilles com avançades (eliptiques), i que a més a més presenten una capacitat de resintonització (tant en termes de freqüència central com d'amplada de banda). Aquestos nous components pasius donaràn solució a les necesitats dels actuals sistemes espacials, que requereixen de majors taxes de transmissió de dades (senyals de major amplada de banda), així com de major flexibilitat en les frequencies de operació, per oferir en un mateix dispositiu distints serveis i prestacions.

Per aquesta raó, es proposen tant modificacions a les estructures del filtres clàsics de microones actuals, com la introducció de noves estructures. Així mateix, també s'investigarà l'us dels tornells d'ajustament post-fabricació dels filtres com a tornells de sintonía metàl·lica i la introducció de tornells de sintonía realitzats amb diferents materials dielèctrics Es pretén, d'aquesta forma, la millora de les respostes del dispositius actuals; reduint la envergadura i els costos de producció (gràcies a la relaxació de les toleràncies de fabricació), abaratint d'aquesta forma la fabricació i futura operació dels filtres mateixos.

Aprofitant aquestos nous dispositius es treballarà també en el disseny, fabricació i mesura de components més complexes, com poden ser els multiplexors de canal i els commutadors amb resposta selectiva en freqüencia, tots ells necessaris en els sistemes de comunicacions espacials i en íntima relació amb els filtres abans esmenats.

Per finalitzar, el desenvolupament de tots aquestos dispositius vindrà acompanyat d'una metodologia de disseny basada en l'us del Mapatge Espacial Agressiu (Aggressive Space Mapping, ASM), especialment adaptat als filtres en guia d'ona.

Abstract

The main objective of this doctoral thesis is the study, development, design and manufacture of new passive microwave components in waveguide technology, such as filters and multiplexers, that operate in the high frequency bands of current and future telecommunication satellite payloads between 12 and 40 GHz (Ku, K and Ka bands). The new solutions developed must offer both classic and advanced (elliptical) responses, as well as the possibility of being reconfigured both in terms of center frequency and bandwidth. The motivation for this research is to address the current and future needs of space communication systems which require higher data rate transmission (that is larger bandwidths), as well as flexibility with respect to the operating frequency to dynamic adaptation to possible changes in user demands.

In this context, we propose in this thesis alternative microwave filter structures in metallic waveguide, as well as novel solutions. We explore different approaches to adjust the filter performance, using both traditional metallic tuning screws as well as tuning elements made with different dielectric materials. We also advance the state-of-the-art by developing more performing Space Mapping procedures for the design, optimization and tuning of the filter structures that we propose. The objective is to improve the response of the devices and reduce, at the same time, their manufacturing time and costs.

As a fundamental element of our work, in addition to theoretical developments, we also apply the findings of our research to the design, manufacture and measurement of a number of more complex components, such as diplexers and integrated switches and filters. They are practical devices to demonstrate the ability of the novel filters that we propose to satisfy the requirements of current and future advanced satellite payloads.

Contents

Resumen **v**

Resum **vii**

Abstract **ix**

Contents **1**

Figure list **5**

Table list **15**

Acronyms **17**

1 Introduction **19**

1.1 Motivation 19
1.2 Objectives. 21

2 State of the art **23**

2.1 Satellite telecommunication links and transponders 24
2.2 Transponders and waveguide technology 27
2.3 Waveguides and microwave filters 29
2.4 Tunable microwave waveguide filters 34

2.5 Full-wave electromagnetic simulators . . . 35
2.6 Design and optimization procedures of microwave waveguide filters . . . 36

3 Filter design using OS-ASM 39

3.1 Cavity perturbation theory . . . 41
3.2 Experimental investigation . . . 41
3.3 Detailed numerical investigation . . . 48
3.4 One-Step Aggressive Space Mapping (OS-ASM) . . . 49
3.5 CAD demonstration . . . 50
3.5.1 Tunable rectangular four-pole filter . . . 51
3.5.2 Tunable rectangular eight-pole filter . . . 56
3.5.3 Classic circular dual-mode filter . . . 60
3.6 More general examples . . . 63
3.6.1 Tunable rectangular four-pole filter with OS-ASM . . . 63
3.6.2 Tunable rectangular four-pole filter with ASM . . . 66
3.6.3 Fully tunable dual-mode filter with OS-ASM . . . 67
3.6.4 Fully tunable dual-mode filter with ASM . . . 70
3.6.5 Folded rectangular waveguide tunable filter with OS-ASM . . . 72
3.6.6 Folded rectangular waveguide tunable filter with ASM . . . 76
3.7 Definition of space alignment . . . 78
3.8 Conclusions . . . 79

4 Tunable and reconfigurable waveguide filters 81

4.1 Circular waveguide dual-mode filter . . . 82
4.1.1 Fixed frequency . . . 84
4.1.2 Tunable frequency . . . 84
4.2 Folded rectangular waveguide filter . . . 90
4.3 Hardware manufacture . . . 92
4.4 Measured results . . . 96
4.4.1 Center frequency tunability . . . 97
4.4.2 Bandwidth tuning range . . . 98
4.5 Comparative discussion . . . 100
4.5.1 Tuning range . . . 100
4.5.2 Insertion losses . . . 100
4.5.3 Out of band performance . . . 101
4.6 Conclusions . . . 102

5 Dielectric materials for tunability of waveguide filters 103

5.1 Phase shift of tuning elements . . . 104

5.2 Passive Intermodulation . . . 110
5.3 Study of one cavity in waveguide . . . 113
5.4 Four-pole inductive filter with tuners . . . 116
5.4.1 Experimental investigation using Teflon tuners . . . 118
5.4.2 Experimental investigation using Sapphire tuners . . . 120
5.5 Comparative discussion . . . 122
5.6 Remote tunability by linear motors for 4-pole inductive filter . . . 123
5.7 Conclusions . . . 129

6 Automatic tuning with a robotuner 131

6.1 Mechanical implementation of the robotuner . . . 132
6.2 Tuning algorithm of the robotuner . . . 135
6.3 Tuning a six-pole inductive filter with metallic tuners . . . 138
6.4 ASM-based technique using robotuner . . . 142
6.5 Conclusions . . . 144

7 Further advances: Quadruplet diplexer and integrated filter switch 147

7.1 Quadruplet filter . . . 148
7.1.1 Filter specifications . . . 148
7.1.2 Filter design . . . 150
7.1.3 High precision design using One-Step Aggressive Space Mapping (OS-ASM) . . . 153
7.1.4 Measured results . . . 156
7.1.5 Conclusions . . . 156
7.2 Quadruplet diplexer . . . 157
7.2.1 Diplexer specifications . . . 158
7.2.2 Out of band response . . . 159
7.2.3 Distributed model . . . 166
7.2.4 Low-accuracy diplexer design . . . 171
7.2.5 High-accuracy diplexer design . . . 175
7.2.6 Multipactor breakdown prediction . . . 181
7.2.7 Measurements . . . 185
7.2.8 Conclusions . . . 187
7.3 Filter-switch . . . 188
7.3.1 Filter & Switch . . . 188
7.3.2 Design procedure . . . 190
7.3.3 Experimental results . . . 194
7.3.4 Remote control . . . 196
7.3.5 Conclusions . . . 197

8 Conclusions and future work **199**

8.1 Conclusions 199
8.2 Future work 201

A Robotuner flow-chart and M-code **203**

A.1 Flow-chart 203
A.2 Get Connection to VNA 203
A.3 Write Robby File 205
A.4 Get Error Traces 205
A.5 Get Measurements from VNA 205
A.6 Start Program 206

B Publications list **213**

Bibliography **215**

Figure list

2.1 Example of satellite communications system. 24

2.2 Example of path loss diagram for satellite telecommunication links. . . 25

2.3 Example of single-beam and multi-beam satellites. 26

2.4 Example of a multi-beam satellite schematic. 27

2.5 Example of bent-pipe satellite transponder diagram. 28

2.6 Field distribution for TE and TM modes in a rectangular waveguide. . 30

2.7 High-pass, band-pass and low-pass filter responses. *fc* (cutoff frequencies), *fs* (stop-band frequencies), *f0* (central frequency) and f_1, f_2 (band-edge frequencies). 31

2.8 Example of a resonant waveguide filter with inductive irises. 31

2.9 Example of waveguide filter with dielectric resonators. 32

2.10 Example of corrugated waveguide filter. 32

2.11 Example of waffle-iron waveguide filter. 33

2.12 Example of waveguide filter with stubs. 33

2.13 Example of dual-mode filter. 34

3.1 Unperturbed and perturbed cavities. 41

3.2 One-pole tunable filter structure. 42

3.3 One-pole tunable filter performance. 42

3.4 HF and LF one-pole tunable filter responses. 44

3.5 HF and LF one-pole *detuned* cavity filter responses. 45
3.6 HF and LF one-pole *detuned* aperture filter responses. 46
3.7 HF and LF one-pole filter simulations near resonance. 46
3.8 HF and LF simulations with *detuned* cavity near resonance. 47
3.9 HF and LF simulations with *detuned* aperture near resonance. 47
3.10 Fully tunable four-pole filter structure. 52
3.11 LF fully tunable four-pole filter performance. 52
3.12 Comparison of LF (blue) and HF (black dots) fully tunable four-pole filter responses. 53
3.13 HF and LF space alignment. 54
3.14 HF final performance vs. LF performance. 54
3.15 Detuned HF performance with random values of tuning element penetration. 55
3.16 HF model performance vs. LF performance. 55
3.17 Fully tunable eight-pole filter structure. 56
3.18 LF model performance. 57
3.19 HF model initial performance vs. LF performance. 58
3.20 Result of the first iteration ASM procedure vs. LF performance. 58
3.21 HF model detuned response vs. LF performance. 59
3.22 Result of the first iteration ASM procedure vs. LF performance. 59
3.23 Classic circular waveguide dual-mode filter structure. 61
3.24 Response of the dual-mode filter. 61
3.25 Initial HF response vs. LF performance. 62
3.26 Final HF filter performance vs. LF performance. 62
3.27 HF model structure with rounded corners and circular screws. 64
3.28 Initial response of the HF model. 64
3.29 Result of the first iteration in HF. 65
3.30 Result of the second iteration in HF vs. ideal response. 65
3.31 Result of the second iteration with the Broyden formula vs. ideal response. 66

3.32 Fully tunable dual-mode filter structure. 67
3.33 Ideal LF filter response. 68
3.34 Comparison between initial HF performance and LF performance. . . . 68
3.35 Result of first iteration in HF. 69
3.36 Result of second iteration in HF. 69
3.37 Final HF filter performance of the third iteration vs. ideal response. . . 70
3.38 Response of the second iteration with the Broyden formula in HF. . . . 71
3.39 Response of the third iteration with the Broyden formula in HF. 71
3.40 Result of the fourth iteration with the Broyden formula in HF filter vs. ideal response. 72
3.41 Filter structure. 73
3.42 Ideal LF filter response. 73
3.43 Comparison between initial HF performance and LF performance. . . . 74
3.44 Result of the first iteration in HF. 75
3.45 Result of the second iteration in HF. 75
3.46 Result of the third iteration in HF filter vs. ideal response. 76
3.47 Response of the second iteration with the Broyden formula in HF. . . . 76
3.48 Response of the third iteration with the Broyden formula in HF. 77
3.49 Response of the fourth iteration with the Broyden formula in HF vs. ideal response. 77

4.1 Basic four-pole, dual-mode filter structure. 82
4.2 Basic four-pole, dual-mode filter performance. 83
4.3 Basic input/output and inter resonator irises. 84
4.4 Tunable input-output iris: (a) Non-penetrated screw; (b) Penetrated screw 85
4.5 Tunable inter resonator iris. 85
4.6 Tunable input iris implementation. 86
4.7 Fully tunable dual-mode filter. 87
4.8 Simulated tuning range with FEST3D. 88

4.9 Resonance of the horizontal screw. 89

4.10 Folded Rectangular waveguide filter. 90

4.11 Simulated tuning range of the folded rectangular waveguide filter. . . . 92

4.12 Fully tunable circular waveguide filter with rounded corners irises and circular tuning screws. 93

4.13 Folded tunable rectangular waveguide filter with rounded corners and circular tuning screws. 93

4.14 Comparison between simulated response in FEST3D and HFSS for the dual-mode circular waveguide filter, tuned at 17.55 GHz of center frequency. 94

4.15 Comparison between simulated response in FEST3D and HFSS for the folded rectangular filter, tuned at 17.3 GHz of center frequency. 94

4.16 The tunable four-pole circular waveguide filter breadboard. 95

4.17 Folded rectangular waveguide filter realized in silver plated aluminum. . 95

4.18 Measured tuning range of the circular waveguide dual-mode filter. . . . 97

4.19 Measured tuning range of the folded rectangular waveguide filter. . . . 98

4.20 Maximum bandwidth for circular waveguide dual-mode filter. 99

4.21 Maximum bandwidth for folded rectangular waveguide dual-mode filter. 99

4.22 Out of band performance comparison. The red curve is the circular waveguide dual-mode filter. 101

5.1 Sections of WR-75 waveguide (length of 100 mm each one). 105

5.2 Phase difference due to an aluminum M3 screw penetrating 2.5 mm. . . 106

5.3 Phase difference due to a stainless steel M3 screw penetrating 2.5 mm. 107

5.4 Phase difference due to a smooth aluminum rod of 3.0 mm in diameter penetrating 2.5 mm. 107

5.5 Phase difference due to a Teflon M3 screw penetrating 9.525 mm. . . . 108

5.6 Phase difference due to a smooth Sapphire rod of 3 mm in diameter, penetrating 4.0 mm. Dielectric constant ϵ_r parallel to cylinder-axis is 11.5, and perpendicular to cylinder-axis is 9.3. 109

5.7 Phase difference due to a ceramic dielectric rod with $\epsilon_r = 50$, penetrating 1.0 mm. 109

5.8 PIM test bed configuration including the DUT. 110
5.9 Simple one pole filter structure. 114
5.10 Performance of a simple one pole filter structure with metallic tuning screws. No penetration: right, 3.5 mm penetration: left. 114
5.11 Structure with fully inserted 2 mm Teflon rods. 115
5.12 Tuning range estimation with Teflon. No penetration: right, fully inserted M2 Teflon rods: center, fully inserted M4 Teflon rods: left. . . . 115
5.13 Performance with almost fully inserted 2 mm Sapphire rods. 116
5.14 Basic four-pole inductive filter structure in rectangular waveguide. . . . 117
5.15 Basic four-pole rectangular waveguide, inductive filter performance. . . 117
5.16 Measured response of the tunable, silver-plated filter. 118
5.17 High-end performance with 2 mm Teflon rods barely inserted. 119
5.18 Low-end performance. All 2 mm Teflon rods: right curve, 2mm Teflon rods in apertures and 4 mm Teflon rods in cavities: left curve. 119
5.19 The hardware being measured. 120
5.20 High-end (right) and low-end (left) performance with 2 mm Sapphire rods. 121
5.21 High-end (right) and low-end (left) performance with 3 mm Sapphire rods. 121
5.22 High-end (right) and low-end (left) performance with 4 mm Sapphire rods. 122
5.23 PQ12-P linear actuator. 123
5.24 PQ12-P control board. 124
5.25 PQ12-P control software. 124
5.26 Support structure for the filter with the motors and Sapphire tuners. . 125
5.27 Detail of the Sapphire tuners centered and fixed in the holes by a 3D-printed piece. 125
5.28 Set-up of the motors, filter and the control boards. 126
5.29 Measurements of the 12.995 GHz channel. 127
5.30 Measurements of the 12.389 GHz channel. 127

5.31 Measurements of the 11.918 GHz channel. 128
5.32 Measurements of the 11.410 GHz channel. 128
5.33 Measurements of the 11.057 GHz channel. 129

6.1 Robotuner arm and workbench. 133
6.2 Robotuner control units. 134
6.3 Main control interface of the robotuner. 135
6.4 Ideal response of a 4-pole filter centered at 12 GHz with 200 MHz of channel bandwidth, and its possible objective mask points. 136
6.5 Ideal response of the 6-pole filter. 139
6.6 Structural view and fabricated prototype of the 6-pole filter. 139
6.7 Specifications of M4 tuners from Tronser. 140
6.8 Initial response vs. ideal response. 141
6.9 Response of the filter after the first step vs. ideal response. 141
6.10 Final response of the filter vs. ideal response. 142
6.11 Response obtained for each tuner modified in the cavities of the filter. . 143
6.12 Response obtained for each tuner modified in the windows of the filter. 143
6.13 ASM-based tuning procedure result using robotuner. 144

7.1 Response of the filter for the maximum and minimum temperature. . . 149
7.2 Final ideal performance of the filter. 150
7.3 Vertical connection of the inductive 4-pole filter with TE_{103}. 151
7.4 Response of the inductive 4-pole filter connected in vertical direction by the 2nd and 3rd cavities. 151
7.5 Ideal structure of the quadruplet filter simulated in FEST3D. 152
7.6 Performance of the quadruplet filter vs. ideal response. 152
7.7 Structure of the quadruplet filter with rounded corners and I/O tappers. 154
7.8 Initial performance of the quadruplet filter in CST. 154
7.9 Final performance of the quadruplet filter in CST vs. ideal response. . 155
7.10 Measured result of the quadruplet filter vs. ideal response. 156

7.11 Quadruplet filter structure. 159
7.12 Final in-band response of the quadruplet filter designed in [131]. 160
7.13 Out-of-band response of the quadruplet filter. 160
7.14 E-plane T-junction. 161
7.15 Performance of the E-plane T-junction in Fig. 7.14. 161
7.16 Electric field distribution at the first TZ. 162
7.17 Electric field distribution at the point of adaptation. 162
7.18 Electric field distribution at the second TZ. 162
7.19 Two-pole filter with capacitive inter-resonator coupling. 163
7.20 Wide-band response of the two-pole filter in Fig. 7.19 164
7.21 Two-pole filter with an additional TZ in the lower rejection band. . . . 164
7.22 Two-pole filter with an additional TZ in the upper rejection band. . . . 165
7.23 Two-pole filter with a double TZ in the lower rejection band. 165
7.24 Lumped element circuit of a quadruplet. 166
7.25 Distributed model of the 4-2 filter. 167
7.26 In-band response of the distributed model compared with the lumped model response given by the coupling matrix. 168
7.27 Out-of-band transmission response of the distributed model compared with the monotonically decaying response of the lumped model. 169
7.28 Filter performance for several values of the parameter θ'. 169
7.29 Filter performance for several values of the parameter θ' but enforcing the near-band transmission zeros at fixed frequency locations. 170
7.30 Response of the quadruplet filter for the diplexer with three TZs in the lower band. Solid lines correspond to the EM response and dashed lines correspond to the distributed model response. 172
7.31 Response of the quadruplet filter for the diplexer with three TZs in the upper band. Solid lines correspond to the EM response and dashed lines correspond to the distributed model response. 172
7.32 Frontal view of the E-field T-junction implemented. A0T and A0B are the design dimensions. 173
7.33 Structure of the diplexer with the T-junction. 173

7.34 Initial response of the complete diplexer structure. 174
7.35 Final response of the diplexer with the T-junction. 175
7.36 Extraction of top filter in FEST3D (coarse space). 176
7.37 Recovered response of the top filter with sharp corners. 177
7.38 Extracted bottom filter with rounded corners in CST (fine space). . . . 177
7.39 Recovered response of the bottom filter with rounded corners. 178
7.40 Extracted T-Junction. (a) sharp corners, (b) rounded corners. 178
7.41 Recovered response of the T-junction. 178
7.42 Initial response of the diplexer in CST after assembly of the separate components. 179
7.43 Comparison of the responses of the final diplexer produced by CST and HFSS 179
7.44 Final structure of the diplexer. Dimensions of the top and bottom filter are numerated with 'T' and 'B' termination, respectively. 180
7.45 CST broadband performance of the diplexer. 180
7.46 Group delay response of the diplexer. 183
7.47 Representation of the E-field and the critical zones in the diplexer for 19.69 GHz. 183
7.48 Multipactor simulation with discharges for the bottom capacitive window at 19.95 GHz. 184
7.49 Fabricated prototype of the diplexer. 186
7.50 Diplexer breadboard. 186
7.51 Comparison between measurement and ideal response. 187
7.52 Possible implementation of the F&S. The device behaves at the same time as a 3-pole filter and as a 1P3T switch. 189
7.53 Modified Tuning Pin (MTP): (a) Hollow M4 screw (blue cylinder) that can be adjusted manually to tune each cavity or aperture; (b) Pin (red cylinder) that can be inserted in the center of the hollow M4 tuning screw to short circuit a cavity or an aperture; (c) MTP detuned state; (d) MTP tuned state. 189

7.54 3-pole filter. The central cavity must be square so that the perpendicular branches can be added later. 190

7.55 Response of the 3-pole filter. In this example, the filer is centered at 12 GHz, and has a bandwidth of 200 MHz. 191

7.56 F&S device. The black circles in the MTPs of branches P3 and P4 indicate that they are in the detuned state. 191

7.57 F&S device. The black circles in the MTPs of branches P2 and P4 indicate that they are in the detuned state. 192

7.58 F&S response with the active path between P1 and P2. All MTPs in branches P3 and P4 are in the detuned state. 193

7.59 F&S response with the active path between P1 and P3. All MTPs in branches P2 and P4 are in the detuned state. 193

7.60 Assembled F&S with the active path between P1 and P2. 194

7.61 F&S response. Active path between P1 and P2. All MTPs in branches P3 and P4 are set to the detuned state. 195

7.62 F&S response. Active path is between P1-P3. All MTPs in branches P2 and P4 are in the detuned state. 195

7.63 Linear actuator used to lift/lower the central pin of each MTP. 196

7.64 Assembled F&S. An Arduino board is used to control 6 servomotors. . 196

A.1 Matlab code flow-chart for automatic tuning with robotuner. 204

A.2 Get connection M-code. 204

A.3 Write Robby file M-code. 205

A.4 Get error traces M-code. 206

A.5 Get Measurements M-code. 207

A.6 M-code of the initial part of the main program. 208

A.7 M-code for obtaining the filters measurements from VNA. 208

A.8 M-code for processing data from measurements. 209

A.9 M-code for setting up the movement of the robotuner. 210

A.10 M-code for starting the optimization (min. max.) loop. 210

A.11 M-code for performing the optimization loop until one stop condition is reached. 211

Table list

3.1 Dimensions of the one-pole structure (mm). 44

3.2 Tuning screw penetrations (mm). 44

3.3 Difference between derivatives of HF and LF simulations. 48

3.4 Dimensions of the four-pole structure in millimeters. All the heights are 9.525 mm. 53

3.5 Comparison of final screw dimensions between LF and HF models in millimeters. 56

3.6 Dimensions of the eight-pole structure in millimeters. All the heights are 9.525 mm. 57

3.7 Comparison of final screw dimensions between LF and HF models in millimeters. 60

3.8 Dimensions of the classic dual-mode filter structure in millimeters. . . . 61

3.9 Comparison of final screw dimensions between LF and HF models in millimeters. 63

3.10 Comparison of final screw dimensions between LF and HF models in millimeters. 67

3.11 Comparison of final screw dimensions between LF and HF models in millimeters. 72

3.12 Dimensions (in mm) of the folded filter structure. All heights are 6.477 mm. 74

3.13 Comparison of final screw dimensions between LF and HF models in millimeters. 78

4.1 FEST3D Filter Dimensions (mm) 88
4.2 Dimensions of the classic dual-mode filter structure in millimeters. . . . 96
4.3 Dimensions of the folded filter structure (mm). All heights are 6.477 mm. 96

5.1 PIM results for Sapphire. 111
5.2 PIM results for Teflon. 111
5.3 PIM results for stainless steel screw. 112
5.4 PIM results for smooth aluminum rod. 112
5.5 PIM results for an aluminum screw. 112
5.6 Theoretical Metallic Tuning Screws Penetrations (mm) 117
5.7 Relative position of the motors for different filter channels (0-100% of penetration). 126

7.1 Monte-Carlo and EM simulations results. 153
7.2 Dimensions of the quadruplet filter in millimeters. 155
7.3 Dimensions of the top filter of the diplexer in millimeters. 181
7.4 Dimensions of the bottom filter of the diplexer in millimeters. 182
7.5 Power threshold of multipactor effect (in Watts) 185

Acronyms

ASM	Aggressive Space Mapping.
CAD	Computer-Aided Design.
CMOS	Complementary metal–oxide–semiconductor.
DUT	Device Under Test.
EM	Electromagnetic.
GEO	Geosynchronous Equatorial Orbit.
GTW	Gateway Link.
HA	High Accuracy.
HF	High-fidelity.
ISDN	Integrated Service Digital Network.
ISL	Inter Satellite Link.
I/O	Input and Output.
LEO	Low Earth Orbit.
LA	Low Accuracy.
LF	Low-fidelity.
LNA	Low-Noise Amplifier.
M-code	Matlab code.
MEMS	Micro-Electro-Mechanical Systems.
MEN	Multi-mode Equivalent Network.
MTP	Modified Tuning Pin.
MUL	Mobile User Link.
OS-ASM	One-Step Aggressive Space Mapping.
PIM	Passive Inter-Modulation.
PSTN	Public Switched Telephone Network.
Q-factor	Quality Factor.
SIW	Substrated Integrated Waveguide.

SM	Space Mapping.
TE	Transversal Electric.
TM	Transversal Magnetic.
VISA	Virtual Instrument Standard Architecture.
VNA	Vector Network Analyzer.

Chapter 1

Introduction

1.1 Motivation

The development of communication satellites has always been motivated by the ever increasing demand for higher transmission capacity. As a consequence, the classic frequency bands used by satellites, namely, from 1 to 12 GHz (L, S, C and X bands), are now saturated. Therefore, the new systems are gradually moving to higher frequencies, namely, from 12 to 40 GHz (Ku, K and Ka bands) where the absolute bandwidth available for each channel is greater [1].

This, in turn, has triggered the investigation of new devices and components that can operate at higher frequencies and that can satisfy the new requirements. In this context, new hardware will need to be developed in mainly three different technologies: metallic waveguide, planar and waveguide-planar hybrids. However, the development of the needed hardware in the 12 to 40 GHz frequency range poses a number of both theoretical and practical challenges.

First, the use of higher frequencies usually comes at the cost of greater signal attenuation due to two main factors, the atmospheric absorption (specially above 12 GHz) [2] and the higher Ohmic losses inside the (passive) components [3]. Second, as can be directly deduced from the relation between frequency (f), wavelength (λ) and the speed of light (c) in equation 1.1, higher frequency implies shorter wavelength. As a consequence, therefore, the physical dimensions of the hardware are reduced, and the complexity of the manufacturing process is increased.

$$\lambda = c/f \tag{1.1}$$

The size reduction can be particularly problematic for waveguide technology. This is because the fabrication tolerances can become significant with respect to the dimensions of the components, and can adversely affect their performance. Furthermore, smaller components generally result into higher internal electromagnetic field strength. This, in turn, can cause undesired high-power effects, like the well-known multipactor and corona effects [4].

All these challenges are particularly relevant for communication satellites because they are extensively based on waveguide components. Waveguide technology is, in fact, the best solution in terms of both power handling and insertion losses [5].

Another challenge for waveguide components in communication satellites is the constant requirement of size and mass reduction of all payloads. This is, in fact, required in order to reduce the launch cost of the satellites.

Moreover, the development of communication satellites with higher communication capacity, normally results in wider total bandwidth and a larger number of channels per satellite, and this can significantly increase the system complexity [6]. The development and use of tunable and/or re-configurable devices then becomes an attractive solution in order to reduce the number of components, and to allow for in-orbit reconfiguration to accommodate variable user requirements.

In this context, it is important to recall that some waveguide devices do currently use metallic tuning screws, that are adjusted manually after manufacturing in order to compensate for the dimensional errors inevitably introduced by the fabrication processes. The screws (also tuning elements or tuners) can indeed change the response of the device and could, at least in principle, be used for the reconfiguration of the device itself [7] and [8]. However, the use of metallic tuning screws can produce undesired effects in the device like increased insertion losses, the generation of passive inter-modulation (PIM) effect, and multipactor effects, thus significantly reducing the power-handling capability of the component [9]. For these reasons, different solutions are investigated in this thesis to implement reconfigurable passive devices in waveguide technology for satellites.

Finally, it is important to note that a common engineering solution for the development of the new devices operating in Ku, K and Ka bands is the adaptation of classic designs developed in the past for lower frequency bands. This can indeed be a viable solution in some cases. However, it can also cause important limitations in terms of power handling and in terms of achievable device performance.

As a result of all of the above discussion, the development of new passive components for communication satellites in Ku, K and Ka bands, with the capability of in-orbit reconfiguration and high power handling in waveguide technologies, has recently become one of the main areas in microwave research.

1.2 Objectives

The main objective of this doctoral thesis is to provide all the information required for the design of different solutions for new tunable components in waveguide technology for communication satellites.

To this end, the design of a number of new components is fully described and validated with the measurement of prototypes. In particular, the subjects discussed are as follows:

- A survey of the state-of-the-art of passive devices for satellite communications, with the objective of identifying how the structures can be effectively modified in order to obtain tunable and reconfigurable devices with the required performance, without reducing power handling capability or introducing undesired high-power effects.
- The development of an efficient methodology for the design of novel tunable filter structures. The approach will be based on the use of the Aggressive Space Mapping (ASM) [10]-[12], adapted for the specific needs of microwave filter design in waveguide technology based on electromagnetic (EM) simulation tools.
- The use of the methodology developed for the design of new waveguide filter structures that, being tunable, can provide greater bandwidths, as well as elliptic responses while reducing size, mass and fabrication costs.
- The implementation of novel tuning devices for both the correction of the manufacturing inaccuracies, and the on-board tuning and reconfiguration of microwave filters. In this context, we will investigate the use of different materials, such as dielectrics, to be used as tuning elements that produce similar or better responses as compared to the classic solutions based on metallic screws.
- Furthermore, taking advantage of the knowledge gained in our research, we will demonstrate the possibility of computer supported tuning of microwave filters in waveguide technology, using high precision stepped motors and a purpose built robotic arm.
- Finally, we will demonstrate the applicability of the basic concepts that we developed to more complex passive waveguide devices, like switches and diplexers, thereby significantly extending the range of potential application of our findings in the area of communication satellite components.

All of our findings have been fully validated through the simulation of the new structures with commercial software tools of known high accuracy, and the fabrication and measurement of several filter prototypes.

Finally, it is important to mention that all the theoretical and practical advancements of the state-of-the-art produced in our work, have been fully described in a number of publications in technical journals and international conferences of high scientific value in the microwave field.

In the next chapters, all information, solutions, and results about the different subjects considered in this doctoral work, are shown and explained in a detailed way.

Chapter 2

State of the art

The Satellite Era started on October 4th, 1957, with the launch of the first artificial satellite (Sputnik). Since that date, enormous advances in satellite technology and applications have been made [13]. One of the most important applications of satellite technology is telecommunications. The advances in this area have been motivated by the constant requirement of achieving ever increasing data transmission rates, flexibility in the use of different frequency bands, as well as higher and more flexible satellite capacity, all with the lowest possible cost.

With this set of general requirements, modern communication satellites have evolved into very complex systems, where a large variety of different technologies work together in order to provide high quality communication links. To reach the current level of sophistication, very significant research efforts have indeed been made in many different technical areas [5]. Technologies needed to improve the performance of communication satellites include, but are not limited to, new mechanically strong and light materials, more efficient solar panels to provide the energy needed to operate the satellite equipment, better thermal shields to protect the satellite payload from the solar radiation, efficient high power amplifiers, and a variety of miniaturized microwave components with advanced performances.

In this context, the objective of this thesis is to advance the state-of-the-art of tunable microwave filters and passive components in waveguide technology to be used in the payload of communication satellites. Specifically, we focus on the microwave channel filters in waveguide technology. Microwave filters are, in fact, one of the key components of all satellite communication systems.

However, before starting our research activity, we deem appropriate to first understand the basic functionality of microwave filters in current communication satellites, and to carry out a survey of the latest developments.

2.1 Satellite telecommunication links and transponders

Basically, a telecommunication link consists of an electromagnetic wave (the carrier) modulated by a signal that contains the information that is being transmitted. This modulated wave is emitted by one piece of equipment and received by another. The most basic telecommunication satellites that orbits the Earth acts then as a mirror, receiving the signal from one point on earth, and re-transmitting the same signal toward another point. The role of the satellite, in addition to routing the signal, is also to compensate for the attenuation experienced by the signal as it travels from the source to the intended destination [5]. Fig. 2.1 shows different possible uses of telecommunication satellite systems.

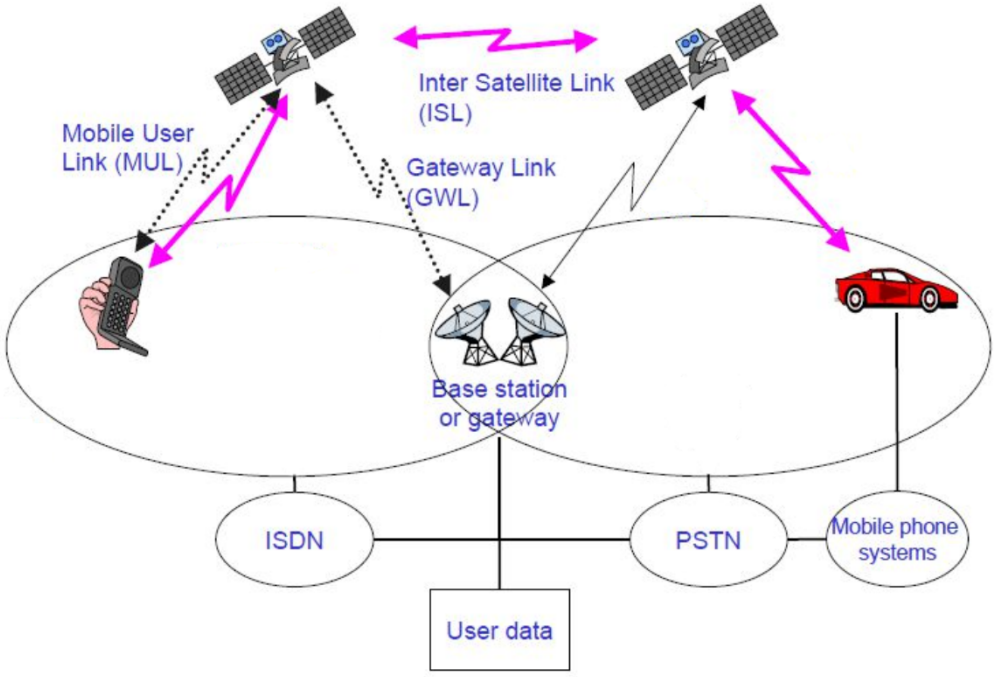

Figure 2.1: Example of satellite communications system.

As we already mentioned, telecommunication satellites orbit the Earth. There are, in fact, many different positions and orbits where satellites are deployed. From low Earth orbit (LEO), typically between 200 to 1200 km, to the geosynchronous equatorial orbit (GEO), at 35786 km from Earth.

This means that the communication link will always suffer significant path losses. The compensation of the losses usually takes place in the satellite, in a piece of equipment called the transponder. Communication satellites generally host many such transponders. Classic (transparent) transponders only compensate for the signal attenuation along the path of the link [14].

The function of a basic transparent transponder is to receive a very weak signal from a transmitting equipment on earth (the emitter), amplify the signal, and re-transmit the exact same signal at much higher power level toward the receiving point at the end of the link. This architecture is known as the bent-pipe architecture. Bent-pipe telecommunication satellites typically re-transmit the signal using one (or a few) very large beams to cover large portion of the Earth. Fig. 2.2 shows the typical power link budget for a communication satellite.

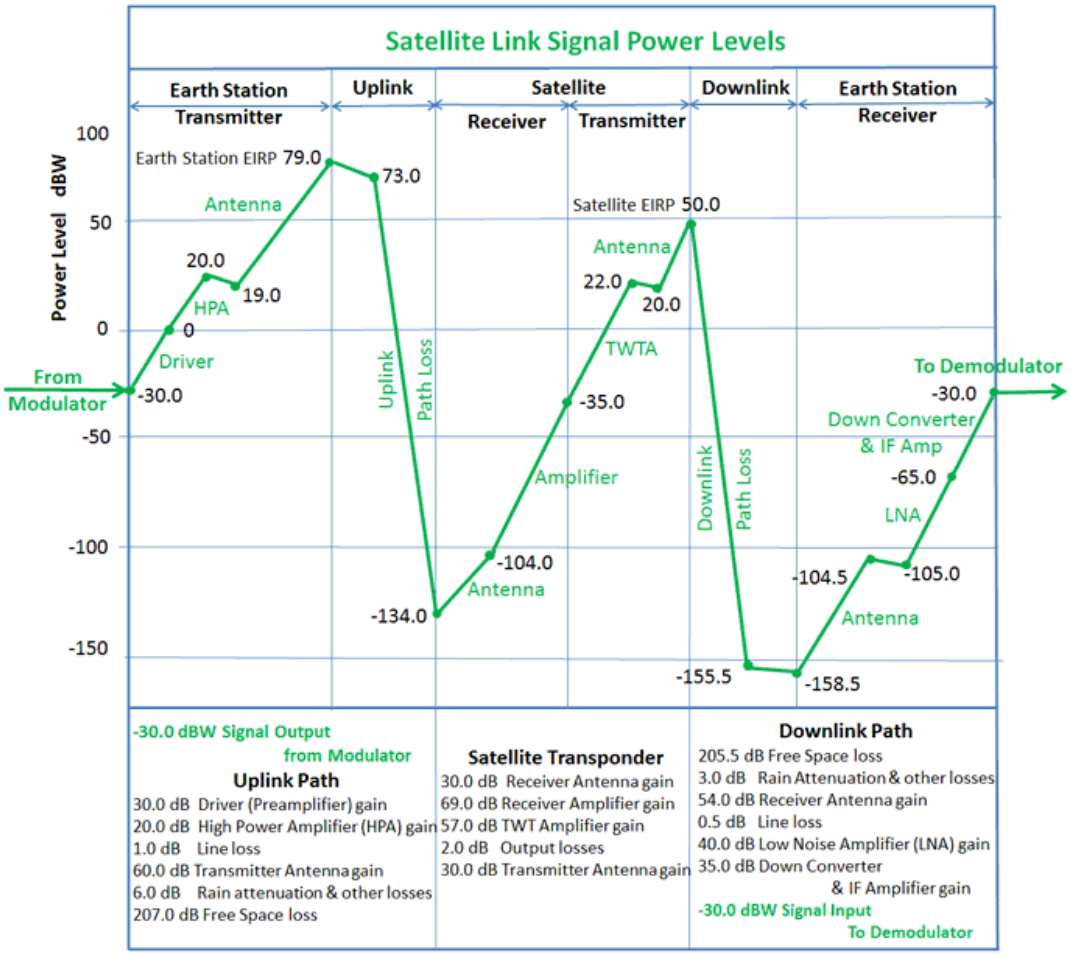

Figure 2.2: Example of path loss diagram for satellite telecommunication links.

The traditional transparent transponders are currently evolving toward more advanced system designs, the so-called regenerative transponders, that can implement many different types of signal processing, of such as de-modulation, decoding, encoding and modulation. Regenerative transponders can also process signals from multiple ground stations, combining (multiplexing) or splitting (de-multiplexing) them for transmission to other multiple ground stations, after the required data processing has been carried out.

A further current evolution trend is toward the use of multiple spot beams to retransmit the signals to the users on earth. These architectures allow to substantially increase the total radiated power and bandwidth of the system, and essentially move the complexity of the telecommunication payload closer to the front end [6]. In particular, the functionality of complex multi-channel manifold multiplexers, common in bent-pipe satellites, is now being replaced by complex multi-beam antenna systems using integrated filtering structures.

This evolution from single-beam configuration to multi-beam configuration, allows the satellite to re-use the available frequencies, increase the radiated power density for a single channel (due to the concentration of the power into small beams) and multiplex different signals to multiple areas, see Fig. 2.3.

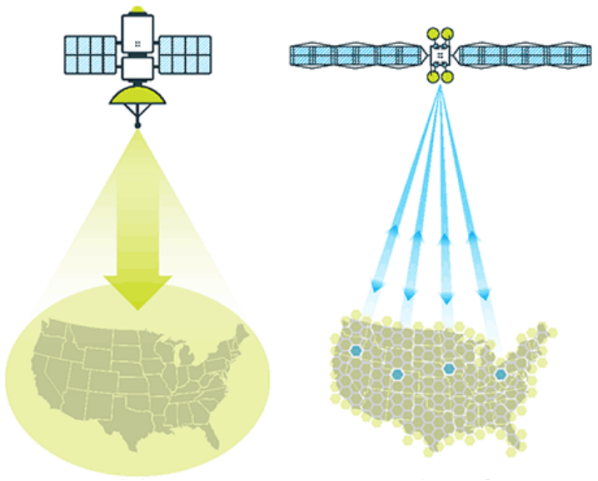

Figure 2.3: Example of single-beam and multi-beam satellites.

To do this, it is necessary to add to the transponder a robust switching network to provide the satellite with the ability to route the signal through all the satellite components correctly, from the receiver antenna to the emitter antenna. Additionally, satellites are provided with a number of redundant equipment in case of malfunctioning of any component in the transponder, making the switching network a critical component of the communication satellite system. Fig. 2.4 shows the typical schematic of a multi-beam satellite, where we can see that the switching network takes a main role.

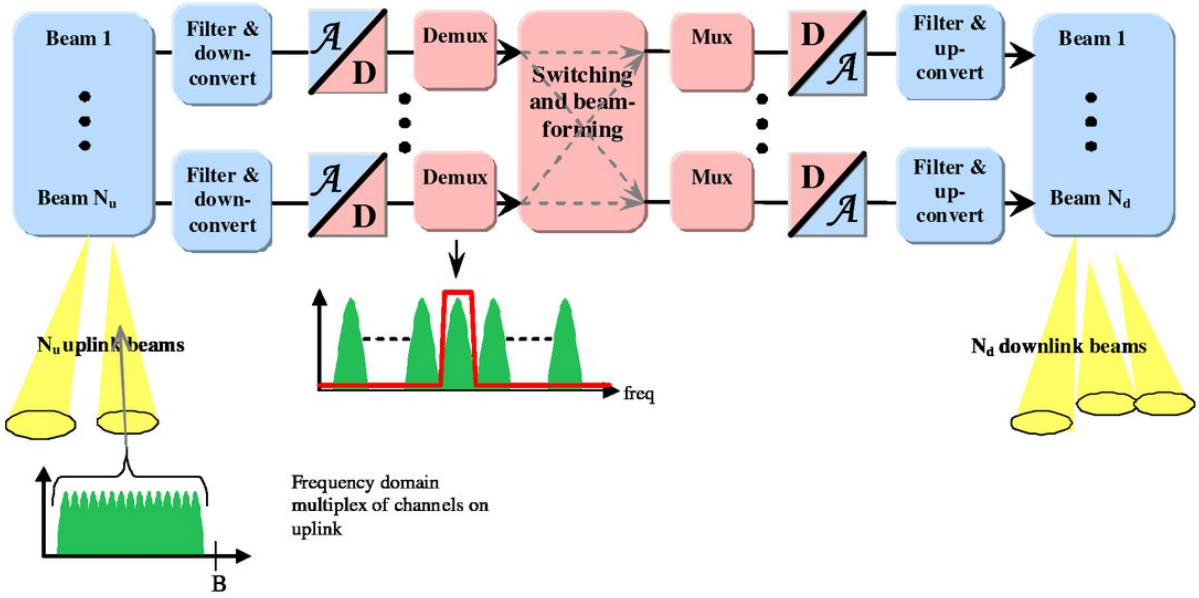

Figure 2.4: Example of a multi-beam satellite schematic.

In conclusion, the whole purpose of a satellite communication system is to support the operation of a (large) number of transponders in a specific location in space, and to keep them functional for as long as possible. This is needed because the cost of development, manufacturing and launch of a satellite is, generally, quite high. As a consequence, for satellite systems to be economically viable, they must have a life time that is as long as possible so that the satellite owners can recover the costs, and make a profit, renting out the communication capacity to their customers.

2.2 Transponders and waveguide technology

The basic function of a transponder (both transparent and regenerative) is to receive the input signal, amplify it to compensate for the path losses, and re-transmit the same identical signal. To this end, for example, the classic (transparent) transponder system is then composed of six main parts or components (Fig. 2.5):

- The input and output (I/O) antennas.
- An input band-pass filter.
- A low-noise amplifier (LNA).
- A frequency converter (composed of an oscillator and a frequency mixer).
- An output band-pass (or low-pass) filter.
- A high power amplifier.
- A high power output filter.

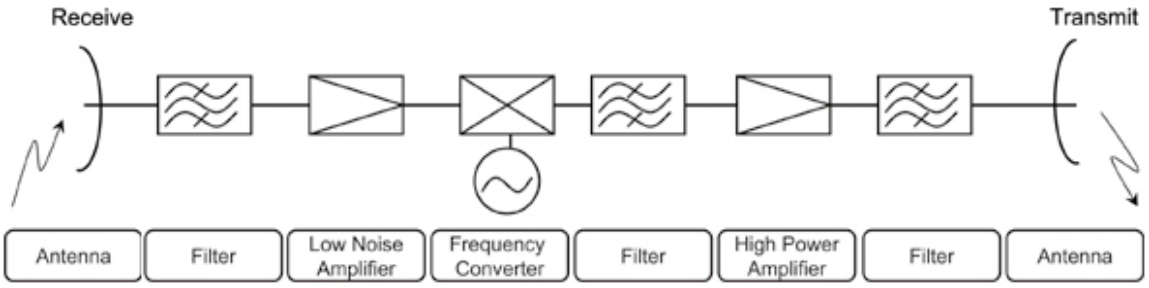

Figure 2.5: Example of bent-pipe satellite transponder diagram.

As we can see, microwave filters are one of the key components of satellite transponders. They take care of selecting the correct input signals, within a predefined range of frequencies, and eliminate (or reduce) all other signals, including the external noise. In the output, they ensure that power is radiated only in the intended frequency range so that other services, operating in near-by frequency ranges, are not affected. For this reason, it is critically important that microwave filters respect the performance requirements that are defined at system level. Along with the filters, other microwave devices are usually installed in the satellite transponders, such as hybrids, couplers and switches, that allow to route the signal through all the payload and create a path between the input and output antenna of the satellite.

Historically, the most common solution for manufacturing satellite equipment has been based on waveguide technology. However, recently, other technologies, like planar micro-strip or, more recently, substrate integrated waveguide (SIW) technologies, have been used to develop the components for specific miniaturized satellites, or pico-satellites [15] and [16]. However, waveguide technology remains today the main choice to develop and manufacture components for satellite communication payloads. This is mainly due to the following attractive features:

- The waveguide technology is well understood, and substantial theoretical information is freely available for the design of all required components.
- Advanced fabrication processes are readily available.
- The resulting hardware is robust and physically stable.
- Very high power handling capability is possible.
- Waveguide devices can exhibit reasonably low signal power losses.

The above features make waveguide technology the ideal choice for the development of the space hardware just described. However, there are also a number of drawbacks when using waveguide technology:

- The fabrication costs may be high.
- Devices may be bulky and have high mass.
- The electrical characteristics may be affected by changes in operating temperature.
- It may be a challenge to assemble all required components in the small room generally available in satellites.

Nevertheless, even if some negative features must indeed be accepted, the waveguide technology has proved itself to be the best choice for innumerable satellite implementations. We hope that our effort to develop tunable and reconfigurable microwave filters, will ensure the continued use of waveguide technology also in future, more advanced telecommunication satellite payloads.

2.3 Waveguides and microwave filters

A waveguide is, basically, a hollow metallic pipe (usually of rectangular or circular cross section) inside which, above a certain frequency called the cutoff frequency, an electromagnetic wave can propagate.

Another important characteristic of waveguides is that they allow energy to propagate within their cross section, but only for a discrete set of specific field configurations called waveguide modes [17]. The number of modes of a hollow waveguide is, in fact, infinite and each mode has its own specific cutoff frequency. The mode with the lowest cutoff frequency is called the fundamental mode. Normally, the fundamental mode is used to carry the signal in a waveguide system. If the cross section of the wave-guide is not changed along the waveguide, the modes remain separate, or rather, *they are independent from each other*. This means that in a waveguide with uniform cross section different modes can propagate without exchanging energy among each other. They can, in fact, be modeled as separate transmission lines.

The waveguide modes can also be divided into two families of modes, depending on their basic electromagnetic field distributions. The two families (or classes) are: transversal electric (TE) or transversal magnetic (TM), Fig. 2.6.

Waveguides are usually operated in the frequency range between the lowest cutoff frequency, and the cutoff frequency of the first higher order mode. Below the cutoff frequency of the lowest mode, energy cannot propagate in a waveguide. Waveguides can therefore be considered to be high-pass devices (or filters).

A waveguide filter, on the other hand, allows the transmission of only a certain specific set of frequency values. This range of frequencies is normally called the filter pass-band. All other frequencies are strongly reduced (or possibly eliminated).

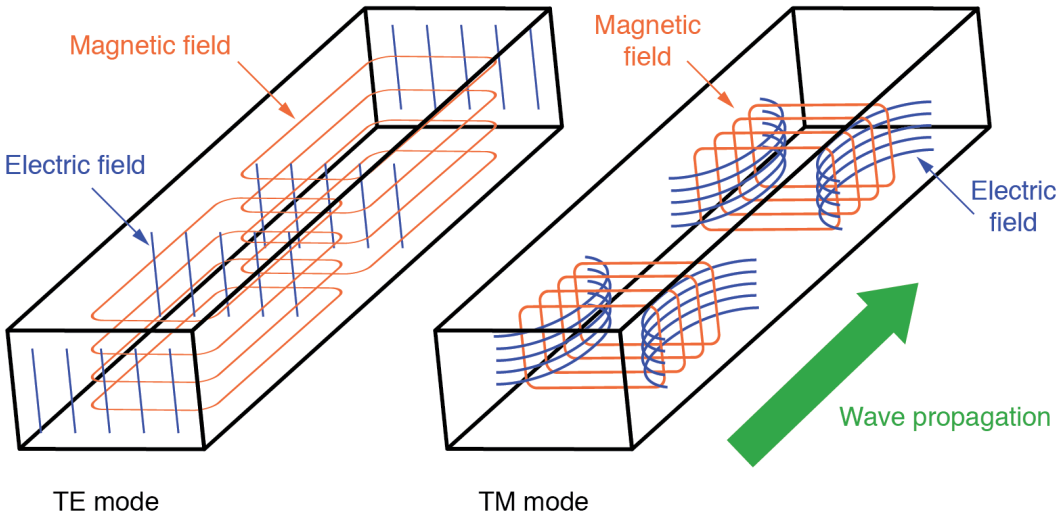

Figure 2.6: Field distribution for TE and TM modes in a rectangular waveguide.

In order to achieve this behavior, the waveguide filter needs to have a specific internal shape. The filter performance is, in fact, determined by the interactions (or interference) caused by the presence of changes in the shape of the cross section of the basic waveguide. The presence of sections of waveguide with a different shape causes the higher order modes of the waveguide to exchange energy with each other. The nature and extent of this energy exchange (or *interference*) is linked directly to the change in waveguide shape. The filter performance is then completely determined by the interactions of the waveguide modes as they propagate through the sections of waveguide with different shapes.

This means that we can obtain the same filter response for a very large number of different kinds of waveguide structures. A filter designer must then be able to select the particular filter shape that produces the best overall performance.

Microwave filters are normally classified according to their frequency response, as follows:

- Low-pass.
- Band-pass.
- High-pass.

Fig. 2.7 shows the different frequency responses of each of such filters.

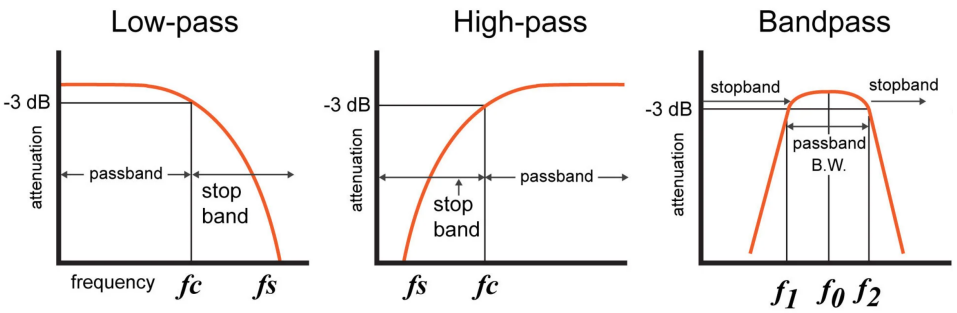

Figure 2.7: High-pass, band-pass and low-pass filter responses. *fc* (cutoff frequencies), *fs* (stop-band frequencies), *f0* (central frequency) and f_1, f_2 (band-edge frequencies).

The vast majority of the filters are designed to work only with the fundamental mode of the waveguide but, we will see that we can also find in the technical literature filters that make use also of the higher order modes of the waveguide [8].

Finally, we can classify the filters according to their physical structure. As already discussed, there are, in fact, many different possible configurations. We briefly describe next some of the most used filter structures:

- Resonant waveguide filters with irises [18]. These are the most basic, and oldest, waveguide filters, usually made in rectangular waveguide and using the fundamental TE_{10} mode. The uniform rectangular waveguide sections are used as resonators, coupled to each other by apertures (windows or irises) in the resonator end walls. The irises can implement inductive or capacitive couplings, see Fig. 2.8.

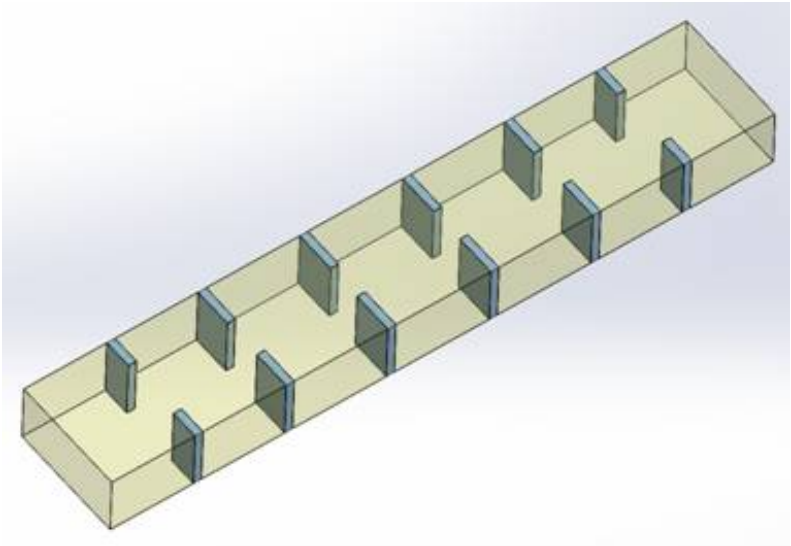

Figure 2.8: Example of a resonant waveguide filter with inductive irises.

- Waveguide filters with dielectric resonators [19] and [20]. These filters use pieces of dielectric material inside the waveguide resonators. They are usually much smaller as compared to those of the classic filters without dielectric. On the other hand, the presence of dielectrics excite a large number of higher order modes making their design more complex, see Fig. 2.9.

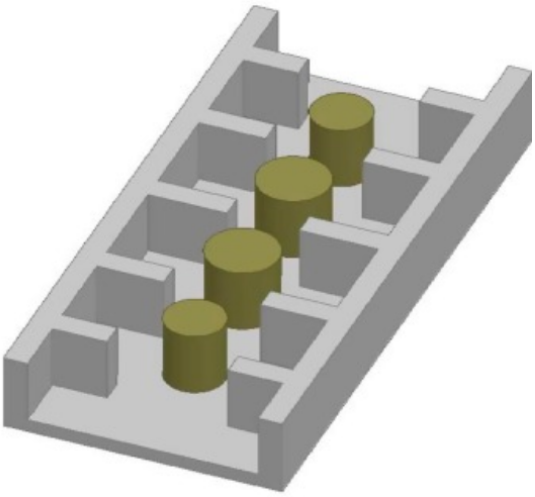

Figure 2.9: Example of waveguide filter with dielectric resonators.

- Corrugated and double-corrugated waveguide filters [21]. These filters are usually employed to implement low-pass band responses. They use a number of ridges along the resonators that provide responses having at the same time a wide low-frequency pass-band and a wide stop-band, see Fig. 2.10.

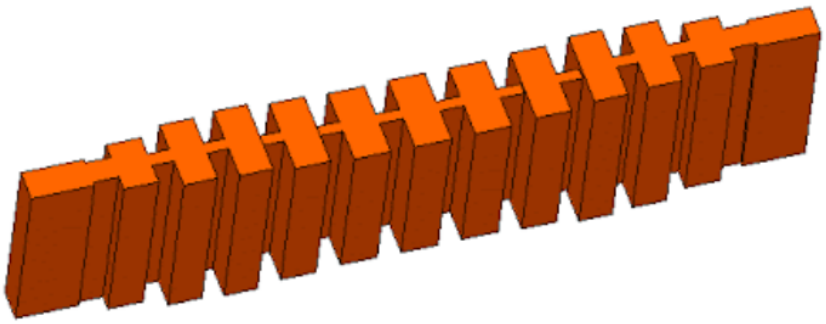

Figure 2.10: Example of corrugated waveguide filter.

This concept can be expanded adding transversal slots cut through the corrugations that suppress the spurious modes present in the filter structure [22]. This kind of filters are also known as waffle-iron filters, see Fig. 2.11.

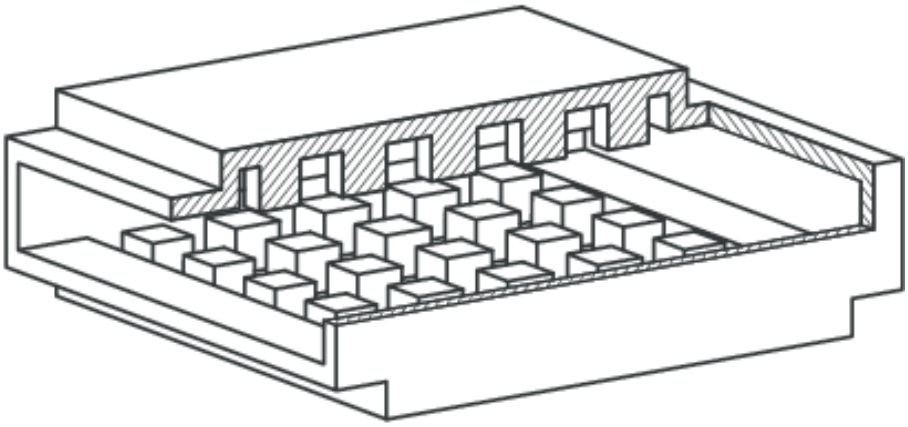

Figure 2.11: Example of waffle-iron waveguide filter.

- Waveguide filters with stubs [23]. The stubs consist in short waveguides connected to the body of the filter in order to implement either an inductance or a capacitance depending on the stub length. The stubs are used to improve the response of the filter, canceling undesired resonances, generating transmission zeros or expanding the bandwidth of the filter, see Fig. 2.12.

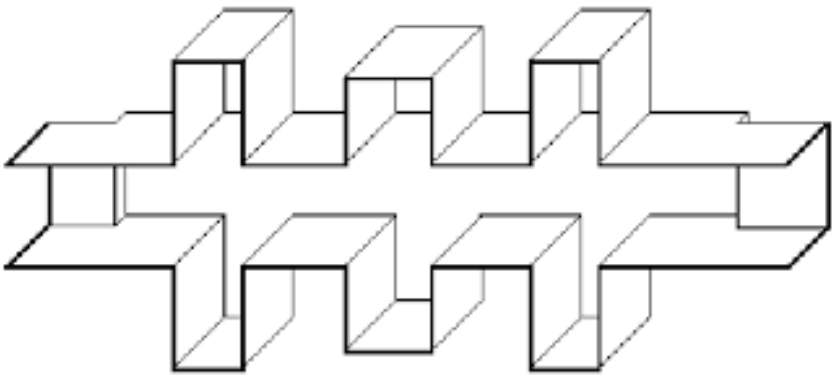

Figure 2.12: Example of waveguide filter with stubs.

- Dual-mode filters [24]-[26]. This kind of filters are also very common in telecommunication satellites. They exploits the existence of degenerate modes (modes with the same cutoff frequency but different field configuration) to highly reduce the size of the device compared to the ones with a classic (single-mode) structure. For example, in the well-known circular waveguide dual-mode filter, the two degenerate modes TE_{111} modes (the vertical and horizontal polarizations) in each cavity are coupled together by a tuning screw rotated 45° (see Fig. 2.13). Then, the two modes are coupled to the corresponding modes of the adjacent cavity by a cross-shape iris.

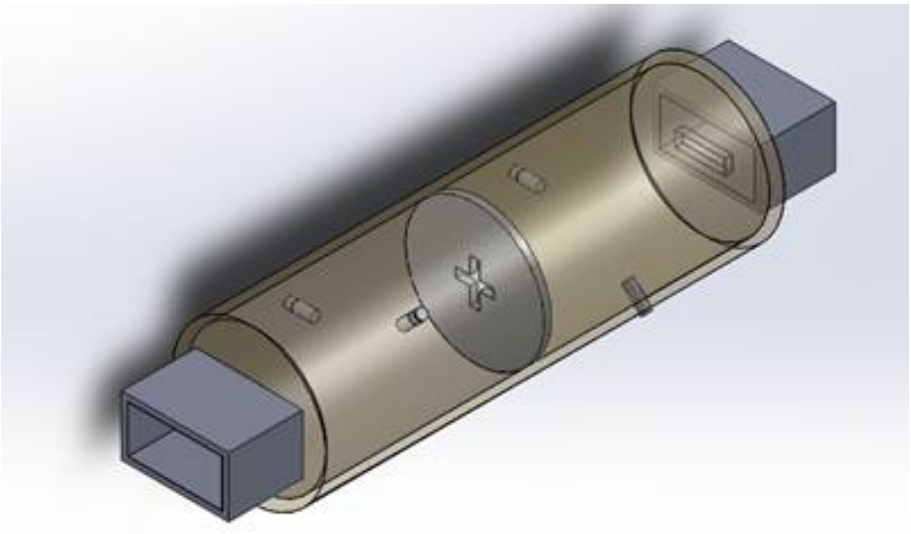

Figure 2.13: Example of dual-mode filter.

As we can see, there are indeed many different types of waveguide filter structures. In addition, it is also possible to combine several basic structures to obtain the response needed for a specific application.

Finally, it is important to note that microwave filters have been designed in the past to operate at a single center frequency, and with a fixed bandwidth. However, the constant demand for modern communication services with increased agility and bandwidth, is changing radically the filter requirements. The old (and classic) filter structures do not allow, for instance, the dynamic re-configuration of the filter responses. This means that new more advanced solutions must be developed to satisfy the novel demands.

2.4 Tunable microwave waveguide filters

Recently, new waveguide solutions have been proposed in the technical literature with the objective of providing remote variation of the response of the filters, changing, for instance, the values of the central frequency, bandwidth or return losses.

However, this has been done using conventional metallic tuning screws [27]. This solution is indeed simple and elegant, but it does have a major disadvantage. The tuning screws must be securely fastened to the body of the filter in order to work properly. Therefore, although the proposed filter structure can indeed be tuned over a wide frequency range, this can only be done manually. Furthermore, the tuning screws can reduce the power-handling capability of the filter due to the generation of undesired high-power effects [9].

Initial investigations using dielectrics rods instead of metallic tuning screws have indeed been discussed in the technical literature [28]. Furthermore, alternative solutions have also been proposed in [29] and [30] to implement the remote tunability of the filters, either based on the use of sliding walls/resonators or applying a magnetic field to an internal ferrite, thus modifying the electromagnetic response of the structure. However, the proposed filters are bulky, and the resulting structures can not be easily manufactured. Additionally, the power handling of the solution proposed in [30] is reduced due to the use of isolators, which also increase the insertion losses.

Finally, further efforts have been focused on developing new tunable dual-mode filter structures, using actuators to change the dimensions of the resonator and the position of the walls [31]. Stepped motors have also been used to control the position of tuning rods [32].

2.5 Full-wave electromagnetic simulators

The introduction of modern EM analysis techniques and simulations changed completely the classic filter design process. In the past, the initial dimensions and optimizations were based on analytical models and empirical adjustment of the dimensions, forcing the fabrication of multiple devices and the use of tuning screws to recover the ideal response [33] and [34]. Now, a wide variety of commercial EM simulators are available, implementing optimization routines and providing accurate EM responses, reducing significantly the cost and time of the design process. EM simulators have, in fact, been used to develop a variety of different approaches for the design of waveguide filters. In this context, the specifications, the technology to be implemented, the best EM simulator available and the experience of the designer will decide which is the best method (in terms of time and cost) to finally design a specific waveguide filter.

The classical starting point for the synthesis of a waveguide filter is to use a function approximating the ideal filter band-pass performance in the low-pass domain (well-known functions are the Butterworth, Chebysev or elliptic functions), or approximating the phase response (Bessel or Rhode functions) and then obtaining the ideal equivalent circuit (usually based on lumped elements LC). Richard's transformation can then be used to transform the inductive and capacitive behavior of the components in equivalent transmission lines (stubs of the same electric length). Kuroda's identities can also be used to facilitate the conversion between the various transmission line realizations [35]. Furthermore, distributed models based on resonant transmission lines and inverters can also be used for this purpose [36]. The next step is to use one of the many methods based on computer-aided design (CAD) tools, to rapidly obtain the physical representation of the waveguide filter based on the ideal circuit model developed in the first step.

Some of the most common CAD commercial packages are based on electromagnetic analysis techniques, which are driven by suitable optimization algorithms.

Finally, multiple EM simulators have emerged in the last years that implement different full-wave analysis techniques (e.g. finite elements methods [37], multimode networks [38], mode-matching [39] and finite integration technique [40], to mention a few), and are all able to simulate accurately and efficiently the EM response of the structures. Moreover, we can also find multiple optimization algorithms that can be used to obtain the ideal response of the filter (e.g. quasi-Newton, gradient, random-search, etc...). Each of them has specific advantages and disadvantages with respect to each filter (with particular features) to be designed.

In the realization of this doctoral thesis, three main commercial EM software tools have been used in order to analyze, design and optimize the different novel filter structures developed. These EM simulators are: HFSS (from ANSYS), FEST3D and CST Studio Suite (from Dassault Systèmes).

2.6 Design and optimization procedures of microwave waveguide filters

As already discussed, to accommodate the continuous changes in filter requirements, new advanced modeling and design techniques have also been developed in recent years. It is, therefore, important to understand and outline how they can be used to design advanced filters. A possible modern filter design process can be described as follows:

- We first obtain a theoretical filter transfer function that satisfies the given requirements, using known mathematical developments from network theory.
- We can then model the ideal transfer function with an ideal circuit composed of transmission lines (resonators), and ideal coupling elements (inverters).
- We can then compute the S-parameters (objective response) of this circuit model.
- We then compare the objective circuit model response with the one given by a real waveguide structure, that implements the circuit elements using waveguide resonators, and waveguide discontinuities as coupling elements. This step is usually carried out with a low accuracy EM simulator that performs the required computations in a very short time.
- Finally, we include in the filter structure all of the features linked to a real manufacturing process (e.g. rounded corners, losses due to the material and tuning elements), and we simulate and optimize the real structure with a high-accuracy full-wave EM simulator.
- The filter can then be manufactured and measured, with good confidence that the experimental results will be very similar to the simulated performance.

As we can see, from the very first step, the use of EM simulators has become absolutely essential in the filter design process.

Another key element in the design process is an efficient optimization tool (or algorithm). In this context, the vast majority of modern EM simulators do provide a number of automatic optimization algorithms, in order to obtain the required response with the waveguide structure that is being simulated. These algorithms can indeed reduce the time required in the design process, however, the time to carry out the computations generally increases exponentially with the number of dimensions (or variables) to be optimized. For this reason, the optimization step in the filter design process is not only based on optimization algorithms, but in efficient procedures that are specifically developed for the filter to be designed. As a result, we can indeed find a very large number of these optimization procedures in the technical literature such as multi-port optimization techniques [41], topology optimization methods [42], and the already mentioned space-mapping techniques [10]-[12].

In conclusion, it is important to note that, the correct combination of the EM simulator and an efficient optimization method is a key aspect in the filter design process. The waveguide filter design does not follow a unique path to obtain the desired result. Depending on the specifications of the filter, topology and available resources, we can select which is the best method and procedure to follow in order to obtain the best outcome. That is, to obtain with the smallest time, cost and filter size/volume, the best response that can match the required filter specifications.

Chapter 3

Filter design using OS-ASM

This chapter describes and extends the results obtained during the research work related to this thesis in the area of Space Mapping. It is important to note that the results described in this chapter have resulted into the following scientific publications:

- J. Ossorio, J. Vague, V. E. Boria, and M. Guglielmi, "Eficient implementation of the aggressive space mapping technique for microwave filter design," *in 47th European Microwave Conference,* pp. 644-647, Oct. 2017.
- J. Ossorio, J. C. Melgarejo, V. E. Boria, M. Guglielmi, and J. W. Bandler, "On the alignment of low-fidelity and high-fidelity simulation spaces for the design of microwave waveguide filters," *IEEE Transactions on Microwave Theory and Techniques,* vol. 66, no. 12, pp. 5183-5196, Dec. 2018.

Space Mapping (SM) was first introduced by professor John W. Bandler in 1994 [10]. SM is essentially an optimization procedure that is based on the use of two different simulation algorithms (or spaces) that describe the same object (a microwave component for instance). In particular, the first is a fast but not accurate simulation algorithm (the coarse or low-fidelity model), while the second is a highly accurate but computationally expensive algorithm (the fine or high-fidelity model). The second model could also simply be the measured electrical behavior of the component. The basic idea behind SM is that, under certain conditions, it is possible to extract useful information about the behavior of the fine model by performing computations with the coarse model only. As the name indicates, the basic objective of SM is to establish a mapping between the coarse and fine models. The correct mapping is usually obtained with an iterative procedure, where the number of steps required is linked to the number of variables that need to be optimized.

A further development of this approach is the Aggressive Space Mapping (ASM) proposed in [11] and [12].

In the ASM approach (see details in [12]), the number of initial fine simulations required in the original implementation of the SM algorithm [10], are reduced by first using the identity matrix as the initial space mapping matrix. Then, the ASM method employs a quasi-Newton iteration together with the update of the space mapping matrix by means of the classic Broyden formula [43]. Due to its simplicity and ease of implementation, this very simple ASM concept evolved, over the years, into an extremely powerful and widely used family of optimization procedures [44]. A very large number of contributions concerning ASM can indeed be found in the technical literature in very different areas of investigation [45].

In particular, initial ASM implementations for the design of microwave filters appear in [46], where ASM is used to design inductive microwave filters with rounded corners. In addition, ASM techniques have also been used for the design of multiplexers based on dielectric-resonator filters [47], where the number of ASM iterations needed are high due to the high number of variables involved in the complete design process.

Furthermore, several contributions have been recently published with the aim of reducing the number of ASM iterations (and the related cost) by focusing the efforts on improving the parameter extraction optimization algorithms ([48]-[50]), on refining the fine models employed (even using measured data) [51], [52], on a variety of other techniques ([53]-[56]). A summary of the practical use of all of these advances with different types of microwave filters can be found in [57].

Our contribution in this area is aimed at improving the efficiency of the ASM technique [58]. We have, in fact, shown that, under certain conditions, it is possible to design a waveguide filter with ASM in just one iteration [59], using as coarse model a Multimode Equivalent Network (MEN) representation of the filter structure [60].

In this context, therefore, the objective of this chapter is to demonstrate how and why, for resonant structures in general, and for waveguide filters in particular, an ASM based design and optimization procedure may converge to the desired target performance in just one step, independently from the number of variables involved in the optimization process. We call this particular methodology One-Step Aggressive Space Mapping (OS-ASM). This remarkable behavior is first justified in terms of the well known EM cavity perturbation theory, and is then fully demonstrated numerically with a basic resonant structure. In addition to theory, a number of practical filter design examples are also discussed, indicating under what conditions an ASM based design and optimization procedure may (or may not) converge in just one step.

3.1 Cavity perturbation theory

The basic behavior of a microwave cavity perturbed by a small shape variation has been known for quite some time [61]. The basic effect that can be observed, by introducing a small perturbation dV in the shape of a cavity (see Fig. 3.1), is a small shift in resonant frequency $\omega_1 - \omega_0$ approximately given by:

$$\frac{\omega_1 - \omega_0}{\omega_0} \approx \frac{\Delta W_m - \Delta W_e}{W_m + W_e} \tag{3.1}$$

where W_m and W_e represent the actual magnetic and electric energies contained in the cavity, and ΔW_m and ΔW_e represent the time-average magnetic and electric energies contained in dV.

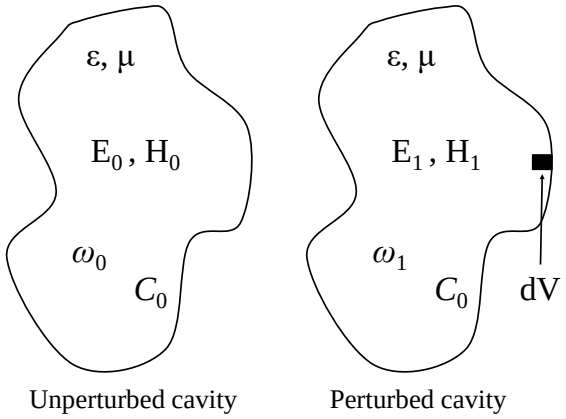

Figure 3.1: Unperturbed and perturbed cavities.

Waveguide filters are usually composed of a sequence of resonant cavities coupled to each other by apertures. Furthermore, tuning elements (screws) are usually introduced both in the apertures and in the cavities in order to compensate the manufacturing errors. In this context, therefore, microwave filters can indeed be viewed as *complex* microwave cavities and, therefore, their behavior must follow the cavity perturbation theory.

3.2 Experimental investigation

To explore this point in more detail, we now perform two simple experiments. Let us consider a filter composed of a single cavity as shown in Figs. 3.2 and 3.3, for the structure and the simulated performance, respectively. This is indeed the simplest possible inductive waveguide filter.

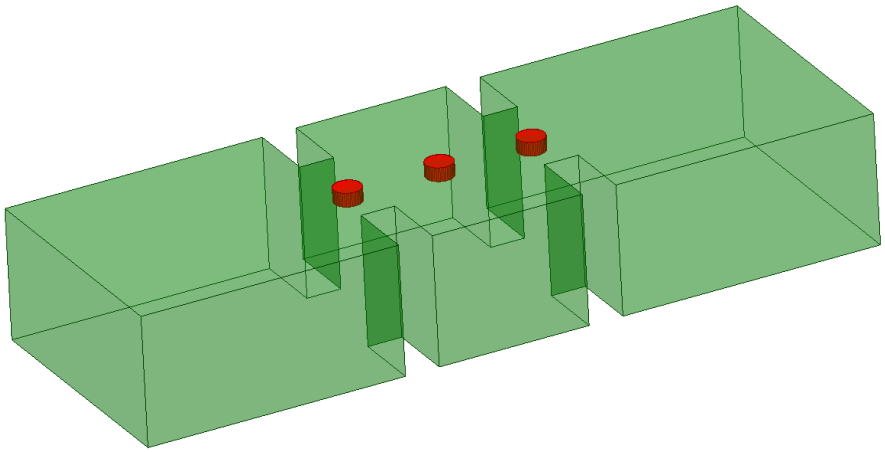

Figure 3.2: One-pole tunable filter structure.

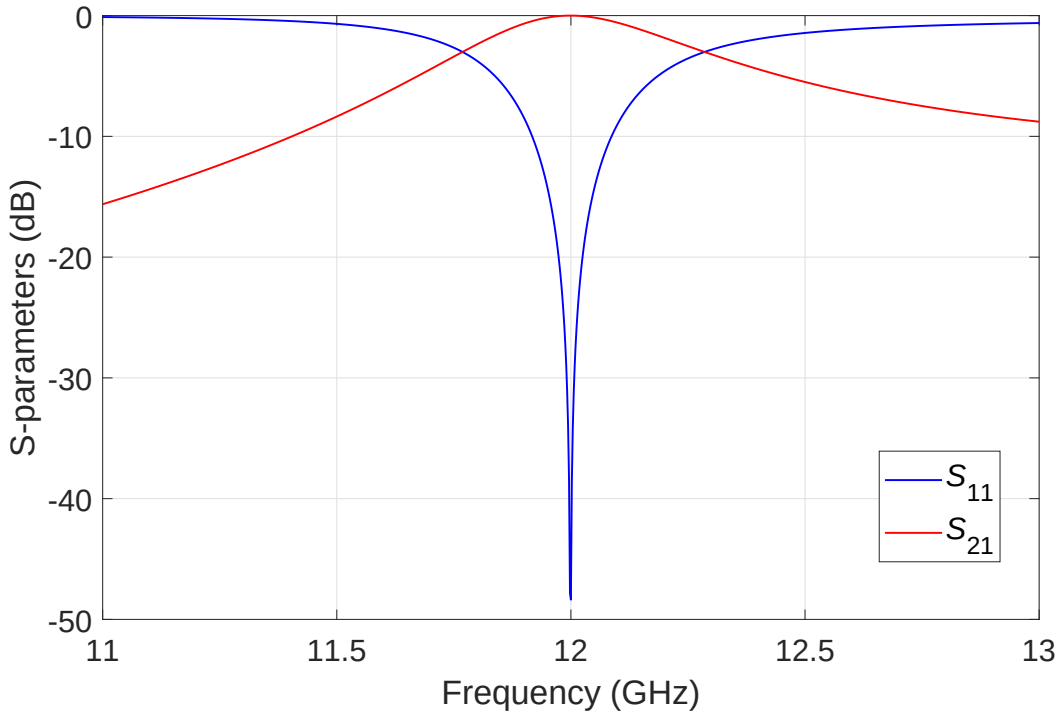

Figure 3.3: One-pole tunable filter performance.

It is interesting to note now that the performance shown in Fig. 3.3 has been obtained with the full-wave electromagnetic simulator FEST3D (from AuroraSat, now with CST and Dassault Systèmes). One particular aspect of FEST3D is that the user can choose the level of accuracy with which the calculations are performed.

The *computational* parameters that affect the accuracy are:

- Accessible modes.
- Green's function terms.
- Number of basis functions.
- Maximum frequency in the tuning cavities.

Furthermore, one additional important point is that in the calculations performed by FEST3D, the geometrical details of the structure are always taken into account rigorously. What changes is the accuracy with which the geometry is represented in terms of the actual capacitance and inductance values in the Multimode Equivalent Network (MEN) produced.

It is important to recall at this point that FEST3D is based on MENs, which are effectively equivalent circuit representations of the structure being analyzed.

A complete and detailed description of the MEN formulation, including the meaning and effect of the computational parameter values can be found in [60] (see page 232). In this context, the numerical values used in this section are as follows:

- Accessible modes = 10
- Green's function terms = 300
- Number of basis functions = 30
- Maximum frequency in the tuning cavities = 50 GHz

With this set of parameters, FEST3D is extremely fast computationally, however, it does not provide the maximum accuracy in terms of the electromagnetic performance of the structure in Fig. 3.2. We will, therefore, call this the low-fidelity (LF) simulation.

We now perform another *experiment*, namely, we change the values of the computational parameters in FEST3D to the following values:

- Accessible modes = 100
- Green's function terms = 3000
- Number of basis functions = 300
- Maximum frequency in the tuning cavities = 100 GHz

With this set of parameters, the accuracy of the EM computations is greatly increased. This will be our high-fidelity (HF) simulation.

Furthermore, the structure has been optimized so that the performance is exactly identical to the one shown in Fig. 3.3. In Fig. 3.4 we can see the two superimposed curves.

As we can see, the two curves are practically coincident.

The dimensions of the considered one-pole filter structure are shown in Table 3.1.

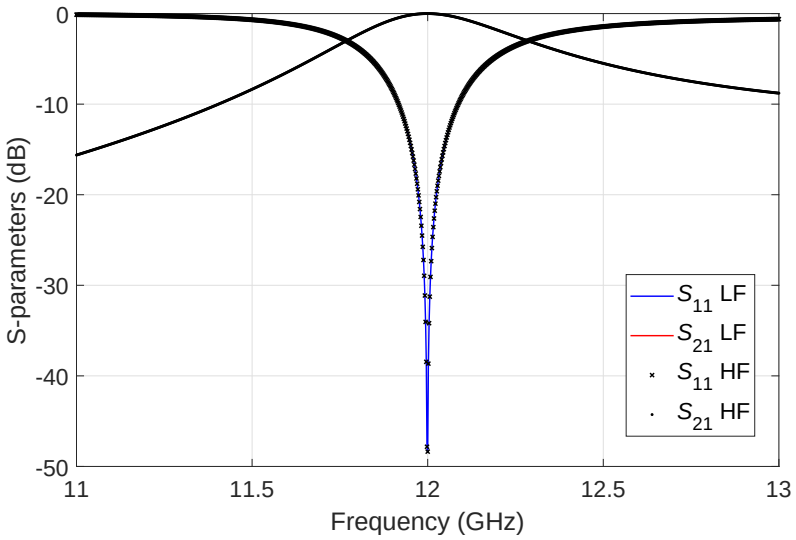

Figure 3.4: HF and LF one-pole tunable filter responses.

Table 3.1: Dimensions of the one-pole structure (mm).

Structure	Height	Width	Length
I/O aperture	9.525	9.488	3
Cavity	9.525	19.05	11.921

Naturally, however, in order to have the same exact response with two different simulations, something must be different in the structural dimensions. Indeed, the value of the penetration of the tuning screws both in the cavity and in the coupling apertures are different. As we can see in Table 3.2, there is a small, but significant, difference in screw penetration.

Table 3.2: Tuning screw penetrations (mm).

Structure	Apertures screw	Cavity screw
LF	1.0	1.0
HF	0.9108	0.9321

We now have two *different* structures, or better, *models* or *equivalent circuits*, that give the same electrical response. It is important to note at this point that, although the two physical structures are slightly different, their respective equivalent circuits must contain the exact same amount of stored electric and magnetic energy. This is, in fact, the direct consequence of the fact that their electrical responses are identical.

Continuing with our experiments, we now make the observation that, if we consider the two simulations as two different *objects*, they must both obey the perturbation theory recalled in the previous section. As a consequence, if we change the screw penetration of the same amount in the two cases, we should obtain the exact same shift in frequency. Fig. 3.5 shows the result obtained by increasing the screw penetration in the cavity by 0.2 mm in both cases.

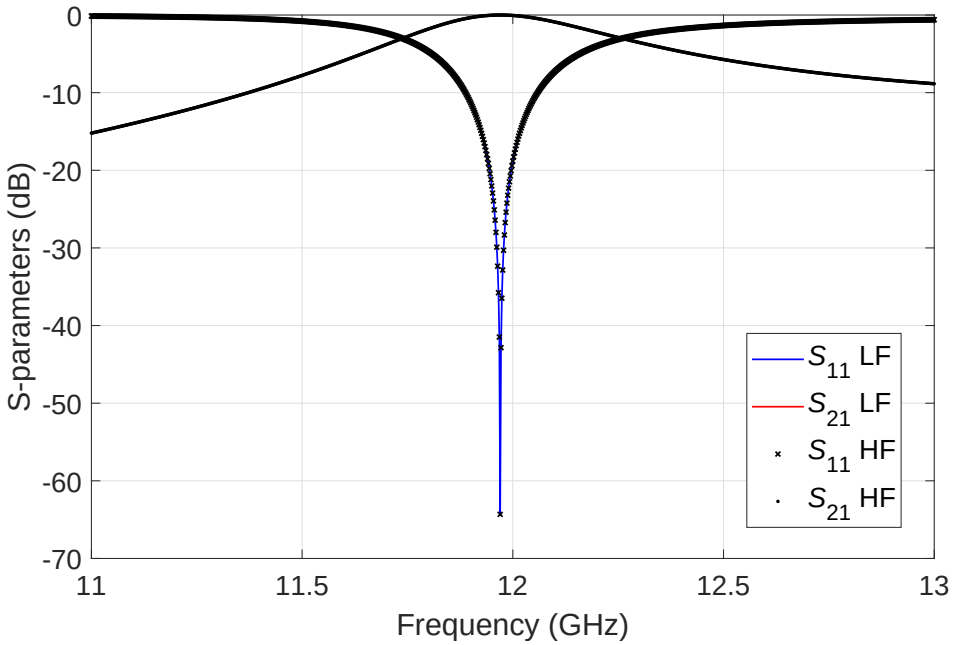

Figure 3.5: HF and LF one-pole *detuned* cavity filter responses.

As we can clearly see, once again we obtain two basically identical responses. To further understand the behavior of this simple one pole filter, we now turn our attention to the tuning screws in the coupling apertures. The following question comes naturally: do we obtain the same behavior if we change the penetration of the tuning screws in one of the apertures?

Fig. 3.6 shows the results obtained with both simulation instances with the tuning screw in one of the apertures penetrating 0.2 mm more.

As we can clearly see, we obtain once again practically coincident results. To explore more in depth the behavior of the one-pole structure in Fig. 3.3, we now compare the numerical results of the HF and LF simulations in the vicinity of the resonance.

As we can see from Fig. 3.7 , the two resonance frequencies are indeed identical, within the numerical accuracy of the simulations.

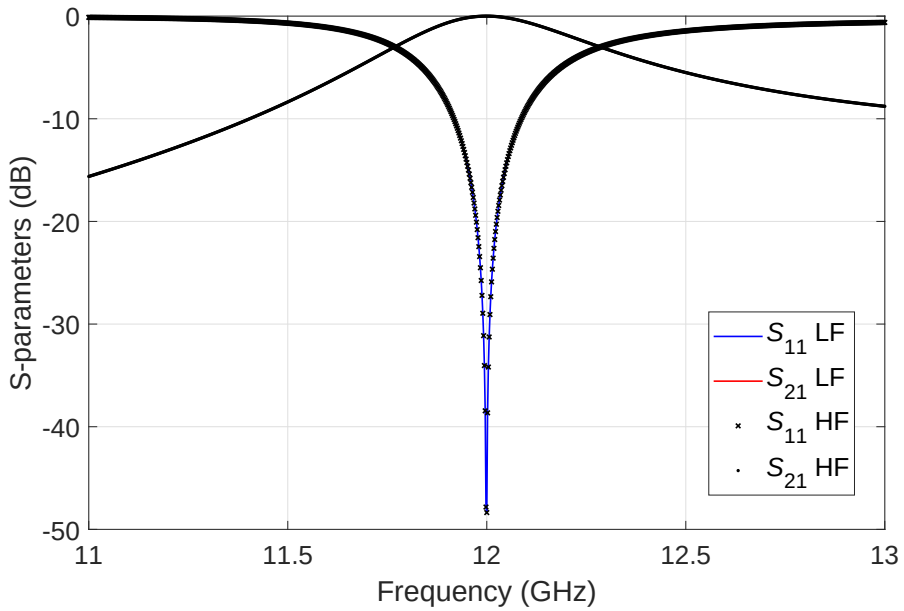

Figure 3.6: HF and LF one-pole *detuned* aperture filter responses.

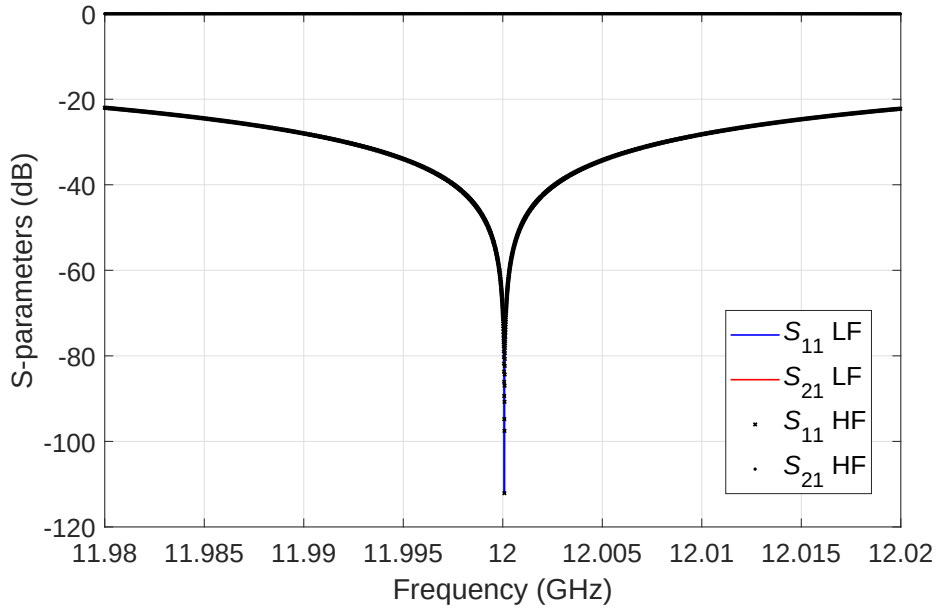

Figure 3.7: HF and LF one-pole filter simulations near resonance.

We now repeat the same comparison but with the cavities detuned by just one micron. As we can see from Fig. 3.8, also in this case the agreement between the detuned LF and HF simulations is virtually perfect (within the accuracy of the simulations).

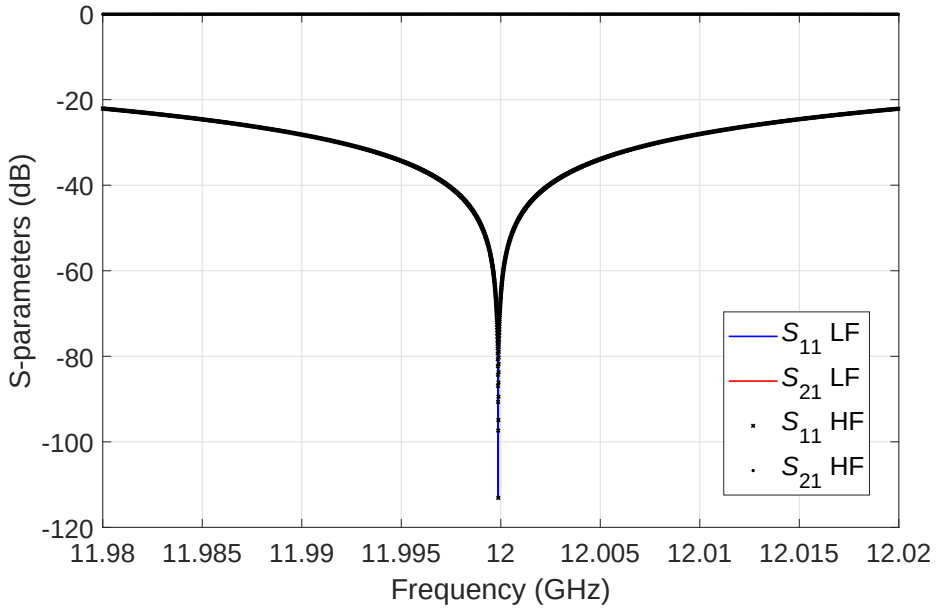

Figure 3.8: HF and LF simulations with *detuned* cavity near resonance.

The next test that we perform is with respect to the tuning screw in one of the coupling apertures. Fig. 3.9 shows the results obtained introducing again a difference of 1 micron. As we can see, once again, the agreement is virtually perfect.

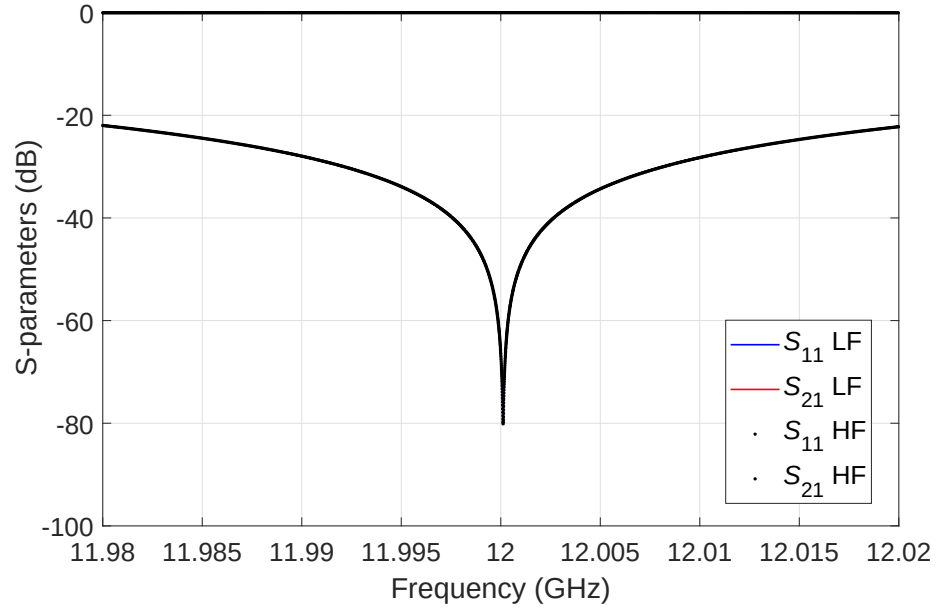

Figure 3.9: HF and LF simulations with *detuned* aperture near resonance.

3.3 Detailed numerical investigation

In order to further study and understand the behavior shown so far, we now look at the values of the numerical derivatives of the scattering parameters with respect to the tuning screw penetrations, in both the LF and HF simulation spaces. The computation of the numerical derivatives is in fact one of the key steps in any optimization procedure.

In this context, therefore, we will use the classic formula to compute the value of the numerical derivative at each frequency point in our simulation range, namely:

$$f'(x_0) \approx \frac{f(x_0 + h) - f(x_0)}{h} \tag{3.2}$$

where $f'(x_0)$ is the derivative value, h is the step (that is equal to the difference in screw penetration), and $f(x_0)$ and $f(x_0 + h)$ represent the previous value of the function, and the new value of the function after the step, respectively. For the step h, we will use, as before, the value of one micron.

We are now going to compute the numerical derivatives (of the scattering parameters) in both the LF and in the HF spaces, and compute the difference. If the difference is zero (or better vanishing small) than the two derivatives can be considered to be identical. The (average) difference is computed using the following standard expression:

$$Av.Err. = \sum_{i=1}^{N} \frac{|f'(x_0)_{LF} - f'(x_0)_{HF}|}{N} \tag{3.3}$$

where N is the number of frequency points where the calculations have been performed, and $f'(x_0)_{LF}$ and $f'(x_0)_{HF}$ are the values of the derivatives for the LF and HF spaces, respectively.

Table 3.3 shows the (average) values obtained for the derivative of the scattering parameters (in dB) with respect to the screw penetrations ($dx = h$ in equation 3.2), and the value of the errors, for a set of points near the resonant frequency (1 dB S_{21} variation on both sides), for both the S_{21} and the S_{11} parameters.

Table 3.3: Difference between derivatives of HF and LF simulations.

Detuned	Av. derivative values (LF-HF)	Av. err.	Err. (%)
$d\|S_{11}\|/dx$ Cavity	0.5872 - 0.5905	0.0033	0.559
$d\|S_{11}\|/dx$ Aperture	0.1621 - 0.1637	0.0016	0.9876
$d\|S_{21}\|/dx$ Cavity	1.8312×10^{-4} - 1.8412×10^{-4}	1.002×10^{-6}	0.547
$d\|S_{21}\|/dx$ Aperture	4.8906×10^{-5} - 4.8939×10^{-5}	3.233×10^{-8}	0.0661

As we can see, the values of the errors are at least two order of magnitude smaller than the values of the derivatives. We have also verified that the error becomes even smaller, if the value of the step is decreased.

We can therefore conclude that the difference in the values of the derivatives is indeed vanishing small (as $h \to 0$), and therefore, the derivatives themselves are essentially identical.

It is now interesting to note that, according to equations (5) and (6) of [44], the fact that the derivatives (or Jacobian) in the LF and HF spaces are identical, implies that the so-called mapping matrix B is, in fact, always equal to the identity matrix. This simple observation has, indeed, a very important consequence in the context of ASM techniques. It indicates that the ASM optimization approach for resonant structures, (and microwave filters in particular) may converge to the desired goal with *only one step* [58].

3.4 One-Step Aggressive Space Mapping (OS-ASM)

Since the One-Step Aggressive Space Mapping (OS-ASM) concept is the central topic of this chapter, we will now explain in more detail what we mean with *One-Step*.

The first step in the conventional ASM design of microwave filters is to obtain a structure in the coarse (or low-fidelity) domain that satisfies the given set of requirements that is our design *target*. What we obtain at the end of this process is a set of numerical values for the physical parameters that define the performance of the microwave filter (for instance, a set of screw penetration values X_c^t).

The next step is the simulation of the exact same structure in the fine (or high fidelity) domain. Naturally, the result that we obtain in the fine domain is a *detuned* performance ($X_c^t = X_f^{dt}$). That is, the filter structure designed in the coarse domain does not satisfy the given requirements if simulated in the fine domain.

The next step is to recover *with one optimization* in the coarse domain the detuned performance obtained in the fine domain. What we obtain at the end of this step is another set of structural parameters that represents, in the coarse domain, the detuned performance obtained in the fine domain (X_c^{dt}). We now have two sets of structural parameters in the coarse domain, and we can compute the *distance* between the two sets of parameters. This distance is, in fact, the difference between the sets of numerical values.

In practice, therefore, what we mean with OS-ASM is that if we add this difference in the inverse direction to the initial set of structural parameters in the fine domain, we obtain directly the desired optimal response in the fine domain.

In other words, from the initial coarse design, we need *only one (optimization) step* to obtain the desired final response in the fine domain. It is interesting to note that what we described verbally in the previous paragraph can also be stated in mathematical terms.

To do that, we first recall that a linear mapping between X_c (coarse domain) and X_f (fine domain) can be written in the form [45]:

$$X_c = B * X_f + C \tag{3.4}$$

where B is the mapping matrix (approximation of the Jacobian of X_c with respect to X_f), and C is an unknown constant. If we now assume that B is the identity matrix, we can write directly:

$$C = X_c^{dt} - X_f^{dt} \tag{3.5}$$

Having an expression for C, we can now use again (3.4), and write:

$$X_f^t = X_c^t - [X_c^{dt} - X_f^{dt}] = X_c^t - [X_c^{dt} - X_c^t] \tag{3.6}$$

We now note that X_f^t is the set of numerical values that will give the desired target response in the fine domain, and the expression between square brackets is the *distance* we discussed in the previous paragraph. In conclusion, starting with the target design in the coarse space X_c^t, we can obtain the target filter dimensions in the fine domain X_f^t *with only one (optimization) step*, as long as the mapping between both model parameter spaces is linear and with a unitary Jacobian of X_c with respect to X_f.

In the reminder of this chapter we show a number of examples that confirm our conclusions.

3.5 CAD demonstration

In this section, we will demonstrate that the OS-ASM behavior anticipated in the previous section is indeed correct. This will be shown using a number of different microwave filters. Each filter will be simulated with FEST3D, as the LF space, and with HFSS (from ANSYS) as the HF space. The computational parameters used in FEST3D are:

- Accessible modes = 5
- Green's function terms = 150
- Number of basis functions = 15
- Stopping criteria in the optimizations: Error = 0.001

On the other hand, the HFSS computation was carried out with the following set of computational parameters:

- Maximum $\Delta S = 0.001$
- Minimum number of passes = 5
- Minimum convergent passes = 3

thereby, ensuring the high level of accuracy of the simulation results obtained.

All the HF simulations will have the same simulation termination criteria, given by the maximum ΔS variance defined in the previous list for the HFSS computations.

For all the examples considered next, we are going to optimize the screw penetrations in order to achieve the desired response. This is convenient, since the tuning screws are the mobile parts that we can also modify when the device is fabricated. In any case, the OS-ASM can be also applied considering other dimensions of the filter structure (e.g. widths and lengths of the waveguides) as optimization parameters.

In this context, it is important to note that the LF simulations carried out with FEST3D take, on average, less than 5 seconds, while the HF simulations carried out with HFSS take, on average, more than 15 minutes. For all computations we have used a computer with an Intel Core i7-6700 @ 3.4 GHz, and with 16 GB RAM.

3.5.1 Tunable rectangular four-pole filter

The first example that we will discuss is a fully tunable four-pole filter in rectangular waveguide. The target ideal structure is shown in Fig. 3.10. The structure contains rectangular tuning elements both in the apertures and in the resonant cavities.

The filter specifications are as follows:

- Return loss $\geq$ 25 dB
- Center frequency = 12 GHz
- Channel bandwidth = 200 MHz

The first step in the design procedure is to design a standard inductive rectangular waveguide filter with the same specifications. This is a convenient starting point, since filters of that type can be synthesized automatically using available commercial software packages. The next step is the transition from the standard inductive filter structure to the low fidelity (LF) model of the tunable configuration. The result obtained is shown in Fig. 3.11.

The procedure that we have followed to perform the transition from the standard inductive rectangular waveguide filter to the structure in Fig. 3.10 is described in [62].

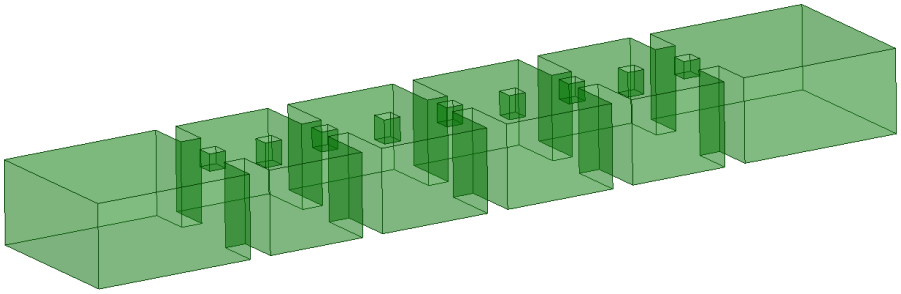

Figure 3.10: Fully tunable four-pole filter structure.

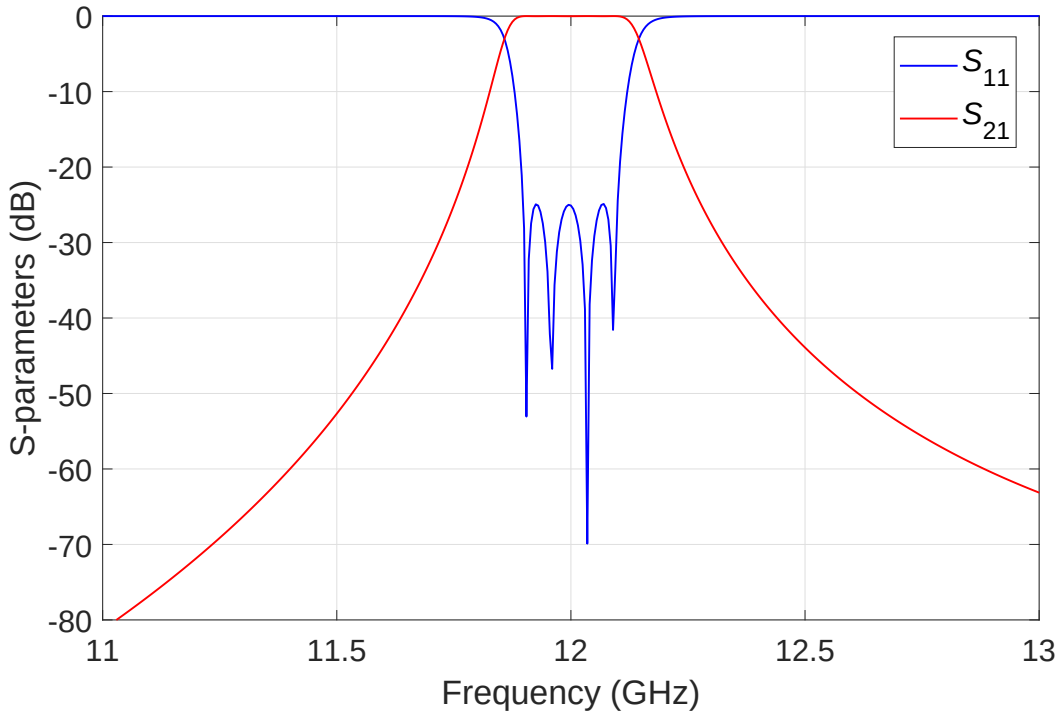

Figure 3.11: LF fully tunable four-pole filter performance.

The final dimensions of the four-pole filter designed are shown in Table 3.4. Note that the filter is symmetric and all the screw penetrations are 2.5 mm.

Now that we have obtained the target response in the LF space, we move to the HF space and perform another simulation using the same screw penetrations obtained with the LF model. Fig. 3.12 shows the comparison of the LF and HF results. As we expect, the performance of the two structures is different.

We will now use the ASM procedure to recover the HF performance in the LF space. Fig. 3.13 shows the results obtained.

Table 3.4: Dimensions of the four-pole structure in millimeters. All the heights are 9.525 mm.

Structure	Width	Length
I/O aperture	8.826	2.5
First cavity	19.05	12.811
Second aperture	5.585	2.5
Second cavity	19.05	14.297
Central aperture	5.159	2.5

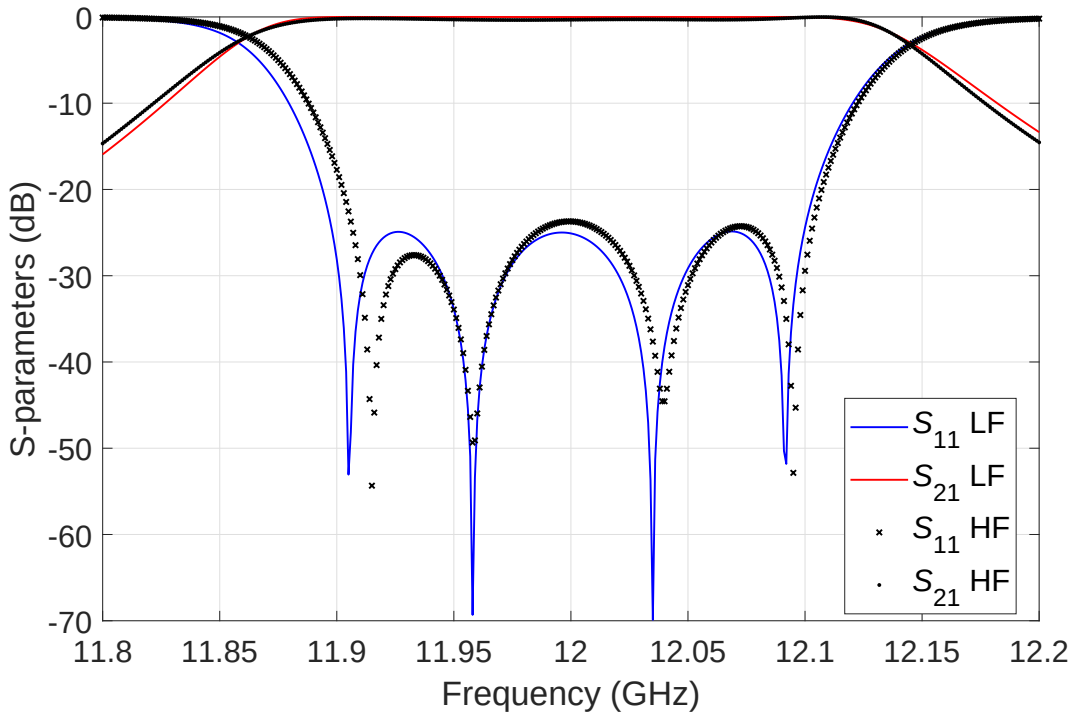

Figure 3.12: Comparison of LF (blue) and HF (black dots) fully tunable four-pole filter responses.

As we can see the two curves are essentially identical. With this step we now have achieved a virtually perfect alignment between the HF and the LF spaces. We will now *measure* the difference in screw penetration between the LF result in Fig. 3.13 and the HF result in Fig. 3.12, and apply it in the opposite direction to the (full) HF model in Fig. 3.10. Fig. 3.14 shows the results obtained using the new set of screw penetrations compared with the target ideal response. Table 3.5 shows the final dimensions of the screws for the LF and HF models.

As we can clearly see comparing Fig. 3.11 with Fig. 3.14, the desired ideal performance has been essentially obtained in *just one step*.

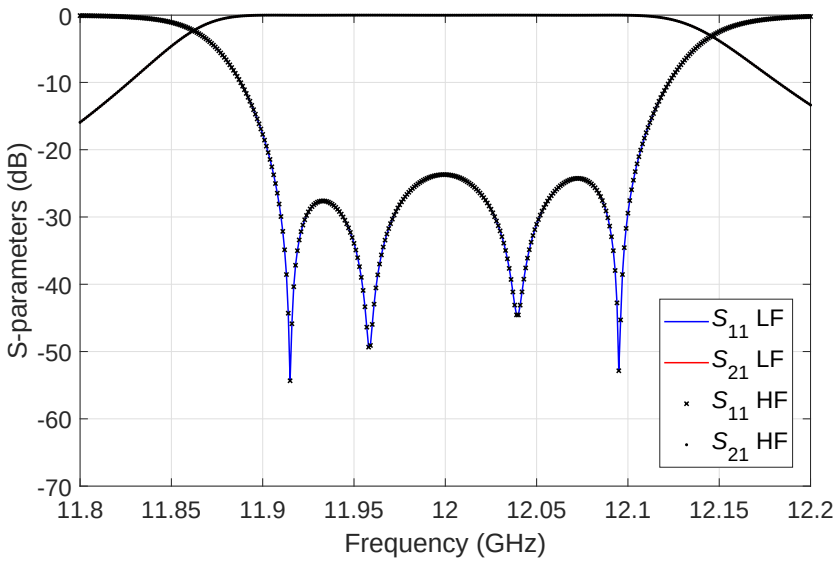

Figure 3.13: HF and LF space alignment.

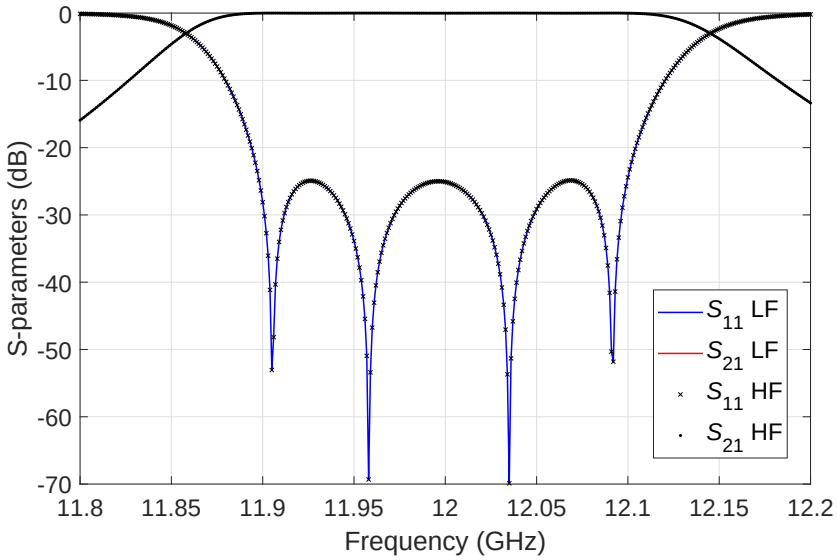

Figure 3.14: HF final performance vs. LF performance.

This first example indeed demonstrates that convergence can be achieved in just one step. However, one can object that initial point (Fig. 3.12) is very close to the actual target. In the next example, to obtain a better demonstration of the OS-ASM behavior, we have significantly detuned the initial filter response in HFSS by changing the screw penetrations with random values (between 0 to ±500 microns). The initial *detuned* response that we have obtained with this change is shown in Fig. 3.15.

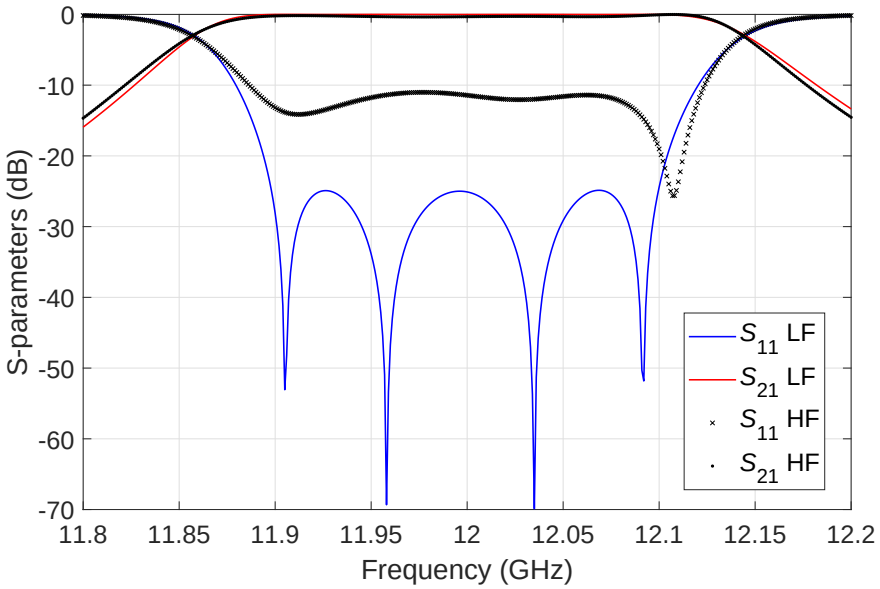

Figure 3.15: Detuned HF performance with random values of tuning element penetration.

Once we have this response we perform the ASM procedure again, recovering first the response with FEST3D and then applying the screw penetration changes to the HF space in the reverse direction. Fig. 3.16 shows the final result. As we can see, the filter performance has been fully recovered with only one step.

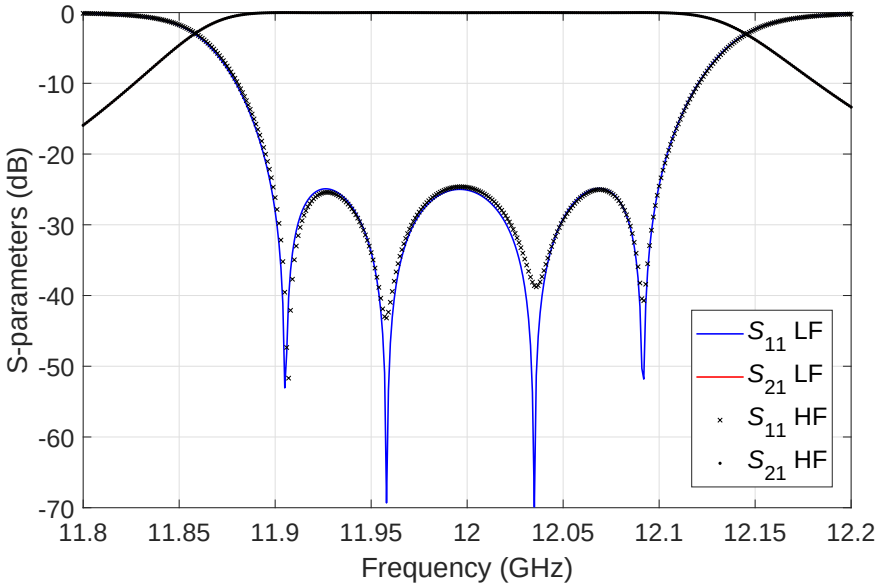

Figure 3.16: HF model performance vs. LF performance.

Table 3.5: Comparison of final screw dimensions between LF and HF models in millimeters.

Screw	LF	HF
1	2.5	2.423
2	2.5	2.552
3	2.5	2.315
4	2.5	2.512
5	2.5	2.733
6	2.5	2.512
7	2.5	2.315
8	2.5	2.552
9	2.5	2.423

3.5.2 Tunable rectangular eight-pole filter

The filter used in the previous example was a simple four-pole filter. We will now demonstrate the OS-ASM with a more complex filter structure, namely, an eight-pole filter with the same center frequency, return loss and bandwidth of the four-pole filter. Following again the filter design procedure described in [62], we obtain the filter structure shown in Fig. 3.17, with the response displayed in Fig. 3.18.

The final dimensions of the eight-pole filter designed are shown in Table 3.6. Note that the filter is symmetric and all the screws penetrate 2 mm.

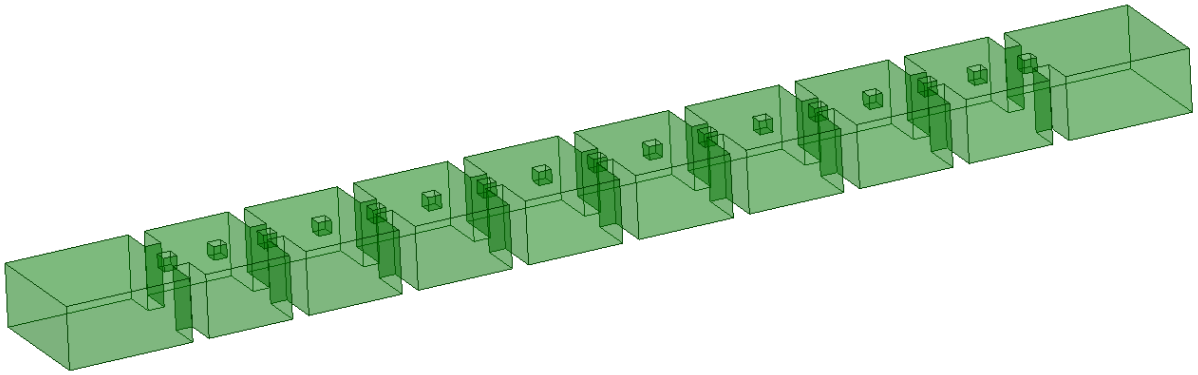

Figure 3.17: Fully tunable eight-pole filter structure.

Next, we simulate the same structure in HFSS and we obtain the results shown in Fig. 3.19.

Once again, the filter performance is detuned. Following the same steps as for the first example, we apply the ASM procedure to recover the HF performance in the LF space. Fig. 3.20 shows the result after only one step.

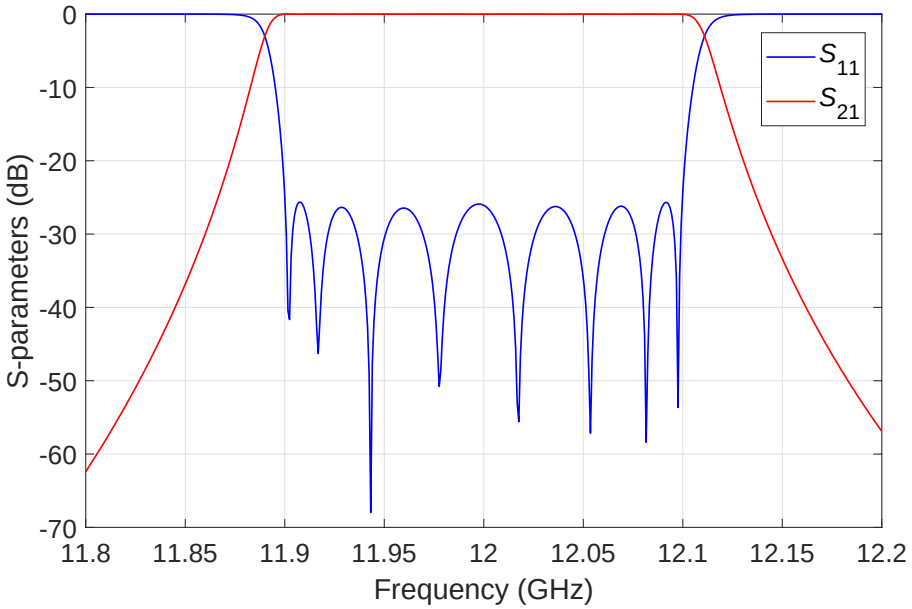

Figure 3.18: LF model performance.

Table 3.6: Dimensions of the eight-pole structure in millimeters. All the heights are 9.525 mm.

Structure	Width	Length
I/O aperture	8.694	2.5
First cavity	19.05	12.938
Second aperture	5.379	2.5
Second cavity	19.05	14.407
Third aperture	4.844	2.5
Third cavity	19.05	14.551
Fourth aperture	4.738	2.5
Fourth cavity	19.05	14.577
Central aperture	4.715	2.5

As we can see, the target performance has been obtained again in just one step. Table 3.7 shows the final dimensions of the screws for the LF and HF models.

Similarly to what we have done in the previous example, we next detuned the filter performance changing the screw penetrations by random values. Fig. 3.21 shows the detuned response of the filter, and Fig. 3.22 the result of the application of the one step space mapping procedure. As we can clearly see, again, we have obtained the ideal target response of the filter in the HF space in just one step.

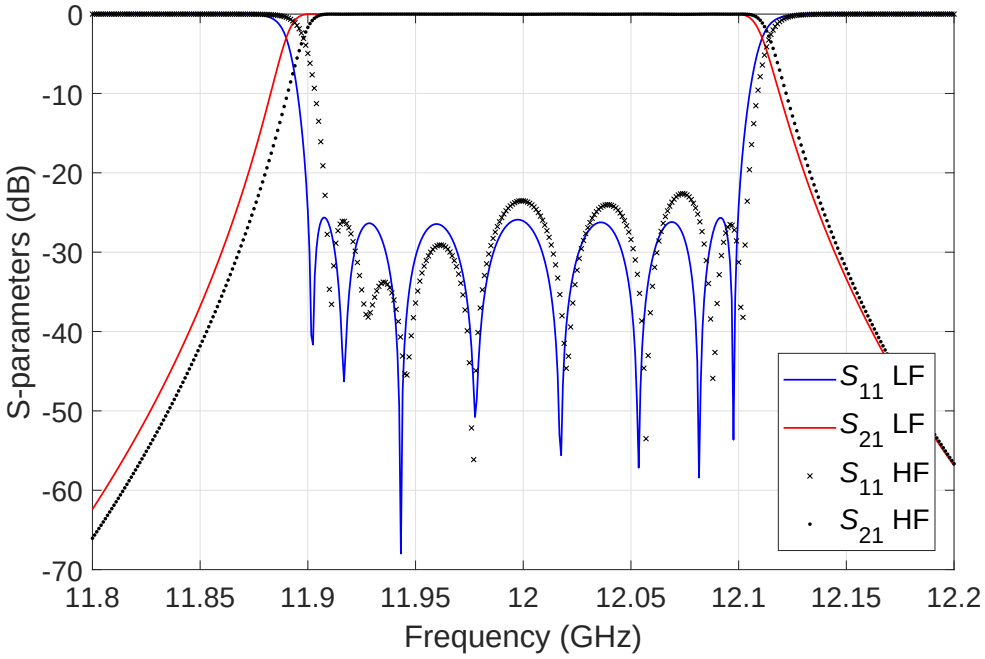

Figure 3.19: HF model initial performance vs. LF performance.

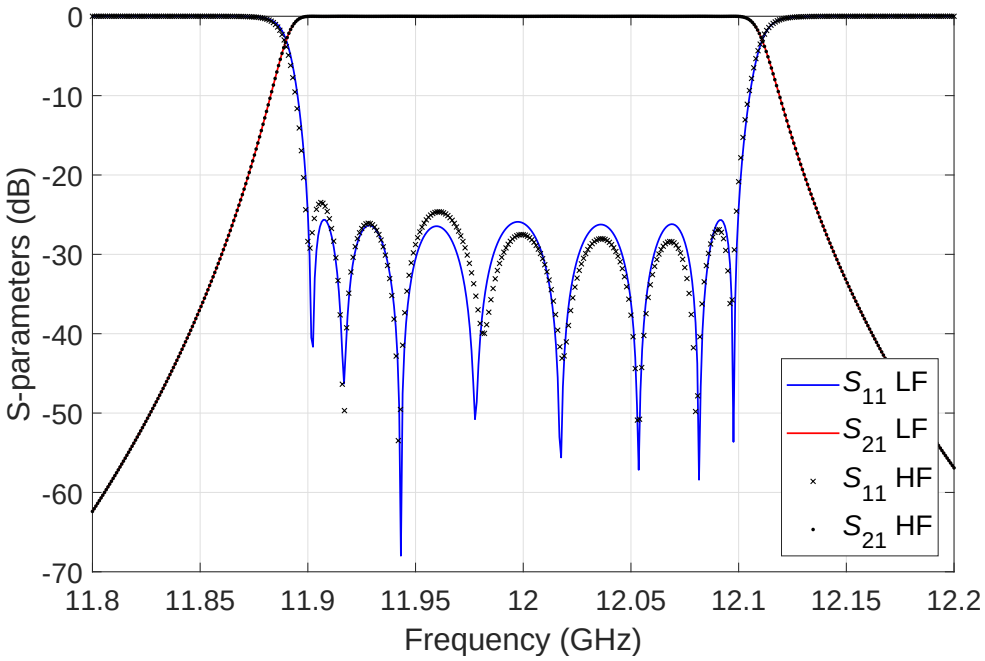

Figure 3.20: Result of the first iteration ASM procedure vs. LF performance.

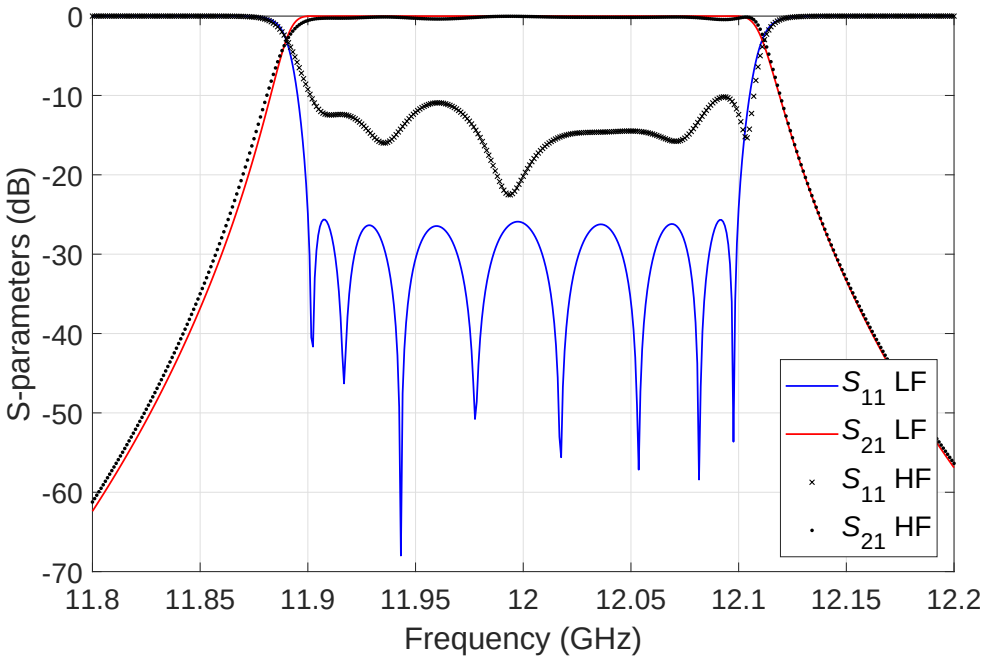

Figure 3.21: HF model detuned response vs. LF performance.

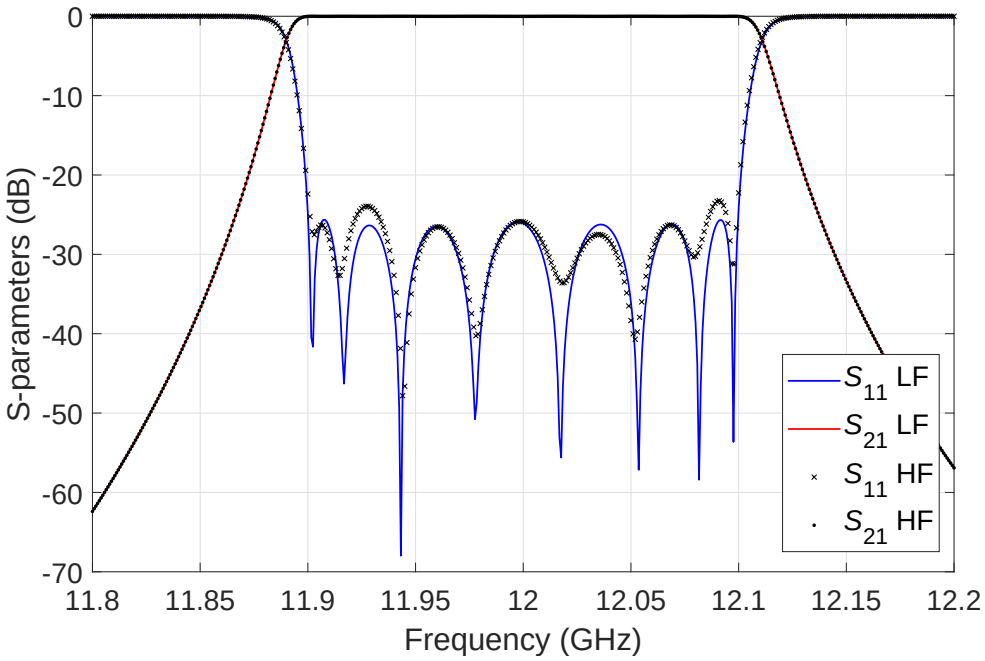

Figure 3.22: Result of the first iteration ASM procedure vs. LF performance.

Table 3.7: Comparison of final screw dimensions between LF and HF models in millimeters.

Screw	LF	HF
1	2.0	2.012
2	2.0	2.112
3	2.0	1.934
4	2.0	1.995
5	2.0	2.053
6	2.0	2.029
7	2.0	2.157
8	2.0	2.006
9	2.0	2.041
10	2.0	2.006
11	2.0	2.157
12	2.0	2.029
13	2.0	2.053
14	2.0	1.995
15	2.0	1.934
16	2.0	2.112
17	2.0	2.012

3.5.3 Classic circular dual-mode filter

The next structure that we discuss is a substantially more complex filter, namely, a classic circular waveguide dual-mode filter. The filter structure is shown in Fig. 3.23.

The filter specifications are as follows:

- Return loss $\geq$ 20 dB
- Center frequency = 17.59 GHz
- Channel bandwidth = 36 MHz

The final dimensions of the classic dual-mode filter designed are shown in Table 3.8. Note that the filter is symmetric and the I/O rectangular waveguide is the standard WR-75.

The initial screw penetrations are 1.855 mm, 1.294 mm and 1.508 mm for the 0°, 45°, and 90° oriented screws in the circular waveguide, respectively.

The filter response in Fig. 3.24 has been obtained with FEST3D using the same set of computational parameters as for the previous examples in the LF space. Simulating the structure with HFSS (HF), we obtain the results shown in Fig. 3.25 with black dots.

Now we can apply the first step of the SM procedure and recover the HF performance in the LF space.

Table 3.8: Dimensions of the classic dual-mode filter structure in millimeters.

Structure	Height	Width	Length	Radius
I/O aperture	2	6.262	1	-
Circular cavity	-	-	32.133	7.959
Central vertical aperture	4.443	1	1	-
Central horizontal aperture	1	2.833	1	-

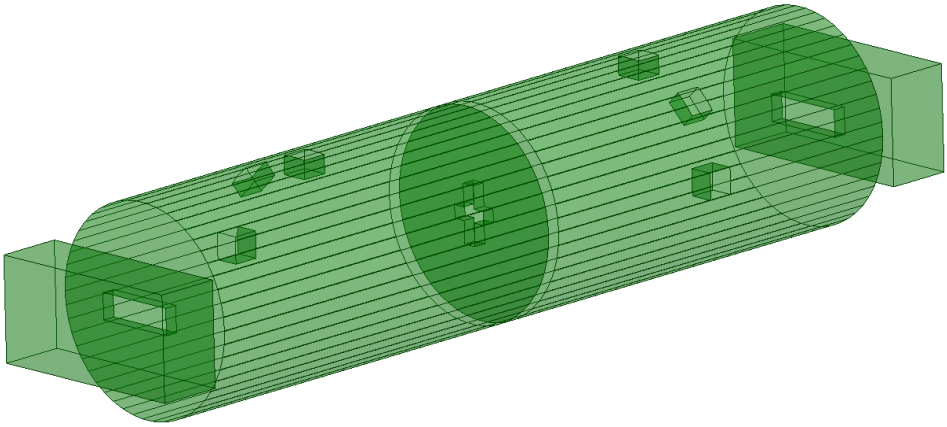

Figure 3.23: Classic circular waveguide dual-mode filter structure.

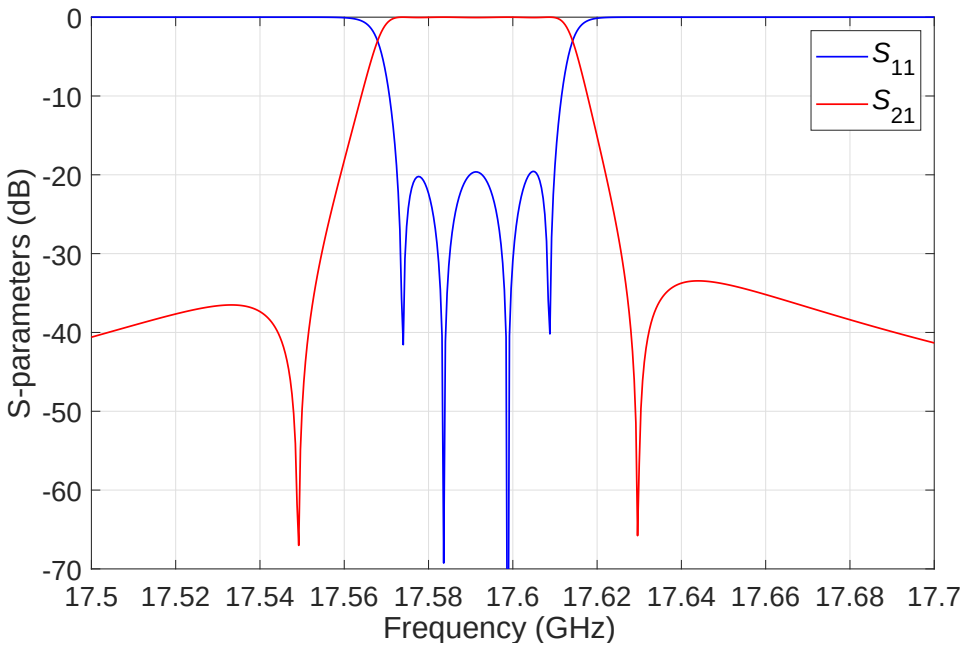

Figure 3.24: Response of the dual-mode filter.

Fig. 3.25 shows the differences between the LF and HF spaces, and Fig. 3.26 the final HF performance obtained by changing only the screws and aperture dimensions in the opposite direction.

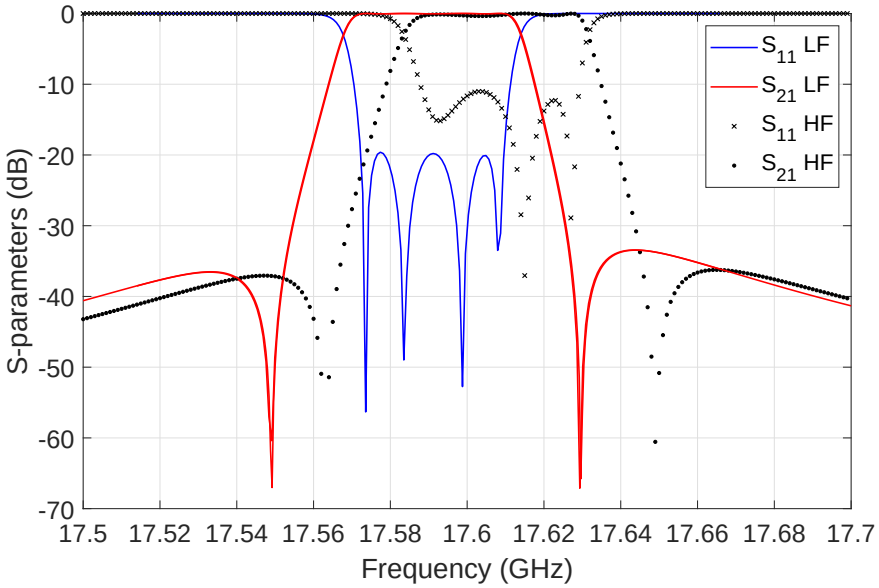

Figure 3.25: Initial HF response vs. LF performance.

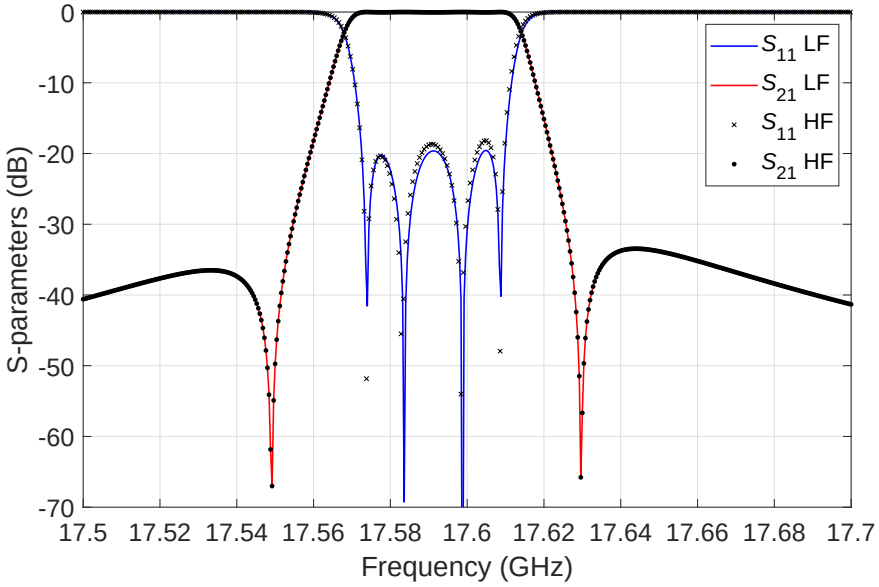

Figure 3.26: Final HF filter performance vs. LF performance.

As we can see, we have again obtained the desired response in the HF space with only one SM step. Table 3.9 shows the final dimensions of the screws for the LF and HF models.

Table 3.9: Comparison of final screw dimensions between LF and HF models in millimeters.

Screw	LF	HF
Vertical 1st resonator	1.855	1.848
45^{o} 1st resonator	1.294	1.278
Horizontal 1st resonator	1.508	1.474
Vertical 2nd resonator	1.855	1.848
45^{o} 2nd resonator	1.294	1.278
Horizontal 2nd resonator	1.508	1.474

3.6 More general examples

Up to now, we have demonstrated the OS-ASM procedure with different filters where in both LF and HF spaces the basic filter structures are almost exactly identical. In real filter design, however, the final structures are always affected by manufacturing errors.

Furthermore, the basic filter structure is usually slightly modified to reduce manufacturing costs (rounded corners), and real cylindrical screws are used as tuning elements instead of square cylinders. In practice therefore, even though the filter design may always start with an ideal structure, the final hardware will inevitably have some small geometrical differences with respect to the ideal starting point. One fact, however, will be unchanged. If the ideal structure and the final structure must have the same identical electrical performance, they must also have the same amount of stored electrical and magnetic energy. Furthermore, the perturbation theory must always be applicable to both structures. It is therefore interesting to see what is the effect on the ASM procedure if the LF and HF structures are not *exactly* identical.

3.6.1 Tunable rectangular four-pole filter with OS-ASM

As a first example we will use as the HF filter the (real) structure in Fig. 3.27 with rounded corners of 2 mm. Fig. 3.28 shows the initial response, obtained with HFSS, if we use as the starting point the dimensions of the structure with sharp corners and square tuning elements that we have used in Fig. 3.10 in the previous section (the LF filter).

As we can clearly see, the filter response is now very strongly detuned. The performance of the filter obtained after the first ASM iteration is shown in Fig. 3.29.

As we can see, in this case we have not recovered the ideal filter performance yet.

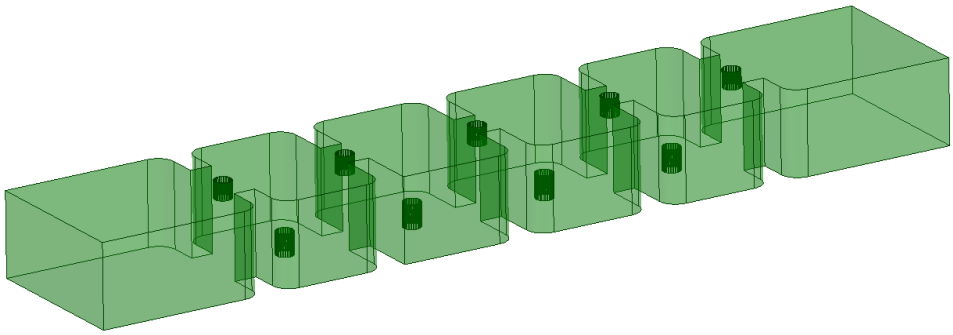

Figure 3.27: HF model structure with rounded corners and circular screws.

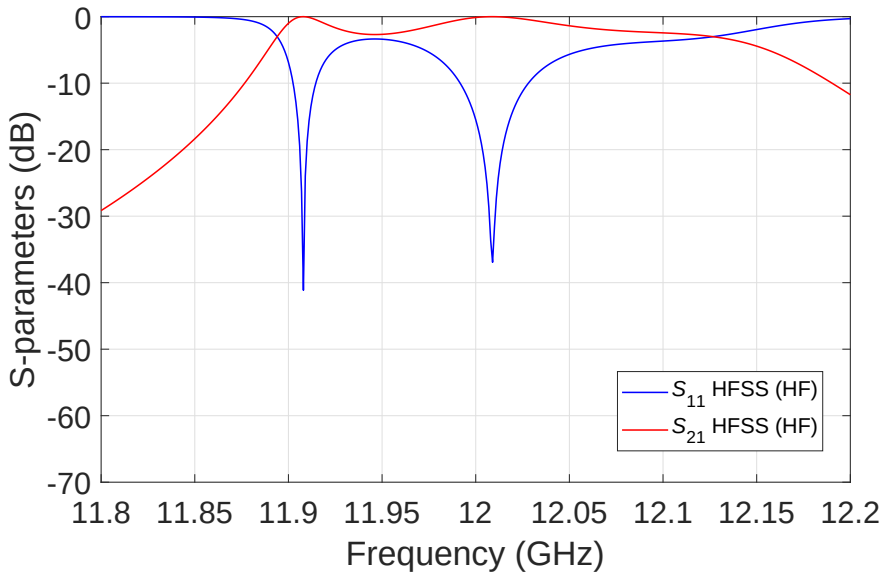

Figure 3.28: Initial response of the HF model.

We need to apply the procedure again (without updating the mapping matrix) in order to recover the ideal response. Fig. 3.30 shows the result of this second iteration. As we can see, with just two iterations we have fully recovered the filter performance.

It is important to note in this context that in this example we have stopped the ASM procedure (the exit condition) when the error given by the optimizer in FEST3D between the target performance and the last HF response is less or equal to one. The same exit condition has been used in all other examples requiring several ASM iterations.

At this point we must raise an important question: what happens if we apply the classic ASM procedure based on the use of the Broyden update, instead of using the identity matrix in the whole process (as we have done so far)?

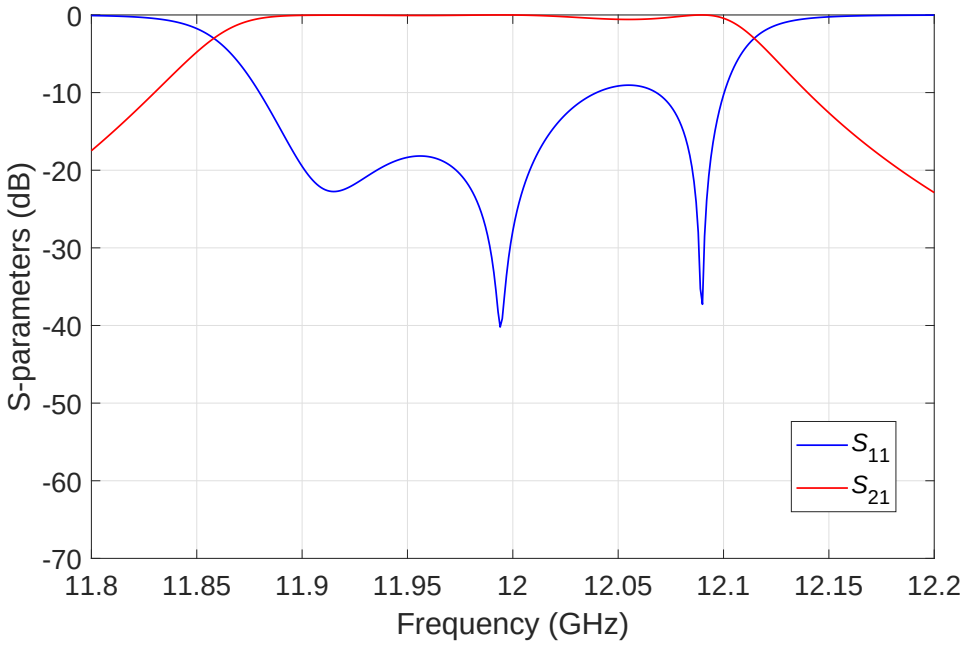

Figure 3.29: Result of the first iteration in HF.

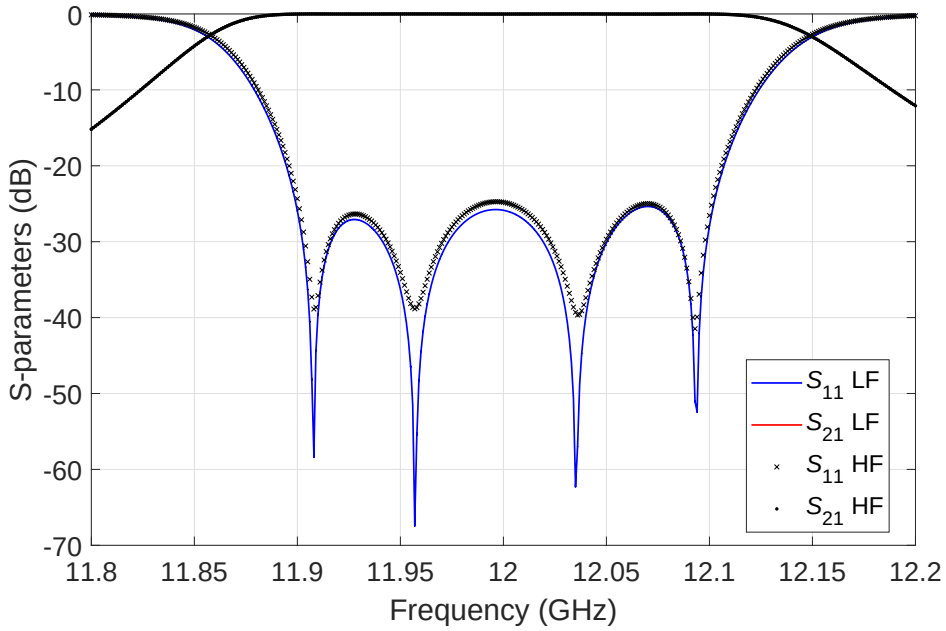

Figure 3.30: Result of the second iteration in HF vs. ideal response.

In the next section we have indeed performed this test in order to compare the results obtained.

3.6.2 Tunable rectangular four-pole filter with ASM

The initial and the first step of the *Broyden* based ASM procedure will produce the same results shown in Fig. 3.28 and Fig. 3.29. After the first two HF computations, we can use the Broyden formula and obtain the result shown in Fig. 3.31.

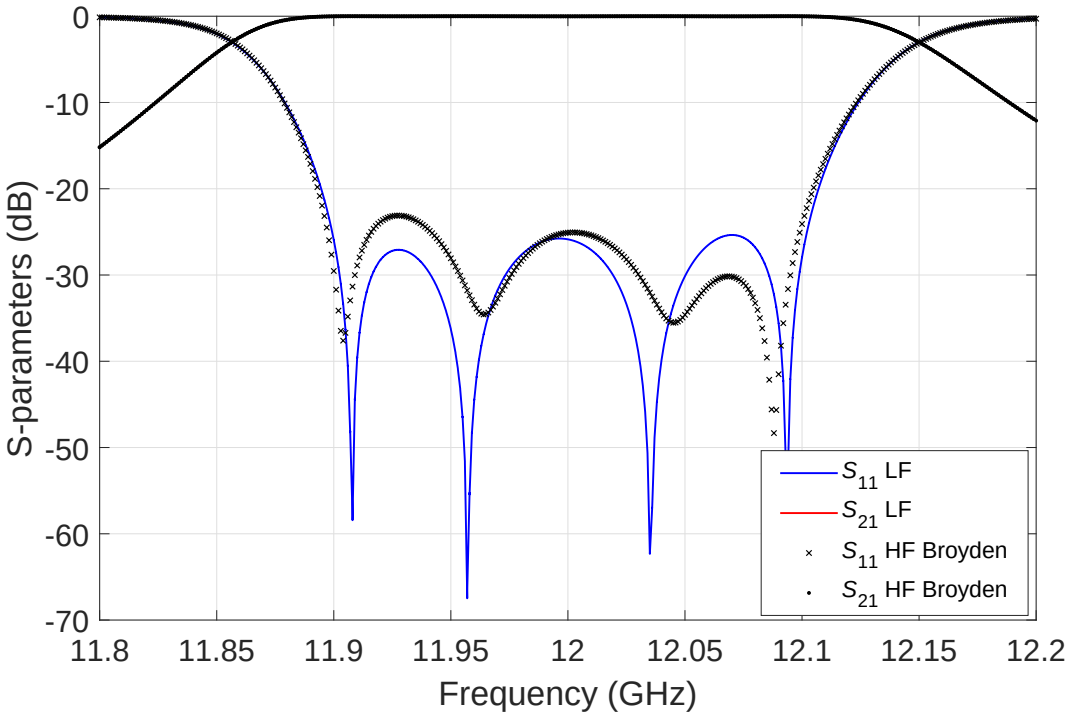

Figure 3.31: Result of the second iteration with the Broyden formula vs. ideal response.

Using the Broyden based ASM procedure we have essentially recovered the ideal filter response. However, if we compare this result with the one shown in Fig. 3.30, we can clearly see that the performance using Broyden is less accurate. From the results obtained in this experiment, therefore, it appears that, even though the LF and HF structures are not exactly identical, it is more efficient to apply the ASM with the identity matrix as the space mapping matrix, instead of updating it by the Broyden formula in every step.

Table 3.10 shows the final dimensions of the screws for the LF and HF models using the identity matrix and the Broyden formula, respectively.

Table 3.10: Comparison of final screw dimensions between LF and HF models in millimeters.

Screw	LF	HF with OS-ASM	HF with ASM
1	2.5	2.423	2.411
2	2.5	2.552	2.502
3	2.5	2.315	2.356
4	2.5	2.512	2.509
5	2.5	2.733	2.657
6	2.5	2.512	2.509
7	2.5	2.315	2.356
8	2.5	2.552	2.502
9	2.5	2.423	2.411

3.6.3 Fully tunable dual-mode filter with OS-ASM

The second filter to be designed with rounded corners and tuning screws will be the fully tunable dual-mode filter discussed in [63]. In this case, all rounded corners have 1 mm curvature radius. Fig. 3.32 and Fig. 3.33 shows the ideal filter structure (if the rounded corners are replaced with sharp corners), and the desired response.

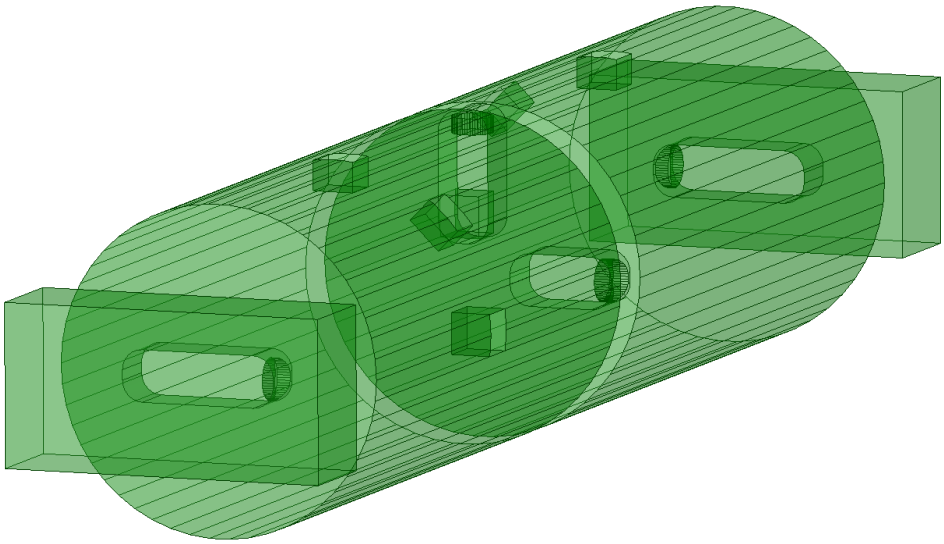

Figure 3.32: Fully tunable dual-mode filter structure.

The software tool HFSS is again used as the HF space, together with the structure shown in Fig. 3.32. Initially, we use in the HF space the same screw penetrations as the ideal model but using now rounded corners. Its response is shown in Fig. 3.34 with black dots.

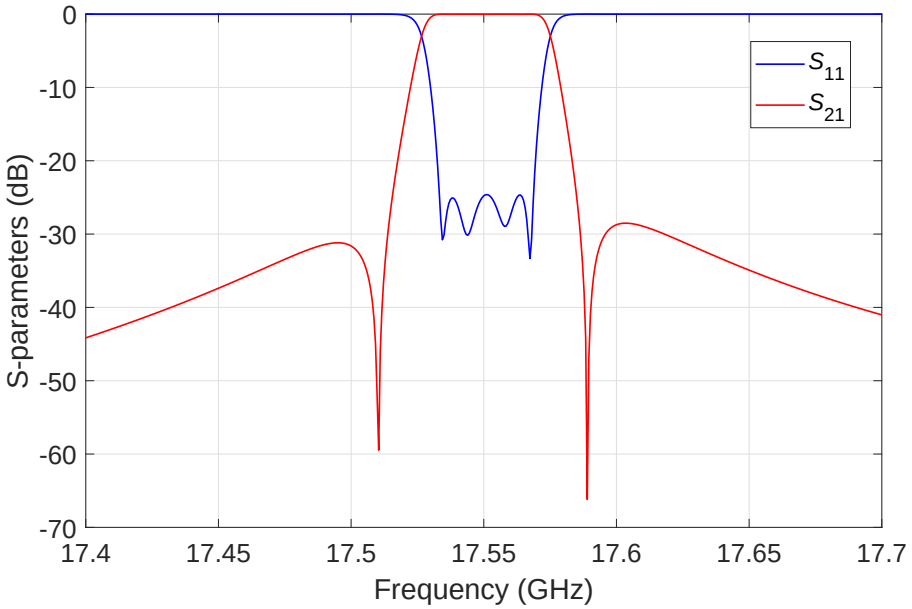

Figure 3.33: Ideal LF filter response.

We next apply the ASM procedure. Figs. 3.34, 3.35 and 3.36 shows the initial response compared with the ideal one, and the next iterations of the process using the identity mapping matrix. Fig. 3.37 shows the final performance of the HF filter.

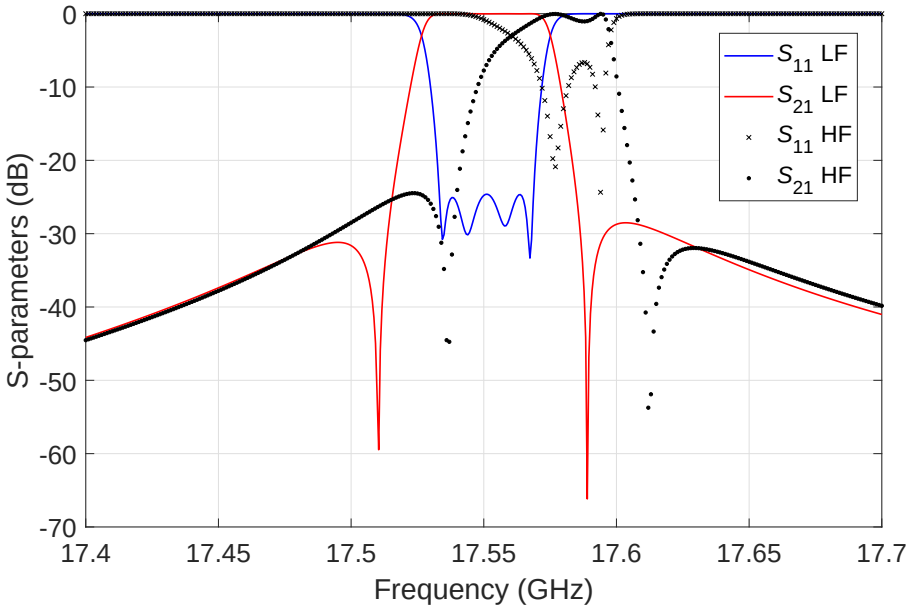

Figure 3.34: Comparison between initial HF performance and LF performance.

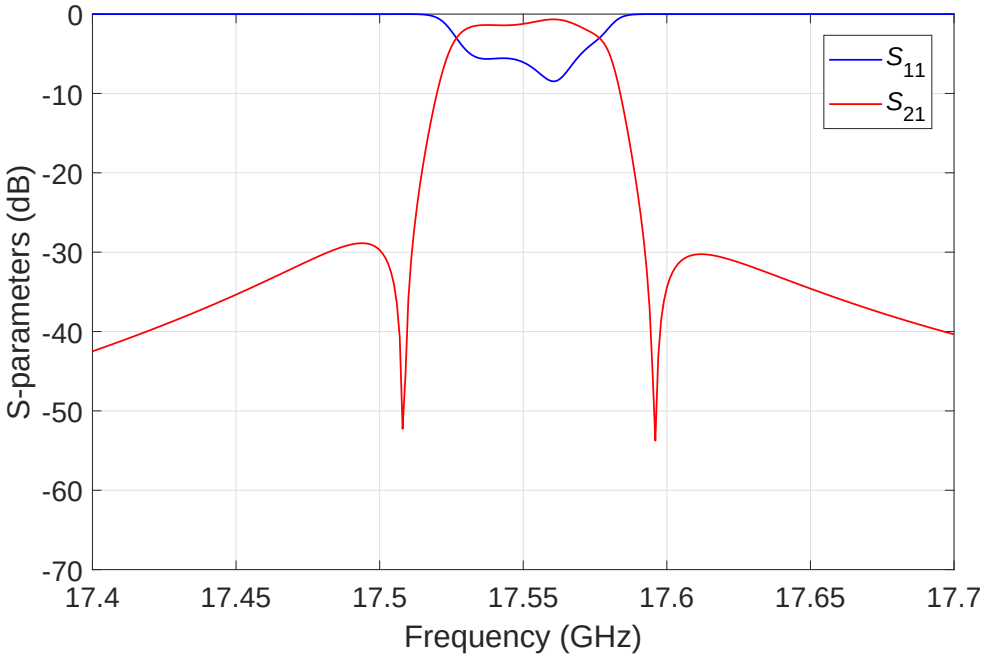

Figure 3.35: Result of first iteration in HF.

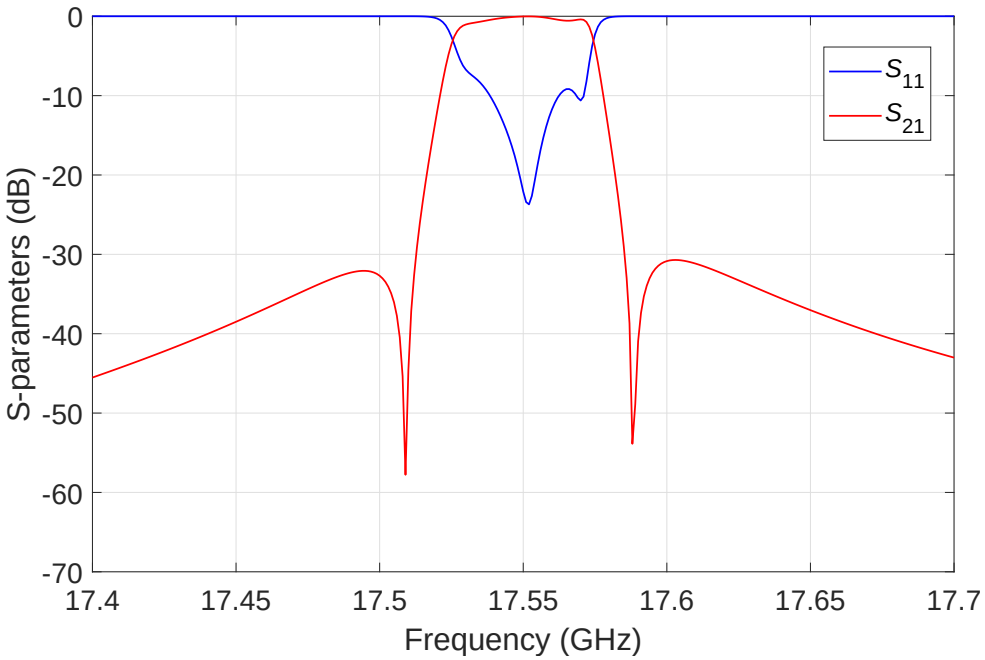

Figure 3.36: Result of second iteration in HF.

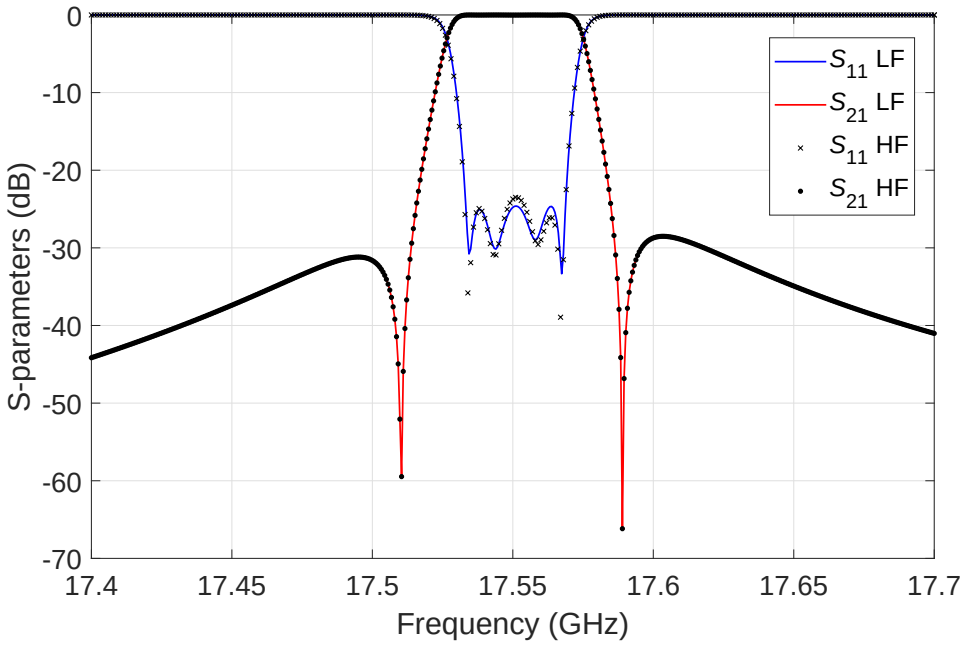

Figure 3.37: Final HF filter performance of the third iteration vs. ideal response.

In this case, we have performed 3 iterations of the OS-ASM procedure to obtain the desired response (always using the identity matrix instead of the Broyden update formula for the space mapping matrix).

3.6.4 Fully tunable dual-mode filter with ASM

We now perform again the design procedure updating this time the space mapping matrix with the Broyden formula in every additional ASM iteration. The first iteration gives the result already discussed.

We therefore start from the result of the first iteration, and recover the response shown in Fig. 3.35 and we apply the Broyden formula. The performance obtained is shown in Fig. 3.38.

We must now perform another iteration, obtaining the response shown in Fig. 3.39. Finally, after four iterations we obtain the desired response shown in Fig. 3.40.

Comparing this result with the previous one using the identity mapping matrix for all the iterations, updating the space mapping matrix with the Broyden formula requires one more optimization step to recover the desired response.

Table 3.11 shows the final dimensions of the screws for the LF and HF models using the identity matrix and the Broyden formula, respectively.

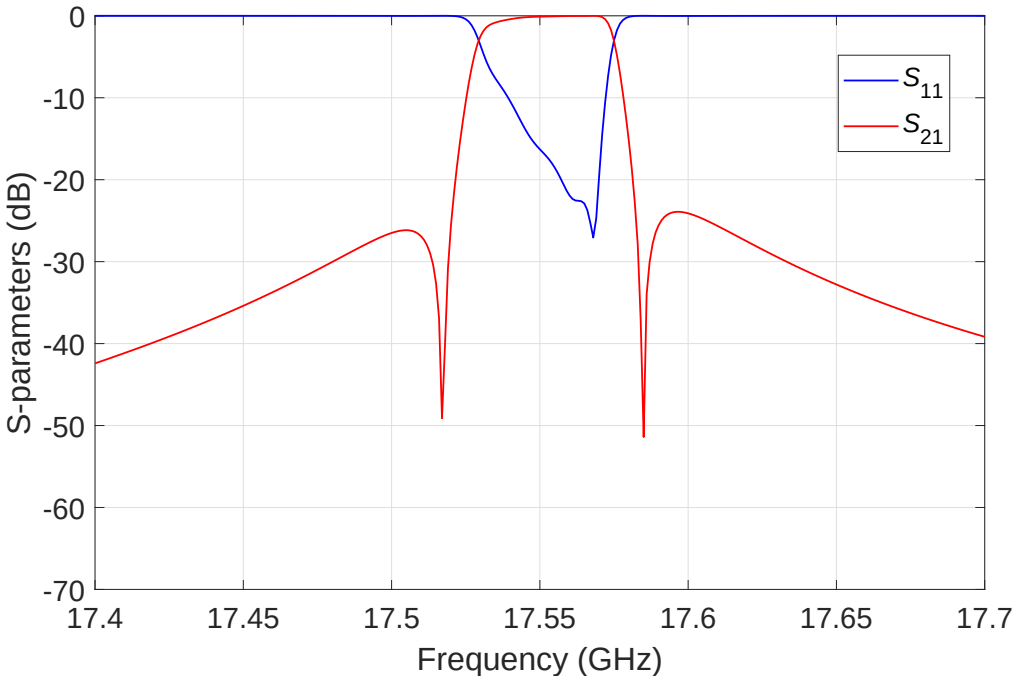

Figure 3.38: Response of the second iteration with the Broyden formula in HF.

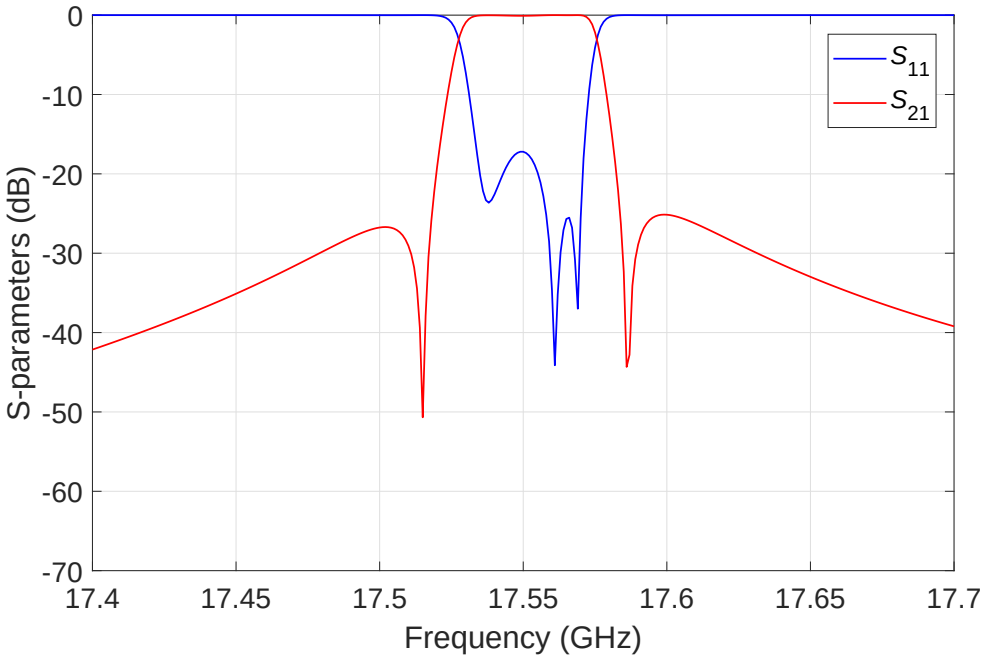

Figure 3.39: Response of the third iteration with the Broyden formula in HF.

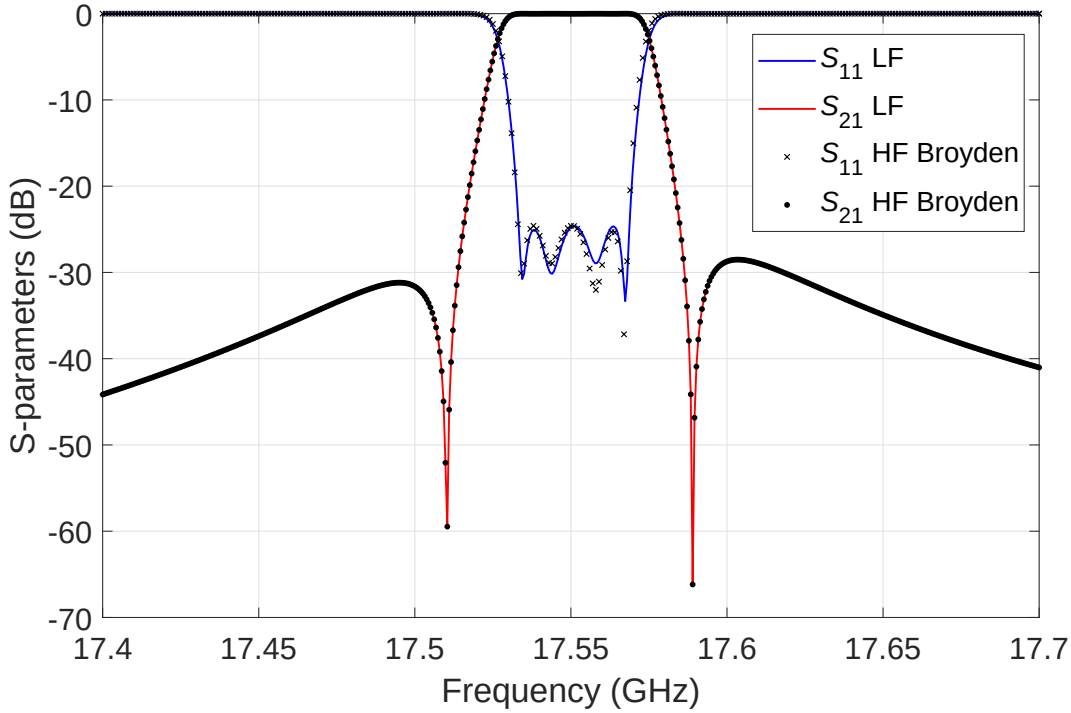

Figure 3.40: Result of the fourth iteration with the Broyden formula in HF filter vs. ideal response.

Table 3.11: Comparison of final screw dimensions between LF and HF models in millimeters.

Screw	LF	HF with OS-ASM	HF with ASM
Vertical 1st resonator	1.855	1.848	1.851
45^{o} 1st resonator	1.294	1.278	1.308
Horizontal 1st resonator	1.508	1.474	1.470
Vertical iris	0.324	0.317	0.315
Horizontal iris	0.778	0.780	0.779
Vertical 2nd resonator	1.855	1.848	1.851
45^{o} 2nd resonator	1.294	1.278	1.308
Horizontal 2nd resonator	1.508	1.474	1.470

3.6.5 Folded rectangular waveguide tunable filter with OS-ASM

The last example that we discuss is the design of a tunable folded filter in rectangular waveguide [64]. The design parameters are:

- Return loss $\geq$ 25 dB
- Center frequency = 17.3 GHz
- Channel bandwidth = 36 MHz

The filter structure in the LF space is shown in Fig. 3.41 (with sharp corners) and its performance in Fig. 3.42.

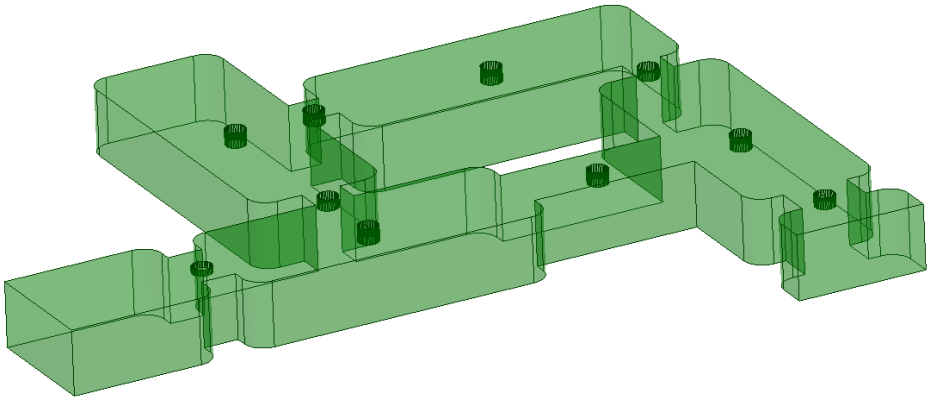

Figure 3.41: Filter structure.

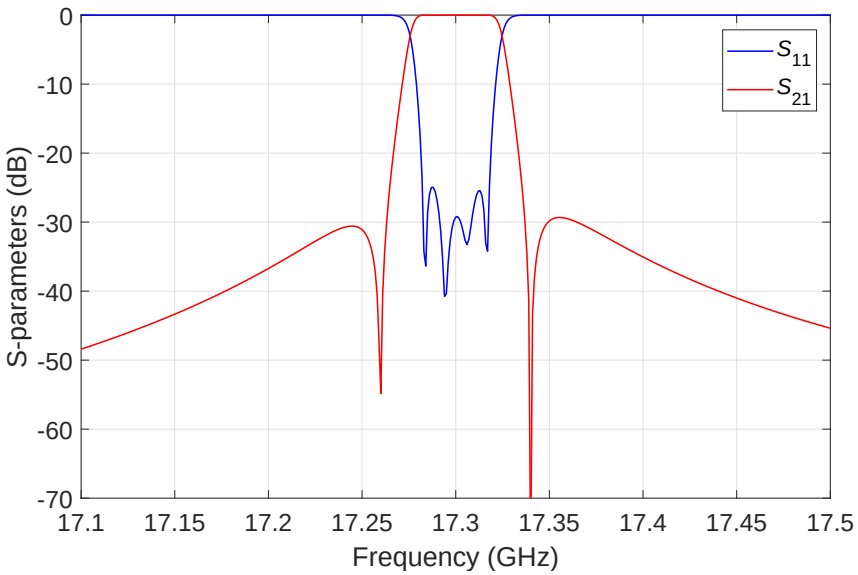

Figure 3.42: Ideal LF filter response.

Following the cavity numeration of [64], Table 3.12 shows the dimensions of the filter structure and the initial screw penetrations. Note that, in this case, the I/O waveguide is the standard WR-51 and rounded corners of radius 2 mm have been considered.

The initial HF performance using the same tuning screw penetrations as in the LF space is shown in Fig. 3.43 with black dots.

Table 3.12: Dimensions (in mm) of the folded filter structure. All heights are 6.477 mm.

Structure	Width	Length	Screw penetration
Input aperture	6.401	3.469	0.633
First cavity	12.954	30.543	1.965
Second aperture	3.899	2.654	1.413
Second cavity	12.954	33.106	1.913
Third aperture	3.990	3.117	1.822
Third cavity	12.954	33.134	1.898
Fourth aperture	3.798	2.654	1.077
Fourth cavity	12.954	30.982	2.002
Fifth aperture	6.661	16.315	2.024
Output aperture	6.5	3.671	1.401

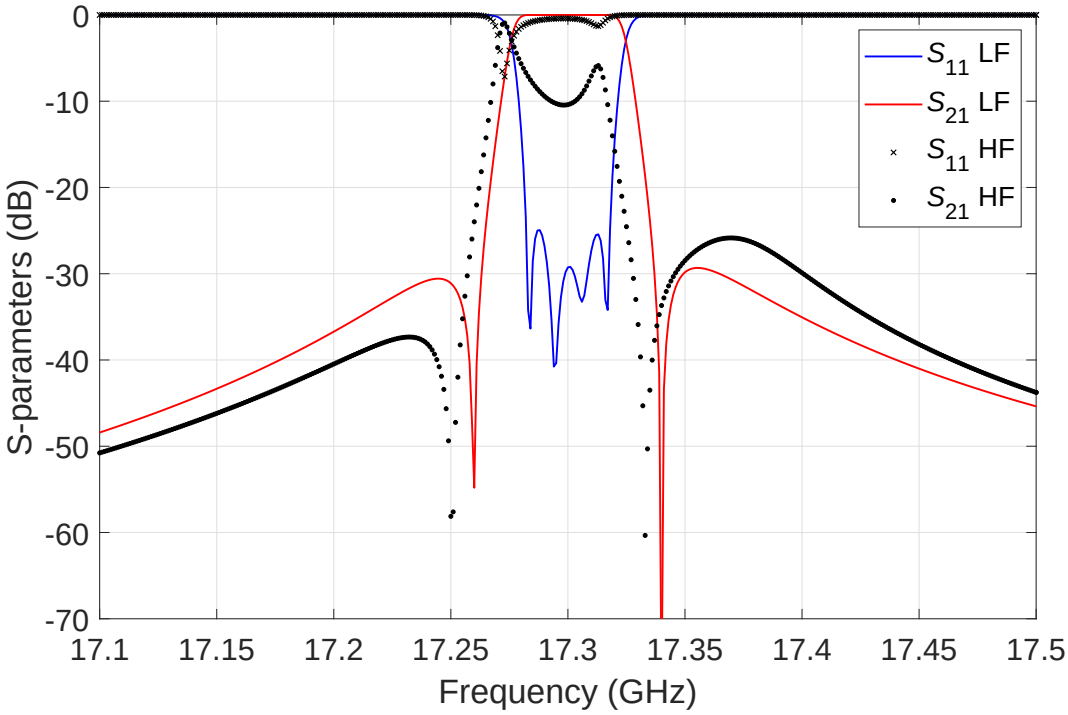

Figure 3.43: Comparison between initial HF performance and LF performance.

We next apply the ASM procedure to recover the desired (ideal) response in the HF space. Figs. 3.43, 3.44 and 3.45 shows the initial comparison and the next iterations of the process. Fig. 3.46 shows the final performance of the HF filter obtained with only three iterations.

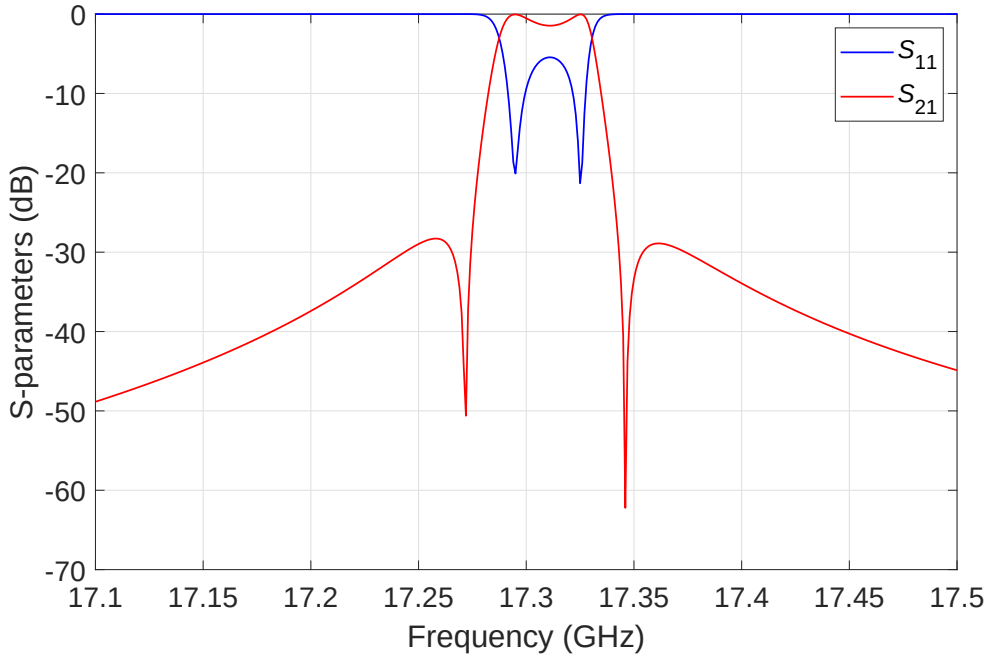

Figure 3.44: Result of the first iteration in HF.

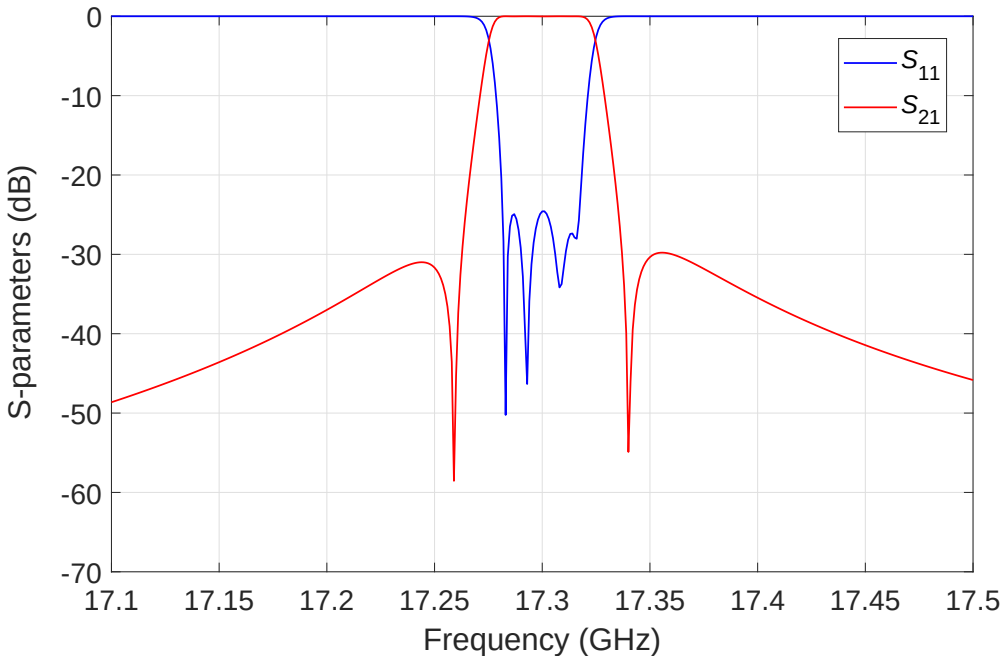

Figure 3.45: Result of the second iteration in HF.

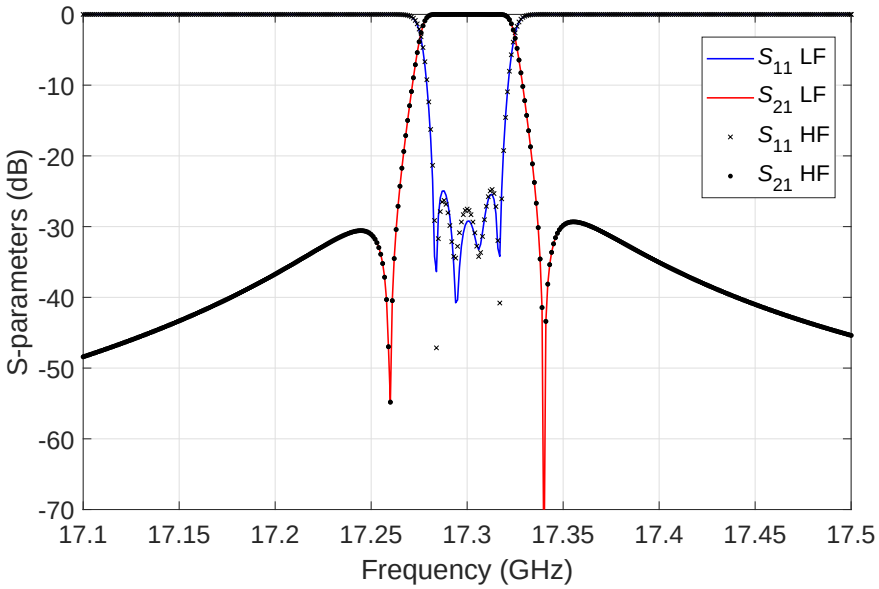

Figure 3.46: Result of the third iteration in HF filter vs. ideal response.

3.6.6 Folded rectangular waveguide tunable filter with ASM

We now perform again the same basic ASM design procedure, but, this time, we update the space mapping matrix with the Broyden formula. We can start with the second iteration of the process.

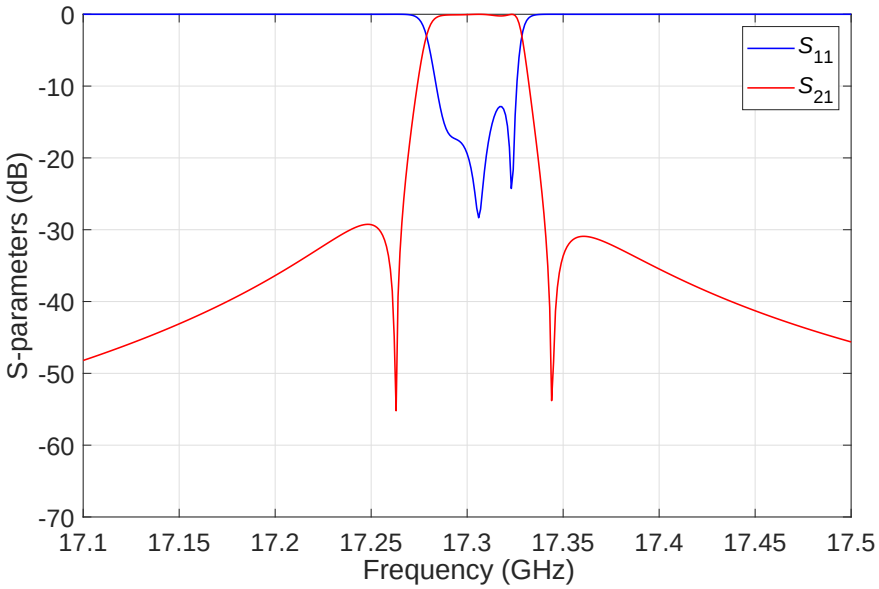

Figure 3.47: Response of the second iteration with the Broyden formula in HF.

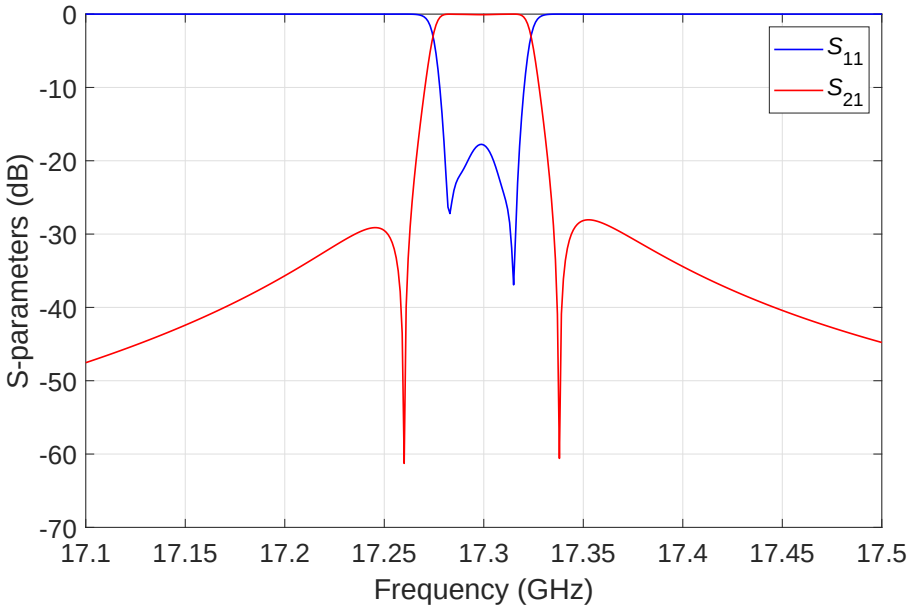

Figure 3.48: Response of the third iteration with the Broyden formula in HF.

Figs. 3.47 and 3.48 shows the different results obtained, and Fig. 3.49 displays the final performance. The final result has been obtained with four iterations.

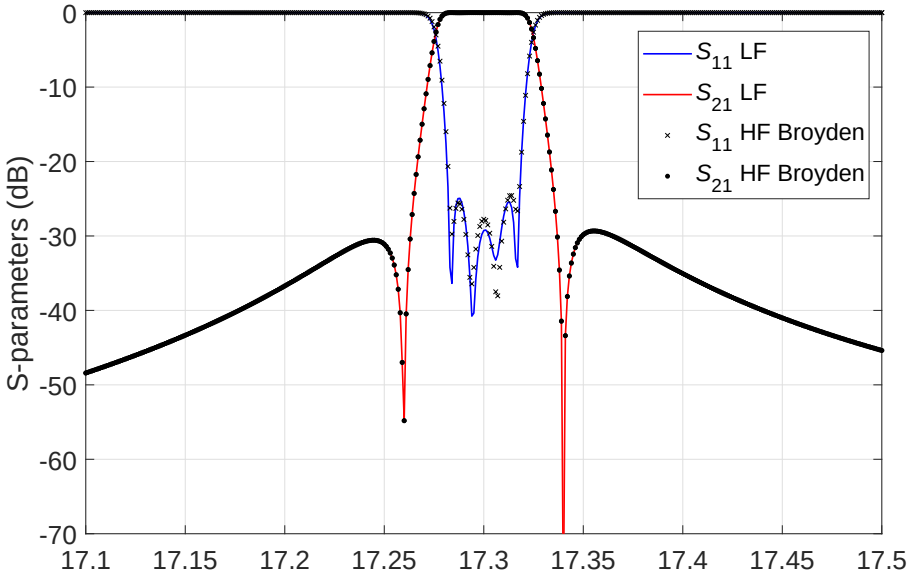

Figure 3.49: Response of the fourth iteration with the Broyden formula in HF vs. ideal response.

Table 3.13 shows the final dimensions of the screws for the LF and HF models using the identity matrix and the Broyden formula, respectively.

Table 3.13: Comparison of final screw dimensions between LF and HF models in millimeters.

Screw	LF	HF with OS-ASM	HF with ASM
1	0.633	0.630	0.641
2	1.965	1.972	1.678
3	1.413	1.405	1.430
4	1.913	1.907	1.902
5	1.822	1.820	1.828
6	1.898	1.894	1.908
7	1.077	1.075	1.061
8	2.002	2.009	2.101
9	2.024	2.122	2.001
10	1.401	1.405	1.398

3.7 Definition of space alignment

Based on all of the above discussion and results, we are now going to propose a definition of alignment between the LF and the HF spaces in the context of ASM.

Two spaces are considered to be perfectly aligned if and only if the following two conditions are satisfied:

1. *Two points in the respective parameter spaces can be found that produce the same identical responses (points of alignment).*
2. *The derivatives (or the Jacobians) of the responses with respect to corresponding physical parameters in the two spaces, evaluated at the points of alignment, are identical.*

Our investigations clearly indicate that, if the two conditions above are satisfied, and the LF and HF structures are identical, we can expect an ASM procedure to converge to the desired performance in *just one step*.

3.8 Conclusions

In the context of microwave waveguide filter design and optimization based on ASM, the choice of the LF and HF spaces (structures, or models) is indeed a key point. Naturally, the HF model must be as close as possible to physical reality. The LF model, on the other hand, must be able to represent the *same* physical reality, in particular with respect to the tuning elements, but needs to produce results with a significantly higher computational efficiency. As we have clearly shown in this chapter, the fact that both models must obey the perturbation theory will ensure that the ASM procedure will converge in just one step if the LF and HF structures are physically identical. In the case in which the LF and HF physical structure are not exactly identical, but differ from each other in relatively small volumes, our investigation clearly shows that the ASM based on the identity space mapping matrix is more efficient than the classic ASM based on the Broyden update formula. Finally, in the case in which the LF and HF models are established in spaces that are not (physically) congruent (i.e., the modeling of a filter using inverters and transmission lines as the LF space, and with full-wave EM software tools as the HF space), we expect that the ASM procedure will converge more efficiently with the help of the Broyden update, so that a proper mapping between the two (very different) spaces can be established faster.

Chapter 4

Tunable and reconfigurable waveguide filters

This chapter describes and extends the results obtained during the research work related to this thesis in the area of tunable and reconfigurable filters. It is important to note that the results described in this chapter have resulted into the following scientific publications:

- J. Ossorio, J. Vague, V. E. Boria, and M. Guglielmi, "Exploring the tunability range of classic circular waveguide dual-mode filters using EM-based CAD," *in IEEE MTT-S International Conference on Numerical Electromagnetic and Multi-physics Modeling and Optimization for RF, Microwave, and Terahertz Applications,* pp. 332-334, May 2017.
- J. Ossorio, J. Vague, V. E. Boria, and M. Guglielmi, "Exploring the tuning range of channel filters for satellite applications using electromagnetic-based computer aided design tools," *IEEE Transactions on Microwave Theory and Techniques,* vol. 66, no. 2, pp. 717-725, Feb. 2018.

As already discussed, the current evolution trends of telecommunication satellites is toward increased bandwidth and service flexibility [65], [66]. Tunable and reconfigurable filters can indeed provide an elegant solution to add versatility and reduce the number of components in the payload, thereby increasing the efficiency of the whole satellite system. In this chapter we will investigate the tuning range of classic dual-mode filters, one of the most used channel filter in satellite communications [67]. In addition, we also investigate new tunable structures in rectangular waveguide that can provide a significantly wider range of tunability.

4.1 Circular waveguide dual-mode filter

The basic structure of a 4-pole dual-mode filter in classical circular waveguide technology is shown in Fig. 4.1. This filter family was first introduced in [25], and has since become the structure of choice for the implementation of output multiplexers (OMUXes) for telecommunication satellites [67].

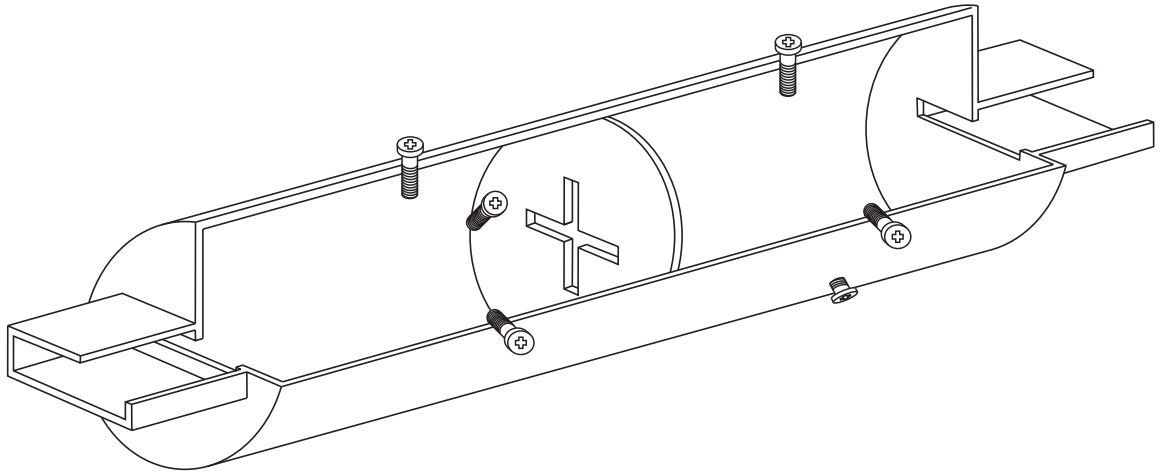

Figure 4.1: Basic four-pole, dual-mode filter structure.

As a result, a very substantial amount of work can be found in the technical literature describing Computer-Aided Design (CAD) techniques for the design of circular waveguide dual-mode filters (see, for instance [68]-[85]).

In addition, it is interesting to note that a number of contributions have also been published concerning dual, or single-mode rectangular waveguide filters, with filtering function similar to the ones of classic dual-mode filters in circular waveguide (see, for instance [86]-[96]).

This type of circular waveguide filter is commonly based on the TE_{11n} (with $n = 1, 3...$) dual resonant modes (with vertical and horizontal polarization), where n is chosen according to the filter requirements in terms of insertion losses and compactness [67]. Dual-mode filters of this type are usually designed to operate at a given center frequency and with a very narrow bandwidth (of 1% or less in relative terms). Usually, both center frequency and bandwidth are fixed to fit specific requirements.

Recently, however, the evolution of telecommunication satellite payloads is requiring the development of new filter structures that can allow for the remote variation of both filter center frequency and bandwidth [97]. In response to this new requirement, initial investigations have appeared in the technical literature discussing new, tunable dual-mode filter structures (see for instance [31], [83], and [98]).

Furthermore, two very recent contributions ([63] and [64]), described the initial results of an investigation aimed at exploring the maximum tuning range for the class of filters based on the structure shown in Fig. 4.1.

The filter response is initially centered at 17 GHz with 36 MHz of channel bandwidth. Fig. 4.2 shows the simulated behavior of the structure in Fig. 4.1. The performance shown in Fig. 4.2 has been obtained using the CAD tool FEST3D, and the filter design procedure described in [82].

The structure contains 6 tuning screws (see Fig. 4.1). However, for the sake of analysis, they have been represented by two lengths of uniform circular waveguide with three metallic ridges of rectangular cross section. This representation is indeed very convenient for the EM-based CAD of the structure. This is because the sections containing the tuning screws can be easily analyzed as sections of uniform circular waveguide with three metal ridges (considered as perfect parallelepipeds).

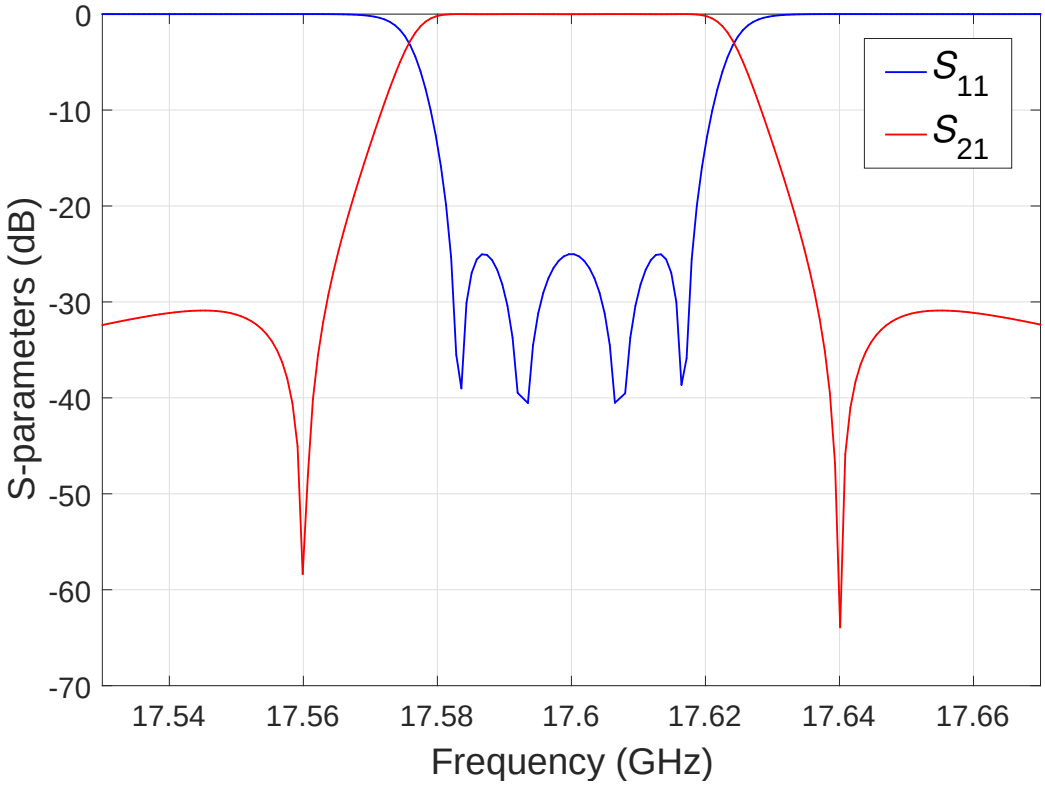

Figure 4.2: Basic four-pole, dual-mode filter performance.

4.1.1 Fixed frequency

It is now convenient to describe in more detail the (well-known) physical behavior of the structure. In this context, we recall that the vertical and horizontal screws in Fig. 4.1 are used to tune the resonant frequency of the cavities, whereas the oblique screws are adjusted to implement the needed inter-resonator couplings. In principle, therefore, to tune the filter at another frequency, one could simply change the penetration of the six screws. This, however, is not sufficient by itself because, to change the operating frequency of the filter, we need to change also the dimensions of all coupling irises. To achieve full tuning, therefore, also the input-output and inter-resonator irises (see Fig. 4.3) must be tunable.

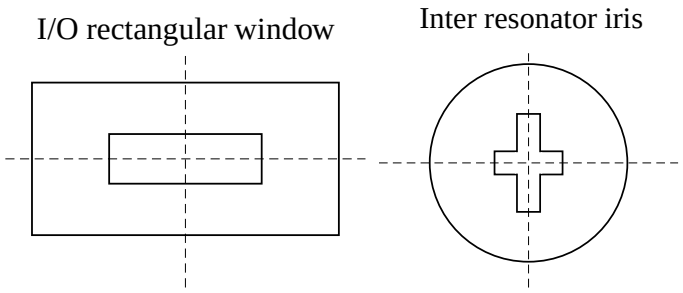

Figure 4.3: Basic input/output and inter resonator irises.

As a matter of fact, the correct dimension of all coupling irises in standard (fixed frequency) dual-mode filter implementations is indeed a very critical problem, that normally requires extreme mechanical implementation accuracy.

In the industrial practice, therefore, when tuning narrow band dual-mode filters, it may actually be necessary to try several irises before one can finally obtain the correct coupling values.

4.1.2 Tunable frequency

A first attempt at tuning an input-output iris, as the one shown in Fig. 4.3, can be found in [99]. The solution proposed in [99] was to insert a tuning screw in the center of the iris along the vertical direction of Fig. 4.3. This solution is indeed effective, but the achievable tuning range is very limited. In addition, placing a tuning screw vertically, may create serious multipactor problems in vacuum. A much better solution, allowing for a much wider tuning range, is the one proposed by Lamming [100], where the tuning screw is inserted laterally, along the horizontal direction, as shown in Fig. 4.4. In [100], however, the configuration in Fig. 4.4 was proposed in the context of a successful experimental study aimed only at recovering the errors introduced by the manufacturing process of the irises.

In this work, we propose to extend the use of this iris tuning technique to the implementation of fully tunable dual-mode filters.

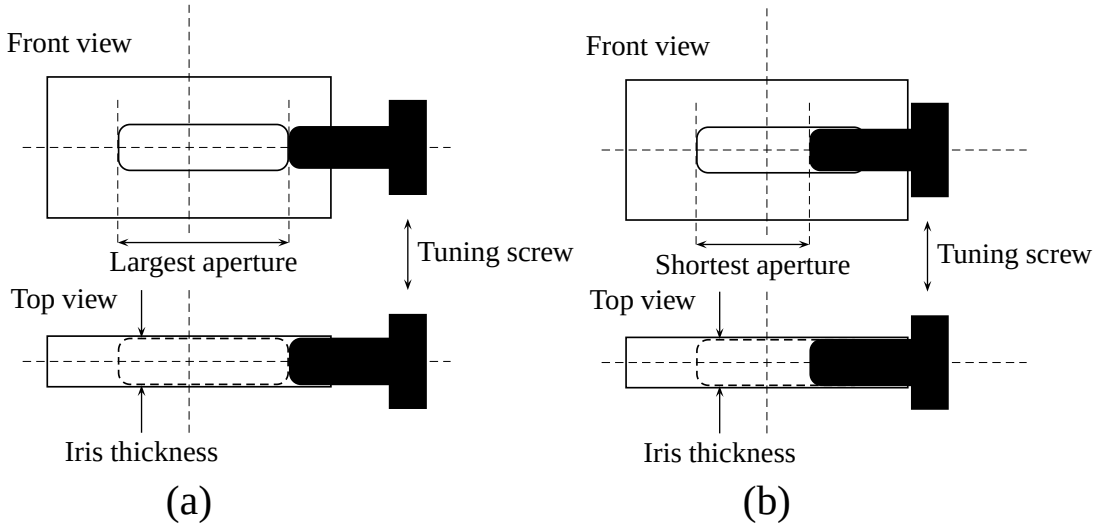

Figure 4.4: Tunable input-output iris: (a) Non-penetrated screw; (b) Penetrated screw

The same tuning concept, however, can not be applied directly to the inter-resonator iris in Fig. 4.3. Inserting the tuning screws directly on the sides of the cross-shaped iris would result in much too long screws. To make the implementation of this simple concept more practical, it is better to split the cross iris into two separate offset irises, as shown in Fig. 4.5.

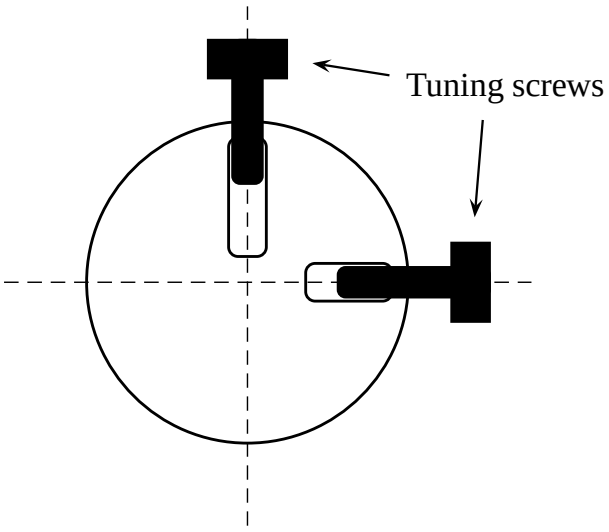

Figure 4.5: Tunable inter resonator iris.

As previously discussed, the full-wave EM simulations in support of this investigation have been carried using FEST3D. As pointed out in the previous chapter, in this CAD tool, all waveguide structures are simply represented by cascaded sections of uniform waveguide, with the appropriate cross section. The junctions between the various sections of uniform waveguide are then represented by MENs.

Cascading the various MENs, we can then obtain the efficient and accurate full-wave EM-Based CAD model of the complete filter structure [60]. A similar approach can also be used to simulate the tunable irises in Figs. 4.4 and 4.5. In this case, what we propose to do is simply to introduce a metallic cylinder of circular cross section (the real tuning screw) of the required length inside the waveguide length that represent the irises. The length of waveguide with the tuning screw inside can then be considered as a 3D rectangular cavity loaded with a post of circular cross section. The theory described in [60], to analyze arbitrary shaped 3D rectangular cavities, can then be used to produce an accurate MEN for the complete tunable iris. Fig. 4.6 shows the geometrical details of the resulting tunable input iris, where it can be observed that the diameter of the tuning screw is less than the iris thickness.

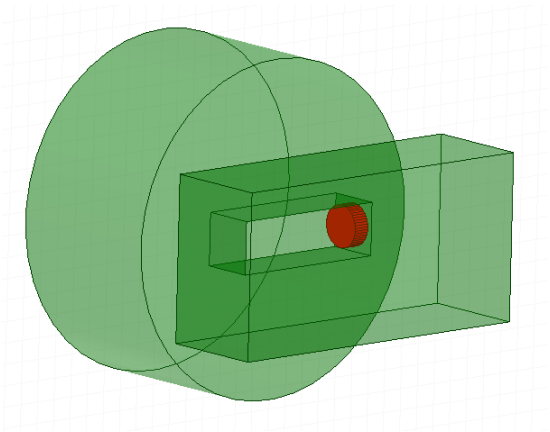

Figure 4.6: Tunable input iris implementation.

Increasing the penetration of the metallic cylinder will reduce the width of the coupling iris, thereby reducing the coupling value. Reducing the penetration of the cylinder wall, on the other hand, increases the width of the iris and therefore the coupling value. There are, however, two important details that need further discussion. The first is that the diameter of the tuning cylinder must be less than the height of the window. This is because having the tuning cylinder and the window with the same height can introduce an electrical contact between the sides of the tuning cylinder and the walls of the irises. This electrical contact, however, cannot be easily kept stable. This instability would then introduce an unwanted filter performance.

It must also be mentioned that the small air gaps between the screws and iris walls are not prone to induce multipactor, due to their size, physical location (low electric field intensity), and the effect of fringing fields [101]. The second is that the length of the tuning cylinder must, in any case, be kept smaller than the resonant length. This is because the resonance of the tuning cylinder would affect very negatively the response of the filter.

The first step is to design with FEST3D the filter at 17.6 GHz, with 36 MHz bandwidth, and two transmission zeros at ± 40 MHz from the filter center frequency. The filter design procedure that we have followed in this case is based on the results presented in [82].

Implementing the tuning concepts described in the previous sections, we obtain the fully tunable filter structure shown in Fig. 4.7.

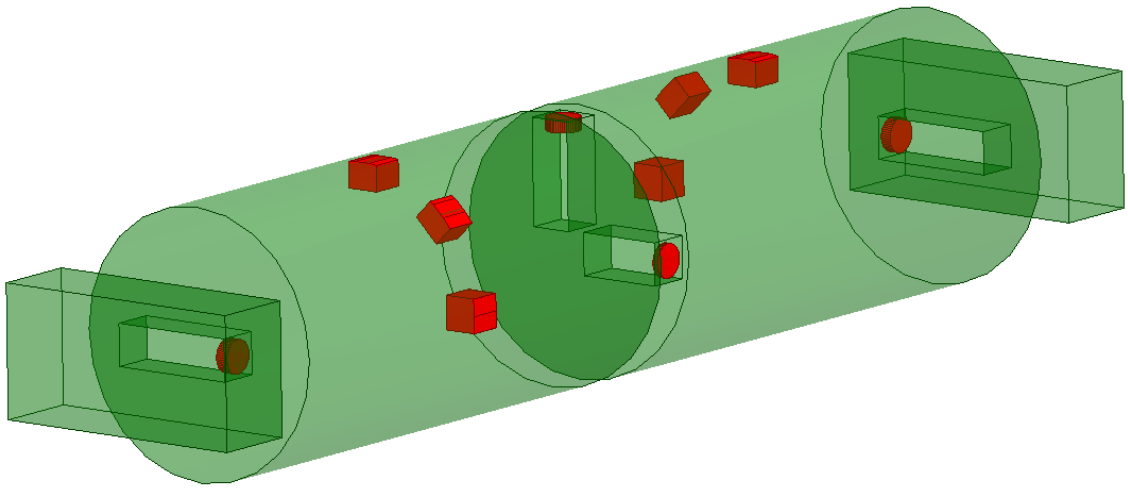

Figure 4.7: Fully tunable dual-mode filter.

We can now use the CAD tool FEST3D to explore the maximum tuning range offered by the structure in Fig. 4.7, with a constant channel bandwidth of 36 MHz.

Fig. 4.8 shows the results obtained. The highest center frequency obtained is 17.64 GHz, whereas the lowest center frequency is 17.55 GHz. A correctly tuned filter response can not be obtained above or below this frequency range.

To better understand this result, it is now convenient to look at the values of the penetration of the various screws, as shown in Table 4.1. Note that all dimensions in Table 4.1 are in mm. Furthermore, all apertures are 2.5 mm high and 2.5 mm thick. All tuning elements have 2 mm diameter.

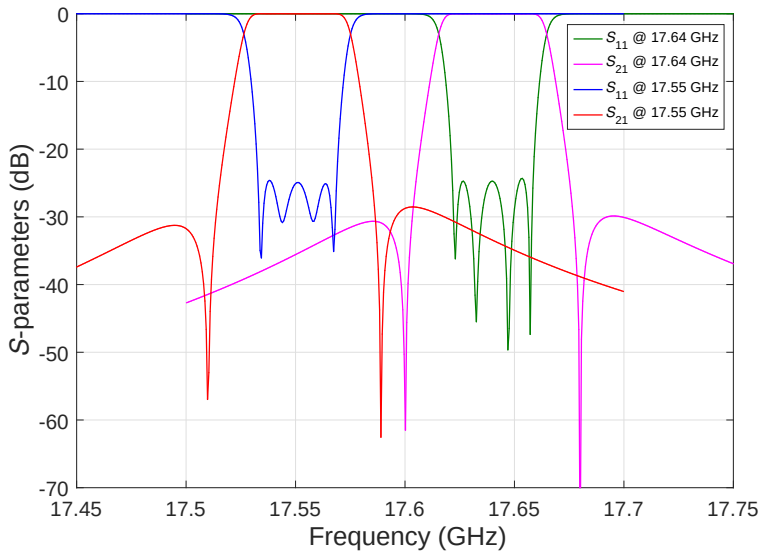

Figure 4.8: Simulated tuning range with FEST3D.

V stands for vertical, H stands for horizontal, O stands for oblique, VIR stands for vertical inter resonator, and HIR stands for horizontal inter resonator. Finally, when two values are given, the first is for the lower frequency, and the second is for the higher frequency.

Tuning the filter at lower frequencies, requires increasing the penetration of the tuning screws in the center of the cylindrical resonators. Tuning the filter below 17.55 GHz, however, brings the resonant frequency of the tuning screws themselves too close to the center frequency of the filter, so that the structure can not be effectively tuned. The horizontal tuning screw, in particular, needs to penetrate more and, therefore, becomes the limiting factor.

Table 4.1: FEST3D Filter Dimensions (mm)

Filter element	Cavity 1	Cavity 2	Inter Cavity
I/O aperture	7.2	7.2	-
I/O screw	0.642 - 0.732	0.635 - 0.772	-
V screw	1.537 - 1.012	1.531 - 1.040	-
H screw	1.980 - 1.775	1.983 - 1.770	-
O screw	1.472 - 0.974	1.443 - 0.957	-
VIR aperture	-	-	5.9
VIR screw	-	-	0.772 - 1.203
HIR aperture	-	-	4.7
HIR screw	-	-	0.939 - 2.131

To better understand this point, we show in Fig. 4.9 the results of a simulation where we have a section of circular waveguide with only the horizontal tuning screw. The simulations have been performed for two values of tuning screw penetration, namely, 2.0 mm and 1.980 mm (this last one given in Table 4.1 for the H screw at the lower frequency). As we can clearly see, from Fig. 4.9, with 2 mm penetration, the resonance of the screw occurs within the tuning range of the dual-mode filter. As a consequence, the filter can no longer be tuned.

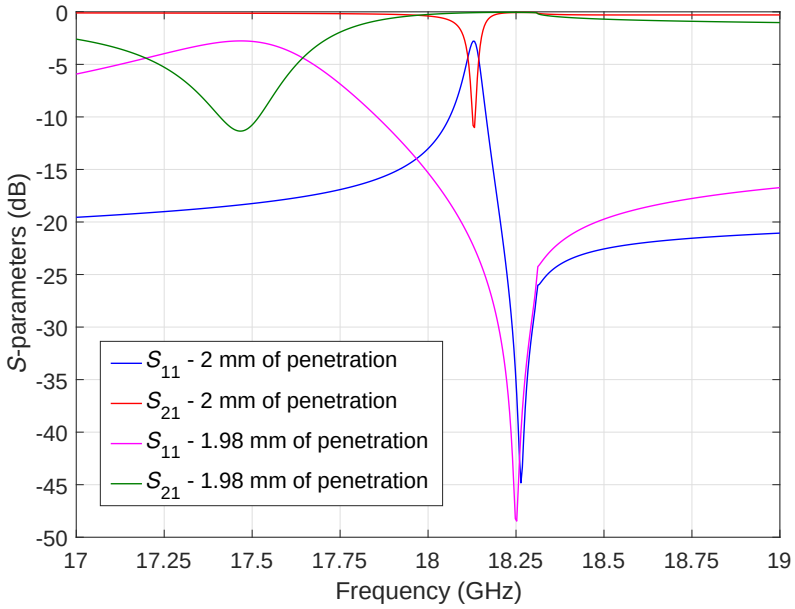

Figure 4.9: Resonance of the horizontal screw.

On the other hand, tuning the filter at higher frequency would require decreasing the size of all coupling irises. However, above 17.64 GHz the size of the HIR iris becomes too small and the filter cannot be tuned successfully. Above this frequency, the width of the VIR iris is large enough to provide also a significant negative coupling between the vertical modes, so that the HIR iris looses its effectiveness. This can be clearly appreciated by taking the difference between the HIR aperture and the HIR screw penetration for the higher frequency tuning value. The value obtained is 2.569 mm, however, the width of the VIR iris is 2.5 mm. It is therefore clear that if the HIR screw penetrates more, its effect will be marginal with respect to the width of the VIR iris. As a result, the center frequency cannot be further increased. In conclusion, the achieved tuning range turns out to be about 90 MHz.

It is interesting to observe that the central frequency of the achieved tuning range is 17.595 GHz.

Expressing the tuning range in terms of the center frequency f_0 would result into approximately $\Delta f_0 = \pm 0.25\%$ tuning range. This is indeed the measure of the tuning range that is most commonly used in the technical literature. However, we propose an alternative definition of the tuning range, namely, in terms of the bandwidth of the filter:

$$\Delta BW = \frac{f_{0,max} - f_{0,min}}{BW} \times 100 \tag{4.1}$$

Using this alternative definition results into approximately $\Delta BW_{cw} = \pm 125\%$ tuning range for the circular waveguide filter (subscript cw). We do believe that this second definition is more meaningful than the first one, since it gives clear information about the movement in frequency of the filter with respect to its own nominal bandwidth.

The same conclusions, in terms of tuning range, have been observed for dual-mode circular waveguide filters providing standard Chebyshev responses (without the two adjacent transmission zeros), and for filter structures where symmetric arrangements are considered for the inter-resonator coupling iris (where two vertical and two horizontal slots are considered).

4.2 Folded rectangular waveguide filter

As an alternative to the classic circular waveguide structure in Fig. 4.1, we propose to investigate in addition the folded rectangular waveguide implementation shown in Fig. 4.10.

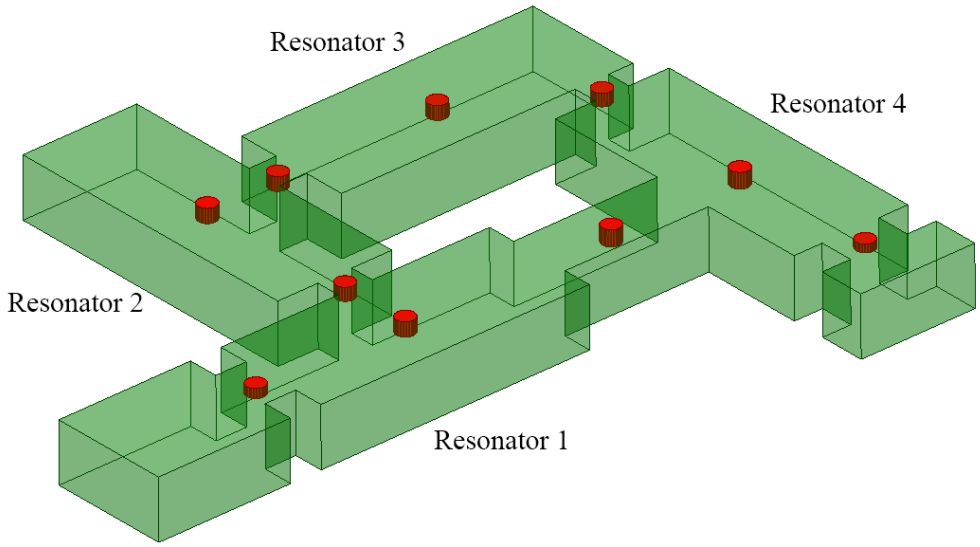

Figure 4.10: Folded Rectangular waveguide filter.

The filter structure in Fig. 4.10 is based on the use of four TE_{103} resonators, and can be designed to have an electrical performance that is approximately identical to the one shown in Fig. 4.2.

In particular, it is well known that in order to generate a pair of transmission zeros, it is necessary to have two signal paths with couplings of opposite signs. This can be easily achieved with the structure shown in Fig. 4.10, where the coupling between resonators 3 and 4 is positioned between the end of the third resonator and the beginning of the fourth one. Because of the alternating sign of the longitudinal field distribution of a TE_{103} resonator, this arrangement results into a 3-4 coupling of opposite sign to the other ones (i.e. between resonators 1 and 2, resonators 2 and 3, as well as between resonators 1 and 4, where the coupling is always located between the middle of one resonator and the end of the other one). It is important to note that for the folded rectangular waveguide structure in Fig. 4.10, the tuning of the electrical parameters of interest, namely, the resonance frequencies and the coupling values, can be very simply achieved by using standard vertical tuning screws in the center of the resonators and the irises.

The only limiting factor is the resonance of the tuning elements themselves. In this case, there are no significant interactions between different coupling apertures. The basic concept behind the tunable filter in Fig. 4.10 is simple. However, the tuning range of this type of structure must be investigated. Furthermore, it is interesting to note that a different tunable filter structure with similar performance has been discussed in the technical literature [27], [102] and [103], where non-resonant circular cavities are used as tunable coupling and reactive elements. However, the structure in Fig. 4.10 is significantly simpler to manufacture and tune than the one proposed in [27], [102] and [103].

To explore the tuning range, we have then decreased the center frequency of the filter by 10 MHz steps, and re-adjusted at each step all tuning screws. In Fig. 4.11 we show the simulated tuning range obtained with the folded rectangular waveguide structure in Fig. 4.10. As we can see from Fig. 4.11, the center frequency can be tuned from 17.6 GHz down to 17.0 GHz.

The achieved tuning range is therefore 600 MHz. Expressing this range in terms of equation 4.1 results into a tuning range equal to approximately $\Delta BW_{rw} = \pm 833\%$. This result is clearly far superior to the one obtained with the circular dual-mode filter ($\Delta BW_{cw} = \pm 125\%$).

The limiting factor in this case is the lower center frequency, which is obtained when all tuning elements are fully inserted in the filter structure. To obtain a lower frequency, we would need to insert the tuning screws further into the structure. This, in turn, brings the resonance of the tuning element itself too close to the filter center frequency, and the desired filter performance can no longer be obtained.

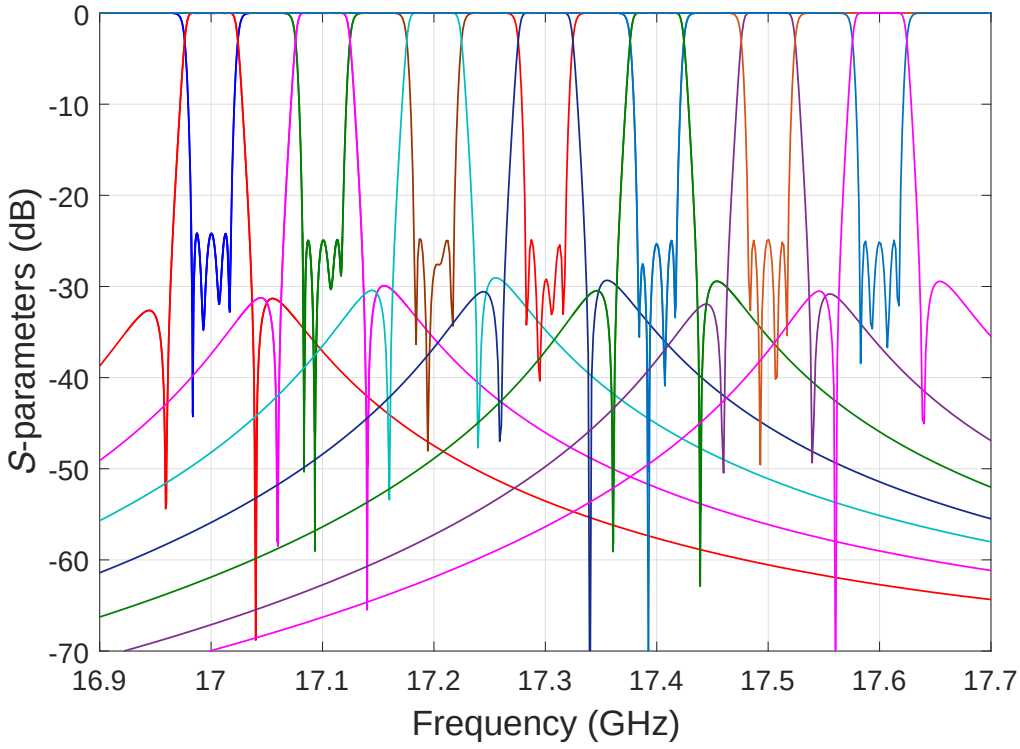

Figure 4.11: Simulated tuning range of the folded rectangular waveguide filter.

4.3 Hardware manufacture

To verify the results of our full-wave simulations, we have built two filter prototypes, one in circular waveguide and the other in rectangular waveguide. Before building the filters, however, the basic designs in Figs. 4.7 and 4.10 have been slightly modified. The original (ideal) structures contain elements with sharp, 90° corners. Although it is indeed possible to build hardware with sharp corners, in the industrial practice it is preferred to use rounded corners. This has two main effects, namely, it decreases the manufacturing cost of the hardware, and improves the quality of the silver plating that is generally used to achieve low insertion losses. Furthermore, the rectangular cross section tuning elements in the center of the circular waveguide cavities of the dual-mode filter have been replaced with circular cross section tuning screws. Finally, the insertion losses due to the material of the filter are also been included in the further simulations.

The transition between the ideal sharp corner structures and the real hardware with rounded corners has been performed using the OS-ASM procedure [59], using FEST3D (with the ideal structures) as the *low accuracy* (LA) space, and ANSYS HFSS and the real hardware as the *high accuracy* (HA) space.

The resulting filter geometries are shown in Fig. 4.12 and 4.13 for the circular and rectangular waveguide filters, respectively.

Naturally, in the low accuracy mode, the computations are much faster (1-10 seconds) than in the high accuracy mode (10-30 minutes). In fact, all the simulations discussed in this chapter so far have been carried out using FEST3D in the low accuracy mode. This has allowed us to carry out in a very short time the very many optimizations required to achieve the (*ideal*) performances that we have shown in the previous sections.

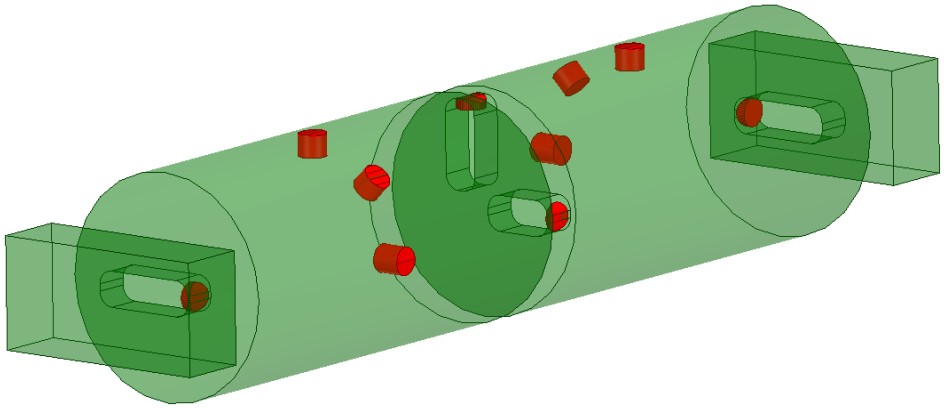

Figure 4.12: Fully tunable circular waveguide filter with rounded corners irises and circular tuning screws.

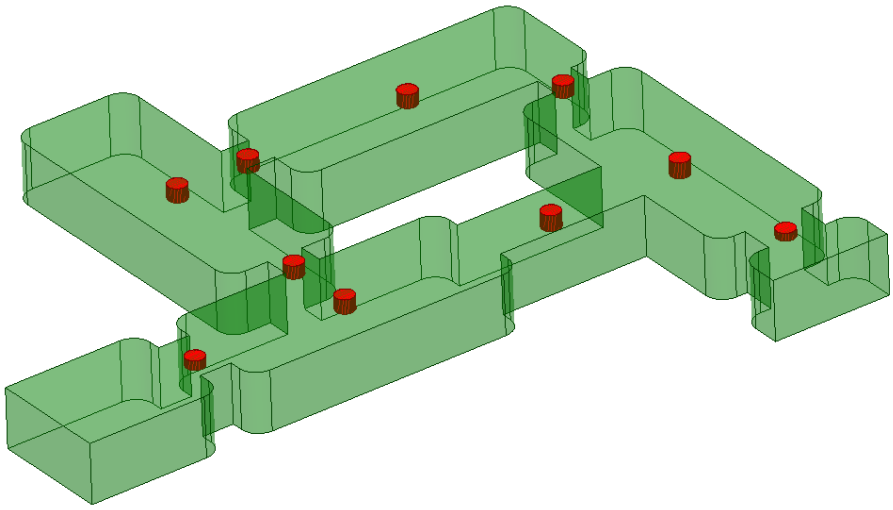

Figure 4.13: Folded tunable rectangular waveguide filter with rounded corners and circular tuning screws.

Figs. 4.14 and 4.15 show the comparison between the simulated response of the ideal LA model and the (*real*) HA performance obtained for the filter, tuned at two different center frequencies.

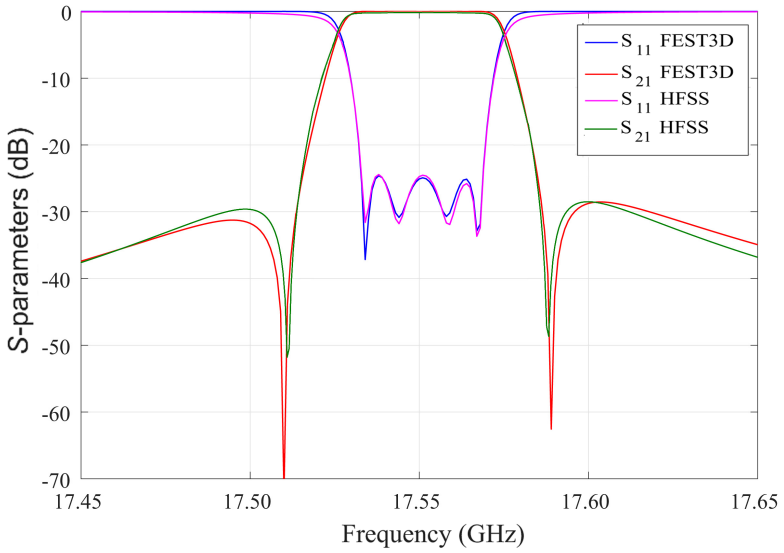

Figure 4.14: Comparison between simulated response in FEST3D and HFSS for the dual-mode circular waveguide filter, tuned at 17.55 GHz of center frequency.

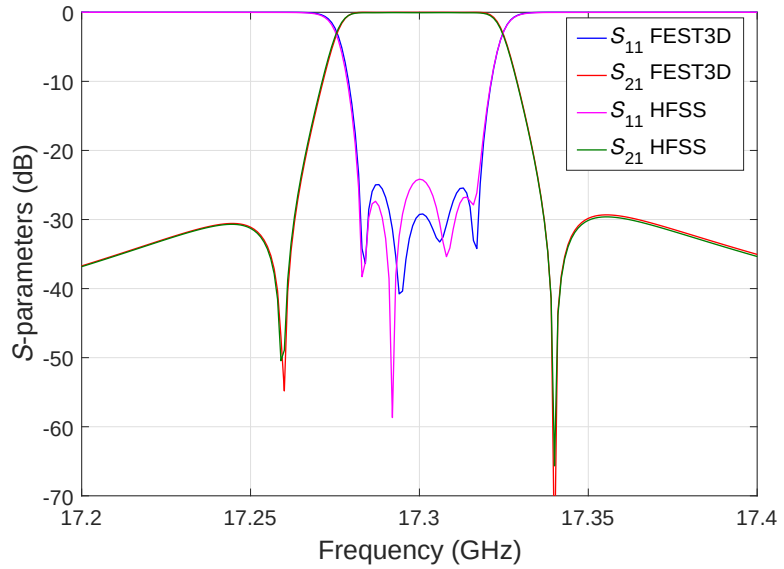

Figure 4.15: Comparison between simulated response in FEST3D and HFSS for the folded rectangular filter, tuned at 17.3 GHz of center frequency.

As we can see, the two results are almost coincident, so that the LA and the HA spaces can be considered to be perfectly aligned. Figs. 4.16 and 4.17 show the real hardware manufactured.

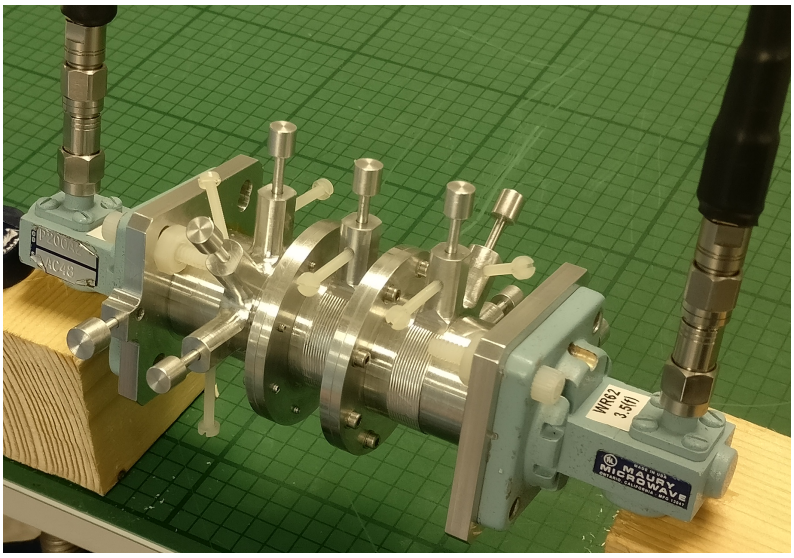

Figure 4.16: The tunable four-pole circular waveguide filter breadboard.

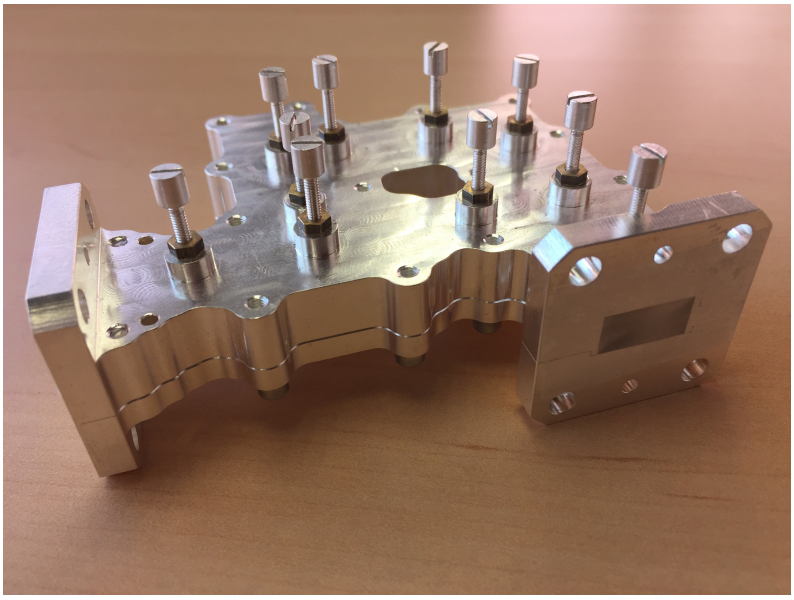

Figure 4.17: Folded rectangular waveguide filter realized in silver plated aluminum.

Table 4.2 and Table 4.3 show the final dimensions of the fabricated tunable four-pole circular waveguide filter and of the folded rectangular waveguide filter, respectively.

As we will show in the next section, once the LA and the HA spaces are aligned, and the HA is very close to the real hardware, the filter will behave as indicated by the simulations in the LA space. In practice, the changes in filter performance will be obtained by changing the penetration of the tuning elements by a very small amount. We, therefore, expect the real hardware to behave as indicated by the simulations in the LA space as a consequence of small dimensional changes. This is, in fact, the very same concept that is at the core of the OS-ASM procedure, which has been demonstrated in the previous chapter.

Table 4.2: Dimensions of the classic dual-mode filter structure in millimeters.

Structure	Height	Width	Length	Radius
I/O aperture	2.5	7.581	1	-
Circular cavity	-	-	31.958	7.959
Central vertical aperture	6.31	1	1	-
Central horizontal aperture	1	5.11	1	-

Table 4.3: Dimensions of the folded filter structure (mm). All heights are 6.477 mm.

Structure	Width	Length
Input aperture	6.401	3.469
First cavity	12.954	30.543
Second aperture	3.851	2.654
Second cavity	12.954	33.106
Third aperture	3.944	3.117
Third cavity	12.954	33.134
Fourth aperture	3.798	2.654
Fourth cavity	12.954	30.982
Fifth aperture	6.661	16.315
Output aperture	6.5	3.671

4.4 Measured results

Once the hardware has been manufactured, we have carried out two sets of measurements. The first is to evaluate the center frequency tuning range, and the second to evaluate the bandwidth tuning range, of both prototypes. The results obtained are reported in the next subsections.

4.4.1 Center frequency tunability

Fig. 4.18 shows the measured results obtained with the dual-mode filter made of silver plated aluminum. In all measured responses, the in-band return losses are around 25 dB.

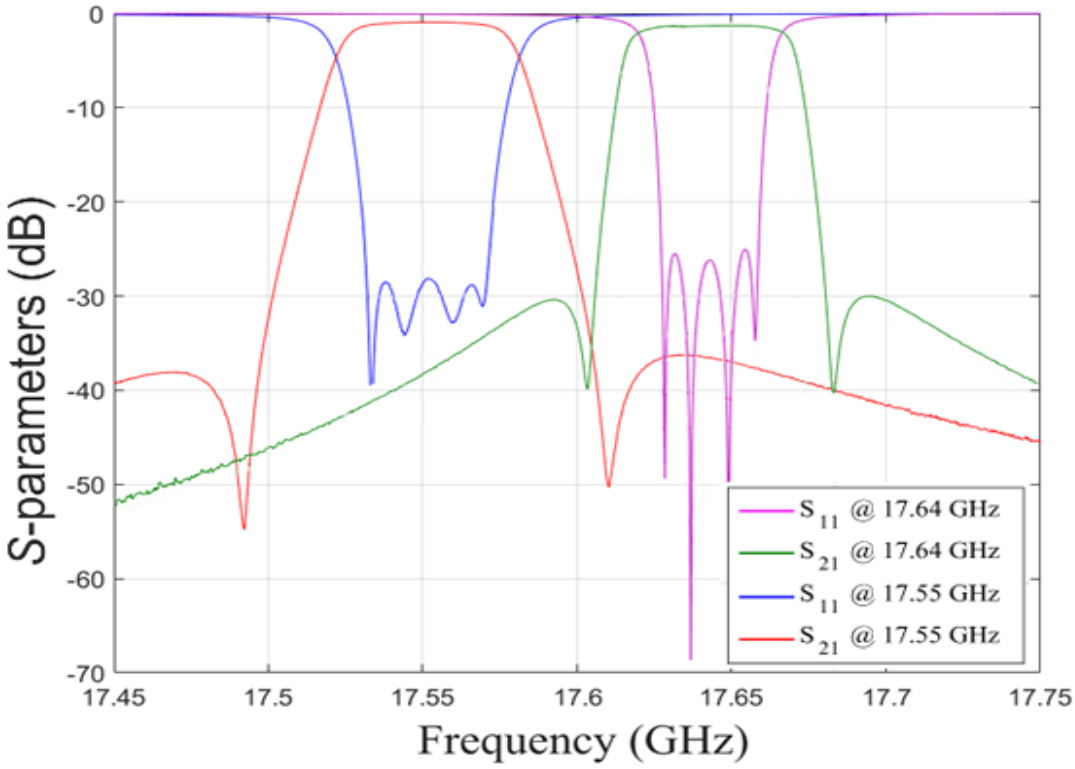

Figure 4.18: Measured tuning range of the circular waveguide dual-mode filter.

As we can see, although the higher frequency filter is slightly narrower in bandwidth (due to manufacturing tolerances observed in the practical implementation of filter irises), the basic tuning performance achieved is the same one as indicated by the LA simulations in Fig. 4.8.

The measured performance of the folded rectangular waveguide filter is shown in Fig. 4.19.

As we can see, the tuning range achieved (keeping always return losses above 22 dB) is about 550 MHz, resulting in a measured tuning range of about $\Delta BW_{rw} = \pm 763\%$. The small difference between the simulated (600 MHz) and the measured range is due to the manufacturing tolerances.

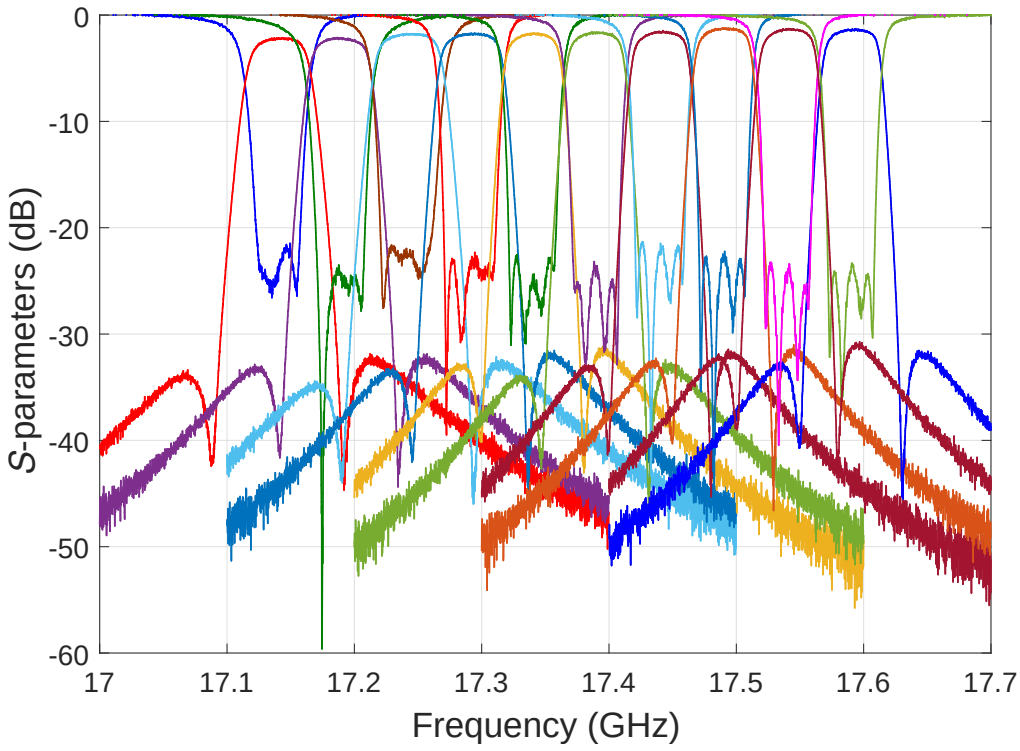

Figure 4.19: Measured tuning range of the folded rectangular waveguide filter.

4.4.2 Bandwidth tuning range

Similarly to what we have done for the center frequency tuning, we have also explored the maximum tuning range for the bandwidth of the two filters (that has been recovered at the central frequency of each tuning range).

The maximum measured bandwidth for the silver plated dual-mode filter turned out to be about 51 MHz, resulting in a tuning range greater than 42% (Fig. 4.20).

Finally, we show in Fig. 4.21 the bandwidth tuning of the folded rectangular waveguide filter. As we can see, the achieved bandwidth is now 69 MHz, resulting in a tuning range greater than 92%.

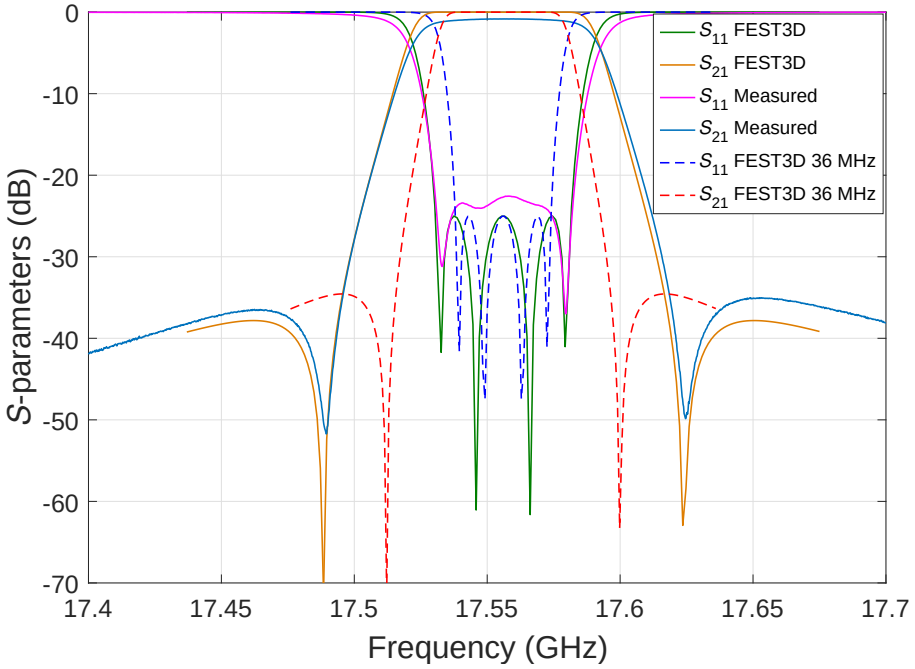

Figure 4.20: Maximum bandwidth for circular waveguide dual-mode filter.

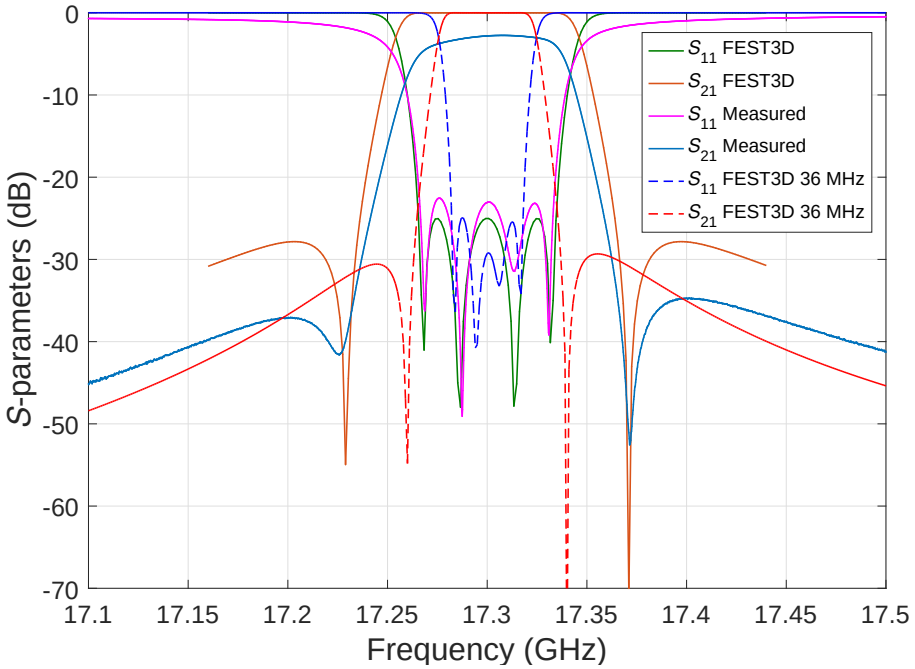

Figure 4.21: Maximum bandwidth for folded rectangular waveguide dual-mode filter.

4.5 Comparative discussion

The results obtained so far can now be summarized in a *comparative* discussion. Three aspects will be addressed in this section, namely tuning range, insertion losses, and out of band performance.

4.5.1 Tuning range

As we can clearly see by comparing the measured results in Figs. 4.18 and 4.19, the single-mode rectangular waveguide implementation can achieve a far superior tuning range than the dual-mode circular waveguide implementation. The reason for this difference is the fact that the use of dual modes imposes conditions on the tuning screw penetrations that result into a limited tuning range. Furthermore, the presence of two resonances in a single cavity introduces also interactions between coupling apertures that further limit the tuning range.

In the single-mode implementation, on the other hand, there are essentially no interactions between tuning screws or coupling apertures, so that the tuning screws can be inserted in the structure to the maximum allowed, and the tuning range results are significantly extended. The only limiting factor in the single-mode case is the resonance of the tuning elements themselves.

4.5.2 Insertion losses

As expected, the circular waveguide implementation achieves lower insertion loss (0.5 dB) than the rectangular waveguide implementation (2.5 dB).

This result is clearly due to different contributions. The lower quality factor of rectangular waveguide resonators as opposed to the circular waveguide resonators is the most important. The more penetration of the tuners inside the filter for the case of the folded filter and the difference due to not be silver-plating also contribute to this difference. It is interesting to note, however, that the height of the rectangular waveguide filter can be increased and this, in turn, can lower the insertion losses, thus bringing it to values that are comparable to the ones achieved by circular waveguide [104].

Obviously, the tuning of this new filter prototype would be achieved with other penetration depths (slightly higher than the previous ones) of the corresponding screws.

4.5.3 Out of band performance

One aspect of the performance of this type of filter that is of key importance is the out of band response. This is particularly important if the filters are to be used in an output multiplexer. Fig. 4.22 shows the comparison of the out of band performance of the two filter types.

It has been checked that the out of band behavior of the proposed circular waveguide dual-mode filter is very similar to the one for the same kind of filter using a classical cross-shaped iris (instead of the one used in this work, see Fig. 4.5), thus confirming that the asymmetric tunable inter resonator iris we use does not generate additional spurious resonant modes.

As we can see, the folded rectangular waveguide filter has a substantially cleaner out of band response.

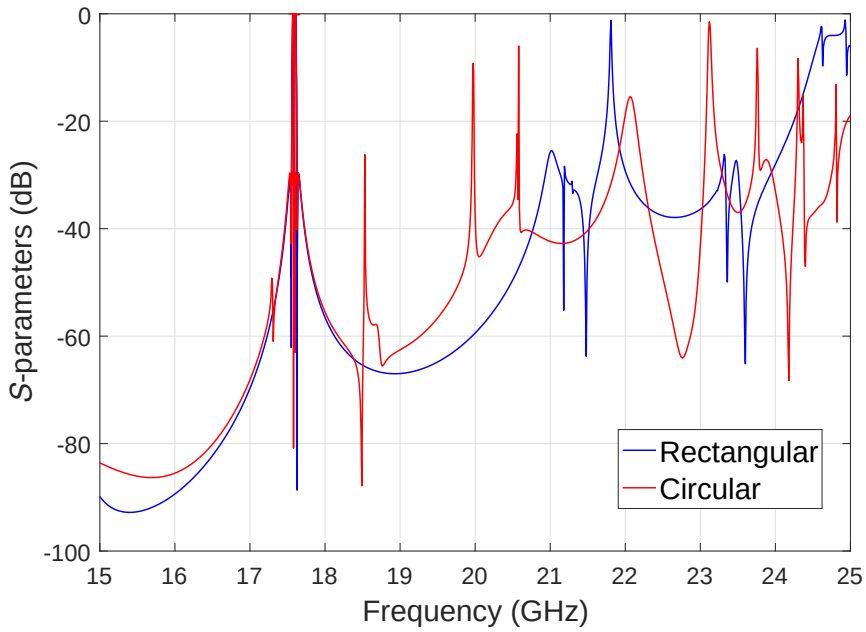

Figure 4.22: Out of band performance comparison. The red curve is the circular waveguide dual-mode filter.

Finally, it is important to note that an alternative configuration for implementing tunable channel filters could indeed be based on a folded configuration using single-mode circular waveguide resonators, coupled through rectangular irises. This structure could probably offer a competitive performance in terms of tuning range and insertion losses, but the limitation in terms of out-of-band performance would still be present.

4.6 Conclusions

In this chapter we have explored and extended the maximum tuning range of two output channel filter structures with the support of EM-based CAD techniques. First, the cross-coupling iris of a classical dual-mode filter in circular waveguide has been modified to provide tunability to the device through the use of metallic tuning screws. Secondly, a simpler folded rectangular waveguide filter has been studied. The results of our investigation clearly show that the folded rectangular waveguide implementation has a measured center frequency tuning performance ($\Delta BW_{rw} = \pm 763\%$) that is far superior to the one of the dual-mode circular waveguide implementation ($\Delta BW_{cw} = \pm 125\%$). Furthermore, the bandwidth tuning of the rectangular waveguide filter is also superior (92%) to the one of the circular waveguide dual-mode filter (42%). Finally, measured results have also been presented showing very good agreement with simulations, thereby fully validating all the results presented.

Chapter 5

Dielectric materials for tuning waveguide filters

This chapter describes and extends the results obtained during the research work related to this thesis in the area of dielectric materials for tuning waveguide filters. It is important to note that the results described in this chapter have resulted into the following scientific publication:

- J. Ossorio, V. E. Boria, and M. Guglielmi, "Dielectric tuning screws for microwave filters applications," *in IEEE MTT-S International Microwave Symposium,* pp. 1253-1256, June 2018.

Metallic tuning screws have traditionally been used in many different types of microwave filters to compensate for both design and manufacturing inaccuracies [7], [8]. As previously shown, precise designs can now be performed using accurate full-wave simulation tools.

However, tuning elements are still widely used to recover the effects of errors in low cost manufacturing (such as combline [105] and dual-mode filters [26], [106]). Furthermore, tuning screws are also used to obtain different responses using the same filter body for low-cost high-yield productions [99], [100] and [107]. There are also particular topologies that are more well-suited for the use of tuning screws, such as evanescent-mode filters [108]. Significant effort has also been devoted in the past to the development of CAD models for the accurate simulation of tuning elements in rectangular waveguide filters [107], in circular waveguide dual-mode filters [68], [109] and [110], and in combline filters [111].

It is also important to note that microwave filters have normally been designed to operate at a single center frequency, and with a fixed bandwidth. Recently, the constant demand of modern communication services for more agility and bandwidth, is radically changing filter requirements [97].

To satisfy the new demands, metallic screws have also been recently proposed as tuning elements in microwave filters that can be tuned over a wide frequency range [27], [31] and [64].

However, the use of metallic tuning screws has a number of drawbacks. They are very sensitive elements, since a small variation in penetration depth can cause an important effect in the filter response (specially for resonators). They can reduce the power-handling capability due to undesired high-power effects [9], [67] and [112]. In addition, it is very difficult to accurately predict the effect of metallic tuning screws by using EM simulation tools [107]. Finally, the main problem with metallic tuning elements is that they must be securely fastened to the filter body (usually with a nut) in order to correctly perform their function. This, in turn, makes remote tuning virtually impossible.

In addition to metallic tuning screws, however, it is also possible to tune microwave filters with dielectric tuning elements. Dielectric resonators are commonly used in microwave filters to implement miniaturized high-performance resonators, [113] and [114]. Although dielectric rods and screws can indeed be found in the market, their use as tuning elements in waveguide filters has not been discussed in detail in the technical literature. To the authors knowledge, only preliminary encouraging results have been published in [28]. In this chapter we will present the most recent advances we have achieved in this research area [115].

5.1 Phase shift of tuning elements

The starting point of our investigation in the context of dielectric tuning elements is the experimental evaluation of the maximum phase shift that can be introduced by a metallic or dielectric tuning element in a rectangular waveguide. The phase shift introduced by a tuning element can, in fact, be directly related to the change in frequency of a resonator that contains the same tuning element.

It is important to note, however, that an alternative would have been to build a one pole resonator, and measure the actual shift in frequency as a result of the changes in tuning element penetration. The choice of the phase shift measurement, instead of measuring the frequency shift of a resonator, has been dictated by the needs of the experimental investigation of the Passive Intermodulation (PIM) behavior described in the next section.

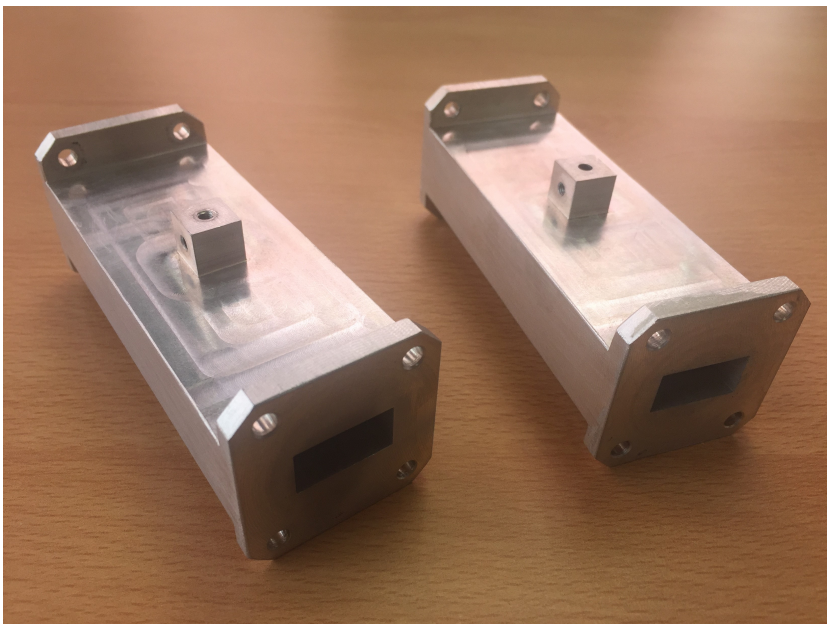

Figure 5.1: Sections of WR-75 waveguide (length of 100 mm each one).

The devices that we have used to measure the maximum phase shift introduced by tuning elements is composed of two identical sections of WR-75 waveguide (Devices Under Test, DUTs), as shown in Fig. 5.1.

Both DUTs have been built using aluminum and spark erosion, and have a hole of 3.0 mm of diameter in the center of the upper wall. However, in one of the DUTs the hole is smooth, while, in the other, the hole is threaded (M3). Using the DUTs shown, we have then measured the phase shift introduced as a function of frequency for the following cases:

- Threaded aluminum screw.
- Threaded stainless steel screw.
- Smooth aluminum tuning rod.
- Teflon screw.
- Smooth Sapphire rod.
- Smooth ceramic dielectric rod.

To perform the actual measurement, the two DUTs were connected in cascade, with a 10 mm silver-plated joining waveguide section. This was done in order to perform all necessary measurements without disconnecting the DUTs from the Vector Network Analyzer (VNA). Furthermore, in each case, the tuning element was inserted to the maximum possible penetration before the appearance of the resonance introduced by the tuning element itself.

Fig. 5.2 shows the result obtained with a threaded aluminum M3 screw penetrating 2.5 mm. The curve in red in Fig. 5.2 (and in all subsequent figures up to Fig. 5.7) is the theoretical result obtained with HFSS.

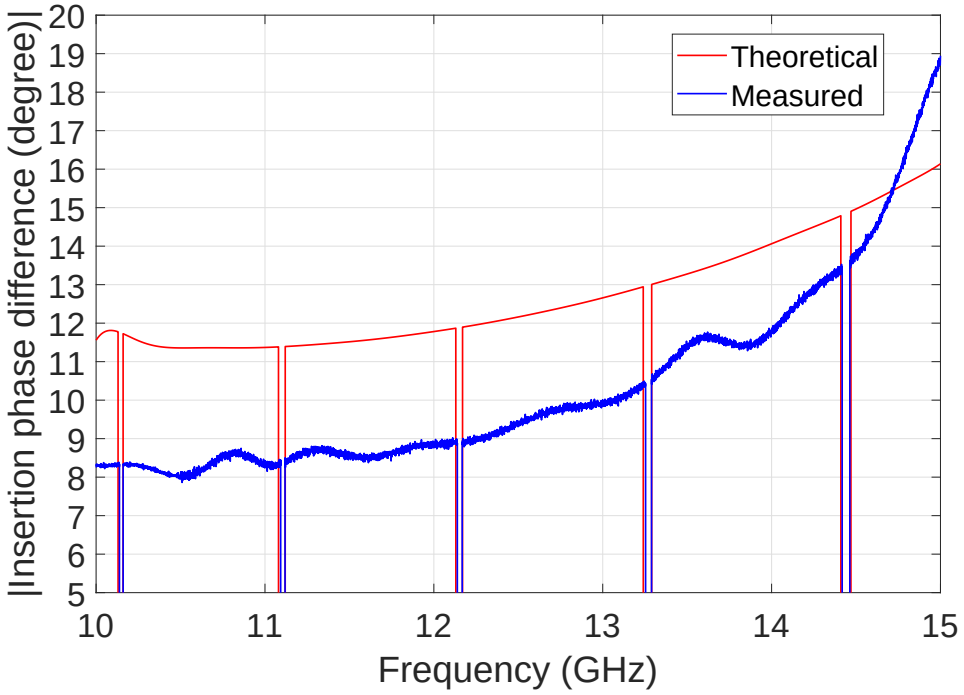

Figure 5.2: Phase difference due to an aluminum M3 screw penetrating 2.5 mm.

Next, we performed the same experiment, using this time a stainless steel M3 tuning screw. Fig. 5.3 shows the result obtained.

The next result we show is the performance of a smooth aluminum rod of 3.0 mm in diameter, see Fig. 5.4.

It is interesting to note that the agreement between measurement and simulation is much better in the case of the smooth aluminum tuning rod than in the cases of the threaded screws. We believe that this is due to the fact that the HFSS simulation does not include the detail of the thread, and the detailed geometry of the end of the screw. More specifically, from the results shown in Figs. 5.2 and 5.4, it appears that a smooth tuning element introduces higher values of phase shift that a threaded tuning element of the same diameter.

This effect may be justified by the fact that the threaded tuning element (a screw) has, indeed, a smaller total volume with respect to a smooth rod of the same diameter and length. As a result, the phase shift introduced by the screw is lower.

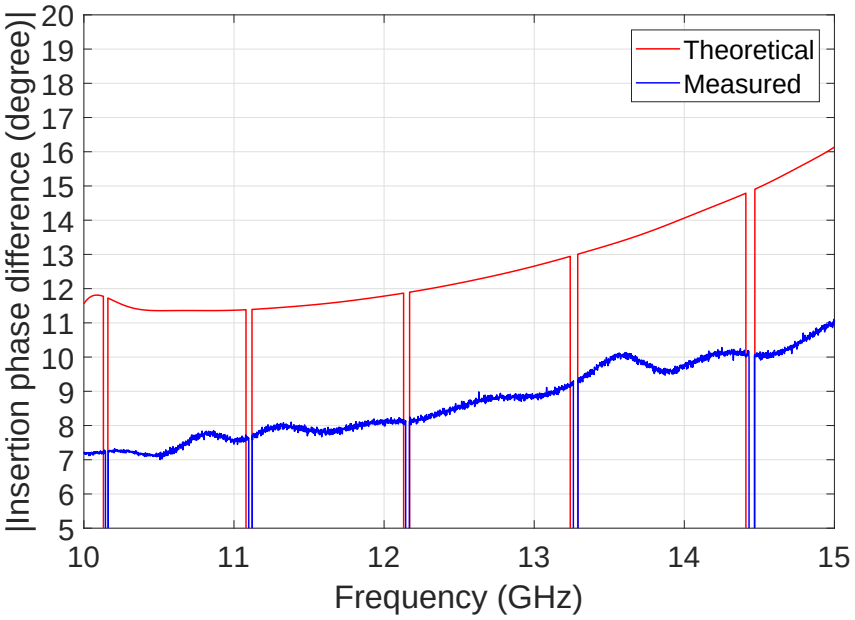

Figure 5.3: Phase difference due to a stainless steel M3 screw penetrating 2.5 mm.

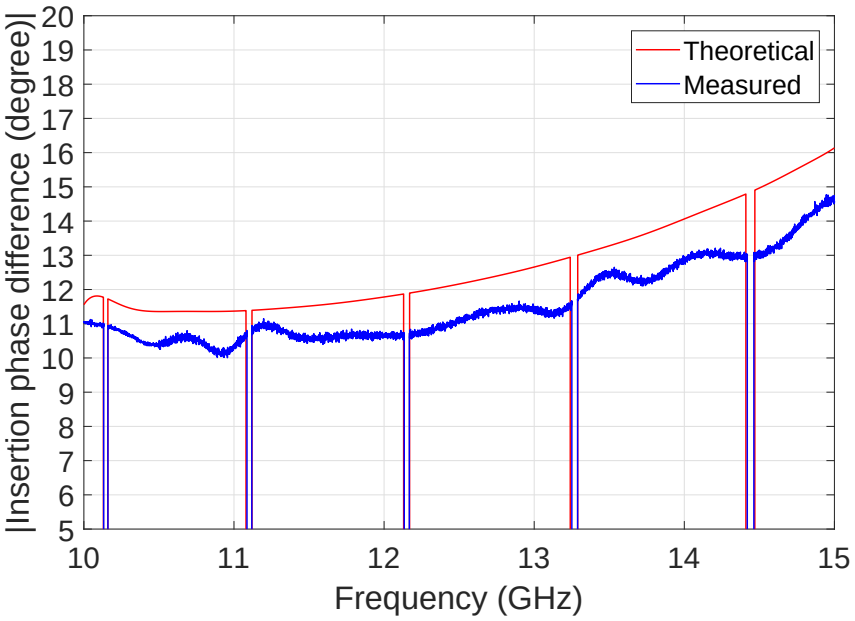

Figure 5.4: Phase difference due to a smooth aluminum rod of 3.0 mm in diameter penetrating 2.5 mm.

Furthermore, it appears that there is also a difference in behavior between the standard stainless steel screw and the aluminum screw, as shown by Figs. 5.2 and 5.3.

This difference may be due to the different metals, but also to the actual detailed physical difference between the two screws. To our knowledge, these differences have not been reported in the technical literature so far.

Next, we show in Fig. 5.5 the results obtained with the Teflon M3 screw. In this case, the screw is allowed to penetrate until the lower surface of the waveguide (9.525 mm). The next results that we show correspond to the phase difference introduced by a smooth Sapphire rod of 3 mm in diameter penetrating 4 mm (see Fig. 5.6). It is important to note that the Sapphire rod has two values of dielectric constant, depending on the direction of electromagnetic field. If the energy propagates along the axis of the cylinder, the value is $\epsilon_r = 11.5$. If the energy propagates in a direction that is orthogonal to the axis of the cylinder, the value is $\epsilon_r = 9.3$. In our case, therefore, we have used $\epsilon_r = 9.3$.

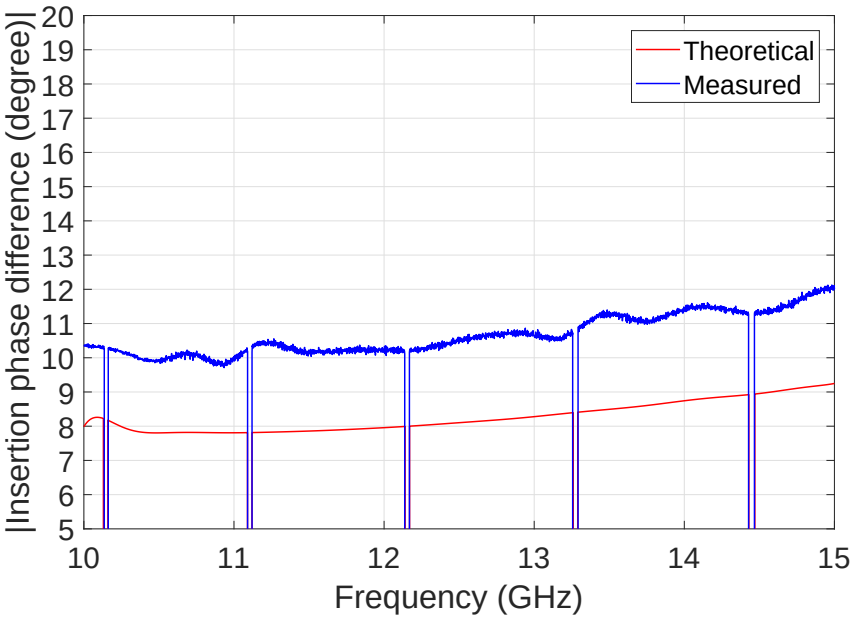

Figure 5.5: Phase difference due to a Teflon M3 screw penetrating 9.525 mm.

The final results we present in Fig. 5.7 are for a dielectric rod of ceramic material with relative dielectric constant equal to fifty ($\epsilon_r = 50$), and with a penetration of 1.0 mm.

As we can see, this material can only be used up to about 12 GHz providing a small phase difference. Furthermore, using a high ϵ_r value reduces very significantly the maximum penetration. We have therefore discarded this material in the rest of the investigation. It is possible, however, that high ϵ_r material could be effectively used at lower frequencies.

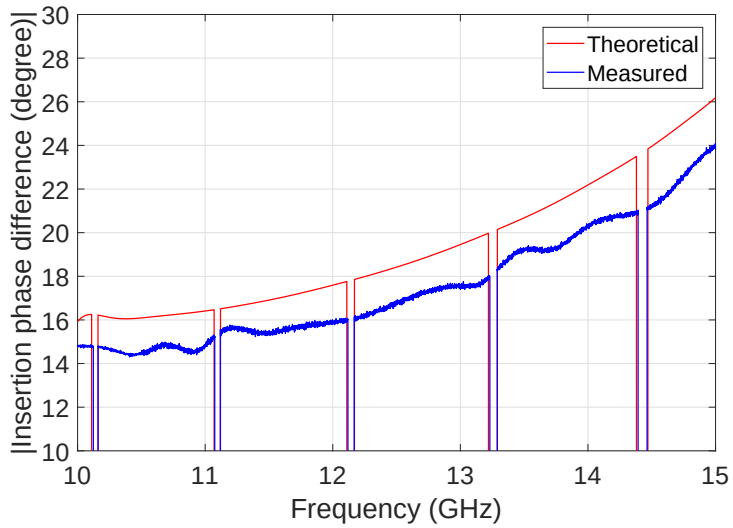

Figure 5.6: Phase difference due to a smooth Sapphire rod of 3 mm in diameter, penetrating 4.0 mm. Dielectric constant ϵ_r parallel to cylinder-axis is 11.5, and perpendicular to cylinder-axis is 9.3.

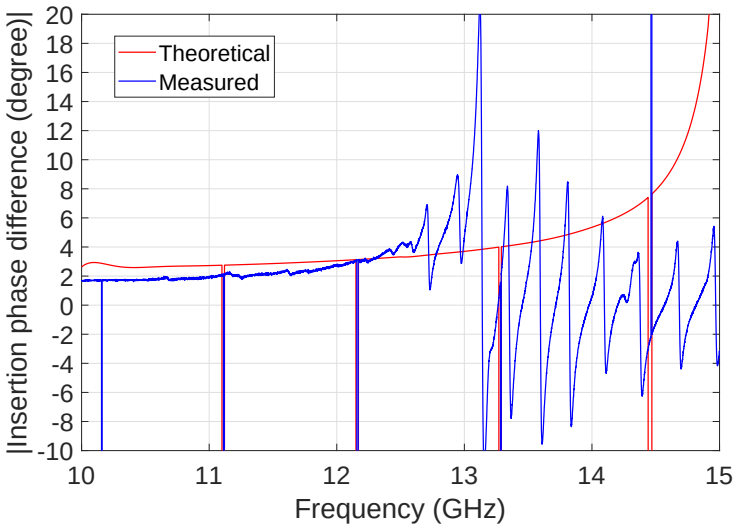

Figure 5.7: Phase difference due to a ceramic dielectric rod with $\epsilon_r = 50$, penetrating 1.0 mm.

Looking at the results obtained so far, we can conclude the following:

1. There is a difference in behavior between a threaded screw and a smooth tuning rod of the same diameter and penetration.
2. The difference between the simulation and measurements in the case of the smooth tuning rod are smaller than the one observed with the threaded tuner.

5.2 Passive Intermodulation

The generation of Passive Intermodulation (PIM) products in high power microwave components in general, and waveguide filters in particular, is an issue that has been known for quite some time [9], [116]. In physical terms, PIM is a non linear effect due to metal to metal contacts. Under certain conditions, a metal to metal contact can have a non linear transfer function, so that an RF current crossing the contact line can result into PIM generation [67], [117]. Intermodulation products can have a very serious degrading effect at system level, so that particular care must be taken to avoid the generation of PIM. It is therefore, a standard industrial practice to measure the PIM generation characteristics of microwave hardware with dedicated measurement benches [118].

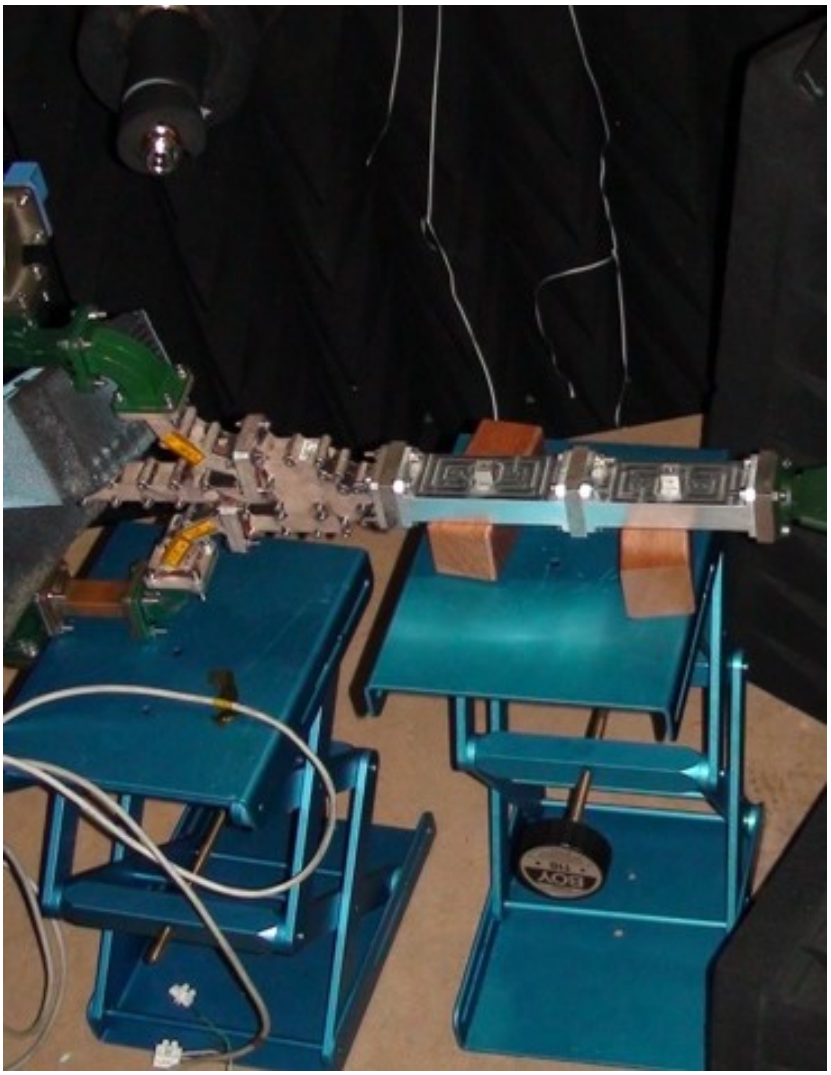

Figure 5.8: PIM test bed configuration including the DUT.

Table 5.1: PIM results for Sapphire.

Penetration (mm)	Power/carrier (W)	PIM (dBm)
Reference	10	-112
0	10	-111
0.5	10	-111
1	10	-111
1.5	10	-111
2	10	-111
3	10	-111
4	10	-111
Reference	10	-110

Table 5.2: PIM results for Teflon.

Penetration (mm)	Power/carrier (W)	PIM (dBm)
Reference	10	-110
9.525	10	-110
Reference	10	-110

In the context of this thesis, it is therefore important to investigate the PIM behavior of the various tuning elements described in the previous section. A PIM measurement was therefore been carried out with the DUTs shown in Fig. 5.1, and with the following measurement parameters:

- Tx1 = 11468 MHz, 10 W CW
- Tx2 = 12735 MHz, 10 W CW
- PIM order 3 = 14002 MHz

Fig. 5.8 shows the DUT within the measurement setup used to obtain the experimental PIM results discussed next.

It is important to note at this point that, although the focus of this thesis is on tunable filters, the DUT selected for the PIM measurement is a straight piece of waveguide instead of a resonator (or a filter). The reason for this choice is that we wanted to focus on the PIM behavior of the tuning element alone. Using a filter with tuning screws as a DUT, would have required a more complex structure with more mating surfaces. The DUTs in Fig. 5.1, on the other hand, are built using spark erosion on a single piece of aluminum, thus reducing to a minimum the required mating surfaces, and therefore drastically reducing any possible source of PIM other than the tuning elements.

Table 5.3: PIM results for stainless steel screw.

Penetration (mm)	Power/carrier (W)	PIM (dBm)
Reference	10	-110
0	10	-111
0.5	10	-110
1	10	-98
1.5	10	-88
2	10	-70
Reference	10	-110

Table 5.4: PIM results for smooth aluminum rod.

Penetration (mm)	Power/carrier (W)	PIM (dBm)
Reference	10	-110
0	10	-111
0.5	10	-109
1	10	-100
1.5	10	-96
2	10	-70
Reference	10	-110

Table 5.5: PIM results for an aluminum screw.

Penetration (mm)	Power/carrier (W)	PIM (dBm)
Reference	10	-110
0	10	-110
0.5	10	-110
1	10	-109
1.5	10	-110
2	10	-110
Reference	10	-110

The first measurement was carried out without tuning elements in the DUTs in order to characterize the measurement setup. A reference (blank scenario) PIM level of -110 dBm was observed with a power of 10 W in each carrier.

Next, we measured the Sapphire rod, obtaining the results shown in Table 5.1 for different penetration values. It is clear that the Sapphire tuning rod does not generate PIM above the residual PIM level of the test facility.

Then, we carried out a measurement with the Teflon screw inserted completely inside the DUT (that is, with a penetration value of 9.525 mm). The results are shown in Table 5.2, and reveal that the PIM produced by this dielectric tuning element is again below the reference (blank scenario) PIM level. The next material we measured is stainless steel (SS). In this case, the tuning screw was properly locked with a locking nut for each penetration value. The results obtained are shown in Table 5.3. It is clear that when the SS screw penetrates more than 1 mm, it does generate strong PIM. This result was, indeed, expected, since the contact between the SS screw and the aluminum body of the DUT introduces a non-linearity in the microwave current flow.

The next measurement was carried out with a smooth aluminum rod (see Table 5.4). In this case, the rod was blocked with a lateral (orthogonal) SS screw (as described in the caption of Fig. 5.1). From the measurement results, we can conclude that when the aluminum rod penetrates more than 1 mm, it also generates strong PIM. Theoretically, a tuning element made of the same metal as the body of the device should not generate PIM. It is possible, however, that the appearance of PIM in this case is due to the lateral SS screw used for blocking the tuning rod. The screw may create a non homogeneous metal-to-metal contact between the rod and the body of the DUT thereby generating PIM.

The last measurement that we carried out is for the aluminum screw locked in place with a nut made of SS (see Table 5.5). It is clear that when the aluminum screw is locked by a nut does not generate PIM above the residual PIM level of the test facility. This is due to the RF current does not go through the discontinuity with the other metal, since that is far away from the waveguide.

5.3 Study of one cavity in waveguide

To estimate the possible tuning range of the classic inductive rectangular waveguide filters, when the metallic tuning screws are replaced by Teflon rods ($\epsilon_r = 2.1$), we have first used the commercial software package HFSS, and we have focused our attention on the simpler structure shown in Fig. 5.9 with the resonant frequency at 13 GHz. The next step has been the introduction of 2 mm diameter metallic tuning screws, both in the cavity and in the apertures, to estimate the maximum tuning range that metallic tuning screws can provide. The result is shown in Fig. 5.10.

This result has been obtained introducing all three metallic screws by 3.5 mm. Increasing more the penetration would bring the resonance of the tuning screw in the cavity too close to the center frequency of the band-pass.

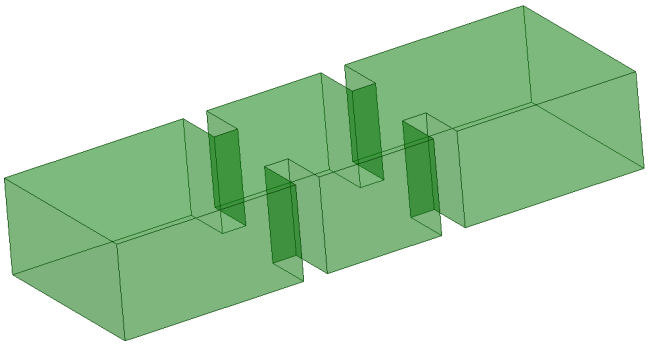

Figure 5.9: Simple one pole filter structure.

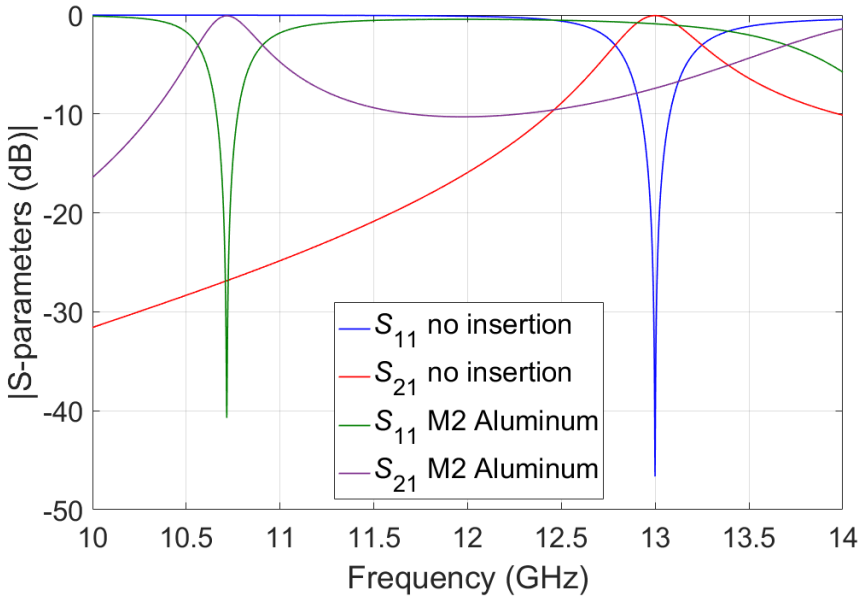

Figure 5.10: Performance of a simple one pole filter structure with metallic tuning screws. No penetration: right, 3.5 mm penetration: left.

As we can see in Fig. 5.10, using metallic screws, the one pole structure can be tuned from 13 GHz down to 10.716 GHz (approximately 2.3 GHz). The next experiment that we perform is to use the same structure as in Fig. 5.9 but using, this time, fully inserted Teflon tuning rods of 2 mm diameter, instead of metallic tuning elements, see Fig. 5.11.

The performance obtained with HFSS is shown in Fig. 5.12. As we can see, with 2 mm diameter Teflon (center curve) we obtain about 1 GHz of tuning range. The next experiment that we perform is to use Teflon rods of 4 mm in diameter. Fig. 5.12 (left curve) shows that, this time, we have achieved 1.882 GHz of tuning range.

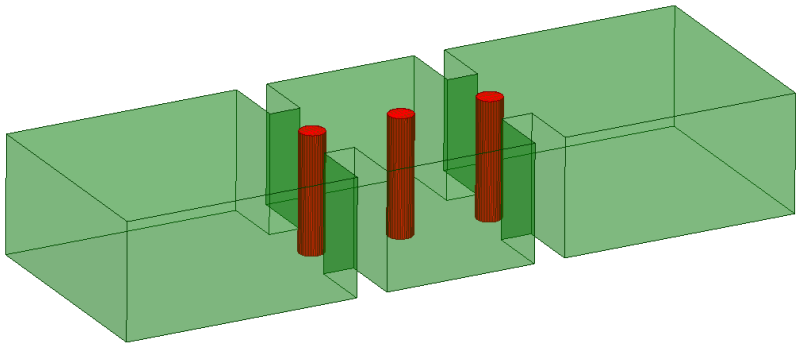

Figure 5.11: Structure with fully inserted 2 mm Teflon rods.

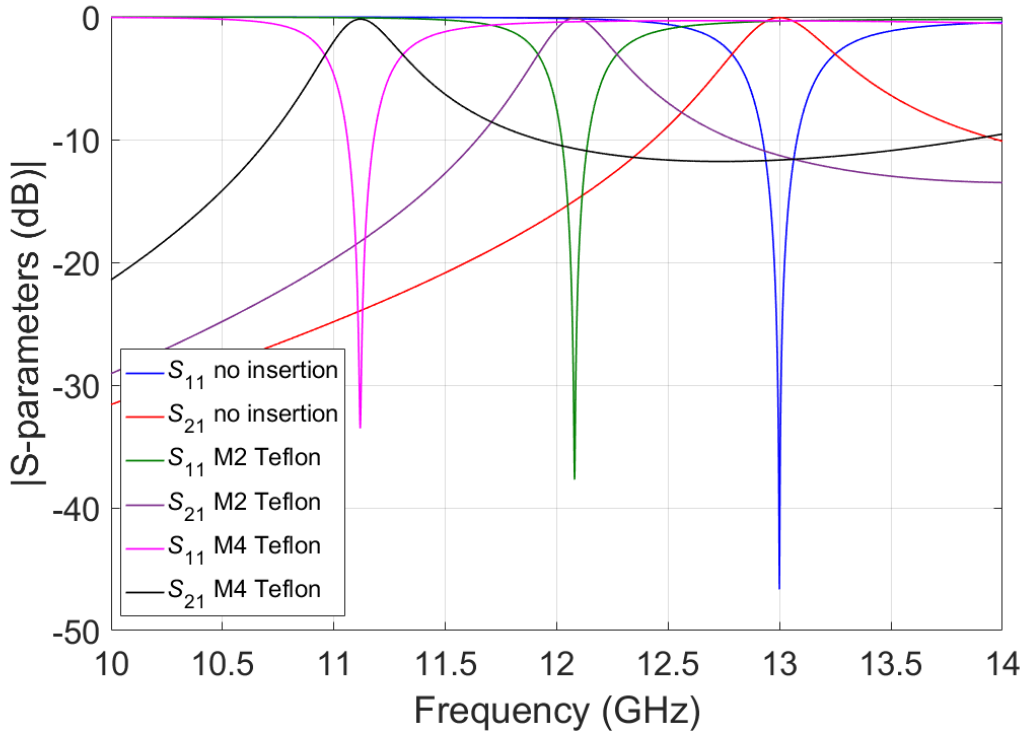

Figure 5.12: Tuning range estimation with Teflon. No penetration: right, fully inserted M2 Teflon rods: center, fully inserted M4 Teflon rods: left.

We can therefore conclude this part of our investigation recognizing that with fully inserted 4 mm diameter tuning rod we can recover almost 80% of the tuning range provided by 3.5 mm penetration of 2 mm diameter metallic screws. Next, we have tried the same experiment using 2 mm diameter Sapphire rods ($\epsilon_r = 10.4$, average value between transversal and vertical ϵ_r Sapphire values). Fig. 5.13 shows the results obtained.

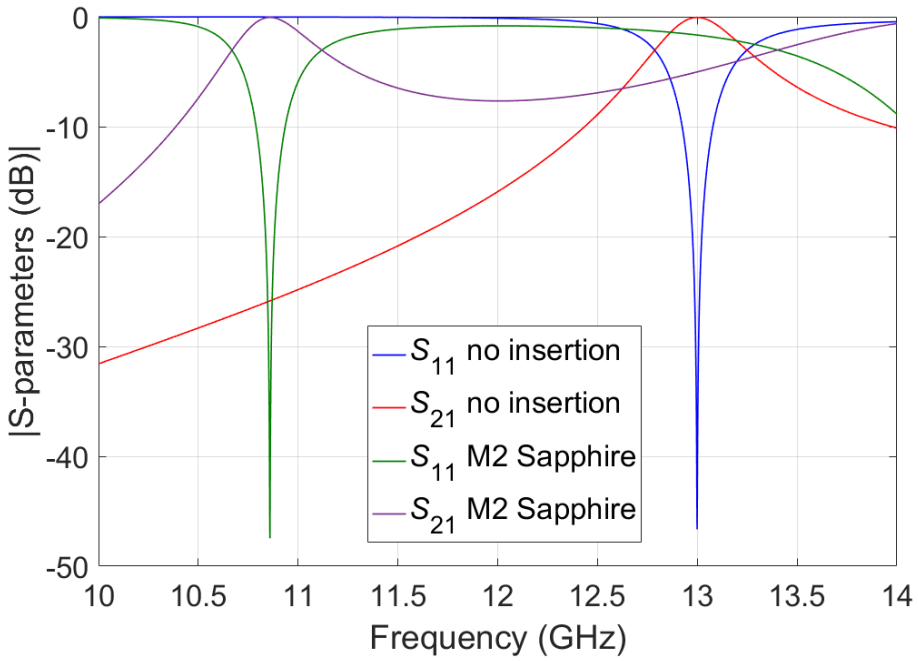

Figure 5.13: Performance with almost fully inserted 2 mm Sapphire rods.

As we can see, in this case we have obtained about 2.1 GHz tuning range. This result is essentially identical to the one obtained with metallic tuning screws. We have also tried Alumina tuning rods ($\epsilon_r = 9.2$) with essentially identical results. However, using Alumina tuning rods produced a much higher value of insertion loss. Alumina was therefore discarded.

5.4 Four-pole inductive filter with tuners

The reference structure that we will use in this investigation is a standard, inductively coupled, rectangular waveguide filter [58], as shown in Figs. 5.14 and 5.15 for the basic structure, and simulated performance at 12 GHz, respectively. For fabrication purposes, the ideal square corners have been replaced with a 2 mm radius. As described in chapter 3, the OS-ASM has been used to design this tunable filter efficiently. In addition, this filter has been realized in silver plated aluminum in order to reduce the insertion losses. Fig. 5.16 shows the measured performance obtained for the highest and the lowest frequency tunable channel. Table 5.6 shows the theoretical values for the penetration of the metallic tuning screws.

It is interesting to note that the insertion loss achieved is approximately 0.44 and 0.40 dB, at 11 and 13 GHz, respectively.

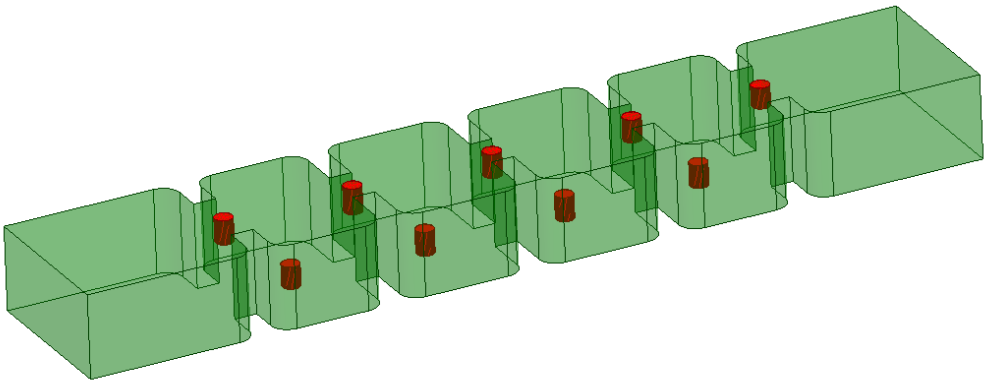

Figure 5.14: Basic four-pole inductive filter structure in rectangular waveguide.

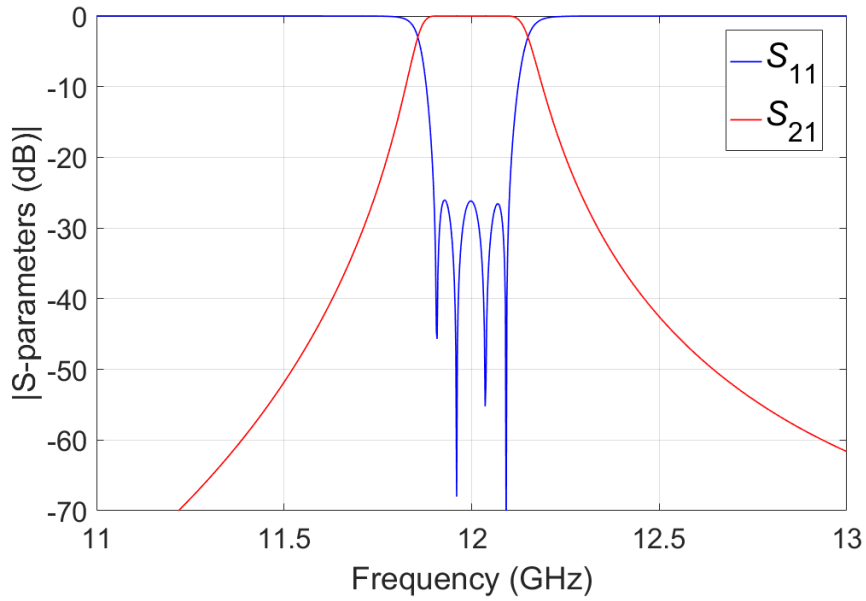

Figure 5.15: Basic four-pole rectangular waveguide, inductive filter performance.

Table 5.6: Theoretical Metallic Tuning Screws Penetrations (mm)

Filter element	11 GHz	12 GHz	13 GHz
I/O aperture	3.61	2.73	0.49
First cavity	3.41	2.48	0.47
Second aperture	3.85	2.89	0.50
Second cavity	3.66	2.69	0.49
Centered aperture	3.76	2.70	0.50

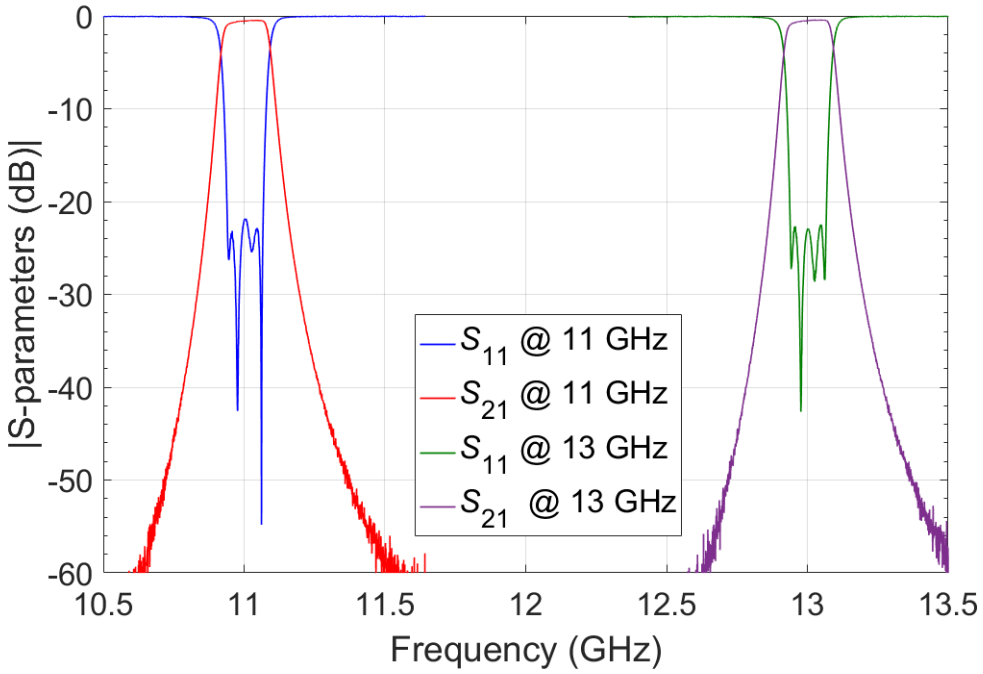

Figure 5.16: Measured response of the tunable, silver-plated filter.

5.4.1 Experimental investigation using Teflon tuners

To confirm our estimate for Teflon, we now perform a series of measurements with the structure in Fig. 5.14, using first 2 mm, and then 4 mm diameter Teflon tuning rods. Fig. 5.17 shows the measured high frequency result obtained with 2 mm tuning rods barely inserted. Fig. 5.18 (right curve) shows the performance achieved with 2 mm Teflon rods with the maximum penetration.

As we can see, the tuning range achieved is about 128 MHz. The next result that we will present has been obtained using 2 mm Teflon rods in the apertures, and 4 mm Teflon tuning rods in the cavities. Fig. 5.18 (left curve) shows the result obtained for the low frequency end. With this arrangement, we have obtained a tuning range of about 575 MHz. In this last case, the limiting factor turns out to be the input-output aperture, where the 2 mm Teflon rod touches the bottom of the cavity at the lower center frequency. The insertion loss obtained in this case is 0.65 dB at the lower center frequency, and 0.61 dB at the higher center frequency. Figure 5.19 shows the filter being measured.

It is interesting to note that we have not been able to correctly tune the filter when all tuning rods of 4 mm in diameter are used. A preliminary investigation shows that this is due to the very strong interaction between the relatively thick and closely spaced dielectric rods.

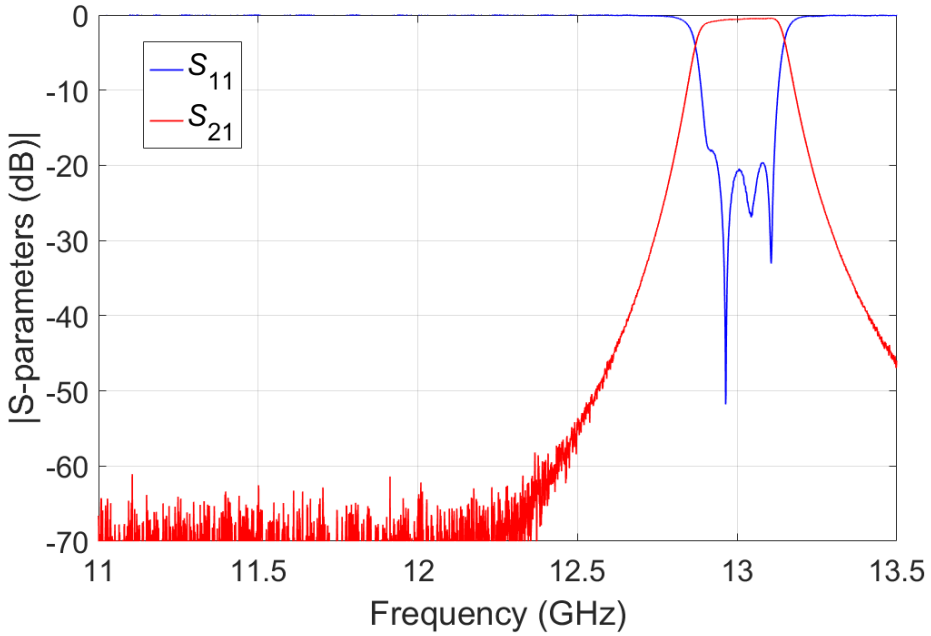

Figure 5.17: High-end performance with 2 mm Teflon rods barely inserted.

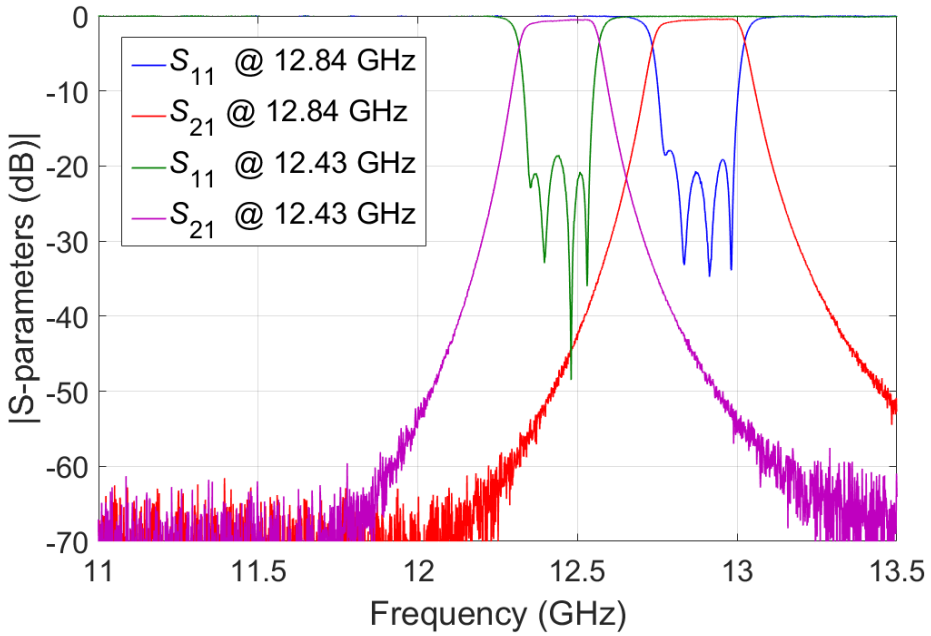

Figure 5.18: Low-end performance. All 2 mm Teflon rods: right curve, 2mm Teflon rods in apertures and 4 mm Teflon rods in cavities: left curve.

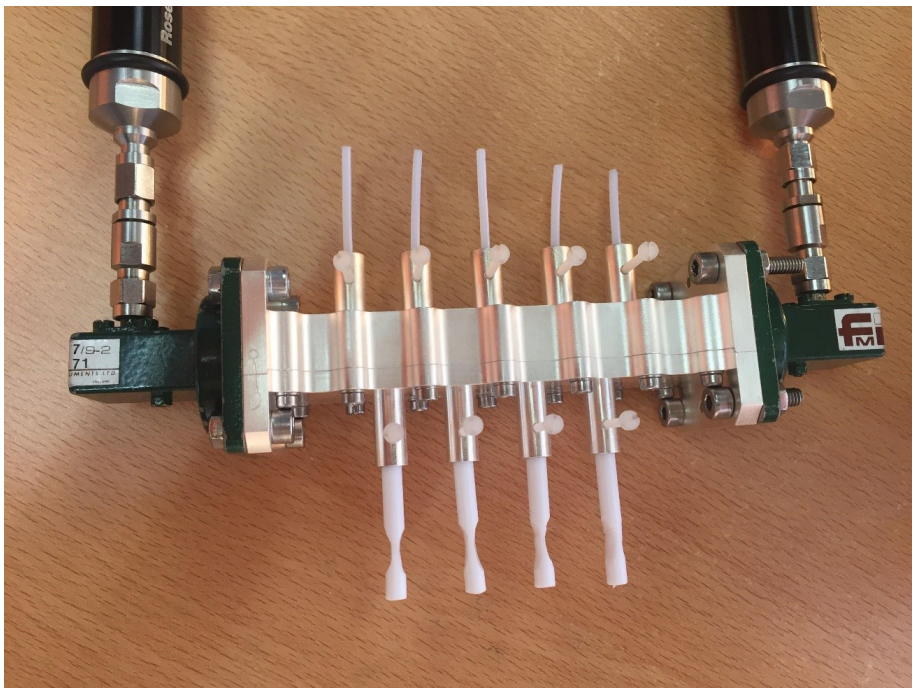

Figure 5.19: The hardware being measured.

5.4.2 Experimental investigation using Sapphire tuners

Next, we discuss the experimental results obtained with Sapphire rods ($\epsilon_r = 9.3$ for propagation perpendicular to the cylinder axis) of different diameters. In the first measurement we have performed, we have used Sapphire rods of 2 mm as tuning elements. In Fig. 5.20 we show the tuned filter responses at the minimum (low-end) and at the maximum (high-end) frequencies of the achievable tuning range that can be obtained with Sapphire.

As we can see in Fig. 5.20, with 2 mm Sapphire rods we have obtained almost the same tuning range given by the silver-plated aluminum rods (as reported in [115]). The insertion loss obtained in this case is 0.74 dB at the lower center frequency, and 0.61 dB at the higher center frequency.

It is important to note that the Sapphire tuning rods are practically fully inserted at the low-end performance (8.5 mm theoretically from previous simulations), indicating that also in this case we have a higher physical movement of the tuning element with respect to the silver-plated aluminum case. Again, this is indeed an advantage since the filter response is less sensitive to small variations in the tuning element penetration.

Finally, we have performed two more measurements using as tuning elements Sapphire rods of 3 mm and 4 mm. Fig. 5.21 and Fig. 5.22 show the results obtained. As we can see, the tuning range achieved is reduced.

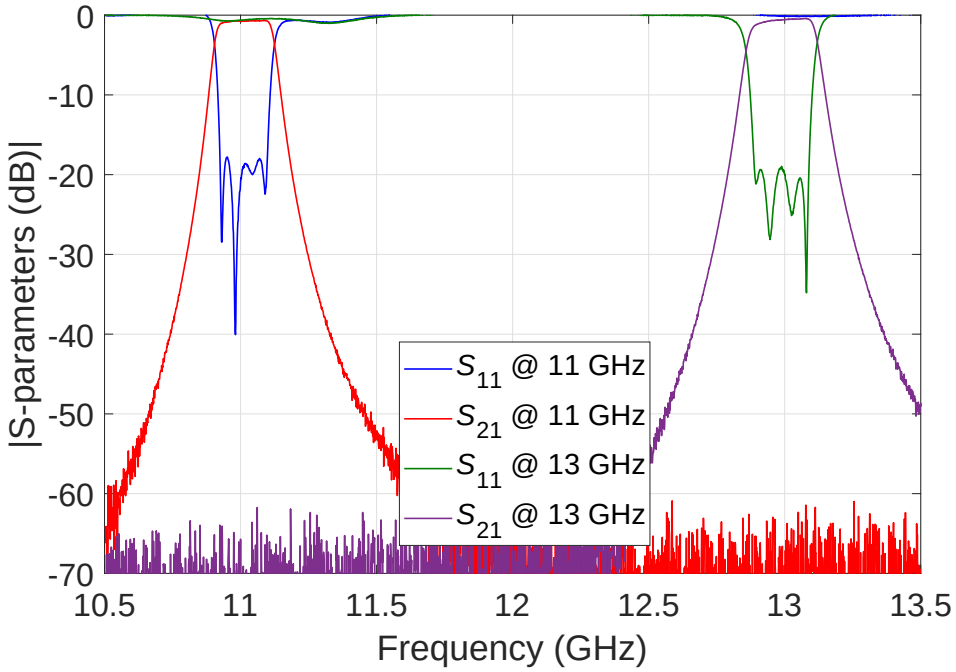

Figure 5.20: High-end (right) and low-end (left) performance with 2 mm Sapphire rods.

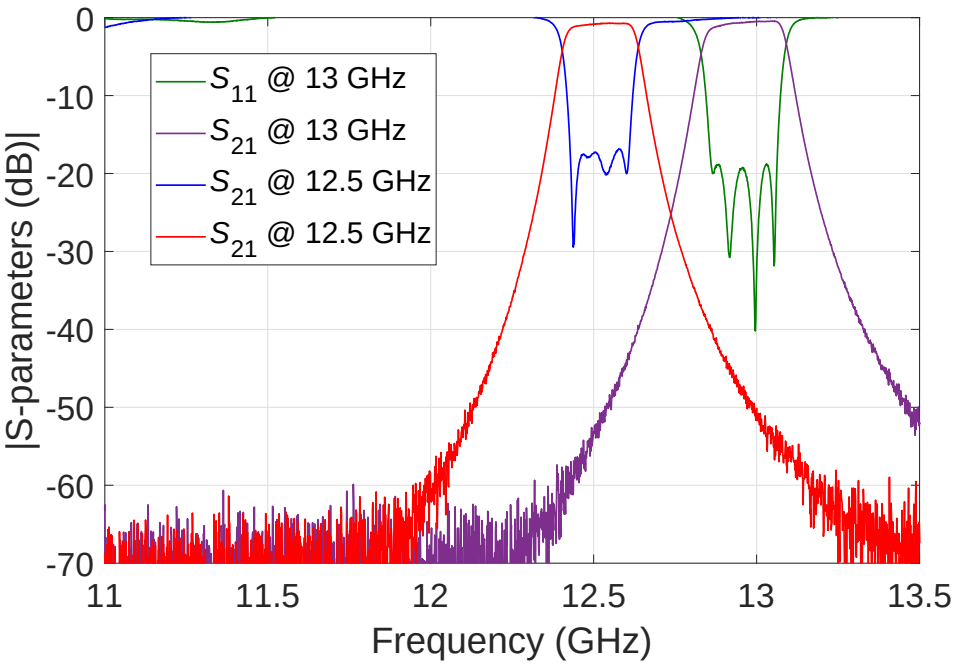

Figure 5.21: High-end (right) and low-end (left) performance with 3 mm Sapphire rods.

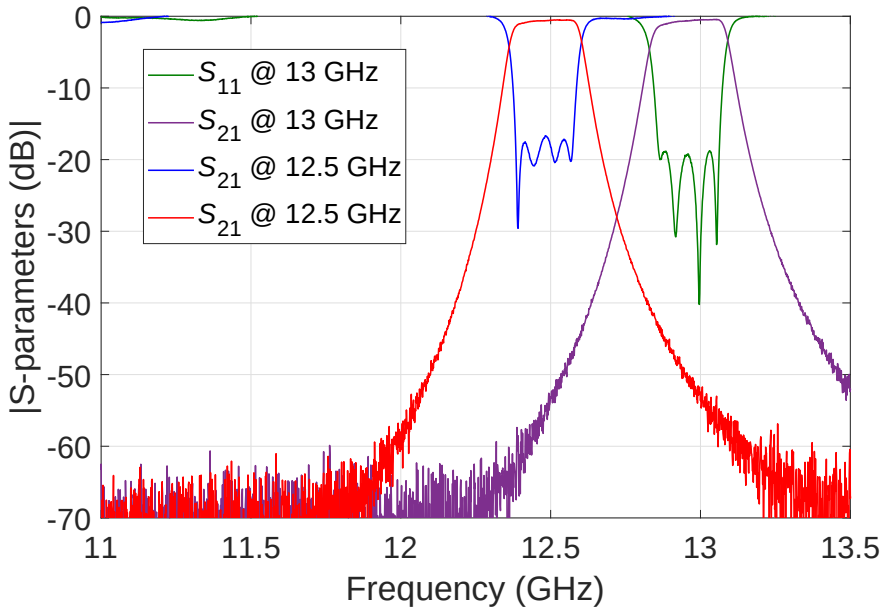

Figure 5.22: High-end (right) and low-end (left) performance with 4 mm Sapphire rods.

We believe that this is because using larger tuning screws introduces an interaction between the dielectric rods, thus reducing the effective tuning range that can be achieved. Therefore, for each dielectric material and specific filter geometry, there will be an optimal choice for the diameter of the tuning rods to achieve the maximum tuning range.

5.5 Comparative discussion

In summary, it appears that it is indeed possible to use dielectric tuning screws, instead of metallic tuning screws, in rectangular waveguide filters of the type shown in Fig. 5.14. The main difference are:

- Dielectric screws generally penetrate inside the filter far more than metallic screws.
- Contrary to metallic screws, dielectric screws do not require a good electric contact with the body of the filter.
- The insertion loss achievable with dielectric tuning elements is comparable to what can be achieved with metallic (silver-plated) tuning elements.

The first and second feature appear to be of particular interest, because they may open the way to practical realizations of remotely tunable microwave filters. Finally, it is important to note that, so far, we have measured only the use of Teflon and Sapphire. However, other dielectric materials are available in the market, with higher dielectric constants and low insertion losses.

5.6 Remote tunability by linear motors for 4-pole inductive filter

We have already demonstrated that dielectric tuning elements can be used for tuning waveguide filters. In this section, we are going to demonstrate their use to perform remote tuning. As we have seen in the previous sections, Sapphire rods provide a wider tuning range, large penetration inside the structure and a behavior similar to metallic rods.

The test will consist in tuning a 4-pole rectangular waveguide inductive filter between 11 to 13 GHz using Sapphire tuning rods of 2.0 mm diameter, and using linear actuators to control their position. The main idea is to tune different channels and verify the repeatability of the measurements.

The motors that we are going to use are the 'PQ12-P Linear Actuator with Feedback' from Actuonix[1], see Fig. 5.23.

Figure 5.23: PQ12-P linear actuator.

These motors are provided with a specific control board and software in order to control the position of the actuator, see Fig. 5.24 and Fig. 5.25.

Additionally, in order to reduce all the possible undesired movements of the all parts and guarantee the repeatability of the measurements, we have designed a support structure where we are going to place the filters and the motors, see Fig. 5.26.

[1] https://www.actuonix.com/PQ12-Micro-Linear-Actuators-s/1825.htm

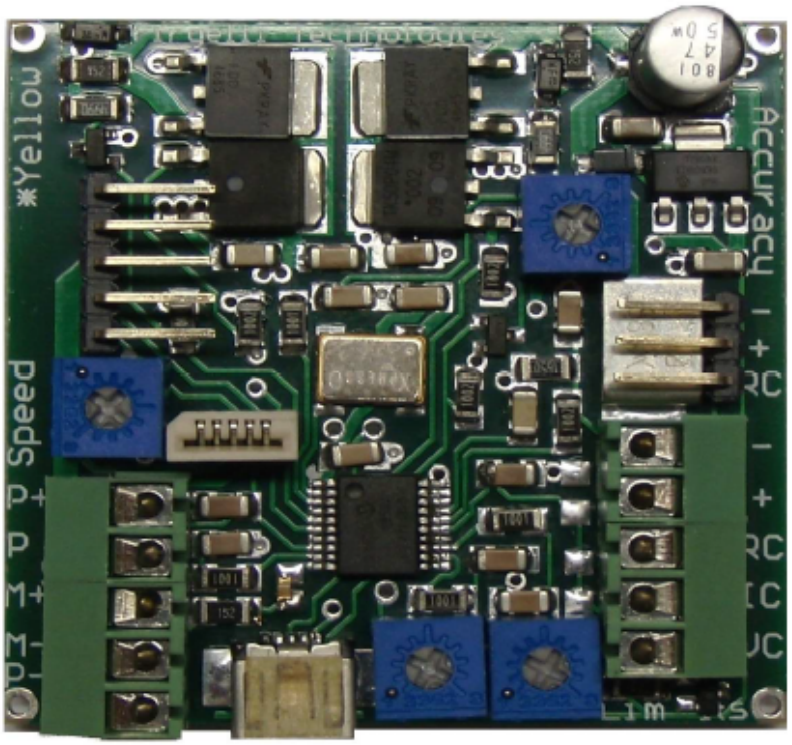

Figure 5.24: PQ12-P control board.

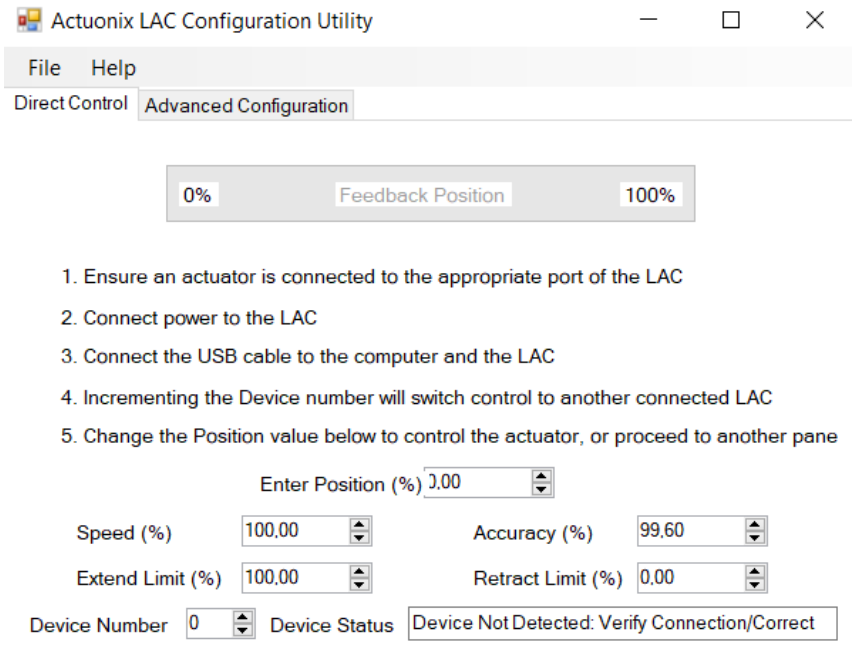

Figure 5.25: PQ12-P control software.

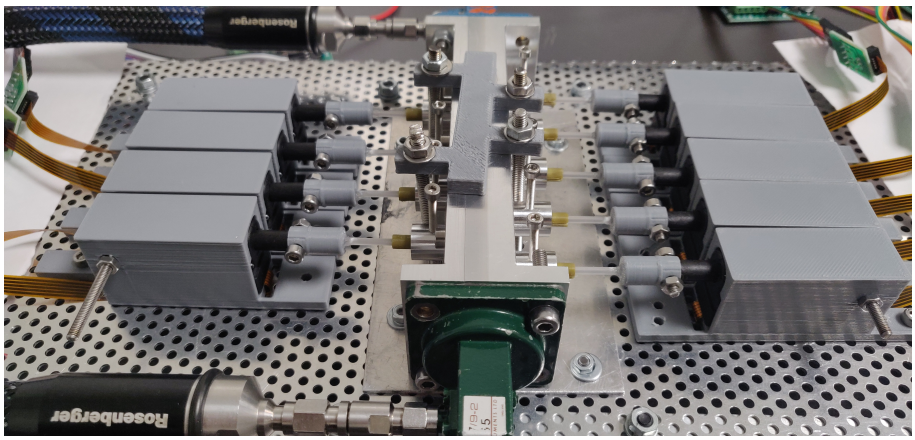

Figure 5.26: Support structure for the filter with the motors and Sapphire tuners.

As we can see, the filter is fixed to the support structure by a top holder and four screws. On both sides of the filters we have the actuators in separate 3D-printed structures fixed to the support structure. Finally, in the mobile part of the actuator we have fixed Sapphire (rod) tuners that are aligned with their respective holes in the filter body. In order to allow for a friction less movement of the tuner, we have included a 3D-printed piece (green part inside the red circle in Fig. 5.27) that keeps the tuner centered.

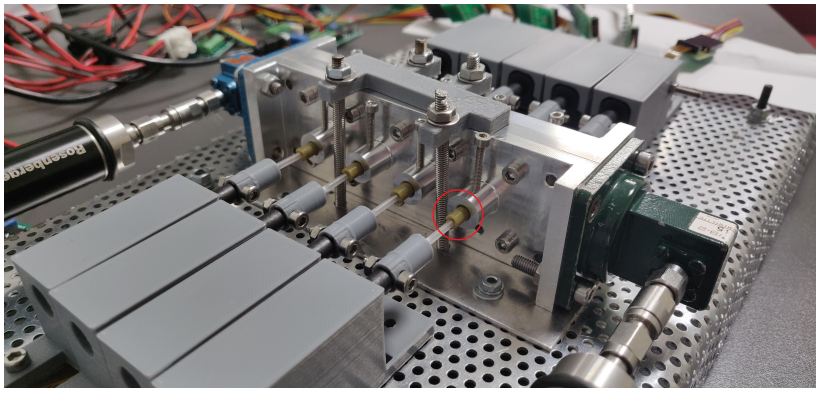

Figure 5.27: Detail of the Sapphire tuners centered and fixed in the holes by a 3D-printed piece.

Finally, all the motors are connected to their control board. Each control board is connected to a USB-hub, in order to control all the motors using one single computer. Additionally, an external power supply is necessary to feed all the boards. In Fig. 5.28 we can see the complete set-up for this test.

The next step is to tune the filter in different channels, and to find the specific positions of each motor for these channels. Table 5.7 shows the relative position of the motors for different channels tuned from 11 to 13 GHz.

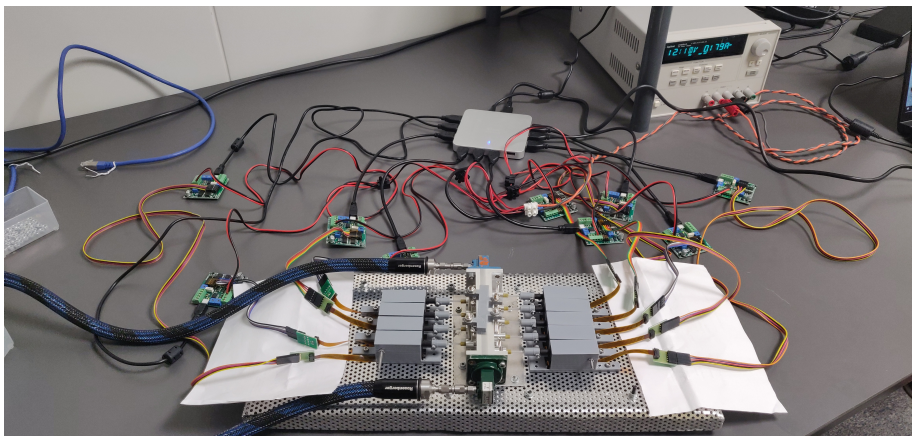

Figure 5.28: Set-up of the motors, filter and the control boards.

Table 5.7: Relative position of the motors for different filter channels (0-100% of penetration).

Frequency (GHz)	Motor 1	Motor 2	Motor 3	Motor 4	Motor 5	Motor 6	Motor 7	Motor 8	Motor 9
11.057	62	58	55	55	55	66	62	62	57
11.410	57	53	50	49	46	56	55	54	52
11.918	49	45	42	41	39	46	44	45	42
12.389	43	38	35	32	31	38	35	37	37
12.995	28	23	20	18	21	19	18	19	20

*Motors 1-4 are placed in the cavities of the filter.
*Motors 5-9 are placed in the apertures of the filter.

As we can see, the results are as expected. When we configure the filter with a lower frequency, the tuners penetrate deeper in the structure and vice-versa.

With all this information we can start the measurements of the filter. For the test we are going to reconfigure the different channel filters introducing in the software of the motors the values from Table 5.7 several times. We re-tune one channel to another one randomly, in order to obtain the maximum possible different cases.

In total we reconfigure and measure the filter 5 times for each channel. Figs. 5.29 to 5.33 show the results of the five measurements for each channel.

As we can see, the results show very good repeatability of the reconfiguration of the different channels of the filter. For the higher frequency channels the measurements are more coincident than for the lower channels. This behavior is expected, since for the lower channels we need to penetrate deeper in the filter and the actuator is far more outside of the motor, obtaining higher position inaccuracy. Nevertheless, the return loss parameter remains below 15 dB (for an initial channel of 20 dB of return loss), so that we can conclude that the filters have been completely recovered.

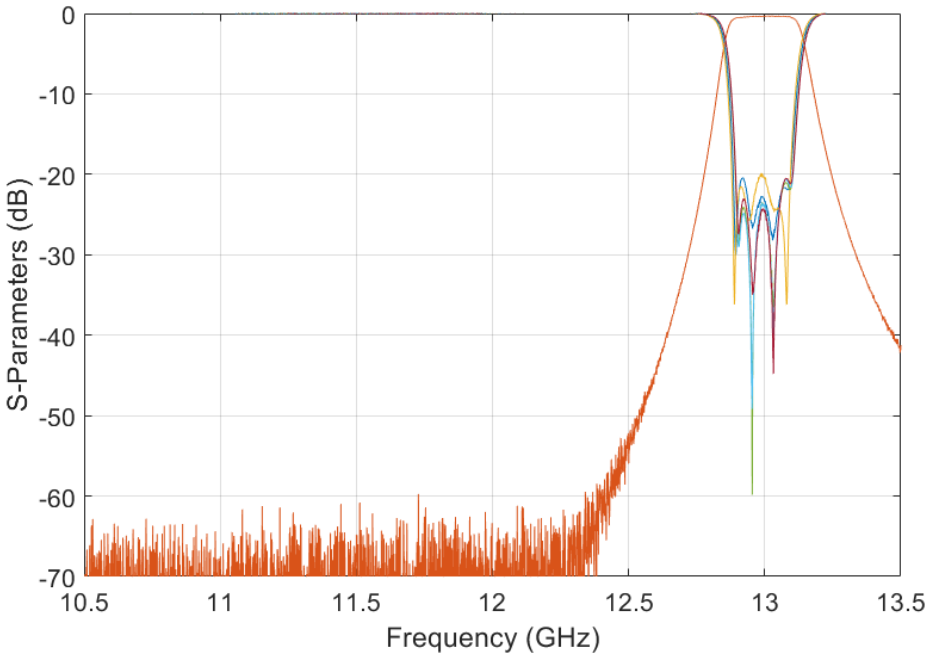

Figure 5.29: Measurements of the 12.995 GHz channel.

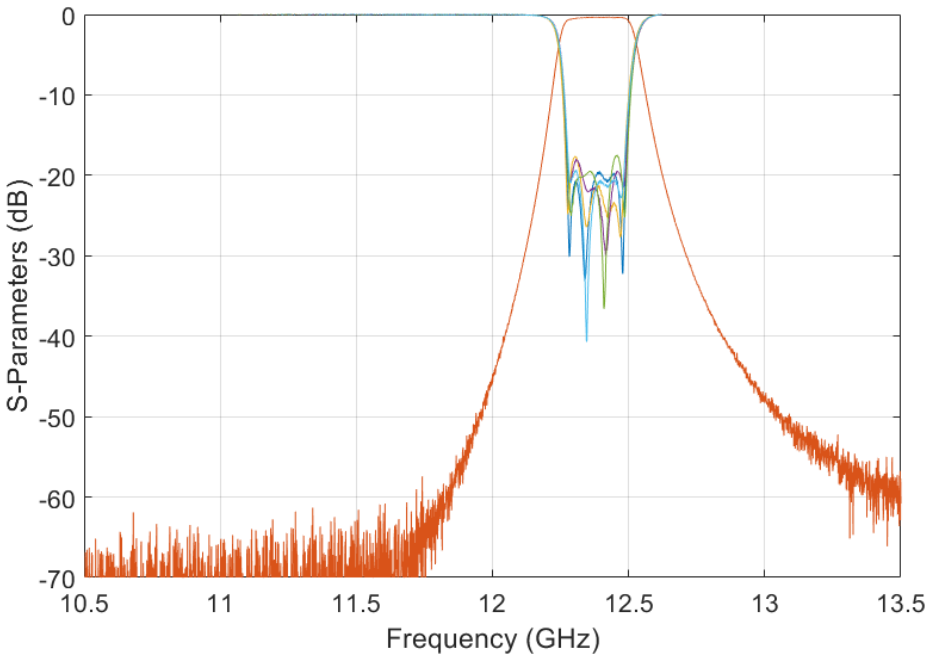

Figure 5.30: Measurements of the 12.389 GHz channel.

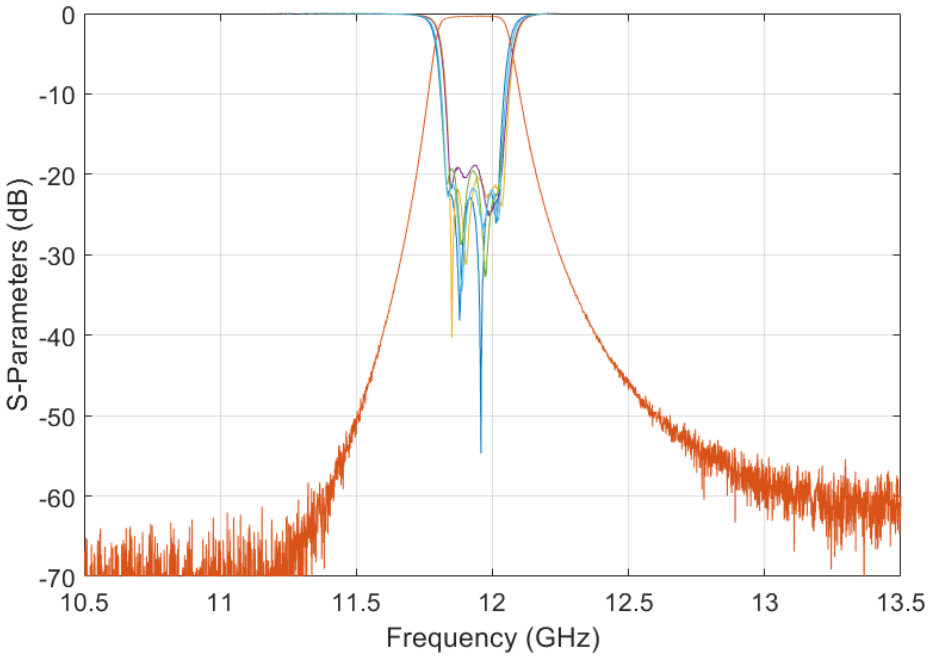

Figure 5.31: Measurements of the 11.918 GHz channel.

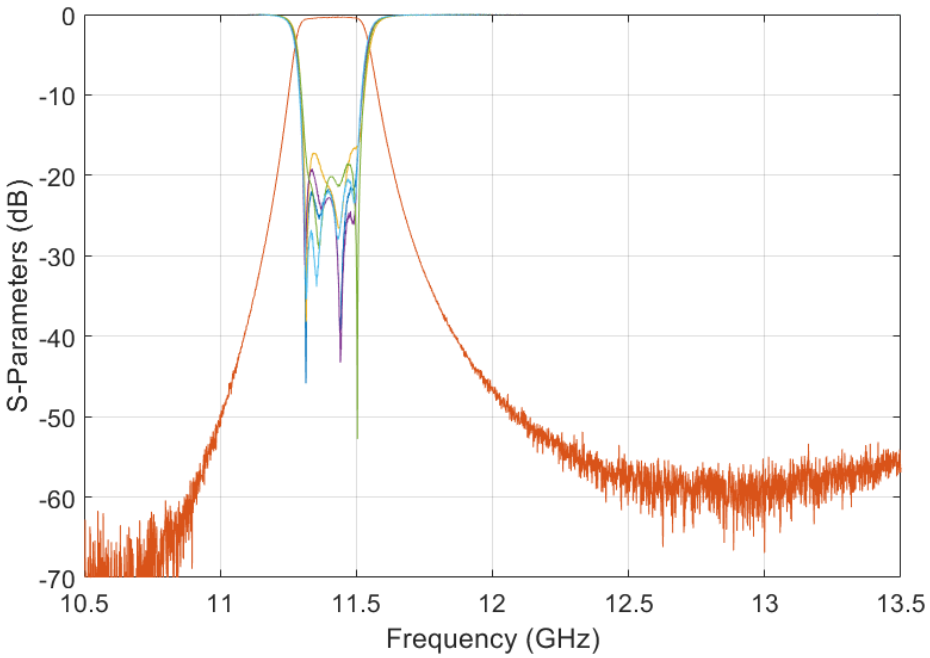

Figure 5.32: Measurements of the 11.410 GHz channel.

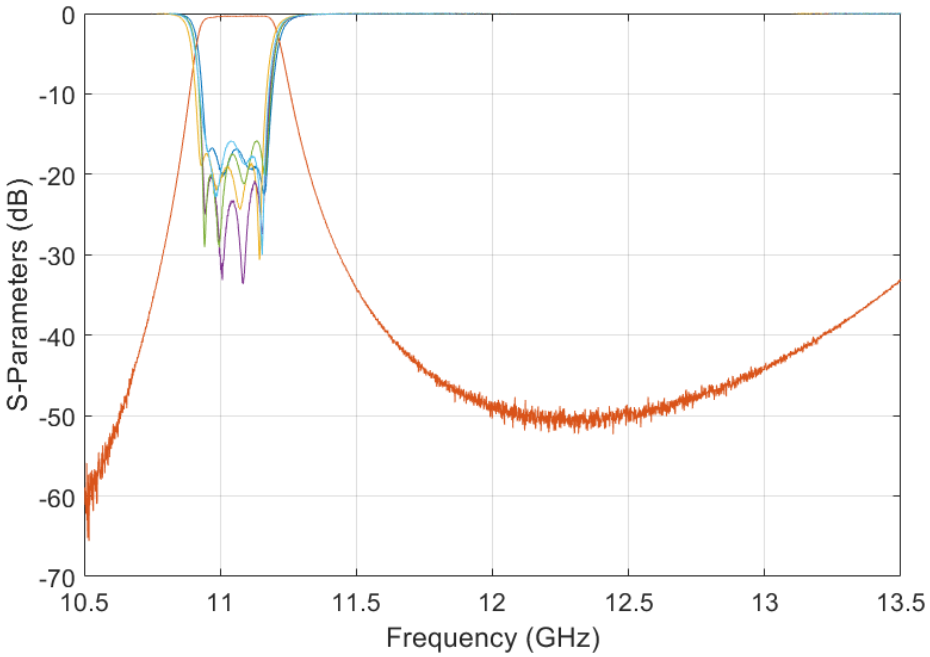

Figure 5.33: Measurements of the 11.057 GHz channel.

With this proof of concept, we verify that the use of Sapphire tuners and electric linear motors allow to reconfigure the filter automatically, using a previously calculated table for the positions of the tuners for each different channel. The different measurements show repeatability of the system for every channel in the design bandwidth, being the lower frequencies more critical since the actuators are further outside of the body of the motor.

5.7 Conclusions

In this section we have investigated the use of dielectric tuning elements in rectangular waveguide inductive microwave filters. In particular, we have explored experimentally the use of Teflon and Sapphire rods of 2, 3 and 4 mm diameter. The results obtained show that, although the tuning range achieved (with Teflon) is smaller than the one achieved with metallic tuning elements, the tuning range can be also significant. On the other hand, using Sapphire rods, we can easily achieve the same tuning range as with metallic screws. Furthermore, we have demonstrated that dielectric tuners are ideal candidates for the development of remotely tunable microwave filters. Finally, although we have demonstrated the use of dielectric tuning elements specifically for rectangular waveguide filters, we do believe that dielectric tuning elements can indeed be used in basically *all* microwave filters that use standard metallic tuning screws.

In conclusion, in this chapter we have given a number of contributions to the state-of-the-art of tunable filters in rectangular waveguide, namely:

- We have shown that the use of threaded or smooth tuning element of the same diameter does not introduce the same phase shift for the same penetration depth. This has been shown for both dielectric and metallic tuning elements.
- We have shown that dielectric tuning elements do not introduce significant passive intermodulation (PIM) products. A series of dedicated measurements has been carried out obtaining consistently the same results (PIM level below the PIM noise floor of the measurement setup).
- We have demonstrated experimentally that Sapphire tuning rods of 2 mm in diameter can achieve essentially the same tuning range performance achievable with metallic tuning elements. The main difference is that dielectric tuning elements can penetrate far more inside the filter than metallic ones. As a result, the use of dielectrics can introduce a very substantial reduction in the positional accuracy of the (dielectric) tuning element itself. This feature is indeed of very practical interest for the potential employment in remotely tunable applications, and has been demonstrated by a series of measurements using simple linear actuators.

Finally, it is important to note that, although the results presented have been obtained using an inductive filter in rectangular waveguide, they are applicable also to any other microwave filter (or device) that uses metallic tuning elements.

Chapter 6

Automatic tuning with a robotic arm (robotuner)

The procedures to design waveguide filters and the related manufacturing techniques have recently experienced very rapid developments. The aims of these developments have been mainly the cost reduction and the increase of manufacturing accuracy. In fact, the more accurate the manufacturing is, the closer the measured response of the filter will be to the theoretical response. There is, however, a limit to the accuracy of all current manufacturing processes (from classical milling technique to electron-erosion and additive manufacturing). As a mater of fact, the cost of manufacturing a filter can be significantly higher if extreme accuracy is required. For this reason, providing the filter with some adjustments capability is mandatory to ensure the correct behavior of the hardware. This becomes even more critical at higher frequencies (Ku, K an Ka bands) because of the reduced dimensions of the devices.

As we have shown in the previous chapters of this document, tuning elements can indeed be very effective in compensating manufacturing errors in microwave filters, as well as providing the filter with re-tuning capability (chapter 4).

However, the manual tuning of a microwave filter is a complex process that can take from a few minutes to several hours [119]. The task becomes specially complex when tuning higher-order filters. Generally speaking, we can therefore say that, the manual tuning of a microwave filter requires a high degree of knowledge of the behavior of the device. There are, indeed, some guidelines on how to adjust manually coupled cavity filters [120], but it is still very time consuming.

A possible improvement, that has been also discussed in the technical literature, is the use of computer-aided procedures. For instance, the machine learning approach was studied in [121] and [122], and fuzzy logic tuning strategies have also been used [123], just to cite a few.

The objective of this chapter is to demonstrate the feasibility of the automation of the post-manufacturing tuning process of microwave filters. The demonstration is based on the development of a robotic arm (robotuner in the remaining of the document) that will change the penetration of the different tuning screws present in the filter structure under the control of a computer. Two different simple algorithms will also be developed to guide the complete system. To demonstrate the use of robotuner, we will also show how to take advantage of the results obtained using ASM in chapter 3, and we will tune an inductive 6-pole filter in rectangular waveguide.

6.1 Mechanical implementation of the robotuner

In order to implement a mechanical automatic tuning machine for waveguide filters, we need four basic capabilities, namely:

- A computer controlled precision mechanism that provides precise mechanical movements and stability through the complete tuning process, including going back accurately to the same position.
- A computer controlled precision actuator that can rotate the tuning element to the desired angular position with the best possible accuracy. The actuator must also be able to return several times to the exact same angular position.
- A computer algorithm (or more than one) that can read measured filter performance from a network analyzer, compare the response with the desired filter response, and produce information we need to change the positions of the tuning elements.
- Finally, we need a tuning element that can change its penetration in the filter with a rotation movement. Additionally, and most importantly, the tuning element must be able to provide excellent electric contact with the body of the filter without using a locking nut.

In the previous chapter, we showed how to implement a remotely tunable waveguide filter using linear motors and Sapphire tuners. As discussed before, we did obtain good results because using dielectric materials we obtain a wider tuning movement of the rods inside the filter. This allows to reduce the accuracy requirements. The precision in the movement obtained, using the same linear motors, will be not enough to provide the repeatability level and precision required when using metallic tuners in standard waveguide filters.

This is why it is necessary to create a robotuner that can position tuning elements with a higher precision. Another important consideration is the cost. There are many possible solutions to implement the mechanism we are discussing. We have chosen, to demonstrate the feasibility of this concept, a solution with the lowest possible cost.

Fig. 6.1 shows the robotuner arm and the workbench that we have developed. Fig. 6.2 displays the required engine control units.

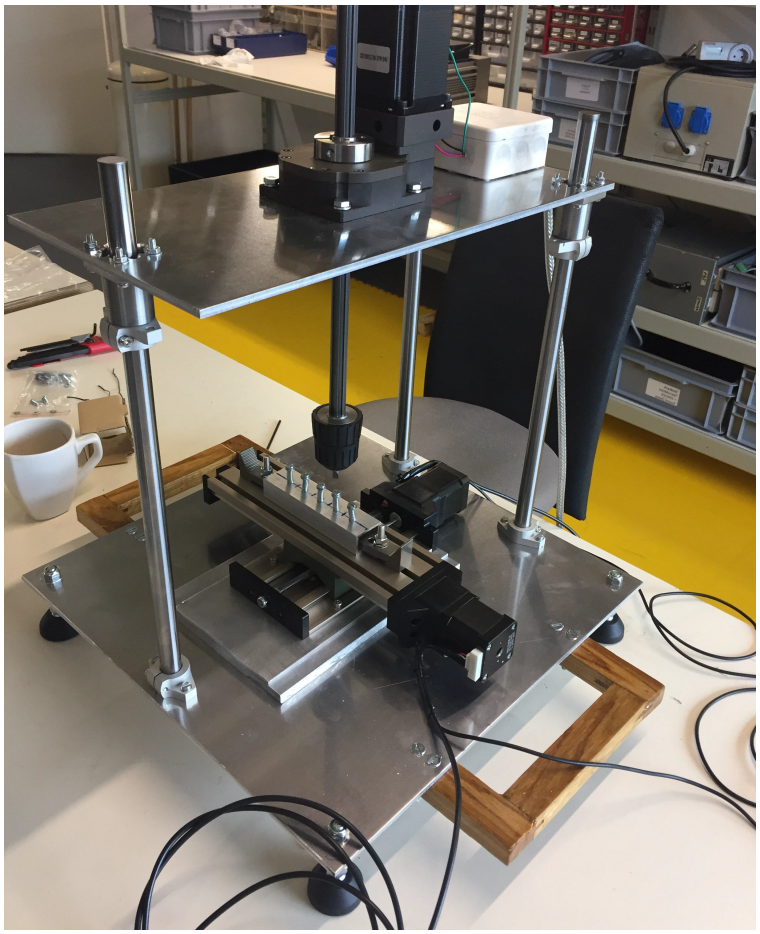

Figure 6.1: Robotuner arm and workbench.

The robotuner is composed of an X-Y table and an arm with an actuator head that controls the rotation of the screws (namely the rotation axis, C). A precision stepped motor is connected to this arm, including gears, to implement a 1:300 reduction. This means that, for a standard tuning screws of M4 dimension, for instance, the robotuner can provide a precision of around 10 microns in screw penetration. This accuracy is enough for our proof of concept if we compare it with the usual mechanical fabrication tolerances (from ± 10 to ± 100 microns).

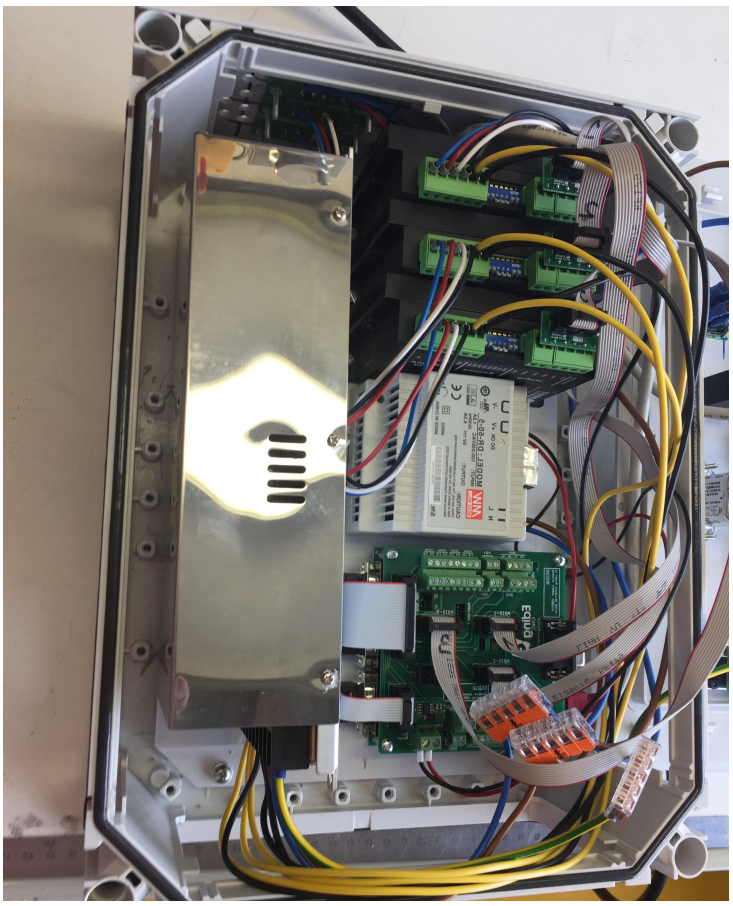

Figure 6.2: Robotuner control units.

It is important to note that, the current robotuner prototype does not provide Z-axis movement. In order to perform the measurements, we will need to manually engage the screwdriver head with each tuning element of the filter. In any case, the robotuner is a modular tool and the Z-axis movement can be added easily in the future.

Moreover, the robotuner includes a control software that allows the visualization and control of all the parameters of the motors and rotation of the actuator. Fig. 6.3 shows the main interface of the robotuner control program. It is important to note that the program allows us to control remotely all the functions of the robotuner.

Additionally, we have developed a number of computer programs that allow us to read the filter measurements from a network analyzer, and to compute the rotations needed to tune a filter. These programs are attached in Appendix A of this document. With this whole set-up, we can now tune efficiently any specific waveguide filter.

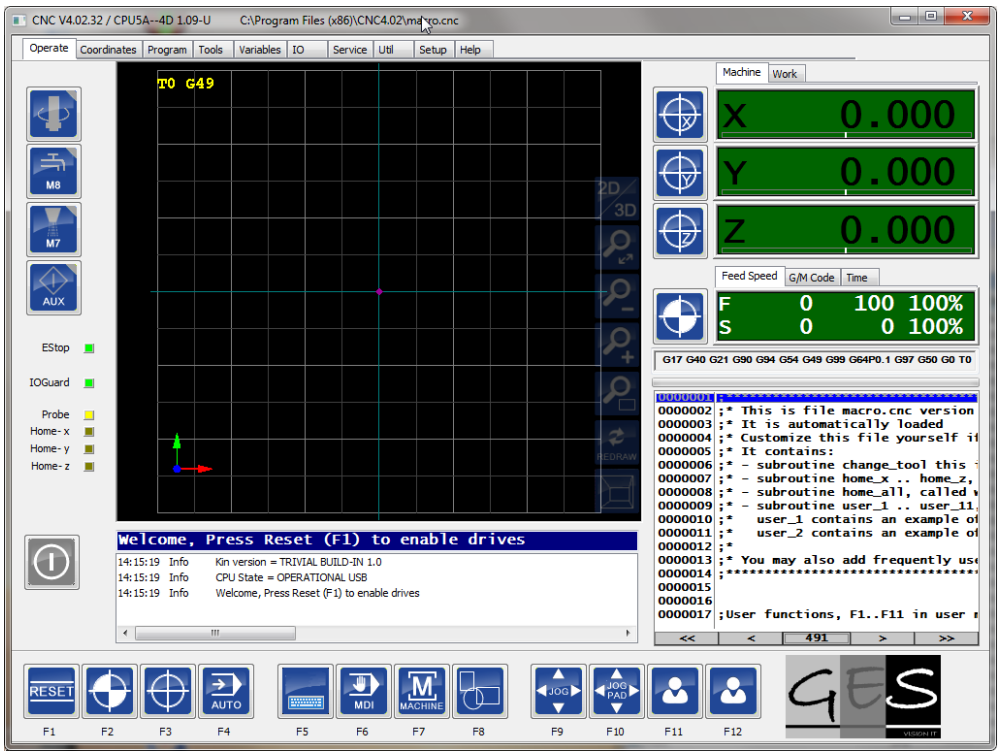

Figure 6.3: Main control interface of the robotuner.

6.2 Tuning algorithm of the robotuner

In this section we describe the algorithm to perform the automatic tuning of a filter using the robotuner, together with a vector network analyzer (VNA). The computer algorithm that we have developed in this context, is based on the search for the minimum error to reduce the difference in performance (the cost function) between the ideal filter and the measured responses. Next, we detail the algorithm and the logic structure of the program, along with the parameters needed for its correct use. This algorithm has been programmed using Matlab-code language and drivers from National Instruments, and it also makes use of the robotuner control program mentioned before. More specific details about the practical implementation of the algorithm can be found in Appendix A.

The objective of this algorithm is to try to minimize the difference between the ideal and the measured responses of the filter, after comparing the different results obtained each time that a tuner of the filter is modified.

Note that, for this purpose, it is mandatory to provide the algorithm with the S-parameters data of the ideal filter (objective response) or a mask. By a mask we mean a defined set of frequency points and values that we want to achieve with the filter response. Fig. 6.4, shows the ideal response for a particular filter and a potential mask.

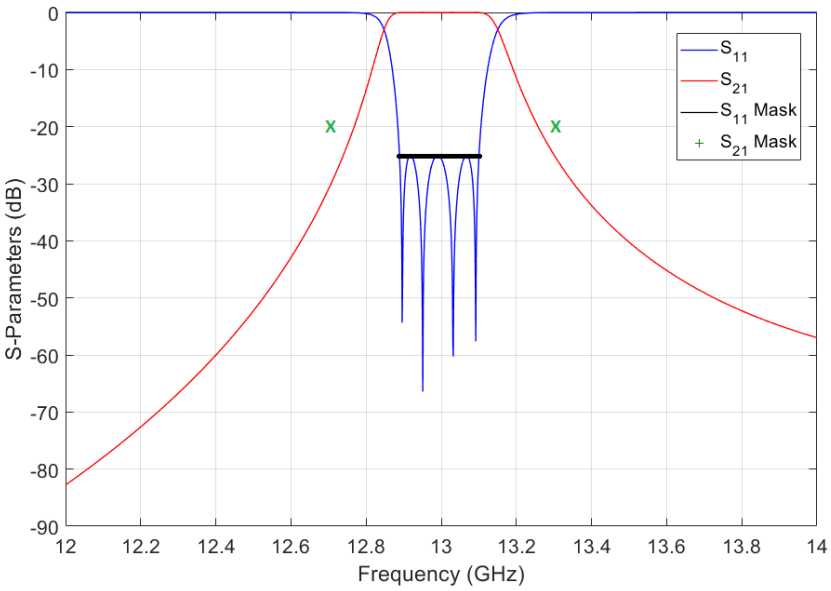

Figure 6.4: Ideal response of a 4-pole filter centered at 12 GHz with 200 MHz of channel bandwidth, and its possible objective mask points.

Basically, with this data, we can easily compute the difference (namely the error in the remaining of the chapter) between the ideal and the measured filter, each time we perform a modification in the screws penetrations.

In order to obtain a representative error value, we compute it as follows:

- For all the points defined inside the in-band frequency of the S_{11} parameter that are above the filter specification (usually -20 or -25 dB) we directly subtract the value (in dB) to the ideal specification. For the points that satisfy this specification, we assign 0 as the error value. Finally, we add the error values obtained for all the points of the S_{11} parameter.
- For the S_{21} parameter, we perform a similar strategy. In this case, only two frequency points (and the corresponding upper limits for the S_{21} parameter, see the green crosses in Fig. 6.4) are specified.

Finally, the total error (E_t) is the summation of S_{11} and S_{21} errors ($E_{S_{11}}$ and $E_{S_{21}}$). If this number is higher than the error objective (E_o), we need to continue tuning the filter. The corresponding equation 6.1, where n represents the total number of frequency points defined in the in-band section of the ideal filter response, and r and q are weight parameters (set to 1 as default value), is included next:

$$E_t = r * \sum_{i=1}^{2} E_{S_{21}} + q * \sum_{i=1}^{n} E_{S_{11}} \tag{6.1}$$

This error value will be the key element to decide the next step of the filter tuning algorithm. Additionally, with this strategy, we can modify the weight (r and q) of each error contribution according to the aimed focus of the tuning process: either to accomplish the S_{21} specification (which helps to center the frequency response) or to accommodate the S_{11} (return loss) level.

The basic idea is to position the robotuner in each tuner, and automatically find the best penetration that minimizes the total error. This step is done by the following iterative process:

- Obtain the total error between the ideal and the measured filter responses prior to any tuner modification.
- Move the tuner to one of the two possible directions (up or down) to a specific value (usually defined in the program as turning degrees of the tuner).
- Compute again the total error with this new filter response.
- Move the tuner to the opposite direction, and compute once more the total error obtained compared to the ideal response.
- Choose the best direction, based on the minimum error obtained for the three possible different cases (moving up, moving down, initial position).

After finding the best direction, a loop is continuously executed until any of the following stop conditions is satisfied. We define three different stop conditions for every iteration of the algorithm:

- Minimum height movement. Once the algorithm has decided the best direction, all the movement is locked to that direction. If the error increases from one iteration compared to the previous one, the algorithm goes back to the previous position and tries to perform the movement with half of the previous movement value. This continues until the minimum height movement defined, or other stop condition, is reached.
- Minimum possible error value. The algorithm stops if none of the possible movements applied to the tuner is able to reduce the error value from the previous configuration.
- Total error value reached. The algorithm stops when the filter is successfully tuned and the total error obtained is smaller than the defined error objective ($E_t \leqslant E_o$).

Once the algorithm has finished for one tuner, we place the robotuner to another one, and proceed again until the *total error value reached* condition is accomplished.

For the practical application of the proposed algorithm, multiple different strategies can be followed, based on the requirements of the tuning process, characteristics of the filter and experience and expertise of the user technician.

For example, if a fully automatic tuning process is required, we can simply implement the algorithm from the first tuner to the last one repetitively, until the filter is completely tuned.

Another different strategy would be to start first with the cavity tuners, and then proceed with the aperture tuning screws. In addition, if multiple identical filters must to be tuned, a predefined initial positions of the tuners, as well as specific tuning directions and height movement values, can be implemented.

In the next section, we will present a practical application example of the automated tuning algorithm just described above. Then, in section 6.4, we will show how this algorithm can be combined with a powerful strategy (based on ASM) to reduce the number of required steps.

Finally, as indicated before, the Appendix A of this document includes a detailed flowchart of the proposed algorithm; as well as the Matlab codes for its practical implementation using robotuner, a VNA and a personal computer.

6.3 Tuning a six-pole inductive filter with metallic tuners

In order to test the robotuner and the tuning algorithm (program) that we have developed, several tuning exercises have been performed using a classic 6-pole inductive filter in rectangular waveguide. The filter specifications are as follows:

- Order = 6
- Return loss $\geqslant$ 20 dB
- Center frequency = 11 GHz
- Channel Bandwidth = 500 MHz

The filter is a classic rectangular waveguide filter made in aluminum. In addition, the filter has been designed with tuners on the top side of the filter in all the apertures and cavities. Fig. 6.5 and Fig. 6.6 show the ideal response, a structural view and the fabricated prototype of the considered filter.

The tuners of the filter are of M4 diameter dimension, and have been purchased from Tronser[1]. They are specifically designed to allow for repeated positioning without mechanical failure, and without loss of electrical contact with the filter body (see Fig. 6.7).

[1] Tronser GmbH, Quellenweg 14, 75331 Engelsbrand, Germany. Web-page: www.tronser.de

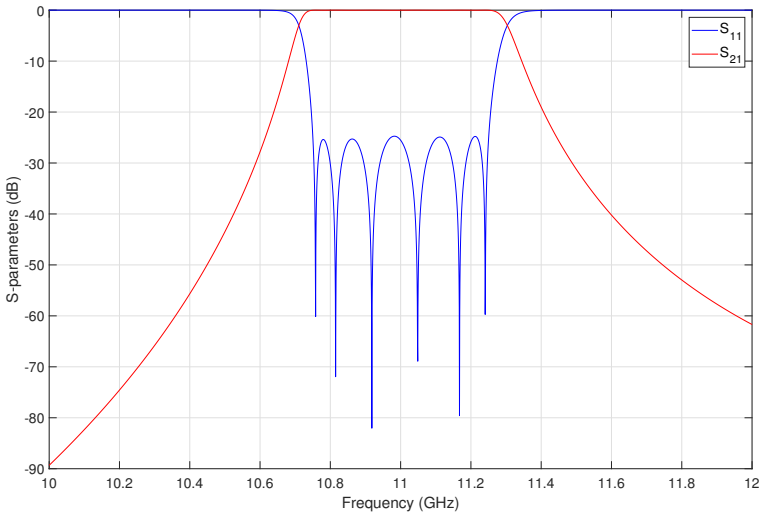

Figure 6.5: Ideal response of the 6-pole filter.

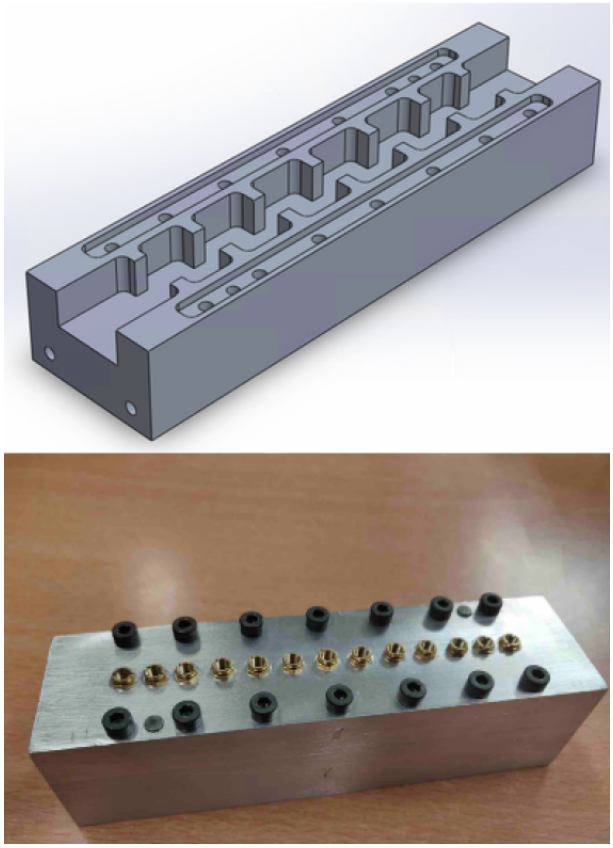

Figure 6.6: Structural view and fabricated prototype of the 6-pole filter.

As pointed out in the introduction of this chapter, the electrical contact between the tuner and the filter body is indeed an important issue, because the electromagnetic fields inside the filter will excite surface currents on the tuner. For the proper functioning of the filter, the currents must be able to reach the filter body with as small a resistance as possible. In addition, this point brings about another issue. In the normal industrial practice, we can see very frequently filters tuned with normal (silver-plated) screws. However, this solution requires the use of a locking nut to fasten the screw to the filter body.

The presence of this locking nut complicates enormously the structure of any robotic tuner. This is why we have chosen to use the tuners from Tronser, which avoid the need of using threaded locking nuts.

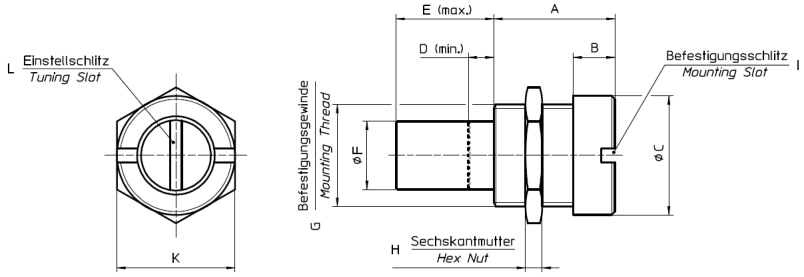

Teile - Nr. *Part - No.*	A [mm]	B [mm]	øC [mm]	D [mm]	E [mm]	øF [mm]	G Gewinde *Thread*	H [mm]	I B x T *W x DP* [mm]	K SW *Hex* [mm]	Befest.-Drehm. *Mounting Torque* max.[Ncm]	L B x T *W x DP [mm]*	Einstell-Drehm. *Tuning Torque* [Ncm]
205-1400-100	14	1,0	5,3	0,0	11,4	3,2	.190-64UNS	1,0	0,8 x 0,6	5,5	30	0,6 x 0,4	0,3 – 3,0

Figure 6.7: Specifications of M4 tuners from Tronser.

Initially, all the tuners are positioned to penetrate 2 mm in the filter. This is indeed the design configuration that we have used to obtain the ideal response centered at 11 GHz. According to the specifications of the tuners (0.397 mm per pitch), this means a total of 5 turns. Fig. 6.8 shows the initial response obtained as compared to the desired ideal performance.

We now run the program described in the previous section. First, we search for the minimum error tuning individually each tuner in the filter. The result of this step is shown in Fig. 6.9.

As we can see, we now have a much better response of the filter. However, we need to go further to obtain a correct response. At this point, there are different strategies that we can follow to finalize the tuning. One possibility is to tune first the tuners in the cavities (in order to center the response of the filter), and then tune the tuners in the windows of the filter (to obtain the correct coupling between cavities).

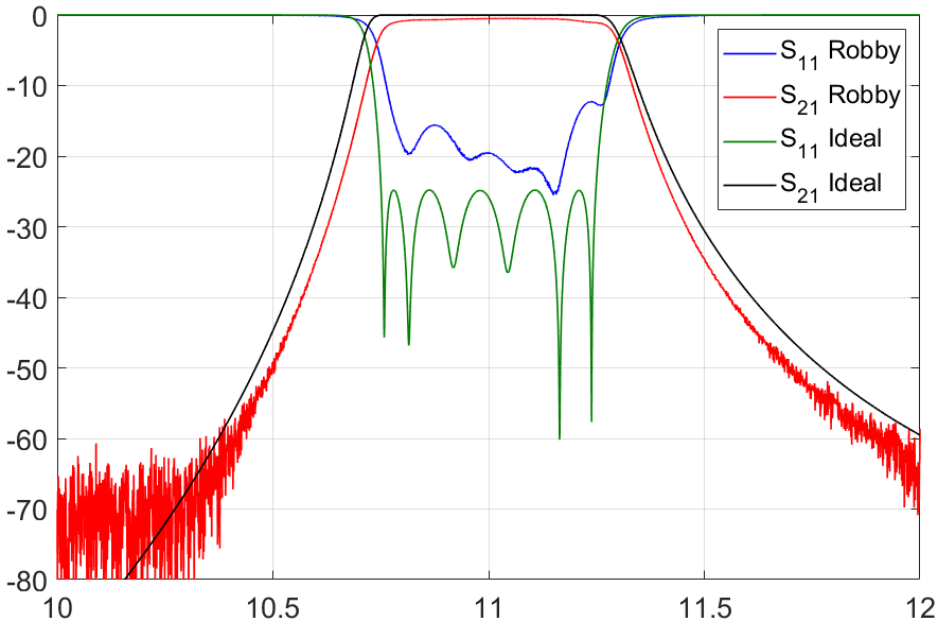

Figure 6.8: Initial response vs. ideal response.

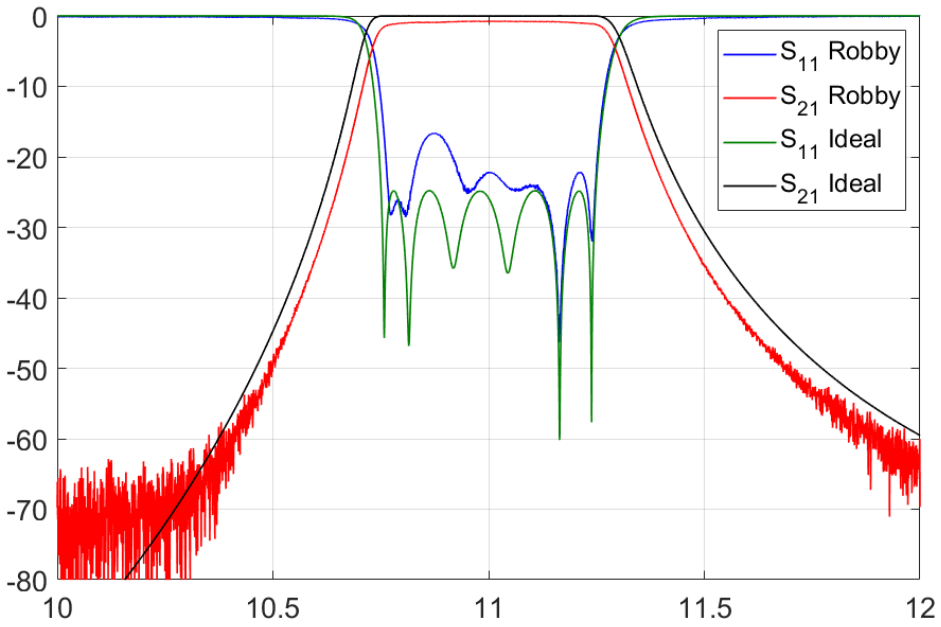

Figure 6.9: Response of the filter after the first step vs. ideal response.

Fig. 6.10 shows the final response that we have obtained with such strategy, and is compared to the ideal filter response.

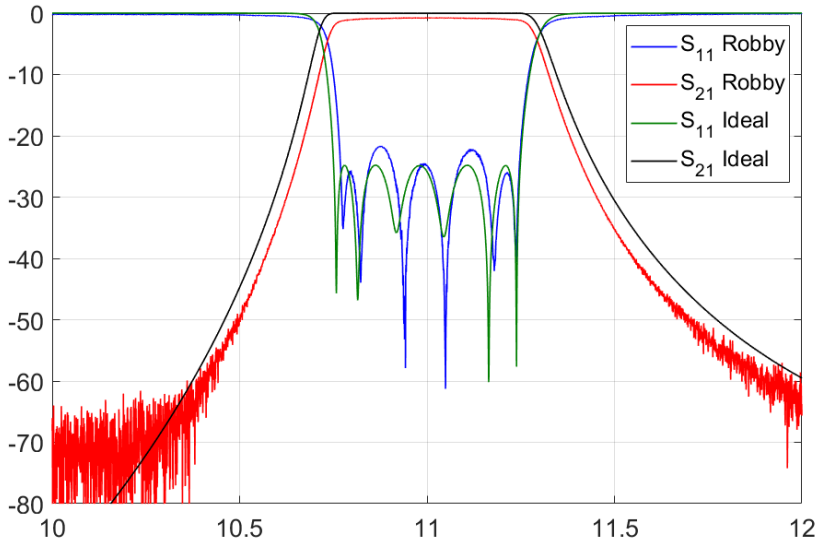

Figure 6.10: Final response of the filter vs. ideal response.

After finishing the automatic tuning process, we have practically recovered the ideal response with the real filter (except for the insertion loss value, which is related to the material of the filter and tuners).

6.4 ASM-based technique using robotuner

In the previous sections, we have validated the viability of using a robotuner for the automatic tuning of waveguide filters using the minimum error method. This approach is indeed a very simple tuning procedure, but requires a large number of measurements.

As we demonstrated in chapter 3, the ASM technique can be a powerful tool for the optimization of waveguide filters. Furthermore, a recent study, based on the use of the aggressive space mapping in combination with the robotuner, has demonstrated that the tuning process can be performed much faster, and can also use a much smaller number of measurements [124].

The key step in the use of the ASM technique to tune a filter is to compute the mapping matrix linking the behavior of the real filter with the behavior of a simpler filter model. For such purpose (computation of the mapping matrix), as indicated in [124], it is necessary to evaluate the responses of the real filter when the penetration of each tuning element is modified, one at the time.

In Fig. 6.11 and Fig. 6.12 we can see the result of modifying each tuner, and how the response changes close to the ideal response. These results will be used for computing the cited mapping matrix (see details in [124]).

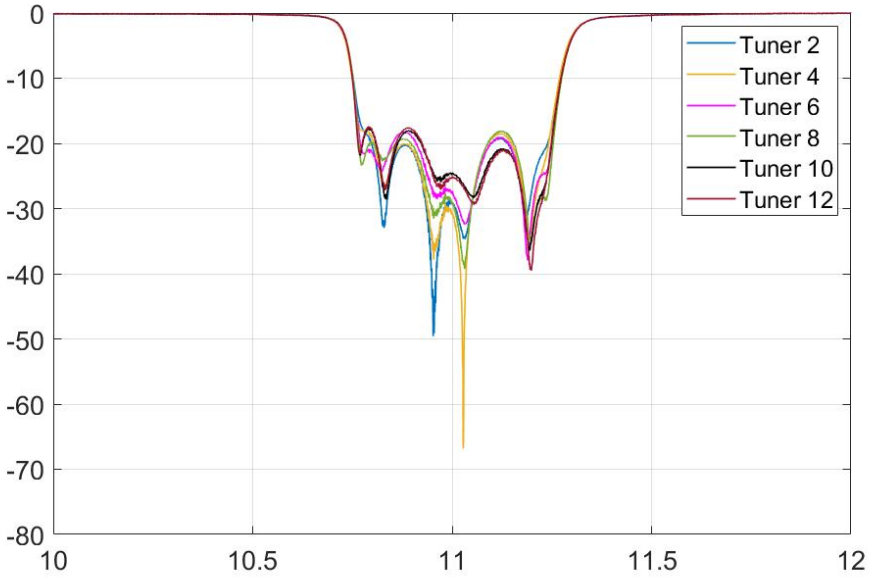

Figure 6.11: Response obtained for each tuner modified in the cavities of the filter.

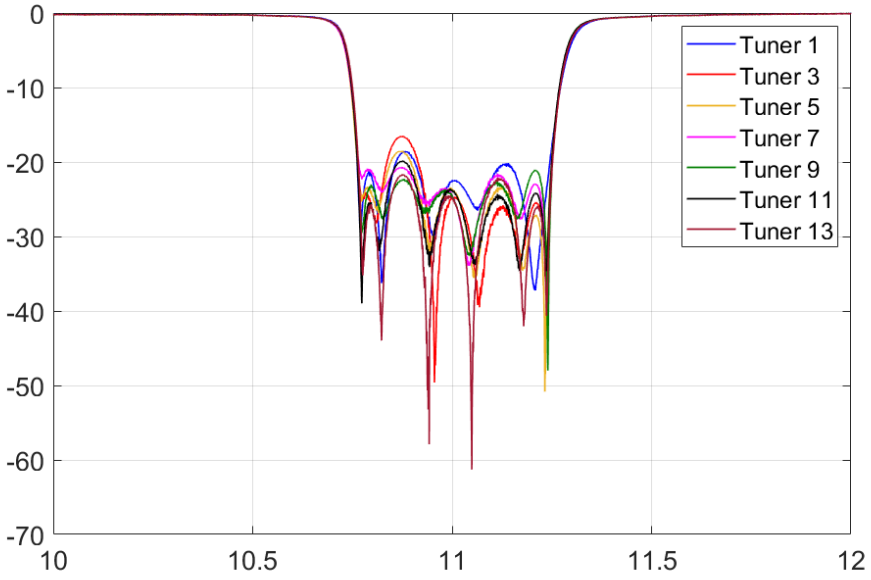

Figure 6.12: Response obtained for each tuner modified in the windows of the filter.

Once the mapping matrix has been computed, one can obtain, in a single computation, the changes required for *all* tuning screws to get the desired filter response (as it is detailed in [124]). In Fig. 6.13 we show the results of the use of this technique in combination with the robotuner. Following this procedure, the steps necessary to correctly tune the considered filter, using only a very low-accuracy model and real measurements of the filter, have been reduced to just 3 ASM iterations.

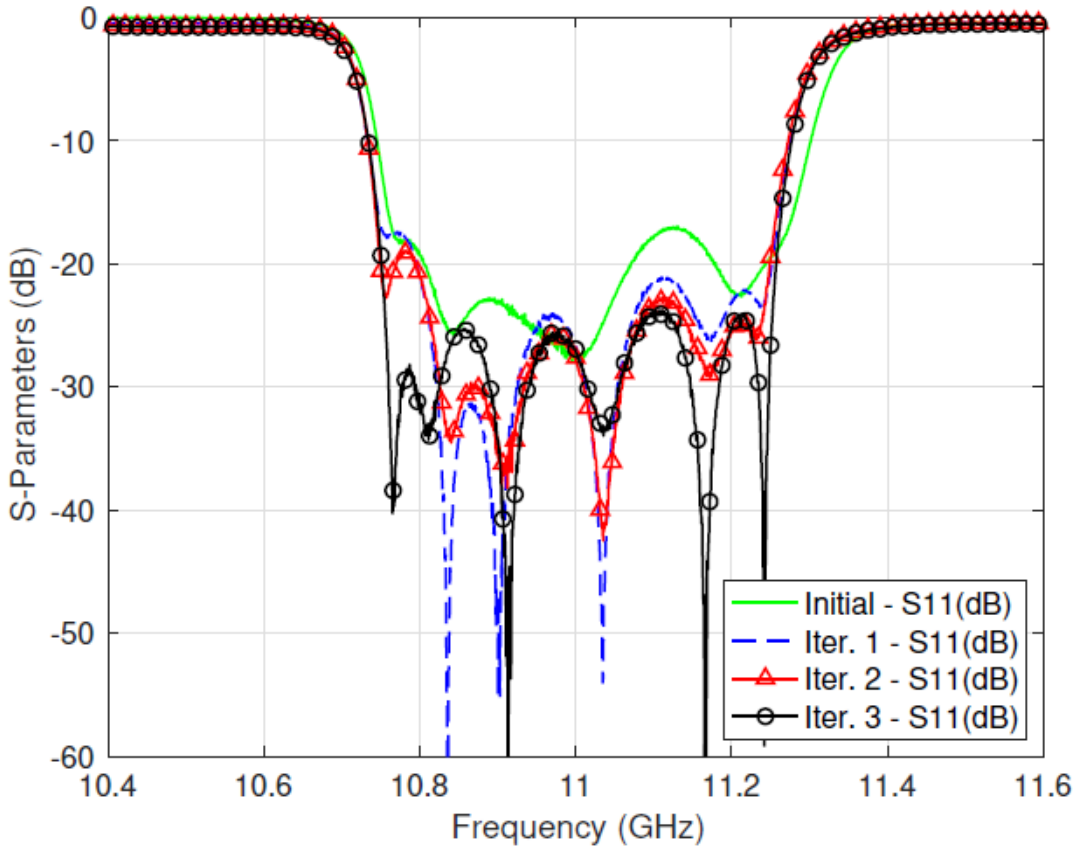

Figure 6.13: ASM-based tuning procedure result using robotuner.

6.5 Conclusions

The results discussed in this chapter, clearly show the feasibility of building a robotuner that can effectively tune a microwave filter automatically. Furthermore, the robotuner allows to develop and implement different tuning methods which are more suitable to the behavior of each particular filter. This is especially useful if we want to automate the tuning of a large number of filters units with the same response.

It is important to note, however, that the robotuner also presents some limitations. The first one is related to the relative positions of the filter and the actuator of the robotuner. If we want to fasten the filter in the robotuner only once, all the tuners must be in the plane that is accessible to the actuator (X-Y plane). Second, the tuners must be able to withstand a number of different movements without loss of good electrical performance. For example, using the algorithm developed for the automated tuning method, the robotuner has to find the correct direction to minimize the error, that means at least to perform three different movements of the tuner for each tuning element.

In any case, the objective of this chapter was to provide a proof of concept for the automatic tuning of waveguide filters, and this objective has been fully achieved. It is important to note that the technique we have demonstrated is particularly useful when a very large number of identical filter must be tuned to the same response, as it is commonly the case for cellular base stations.

Chapter 7

Further advances: Quadruplet diplexer and integrated filter switch

This chapter describes and extends the results obtained during the research work related to this thesis concerning further advances in rectangular waveguide filters. It is important to note that the results described in this chapter have resulted into the following three scientific publications:

- J. Ossorio, S. Cogollos, V. Boria, and M. Guglielmi, "Rectangular waveguide quadruplet filter for satellite applications," *in IEEE MTT-S International Microwave Symposium,* pp. 1359-1362, June 2019.
- J. Ossorio, J. C. Melgarejo, S. Cogollos, V. E. Boria and M. Guglielmi, "Waveguide Quadruplet Diplexer for Multi-Beam Satellite Applications," *in IEEE Access,* vol. 8, pp. 110116-110128, June 2020.
- J. Ossorio, J. C. Melgarejo, V. E. Boria and M. Guglielmi, "On the Integration of Microwave Filters and Waveguide Switches," *in IEEE Microwave and Wireless Components Letters,* Dec. 2020.

As mentioned in section 2.1, modern satellite communication systems are currently evolving from the standard bent-pipe configuration to new multi-beam regenerative payloads [6] and [125]. As a consequence, very selective and compact filter structures are currently being required to fit the new stringent specifications [126].

In this context, therefore, we discuss in this chapter two new devices to be used in multi-beam satellite payloads. The first is a very compact and selective diplexer, based on a novel folded topology for quadruplet filters. The second is a novel device that integrates in one single component the functions of microwave filter and waveguide switch.

7.1 Quadruplet filter

Since their introduction in 1970's, [25] and [26], dual-mode filters in circular waveguide have been the standard solution for multichannel manifold multiplexers for satellite communications [127]. This is because of the clear advantages offered by dual-mode filters in terms of performance and compactness with respect to other topologies (see chapter 4). However, dual-mode filters in circular waveguide usually require the use of tuning screws in order to adjust the performance of the filter. This is not a problem for the implementation of a manifold multiplexer, but it becomes a problem when the filtering structures must be integrated in the front end of the payload, due to the reduced space available. For this reason, more compact topologies without tuning screws need to be developed.

Furthermore, alternative dual-mode filter structures without the use of tuning screws have also been presented in the technical literature, [128], [129]. In addition, new compact configurations, based on single-mode rectangular waveguide, that implement transmissions zeros using cross-coupled sections, have also been presented in [126] and [130].

In this context, therefore, we present in this section a new single-mode rectangular waveguide structure without tuning elements, that can generate two symmetric transmission zeros using the cross-coupling concept.

In the proposed filter structure, the cavities are suitably arranged in order to reduce the footprint of the device, and to achieve, at the same time, a high-selectivity response.

7.1.1 Filter specifications

We are going to design the filter using WR-42 rectangular waveguide input and output connections. The filter specifications are inspired by the requirements for a satellite diplexer, as discussed in [131]. The filter specifications are as follows:

- N = 4
- Return loss $\geq$ 20 dB
- Useful bandwidth = 220 MHz
- Center frequency = 19.95 GHz
- Temperature excursion = -50°C to +100°C
- Attenuation out-band = 30 dB @ CF $\pm$ 500 MHz

It is important to note at this point that, in order to obtain a compliant filter design, the expected temperature variations must be taken into account from the very beginning. The main effect of temperature variation is to modify the filter center frequency. This frequency variation can be estimated as follows:

$$\Delta f = \alpha(20 - T) f_0 \tag{7.1}$$

where Δf is the frequency excursion of the filter, α is the temperature expansion coefficient of the material used, and T the expected maximum and minimum temperature of the device in degrees Celsius (°C). We use eq. (7.1) for both the lower and the higher temperature in order to calculate the maximum center frequency variation of the filter.

For aluminum, using $\alpha = 23.1^{-6}K^{-1}$ in eq. (7.1), and a filter bandwidth of 300 MHz, we obtain a compliant response with respect to the temperature variations, as we can clearly see in Fig. 7.1.

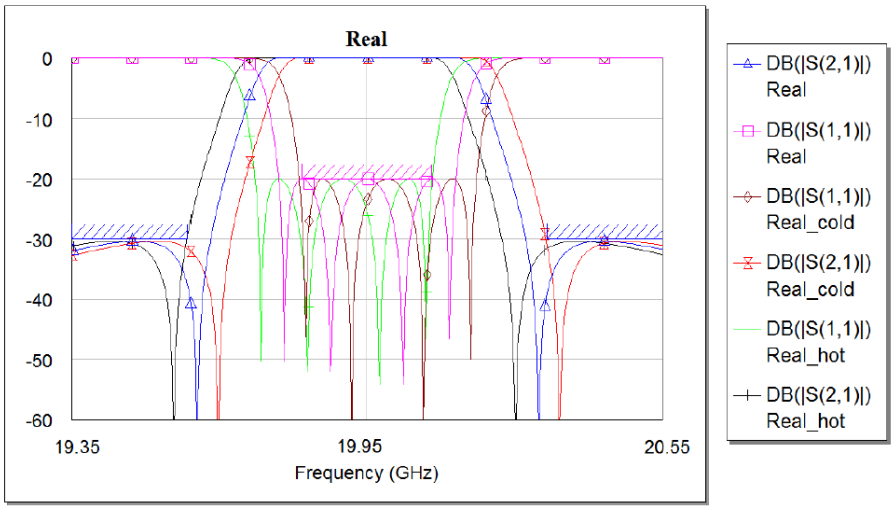

Figure 7.1: Response of the filter for the maximum and minimum temperature.

Furthermore, it is now important to recall that the guided half-wavelength at 19.95 GHz is approximately 15 mm. As a consequence, using standard half-wavelength rectangular waveguide resonators, namely, the TE_{101} resonance, will result in very stringent accuracy requirements in the fabrication process. In order to effectively address this issue, we will design the filter using the TE_{103} resonant mode. This choice has two favorable effects. The first is that it will allow us to avoid using tuning screws in the final structure (we will justify this design decision through a Monte-Carlo statistical analysis and EM simulations of the final design structure in section 7.1.2).

The second positive effect of using the TE_{103} resonant mode is to increase the quality factor of the resonators, thereby reducing the insertion losses. This choice, on the other hand, will produce a larger filter. The final filter structure, however, will be made more compact using an optimized filter topology, as we will show in the next section.

An additional detail is that we will increase the return loss specification to 25 dB in the design process of the filter. We do this in order to introduce a margin to take into account the deviations due to the fabrication tolerances. Fig. 7.2 shows the final ideal response of the 300 MHz band-pass filter to be designed.

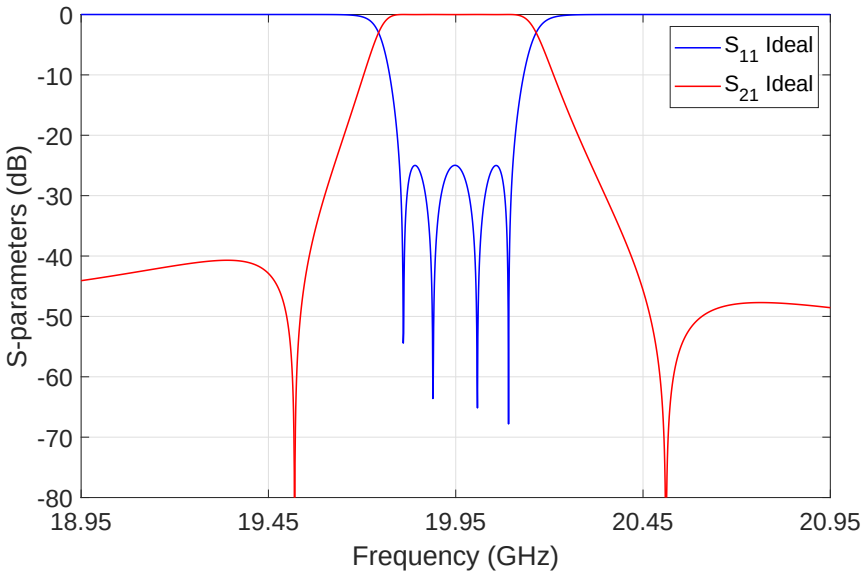

Figure 7.2: Final ideal performance of the filter.

7.1.2 Filter design

The filter design procedure that we have used is based on the results discussed in [60]. To start, we design first a filter with the right in-band response. To this end, we can use a classic inductive 4-pole filter with no transmission zeros that can be designed automatically using FEST3D. Once the basic in-line four-pole filter structure has been obtained, we can fold the filter in the middle and connect the cavities 2 and 3 through an inductive aperture as shown in Fig. 7.3. As we can see, in Fig. 7.4, this modification does not generate undesired effects in the final performance of the filter.

The next step in the design process of the filter is to add the transmission zeros to the response. This can be achieved by adding a small capacitive window between cavities 1 and 4. The filter performance is then re-optimized using as reference the ideal response shown in Fig. 7.2. The final filter structure obtained is shown in Fig. 7.5.

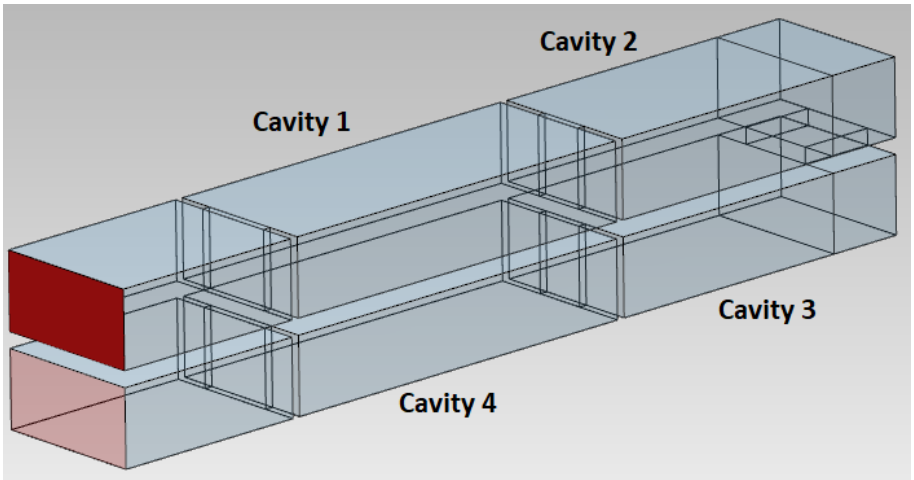

Figure 7.3: Vertical connection of the inductive 4-pole filter with TE_{103}.

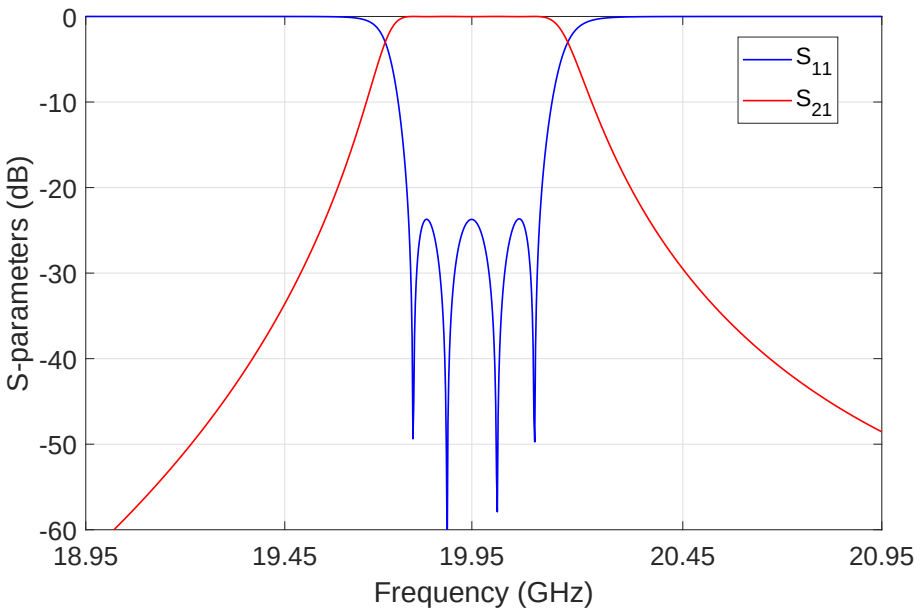

Figure 7.4: Response of the inductive 4-pole filter connected in vertical direction by the 2nd and 3rd cavities.

As we can see, the structure contains a capacitive 1-4 coupling. In addition, we have also added to the basic filter structure two corners in the 1st and 4th cavities in order to reduce the total length of the filter. Furthermore, the 2nd and 3rd cavities have been folded in a 'C' shape, in order to reduce also the total height of the structure.

These modifications do not affect the performance of the filter, as shown in Fig. 7.6, where the performance of the quadruplet filter is compared with the ideal response.

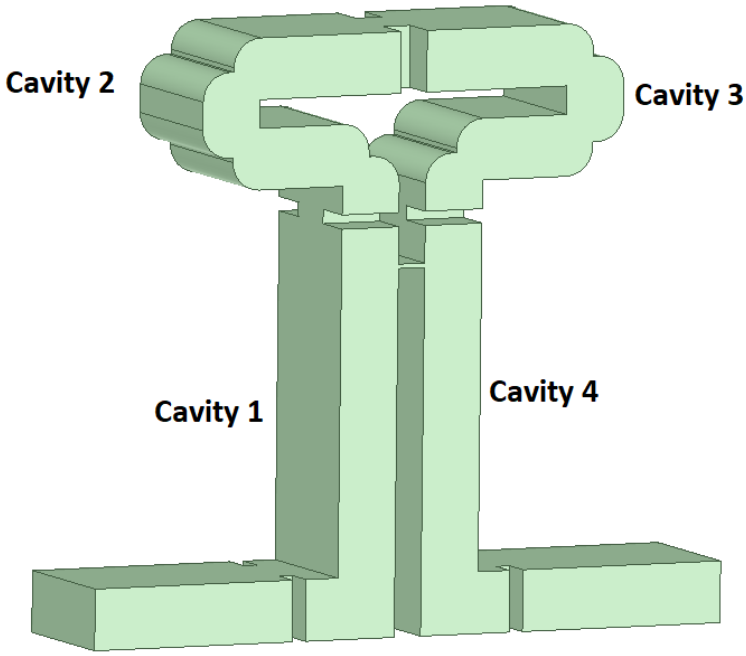

Figure 7.5: Ideal structure of the quadruplet filter simulated in FEST3D.

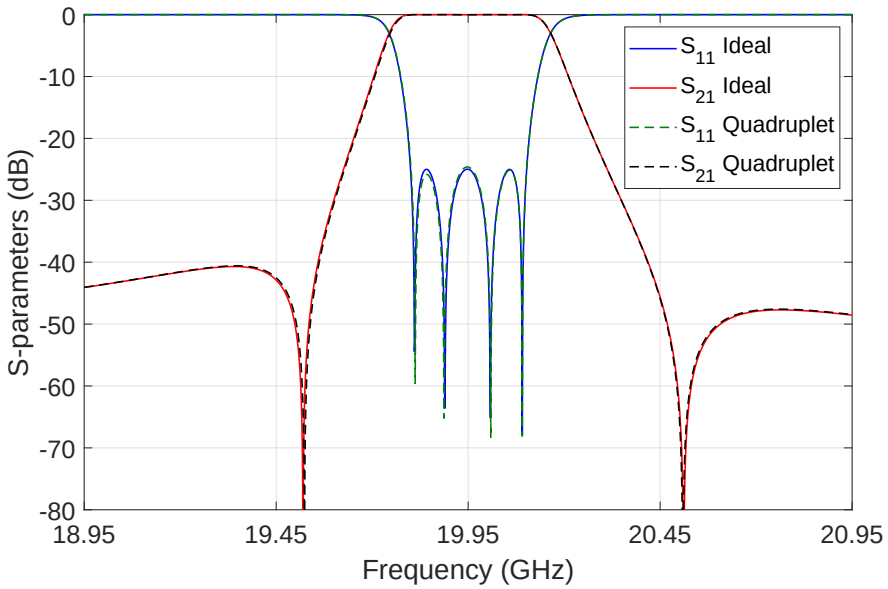

Figure 7.6: Performance of the quadruplet filter vs. ideal response.

Finally, as we discussed in the previous section, we have performed a Monte-Carlo yield analysis for the final structure, using both TE_{101} and TE_{103} resonant modes, in order to verify the advantages of using the TE_{103} mode over the TE_{101} mode.

Table 7.1 shows the results obtained, for each resonant mode, with a standard deviation (STDDev) of 5 and 10 microns, respectively. The acceptance limit is -20 dB for the in-band S_{11} parameter of the filter (from original filter specifications). The material chosen for the EM simulations of the filters with losses is aluminum.

Table 7.1: Monte-Carlo and EM simulations results.

Simulation	TE_{101}	TE_{103}
Monte-Carlo (STDDev = 5 microns)[1]	43	82
Monte-Carlo (STDDev = 10 microns)[1]	20	53
EM S_{21} Losses (dB)	0.442	0.317

[1] The numbers indicates the percentage of positives cases over 1000 random simulations for each mode.

From the results shown in Table 7.1, we can see that with the TE_{103} resonance, and with an accuracy between 5 and 10 microns, we should be able to obtain an acceptable yield. This is indeed a challenging accuracy requirement, but it is feasible with current high precision manufacturing techniques.

7.1.3 High precision design using One-Step Aggressive Space Mapping (OS-ASM)

At this point, we have an ideal quadruplet structure that satisfies all the specifications. However, all simulations performed so far have been carried with FEST3D using a set of parameters that allows for fast computations, but with reduced accuracy. To manufacture the hardware, on the other hand, we need to obtain the same performance but using a more accurate electromagnetic (EM) simulator. Moreover, the ideal structure uses ideal 90° corners and no material losses. In order to simulate a realistic device, we need also to introduce rounded corners in the structure and include in the simulations the material (aluminum) losses.

Furthermore, in order to reduce the fabrication cost of the device, we can increase the height of the waveguides of the filter, to have more space for the movement of the cutting tools. An additional positive effect of this choice is that it further reduces the in-band insertion losses of the filter. The standard waveguide dimensions will then be recovered with tapered input and output waveguide sections.

With these modifications, the structure is now ready to be simulated using CST (now with Dassault Systèmes) Microwave Studio. Fig. 7.7 and Fig. 7.8 show the new structure of the filter with rounded corners and the result of the full-wave simulation with CST, respectively. As we expected, the filter response obtained using the new structure is significantly detuned. We now need to recover the ideal response of the filter.

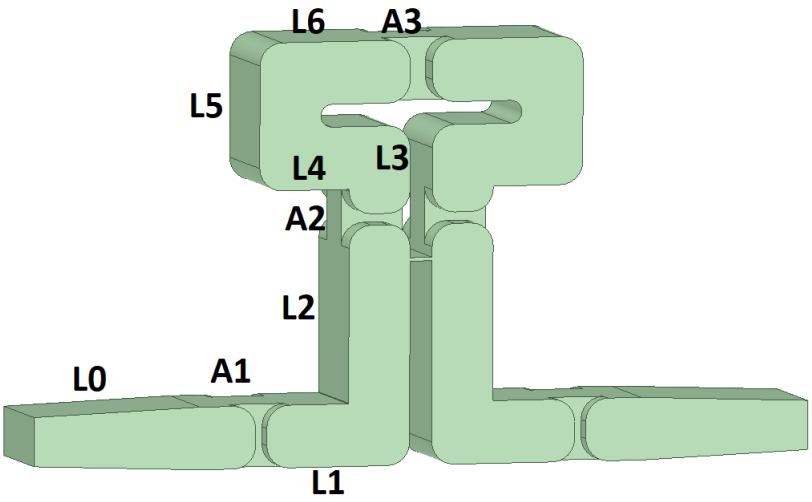

Figure 7.7: Structure of the quadruplet filter with rounded corners and I/O tappers.

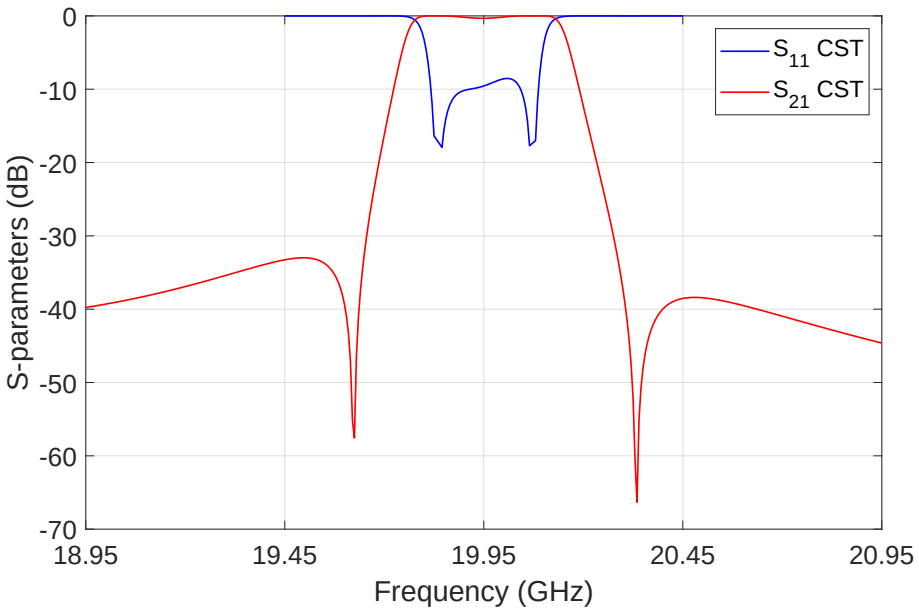

Figure 7.8: Initial performance of the quadruplet filter in CST.

In order to avoid costly optimizations in CST, we are going to use the well-known OS-ASM proposed in this thesis (see chapter 3). We will follow the procedure described in [59] using CST as high-accuracy space, and the Multimode Equivalent Network (MEN) of FEST3D, used in the previous section for the initial filter design, as low-accuracy space. After 6 iterations we obtain the performance shown in Fig. 7.9 where it is displayed together with the ideal response.

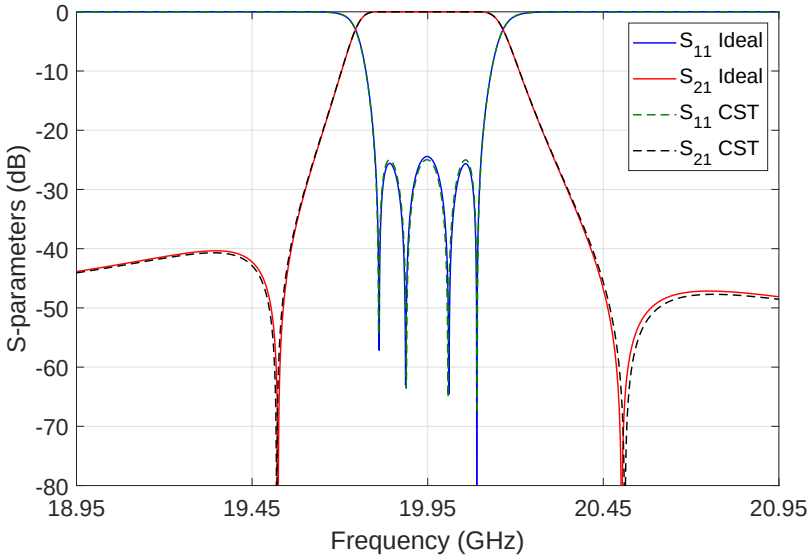

Figure 7.9: Final performance of the quadruplet filter in CST vs. ideal response.

We can finally conclude that we have indeed recovered the ideal performance of the filter with a structure that can now be manufactured. Table 7.2 shows the final dimensions of the filter.

Table 7.2: Dimensions of the quadruplet filter in millimeters.

Structure[1]	Height	Width	Length
I/O Tapper L0	4.318 to 5.5	10.668	20
Inductive aperture A1	5.5	7.278	1
Cavity 1 L1	5.5	10.668	12.891
Cavity 1 L2	15.643	10.668	5.5
Inductive Aperture A2	2	5.095	5.5
Cavity 2 L3	7.685	10.668	5.5
Cavity 2 L4	5.5	10.668	8.021
Cavity 2 L5	2	10.668	5.5
Cavity 2 L6	5.5	10.668	13.571
Inductive aperture A3	5.5	5.535	2
Capacity aperture[2]	0.3	5.5	2

[1] The filter is symmetric in the XY plane. All the corners are 2 mm rounded.
[2] The capacity aperture is placed in the filter at 17.91 mm from the bottom.

7.1.4 Measured results

We have manufactured the filter in order to verify the theory and the EM simulations. Fig. 7.10 shows the comparison of the measured versus the ideal response of the filter.

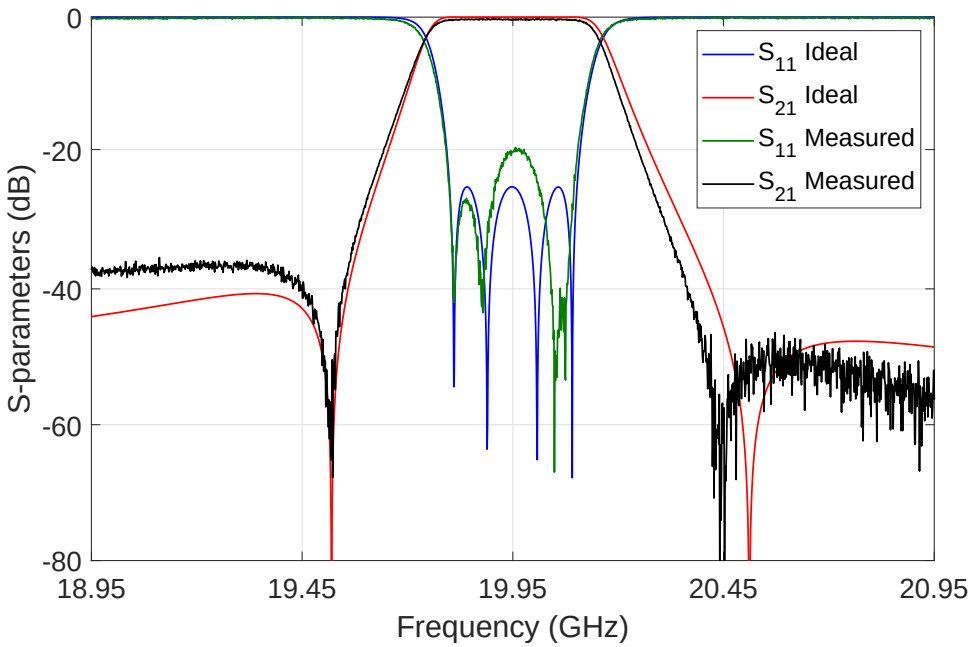

Figure 7.10: Measured result of the quadruplet filter vs. ideal response.

As we can see, although the S_{11} is slightly narrower in bandwidth (due to manufacturing tolerances), the performance achieved is below -20 dB for the S_{11} parameter and is practically coincident with the ideal response, thus validating the new filter structure.

7.1.5 Conclusions

In this section we have described the complete design process of a new quadruplet filter structure that is suitable for modern multi-beam space communication payloads. Real specifications for space applications have been used in the design process.

The filter has been first designed using fast MEN models. The design has then been finalized using accurate EM simulations (i.e. FEST3D and CST Microwave Studio, respectively), and an efficient OS-ASM procedure.

The results clearly indicate that the initial low-accuracy performance has been fully recovered by the highly accurate hardware. Finally, the measured prototype performance shows very good agreement with the simulations, thereby fully validating the novel filter structure and the employed design procedure.

7.2 Quadruplet diplexer

Now that we have fully demonstrated the design of a single filter, we can start the design of a diplexer.

The diplexer is one of the key elements of multi-beam satellite payloads. Diplexers are used to split or combine two different frequency channels that use the same antenna [67]. The need for high power handling and low losses makes the rectangular waveguide diplexer a very attractive solution for the considered space application.

In most cases, diplexer structures consist of a 3-port waveguide junction connecting two band-pass filters to a common port [132]. Many different solutions have been discussed in the technical literature [133]-[137]. Typically, each filter is connected to the common port with a length of waveguide that is adjusted to optimize the performance of the diplexer. Many different solutions have also been discussed with the objective of reducing the footprint of the diplexer (see for instance [138]-[140]).

More recently, alternative designs have also been presented, based on filters implementing TZs to increase the selectivity and reduce the diplexer footprint, as in [126] and [141].

In this context, therefore, the objective of this section is to significantly extend the results for quadruplet filters presented before, discussing the detailed design of a very compact, low-loss rectangular waveguide diplexer [142].

The material to be considered next is summarized as follows:

1. An in-depth investigation providing a physical justification, for the presence of additional TZs implemented with capacitive inter-resonator couplings in the quadruplets filters.
2. The complete design procedure of the proposed diplexer structure.
3. The theoretical verification of the full diplexer design through a comparison with commercial EM simulators.
4. The prediction of the high-power multipactor discharge behavior.
5. The validation of the new structure diplexer through a comparison with the measurement of a prototype fabricated using aluminum.

7.2.1 Diplexer specifications

The specifications that we have chosen as a target for our diplexer design are as follows:

- I/O interface: WR-42 (a=10.668 mm, b=4.318 mm)
- Center frequency 1 (CF_1): 19.820 GHz
- Center frequency 2 (CF_2): 20.082 GHz
- Useful channel bandwidth (BW): 245 MHz
- In-band return loss (RL): $\geq$ 20 dB
- Insertion loss at CF_x: $\leq$ 0.3 dB
- Narrow band isolation:
  - Contiguous edge:
    $\geq$ 20 dB @ $CF_x \pm$ 144 MHz
    $\geq$ 40 dB @ $CF_x \pm$ 381 MHz
  - Non-contiguous edge:
    $\geq$ 20 dB @ $CF_x \pm$ 192 MHz
- Maximum operating RF input power: $\leq$ 200 W
- Maximum dimensions: $\leq 130 \times 130$ mm
- Maximum mass: $\leq$ 500 g

These specifications are inspired by the requirements for multi-beam payloads of actual space applications [131]. It is important to note, however, that the specifications are not exactly identical to the ones indicated in [131]. After significant efforts we realized that it was not possible to satisfy all the original requirements at the same time with a reasonable diplexer structure.

Our effort, therefore, has been devoted to the development of a feasible structure that could give the best possible response while maintaining a small volume and a low cost fabrication. This situation is very common in the initial development activities for new payload configurations, where the main objective is to establish a proof of concept and not to deliver flight hardware.

Furthermore, following the same strategy as for the single quadruplet filter in previous section, we have increased the return loss to 25 dB in the design process of the diplexer, in order to have a margin to account for the possible deviations due to the fabrication process.

7.2.2 Out of band response

Before going any further with the description of the design procedure for the diplexer, it is now convenient to discuss the out-of-band behavior of the quadruplet filter shown in Fig. 7.11. In Fig. 7.12 we recall the in-band response of the filter from the previous section, and Fig. 7.13 shows the out-of-band response of the same filter.

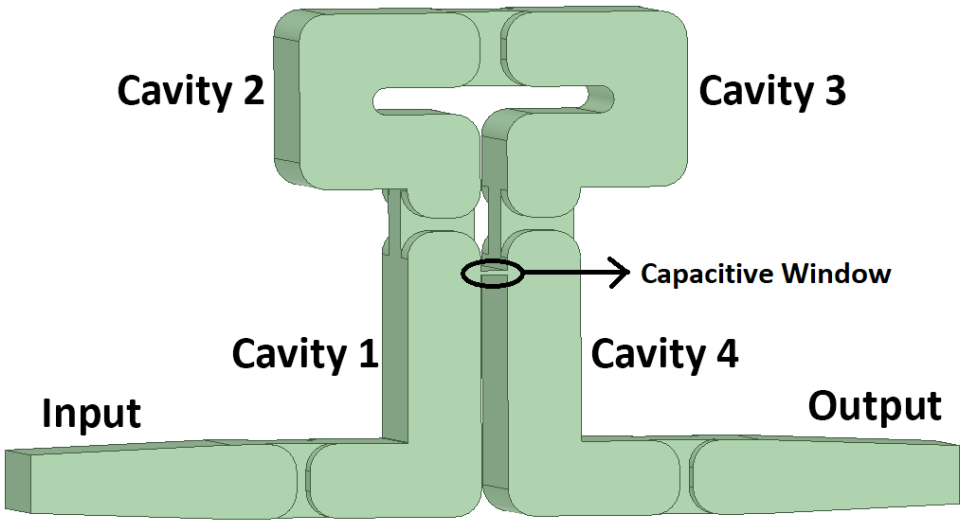

Figure 7.11: Quadruplet filter structure.

As we can see, in the frequency range that we have simulated, there are three replicas of the filter pass band. This is because the filter is designed to operate with the TE_{103} resonance. The response of interest is the one centered at 20 GHz. However, if we look carefully at the S_{21} curve in Fig. 7.13, we can see that, in addition to the transmission zeros (TZs) near the pass-band, there are also two additional TZs.

The first additional TZ is located at about 17 GHz, that is inside the second pass band, while the second one is located at approximately 22.2 GHz.

In order to better understand the origin of the two additional TZs, we now focus our attention on the E-plane T-junction shown in Fig. 7.14 (where the output port, parallel to 1, is short-circuit).

The performance of the T-junction computed with CST Microwave Studio from CST (Computer Simulation Technology, now with Dassault Systèmes) is shown in Fig. 7.15.

As we can see, this structure produces an alternating sequence of TZs and points of adaptation. Figs. 7.16, 7.17, and 7.18 show the electric field inside the T-junction at the frequencies of the first TZ, at the frequency of adaptation (S_{11} less than -20 dB), and at the frequency of the second TZ, respectively.

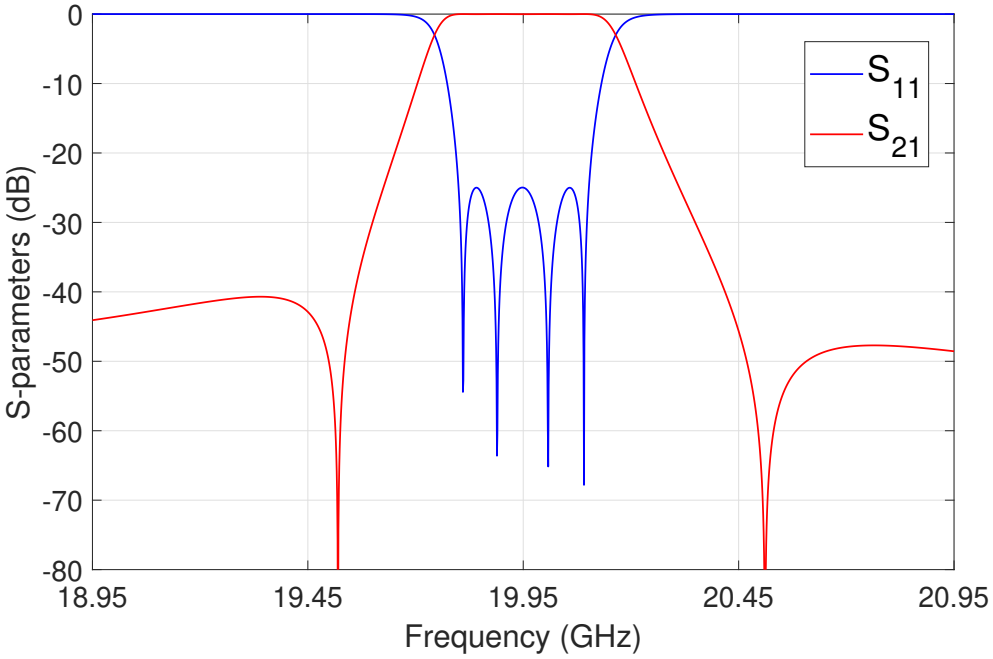

Figure 7.12: Final in-band response of the quadruplet filter designed in [131].

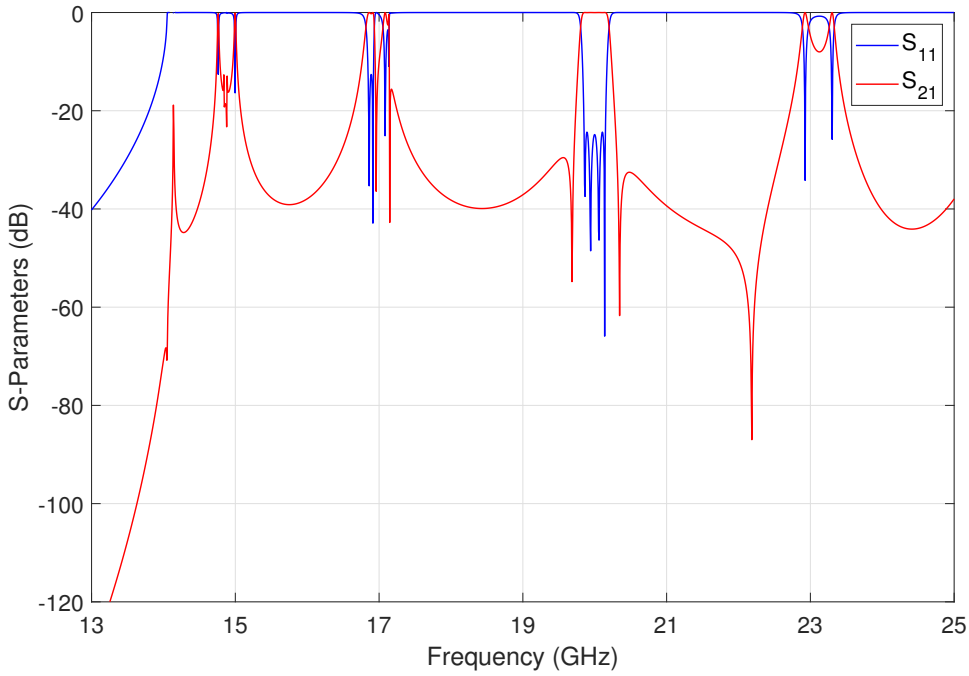

Figure 7.13: Out-of-band response of the quadruplet filter.

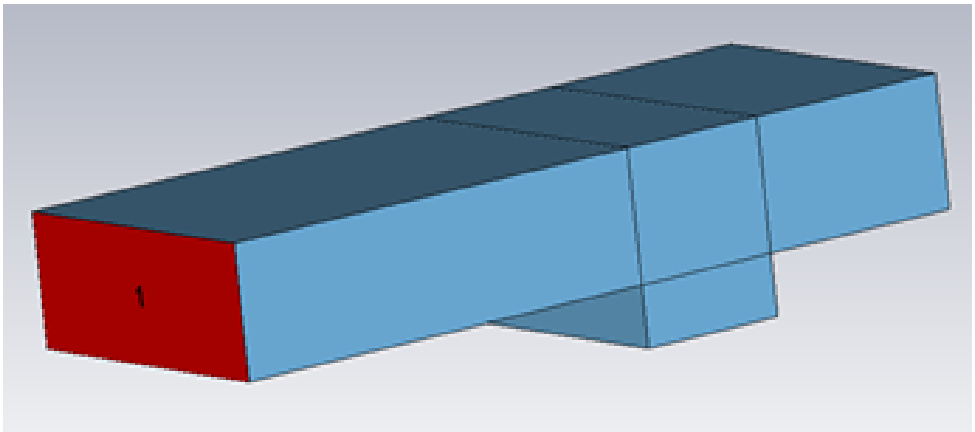

Figure 7.14: E-plane T-junction.

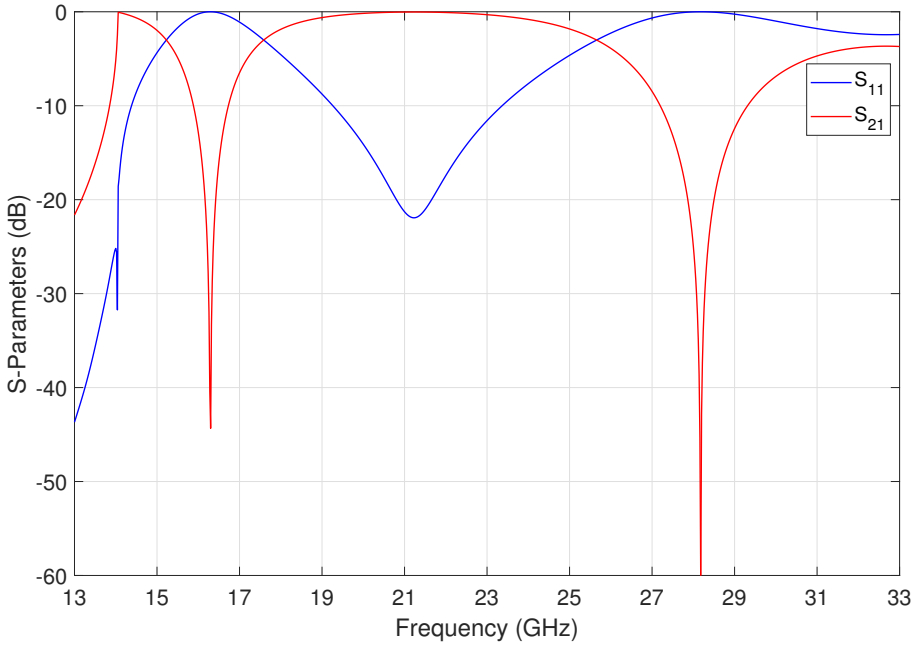

Figure 7.15: Performance of the E-plane T-junction in Fig. 7.14.

As we can clearly see, the electric field has a maximum just at the location of the T-junction when a TZ is produced. This is because the electric field has an even distribution with respect to the branch of the T-junction, so that the fundamental mode in the branch waveguide is not excited, hence the TZ. At the frequency of adaptation, on the other hand, we can clearly see in Fig. 7.17 that the electric field has a strong odd component at the same location, thereby generating a point of adaptation for the fundamental mode of the branch waveguide.

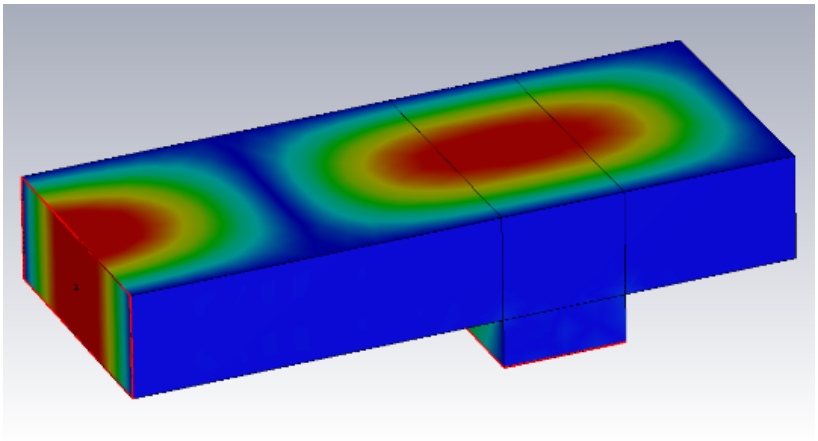

Figure 7.16: Electric field distribution at the first TZ.

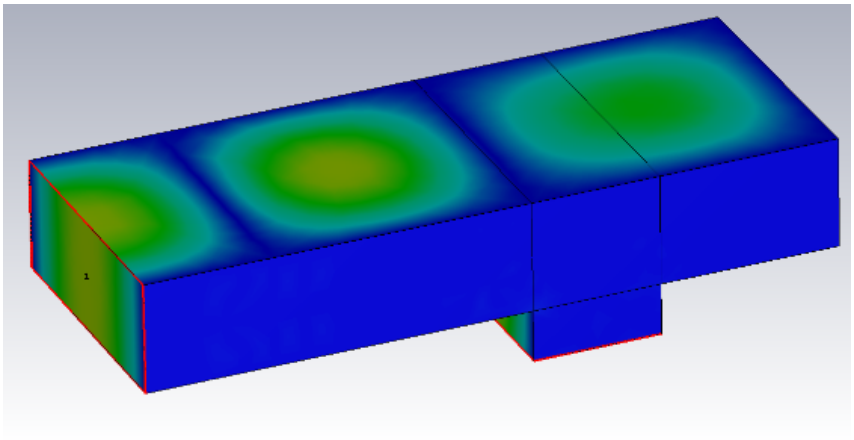

Figure 7.17: Electric field distribution at the point of adaptation.

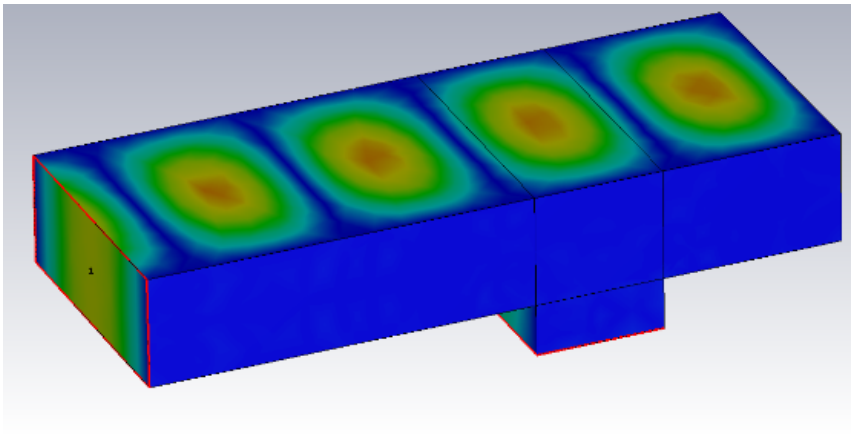

Figure 7.18: Electric field distribution at the second TZ.

This behavior is due to the interference between the E-plane T-Junction and the short-circuited end of the manifold. This is indeed well-known, and has been exploited in the past to define the optimum manifold configuration in manifold multiplexers [67] and, more recently, to generate transmission zeros in rectangular waveguide filters [143]. Our investigations indicate that this interference phenomenon is indeed the cause of the additional TZs that can be observed in the wide-band response in Fig. 7.13.

To further investigate this point, we now look at a simplified version of the quadruplet filter, namely, a two-pole filter with a capacitive inter resonator coupling. Fig. 7.19 shows the basic structure of the two-pole filter, and Fig. 7.20 shows the simulated wide-band performance. As we can clearly see in Fig. 7.20, this two-pole filer produces two TZs in the same approximate location (around 23 GHz) as the one produced by the original quadruplet filter (at 22.2 GHz).

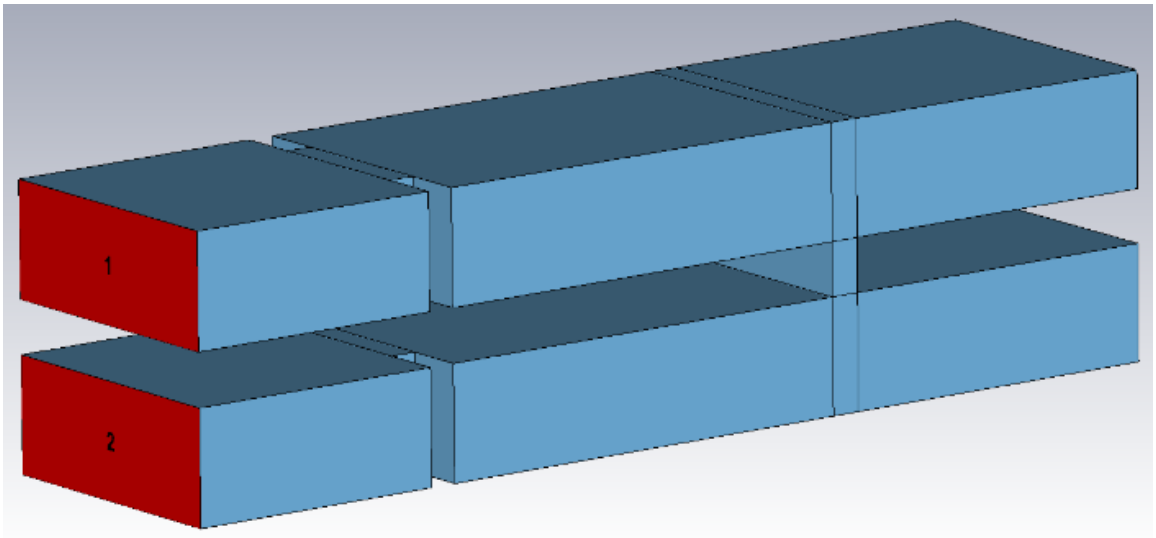

Figure 7.19: Two-pole filter with capacitive inter-resonator coupling.

If we now change the distance of the capacitive iris from the end of the cavity to 18.0 mm, and to 12.0 mm, we obtain the results shown in Fig. 7.21 and 7.22, respectively.

As we can clearly see, changing the distance of the capacitive inter-resonator iris, we can effectively change the location of the additional TZs generated by the T-juncion, while maintaining (via optimization) the same basic filter in-band response.

It is important to note that, since we actually need two T-junctions to implement a capacitive inter-resonator coupling, each one of the TZs is actually a *double* TZ. This is clearly shown in Fig. 7.23, where we have introduced a slight asymmetry in the structure of the two-pole filter with the TZ in the lower rejection band (Fig.7.21).

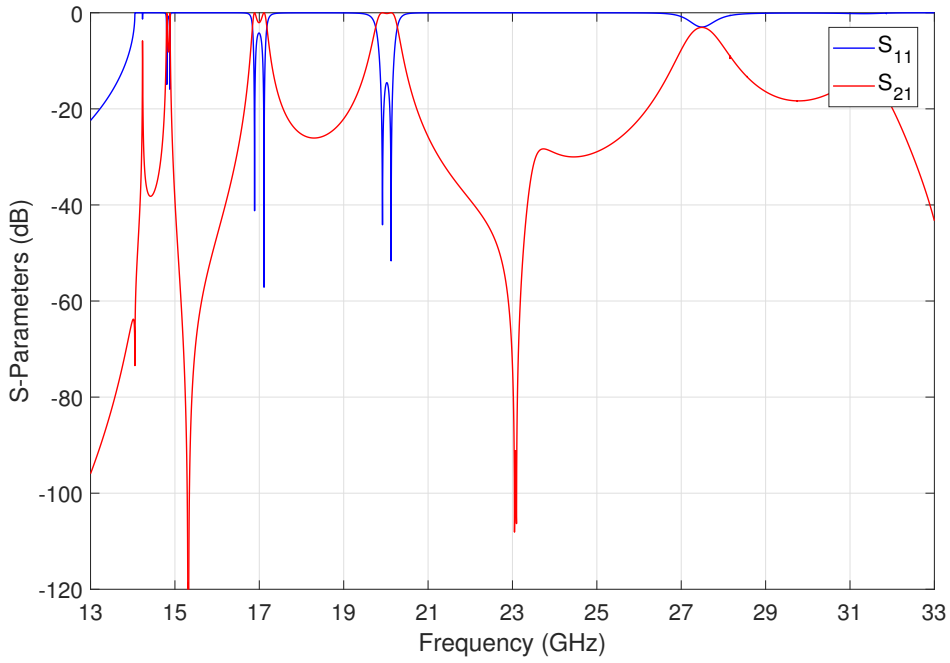

Figure 7.20: Wide-band response of the two-pole filter in Fig. 7.19 .

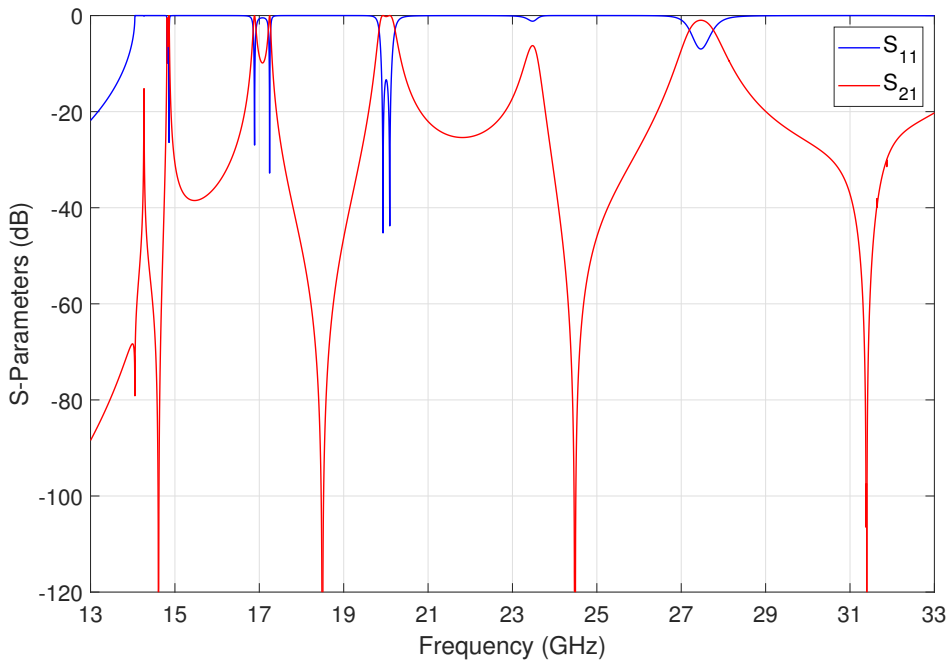

Figure 7.21: Two-pole filter with an additional TZ in the lower rejection band.

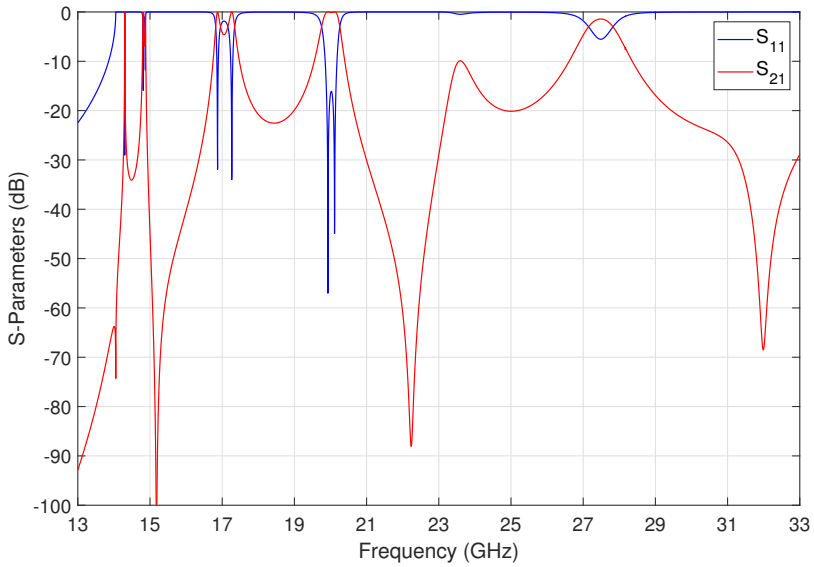

Figure 7.22: Two-pole filter with an additional TZ in the upper rejection band.

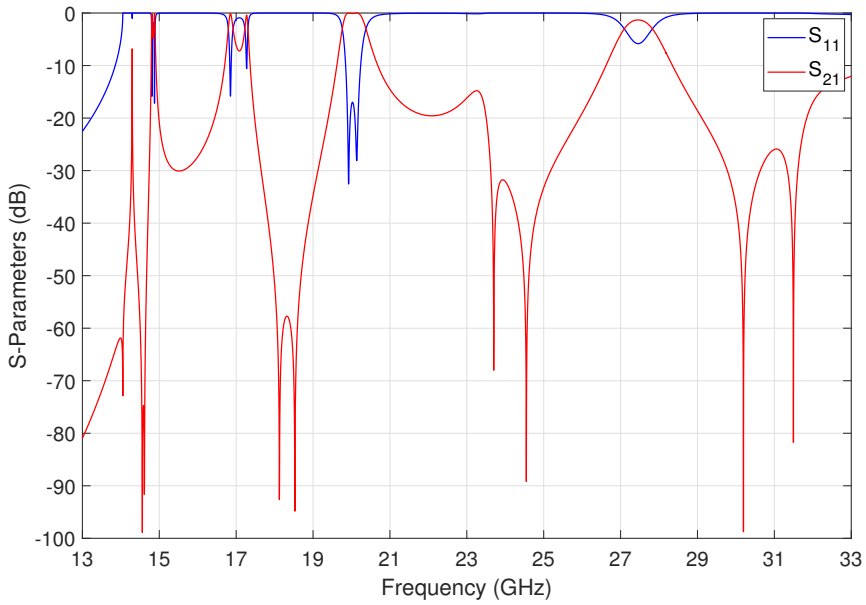

Figure 7.23: Two-pole filter with a double TZ in the lower rejection band.

This feature of the filter structure described in this chapter can be very effectively exploited to design a diplexer, as will be discussed in the reminder of this section.

7.2.3 Distributed model

To start the design of the diplexer, we first need to design two separate filters centered at the frequencies given in the specifications. Both filters are based on the basic rectangular waveguide quadruplet filter proposed in the previous section 7.1.

In this section, we are going to analyze and explain the behavior of the quadruplet filter in terms of an equivalent distributed model.

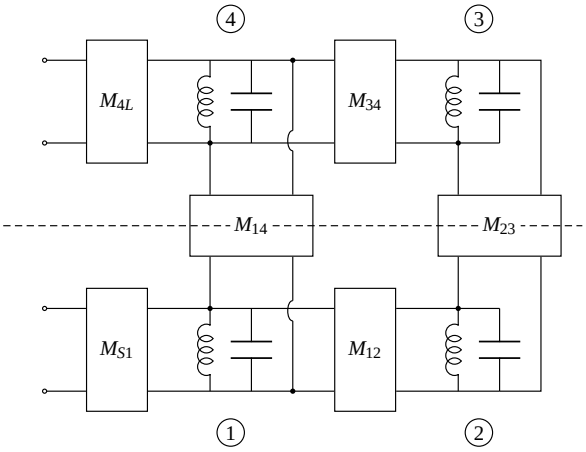

Figure 7.24: Lumped element circuit of a quadruplet.

A typical quadruplet topology with lumped elements for a 4-2 filter is the simple, well-known folded configuration shown in Fig. 7.24. Since the circuit is symmetric, we can write $M_{S1} = M_{4L}$ and $M_{12} = M_{34}$. For an in-band $RL > 20$ dB and rejection higher than 40 dB, we obtain the following values:

$$\begin{aligned} M_{S1} &= M_{4L} = 1.074145 \\ M_{12} &= M_{34} = 0.935874 \\ M_{23} &= 0.766639 \\ M_{14} &= -0.106916 \end{aligned} \tag{7.2}$$

To convert the lumped element circuit into a distributed one, we can replace the resonators with lengths of transmission lines. Instead of resonators 2 and 3, we now have transmission lines of a length that is an integer number of half-wavelengths ($n\lambda_g/2$). However, resonators 1 and 4 are connected through an inverter.

We now need to decide what kind of connection we are going to use between resonators 1 and 4, namely, series or parallel. Since we want to use in the real prototype an E-plane T-junction, the connection must be a series one (see [144]).

The resulting equivalent distributed network is, therefore, the one shown in Fig. 7.25 where $\phi = n \times 180°$ and $\theta' + \theta'' = n \times 180°$.

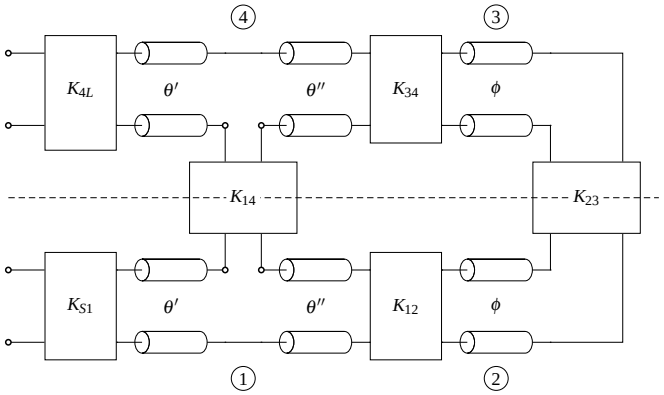

Figure 7.25: Distributed model of the 4-2 filter.

The expressions for the inverters are now:

$$\begin{aligned} K_{S1} &= K_{4L} = M_{S1}\sqrt{\frac{n\pi}{2}\mathcal{W}} = M_{4L}\sqrt{\frac{n\pi}{2}\mathcal{W}} \\ K_{12} &= K_{34} = M_{12}\frac{n\pi}{2}\mathcal{W} = M_{34}\frac{n\pi}{2}\mathcal{W} \\ K_{23} &= M_{23}\frac{n\pi}{2}\mathcal{W} \\ K_{14} &= M_{14}\frac{n\pi}{2}\mathcal{W} \end{aligned} \tag{7.3}$$

where $\mathcal{W}$ is the fractional bandwidth (in terms of frequency if we use TEM lines or in terms of wavelength if we use waveguides).

We still have to determine the individual values for θ' and θ''. The derivation for the values of the network elements, following the procedure described in [82], results in two possible equivalent solutions $\theta' = 0°$ and $\theta' = n \times 180°$. For the time being, we will use the solution $\theta' = 0°$. The in-band response that we obtain with this choice is shown in Fig. 7.26 with $n = 1$, a center frequency $f_0 = 20$ GHz, and bandwidth $BW = 200$ MHz.

As we expect, there is a pair of TZs close to the pass band of the filter due to the 1-4 negative coupling. The agreement of the distributed model with the lumped model response is extremely good, even though we have used the dispersion of the TE_{10} mode of the WR-42 waveguide ($a = 10.668$ mm, $b = 4.318$ mm) in the distributed resonators.

It is interesting now to look at the out-of-band response shown in Fig. 7.27. As we can see, there are two pairs of TZs far away below and above the pass band. This behavior is, in fact, identical to the one discussed in the previous section.

It is important to note that in these simulations, we have used $n = 1$ simply to obtain a single filter response so that the additional TZs could be seen more clearly. Using $n = 3$ would have still produced the additional TZs, but would have also produced additional pass bands, just as in Figs. 7.20 to 7.23, and the additional TZs would have not been so clearly visible.

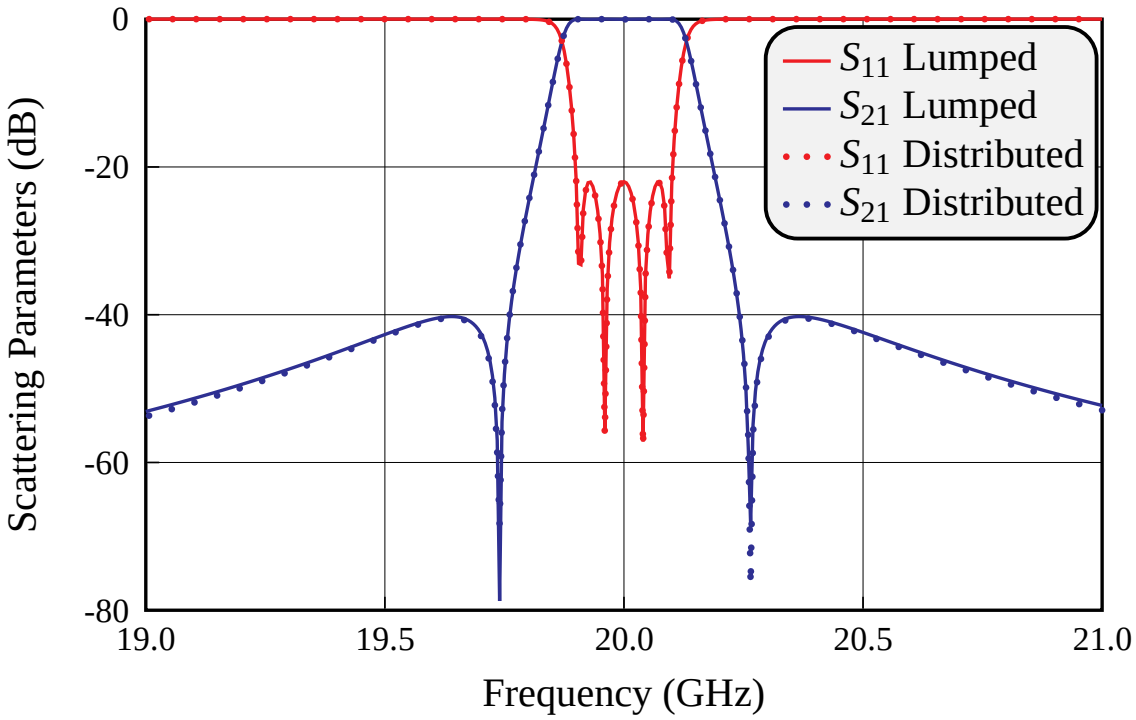

Figure 7.26: In-band response of the distributed model compared with the lumped model response given by the coupling matrix.

As already discussed in section 7.2.2, we can indeed change the frequency location of the extra zeros by simply increasing θ'. That will, of course, degrade the in-band performance, but this degradation can be compensated with a fast optimization of the inverter values in order to recover the desired in-band return loss level.

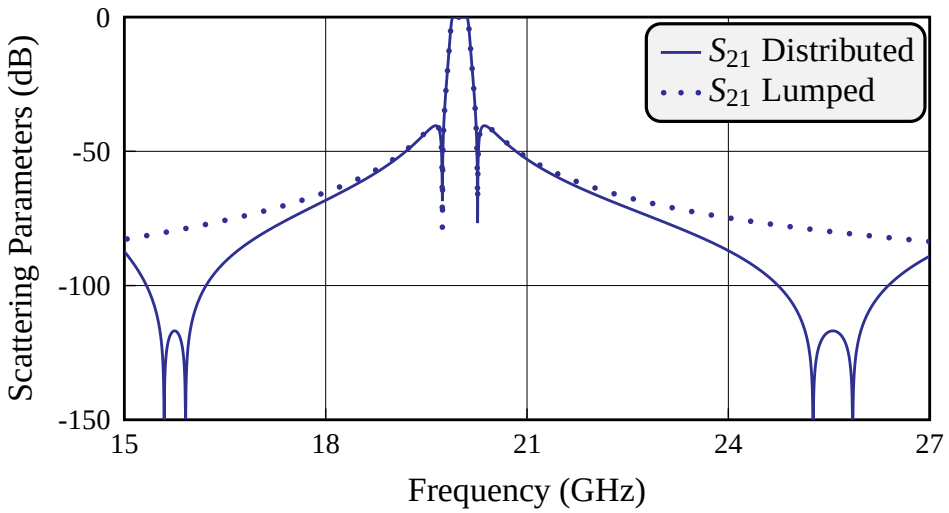

Figure 7.27: Out-of-band transmission response of the distributed model compared with the monotonically decaying response of the lumped model.

An example of the influence of θ' in the location of the transmission zeros can be observed in Fig. 7.28, where the only parameter changed is θ'. It is important to note that, to obtain the result shown in Fig. 7.28 we have used again the real dispersion of the TE_{10} mode in a WR-42 waveguide.

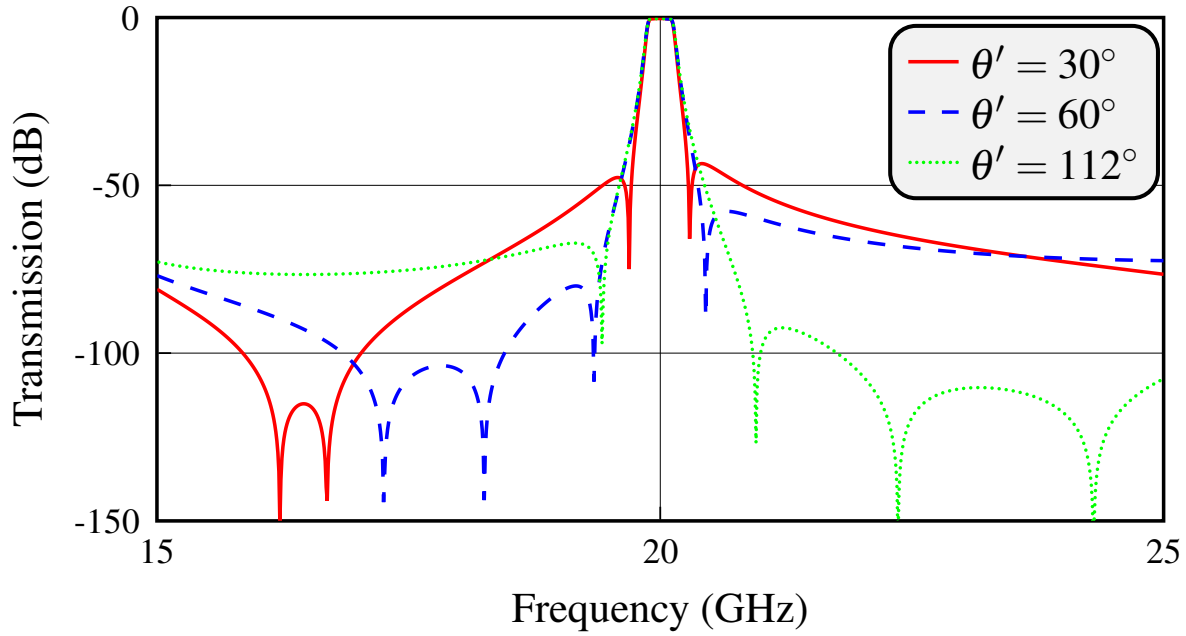

Figure 7.28: Filter performance for several values of the parameter θ'.

The electrical response of Fig. 7.28 shows a typical near-band asymmetry when the additional TZs approach the pass band. We can, however, still maintain the near-band TZs and the in-band performance with a rapid optimization of the inverter values.

There are, however, some limitations. If the extra TZs approach the near-band zeros, it will be difficult to maintain the TZs at the same positions and, consequently, the rejection lobe levels. It is still possible to move the parameter θ' in Fig. 7.28 and keeping the TZs in the same positions through optimization of the inverter values giving the result shown in Fig. 7.29, where the near-band TZs are kept at their original positions.

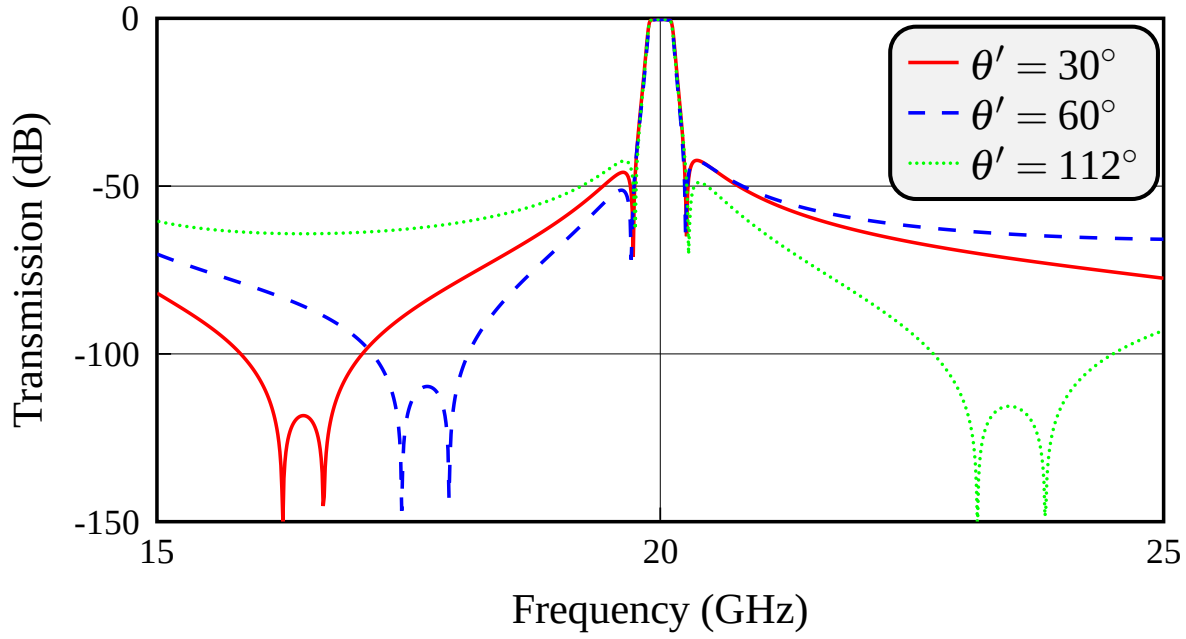

Figure 7.29: Filter performance for several values of the parameter θ' but enforcing the near-band transmission zeros at fixed frequency locations.

Furthermore, it is interesting to observe that if $\theta' > 90°$ the additional transmission zeros in the higher rejection band can be moved closer to the filter pass band, as it is shown in Fig. 7.29.

Once we decide the location of the transmission zeros, the remaining dimensions can be obtained from the distributed model as described in [82].

Additionally, the resonators have been designed using the TE_{103} mode in order to increase the quality factor (using $n = 3$ in eq. (7.3)). It is important to note that this specific feature of the basic filter structure we are discussing can be very effectively exploited in the diplexer design.

To summarize, the features of this structure are:

- The number of TZs implemented is $N_{TZ} = 4$. Two are given by the coupling matrix, and are placed one below and one above the pass band. The other two can be located either to the left ($\theta' < 90°$) or to the right ($\theta' > 90°$) of the pass band.
- The extra TZs can be moved together by changing θ'. However, the convergence of the optimization process becomes slower as the extra TZs are closer to the pass-band.
- The extra TZs can only be moved together and cannot be allocated separately. This is because we have at our disposal only two geometrical parameters, namely the length θ', and the strength of the capacitive coupling.

7.2.4 Low-accuracy diplexer design

To continue with the diplexer design, we now use the structure just described to design the two separate ideal waveguide filters that fit the specifications of the two channels of the diplexer. The design has been carried out using FEST3D (from AuroraSat, now with CST and Dassault Systèmes). The procedure is as follows:

1. Start with the coupling matrix giving the in-band performance and the near-band TZs.
2. Use the distributed model to increase θ' until the extra TZs are located where desired.
3. Optimize the inverter values to retrieve the in-band response and the near-band TZs where desired. This stage is very fast since we work only with the distributed model. No EM optimization is required at this point.
4. The initial physical dimensions of the structure are then obtained following the standard procedure described in [82]. At this point the EM simulations are performed over individual parts of the filter. Therefore, this step is also very fast.
5. We can now assemble the whole filter and perform a full-wave simulation. This will give a very good initial point for the EM optimization. With a few iterations, the optimization will now produce a response that is very close to the one given by the ideal distributed model.

At the end of the design process, we obtain two separate filters. Fig. 7.30 and Fig. 7.31 show the performance of the two separate filters compared with the distributed model.

To continue with the design process, we now need to join the two filters in order to obtain a diplexer. After exploring a number of possible solutions, we decided to use an E-field T-junction, as shown in Fig. 7.32. Fig. 7.33 shows the complete structure.

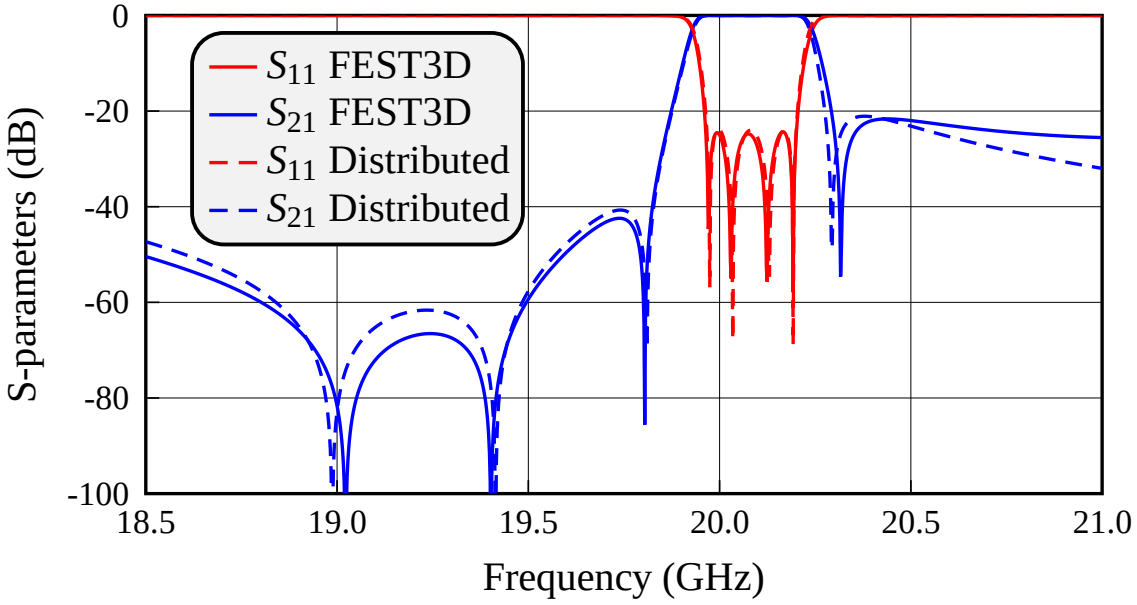

Figure 7.30: Response of the quadruplet filter for the diplexer with three TZs in the lower band. Solid lines correspond to the EM response and dashed lines correspond to the distributed model response.

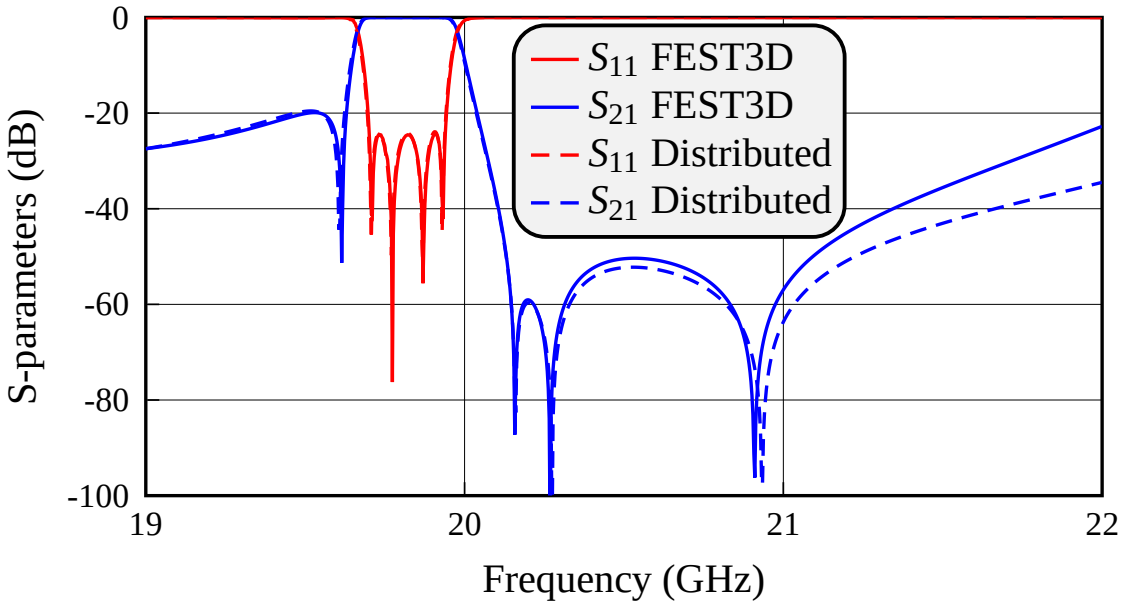

Figure 7.31: Response of the quadruplet filter for the diplexer with three TZs in the upper band. Solid lines correspond to the EM response and dashed lines correspond to the distributed model response.

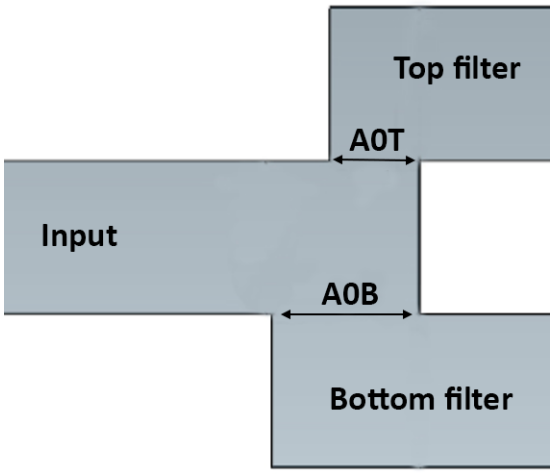

Figure 7.32: Frontal view of the E-field T-junction implemented. A0T and A0B are the design dimensions.

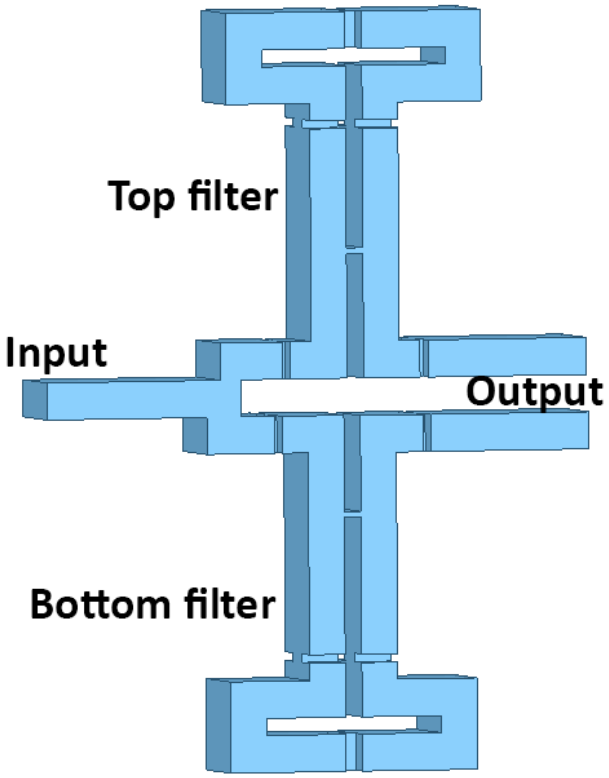

Figure 7.33: Structure of the diplexer with the T-junction.

Fig. 7.34 shows the initial response of the diplexer. As expected, the diplexer is not tuned correctly.

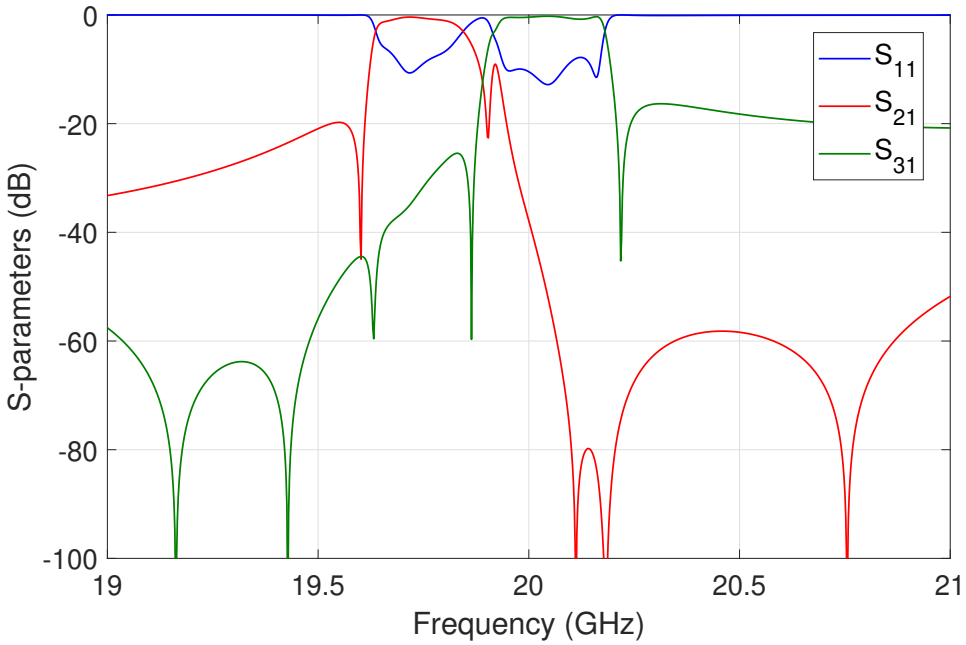

Figure 7.34: Initial response of the complete diplexer structure.

The next step is to use the procedure described in [38] to obtain the performance shown in Fig. 7.35.

The procedure essentially consists of recovering the ideal response by optimizing the structure cavity-by-cavity.

At this point, we have a diplexer structure that satisfies all the specifications. However, all simulations performed so far have been carried out with FEST3D using a set of parameters allowing fast computations with reduced accuracy. We now need to move from a low-accuracy design to a high-accuracy design that can be successfully manufactured.

Furthermore, the diplexer we just designed uses 90° corners, and the effects of material losses have not been included. For the sake of manufacturing, it is now convenient to introduce rounded corners in the structure, and to include in the simulations the losses (due to the use of aluminum in this case).

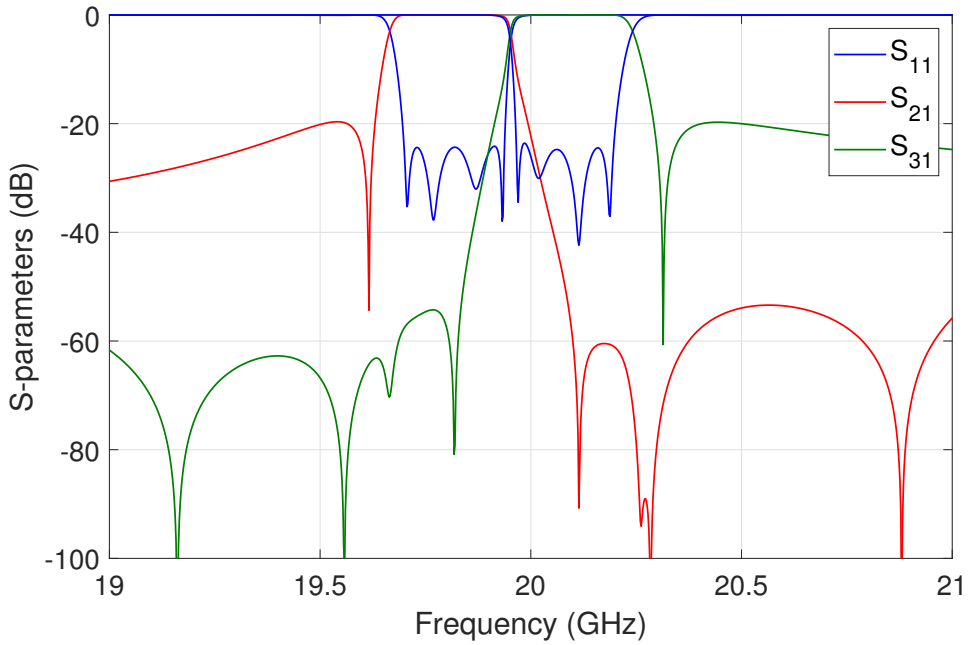

Figure 7.35: Final response of the diplexer with the T-junction.

7.2.5 High-accuracy diplexer design

The software used to carry out the high-accuracy design is CST Microwave Studio. One possible approach could be a direct optimization using this software tool. This approach, however, is extremely time-consuming due to the complexity of the hardware. A much more efficient procedure is as follows:

1. The first step consists in separating the individual filters of the diplexer shown in Fig. 7.33. After the separation, each filter becomes a 2-port network that can be treated independently. The 2-port structures are then simulated with the high-accuracy simulator. Naturally, the CST response will differ from the ideal one. The OS-ASM procedure described in chapter 3 (see also [59]) is now applied to recover the ideal response. The coarse space in this case is the one shown in Fig. 7.36, the fine space is the model in CST. After three iterations, the desired performance is obtained in the high-accuracy simulator. Fig. 7.37 shows the final response obtained with CST as compared to the ideal low-accuracy result obtained with FEST3D.
2. The following step is to add round corners to the cavities (see Fig. 7.38), and then simulate again each filter with the high-accuracy simulator. In this case, three iterations of the procedure described in [59] are sufficient to recover the ideal performance. The final response of one of the filters is shown in Fig. 7.39.

3. Following a similar procedure, the T-junction shown in Fig. 7.33 is now extracted and treated as an isolated 3-port network (see Fig. 7.40). After adding the round corners, the T-junction is simulated in CST. The same procedure described before is used to recover the ideal T-junction response. Fig. 7.41 shows the final response in CST as compared to the ideal performance obtained with FEST3D.
4. After the two filters and the T-junction have been designed separately, the three parts are combined and simulated with CST. Fig. 7.42 shows the initial response after assembling the diplexer. This last high-accuracy result includes also the losses due to aluminum. Only one more OS-ASM iteration (using the identity space mapping matrix) is now enough to obtain the final response.

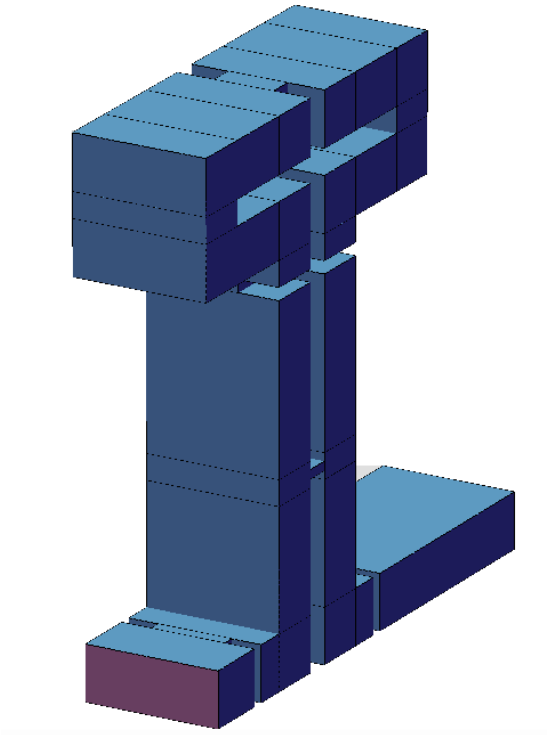

Figure 7.36: Extraction of top filter in FEST3D (coarse space).

As a final verification of our design, we now simulate the final diplexer structure with HFSS (from Ansys).

As we can see in Fig. 7.43, the CST and HFSS simulations are almost exactly coincident. Therefore, we can conclude that we have obtained a diplexer structure that is ready to be manufactured.

Finally, one last modification has been introduced, that is to extend the output waveguide from the two filters of the diplexer in opposite directions.

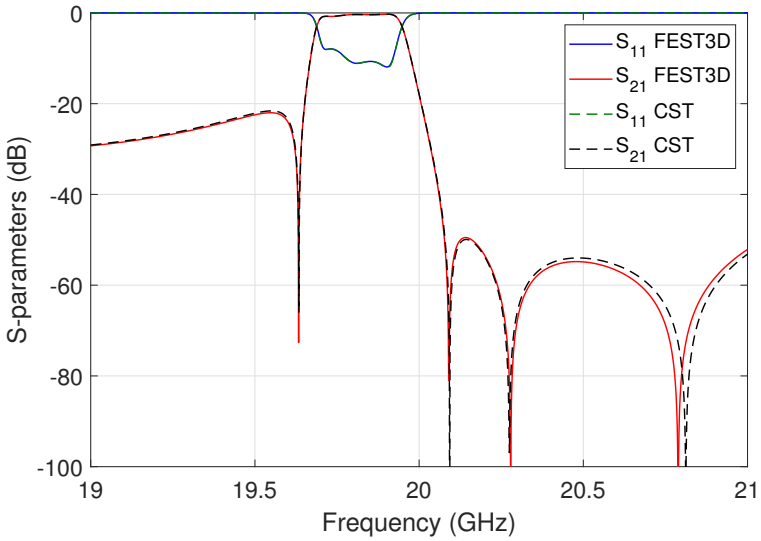

Figure 7.37: Recovered response of the top filter with sharp corners.

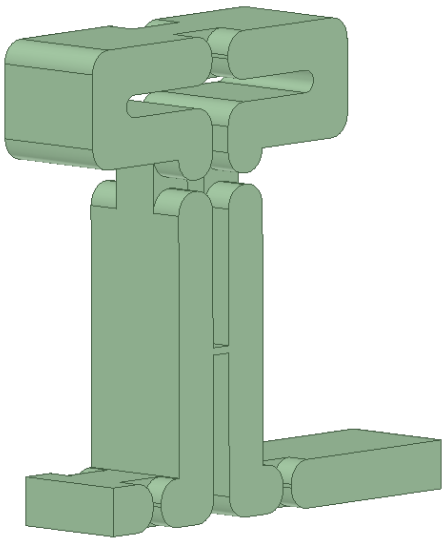

Figure 7.38: Extracted bottom filter with rounded corners in CST (fine space).

This has been done in order to have enough space for the connection of the waveguide flanges needed to measure the device. This modification, however, does not affect the performance of the diplexer. Fig. 7.44, Table 7.3 and Table 7.4, show the final structure and the dimensions of the top and bottom parts of the diplexer, respectively.

To conclude, in order to complete the EM analysis of the diplexer, Fig. 7.45 shows the CST broadband performance of the device. As we can see, the diplexer does have a very good out-of-band rejection between 18 and 22 GHz.

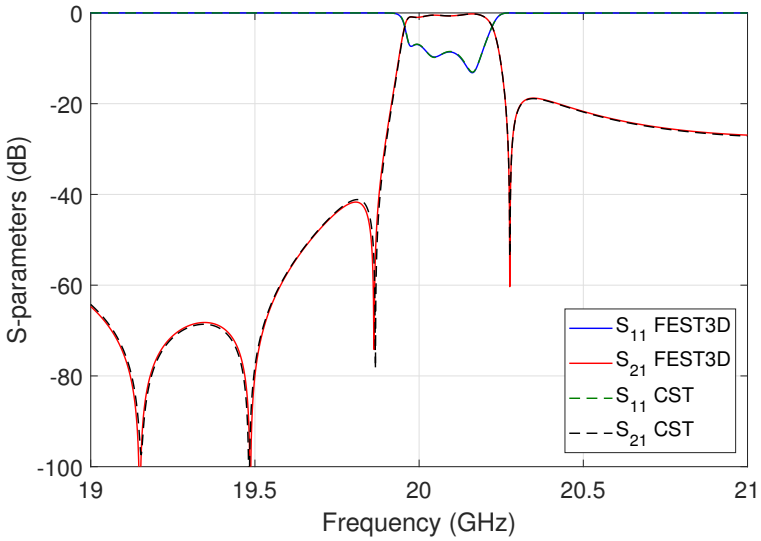

Figure 7.39: Recovered response of the bottom filter with rounded corners.

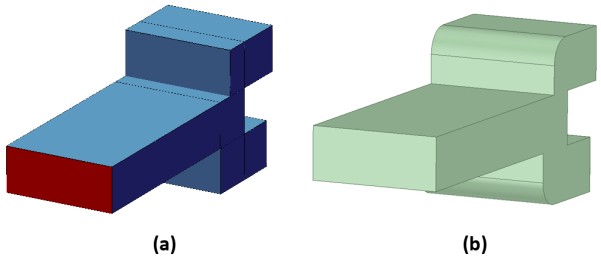

Figure 7.40: Extracted T-Junction. (a) sharp corners, (b) rounded corners.

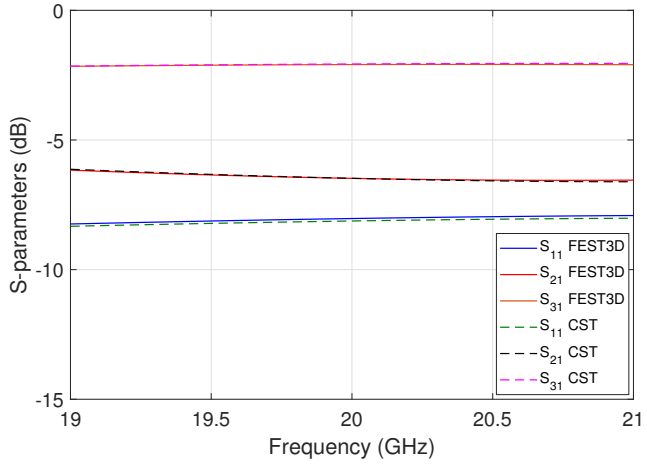

Figure 7.41: Recovered response of the T-junction.

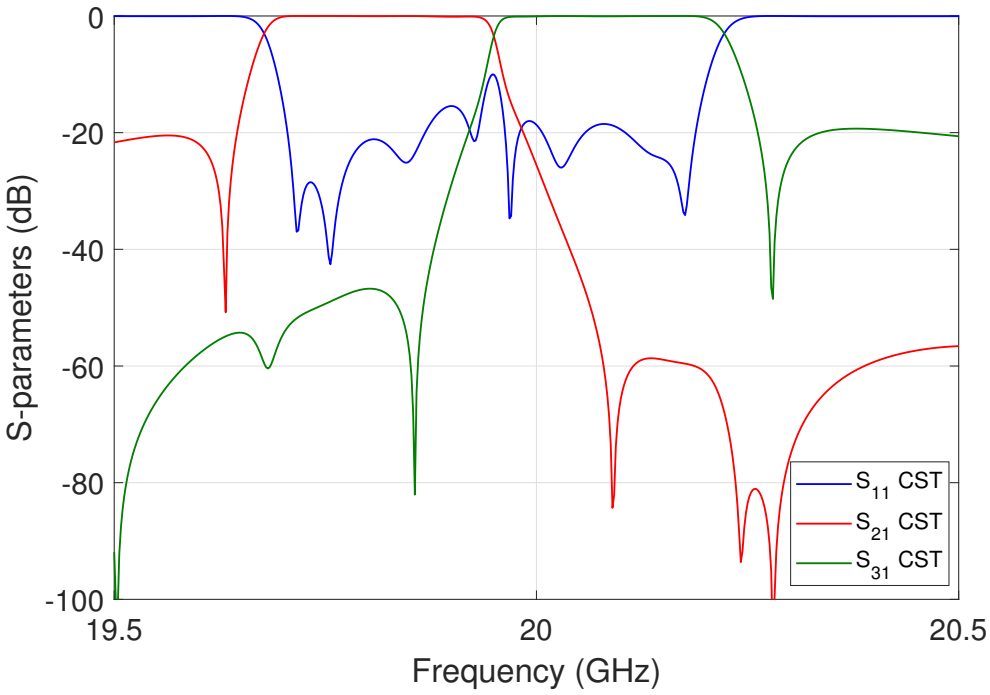

Figure 7.42: Initial response of the diplexer in CST after assembly of the separate components.

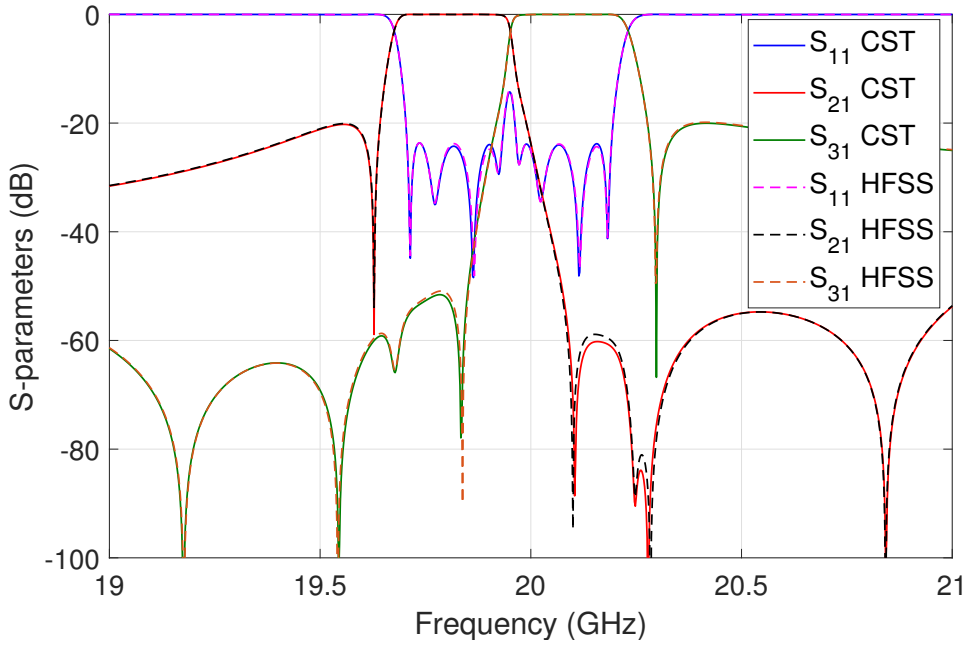

Figure 7.43: Comparison of the responses of the final diplexer produced by CST and HFSS .

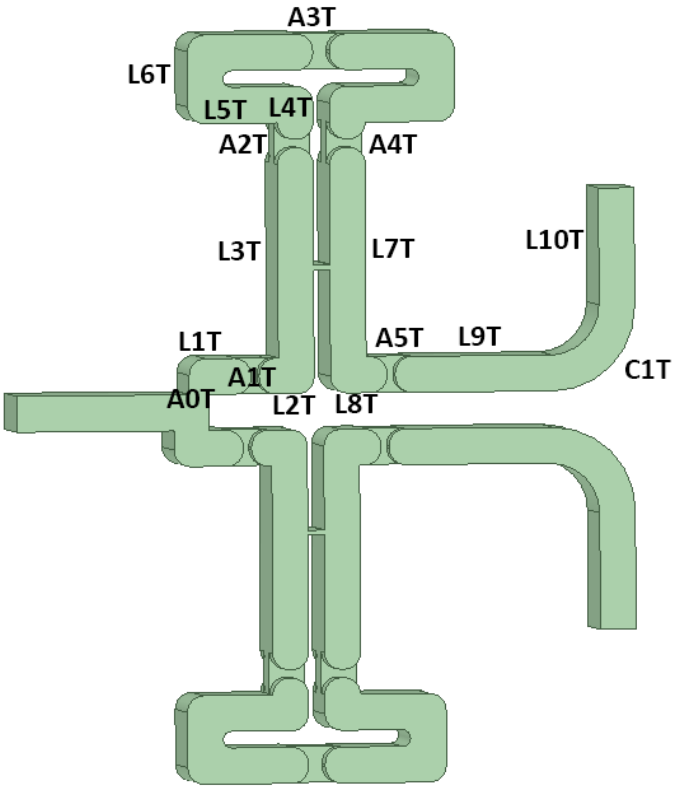

Figure 7.44: Final structure of the diplexer. Dimensions of the top and bottom filter are numerated with 'T' and 'B' termination, respectively.

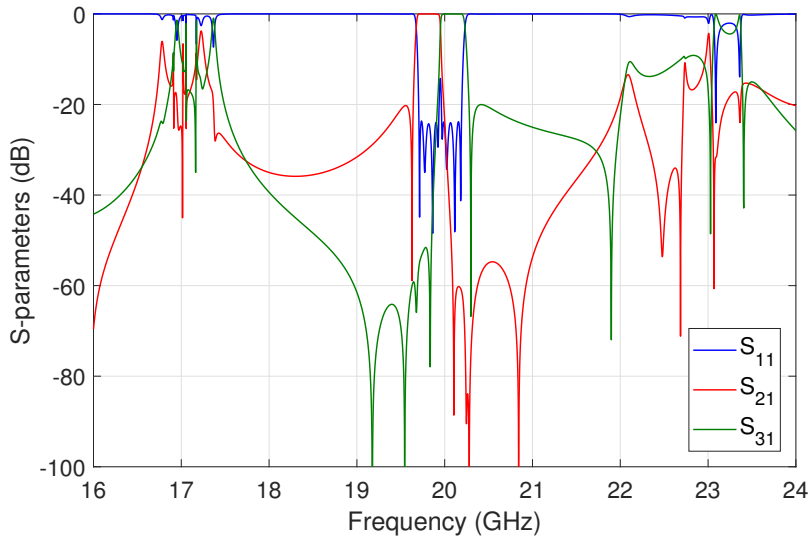

Figure 7.45: CST broadband performance of the diplexer.

Table 7.3: Dimensions of the top filter of the diplexer in millimeters.

Structure[1]	Height	Width	Length
Aperture A0T	0	10.668	2.448
Input L1T	4.318	10.668	7.471
Inductive aperture A1T	4.318	6.442	1
Cavity 1 L2T	4.318	10.668	6.648
Cavity 1 L3T	29.537	10.668	4.318
Capacity aperture[2]	0.7	10.668	2
Inductive aperture A2T	1	4.509	4.318
Cavity 2 L4T	6.318	10.668	4.318
Cavity 2 L5T	4.318	10.668	15.193
Cavity 2 L6T	10.636	10.668	4.318
Inductive aperture A3T	4.318	5.074	2
Inductive aperture A4T	1	4.727	4.318
Cavity 4 L7T	29.502	10.668	4.318
Cavity 4 L8T	4.318	10.668	6.833
Inductive aperture A5T	4.318	6.332	1
Output L9T	4.318	6.332	17.05
Output L10T[3]	4.318	6.332	14

[1] The diplexer has XY-plane symmetric dimensions in L4T, L5T and L6T. All the corners are 2 mm rounded.
[2] The capacitive aperture is placed in the filter at 16.959 mm from the center axis of the diplexer.
[3] The curve C1T is a 10 mm length of rectangular waveguide with 10 mm of radius.

7.2.6 Multipactor breakdown prediction

The multipactor effect is one of the main problems that affects high power satellite devices [145]. A multipactor analysis is therefore mandatory [146]. To carry out this analysis we will use SPARK3D (from AuroraSat, now with Dassault Systèmes).

For the sake of efficiency, the usual procedure is to focus the simulations in the areas where the multipactor effect can be expected. In order to identify these areas we need to know two key data, namely, the frequencies where the group delay is maximum for both filters, and where the E-field maximum is located at those frequencies. This information will give us an idea of where the multipactor effect may be expected and we need to simulate with the indicated software.

The critical frequencies for the diplexer are 19.69 GHz, 19.95 GHz and 20.24 GHz, as shown in Fig. 7.46. We now simulate the behavior of the diplexer at each frequency,

Table 7.4: Dimensions of the bottom filter of the diplexer in millimeters.

Structure[1]	Height	Width	Length
Aperture A0B	0	10.668	4.321
Input L1B	4.318	10.668	8.377
Inductive aperture A1B	4.318	5.871	1
Cavity 1 L2B	4.318	10.668	6.755
Cavity 1 L3B	28.801	10.668	4.318
Capacity aperture[2]	0.5	10.668	2
Inductive aperture A2B	1	4.643	4.318
Cavity 2 L4B	6.318	10.668	4.318
Cavity 2 L5B	4.318	10.668	14.666
Cavity 2 L6B	10.636	10.668	4.318
Inductive aperture A3B	4.318	4.979	2
Inductive aperture A4B	1	4.629	4.318
Cavity 4 L7B	28.807	10.668	4.318
Cavity 4 L8B	4.318	10.668	6.927
Inductive aperture A5B	4.318	6.006	1
Output L9B	4.318	6.332	17.05
Output L10B[3]	4.318	6.332	14

[1] The diplexer has XY-plane symmetric dimensions in L4B, L5B and L6B. All the corners are 2 mm rounded.
[2] The capacitive aperture is placed in the filter at 14.321 mm from the center axis of the diplexer.
[3] The curve C1B is a 10 mm length of rectangular waveguide with 10 mm of radius.

and identify the locations of the volt maxima. Fig. 7.47 shows one of the simulations performed with CST. As we can see, the critical areas are the corners of the filters and the capacitive windows between cavities 1 and 4.

Now that we have all the information we need, we can perform several simulations with SPARK3D to obtain the multipactor power thresholds that can initiate multipactor effects in the device.

Several different simulations have been performed to obtain the thresholds for the different areas identified. The parameters used are as follows:

- Initial number of electrons: 10000
- Multipactor criterion growth factor: 10^2
- Initial power: 100 W, 5000 W and 10000 W
- Maximum power: 5000 W, 20000 W and 30000 W

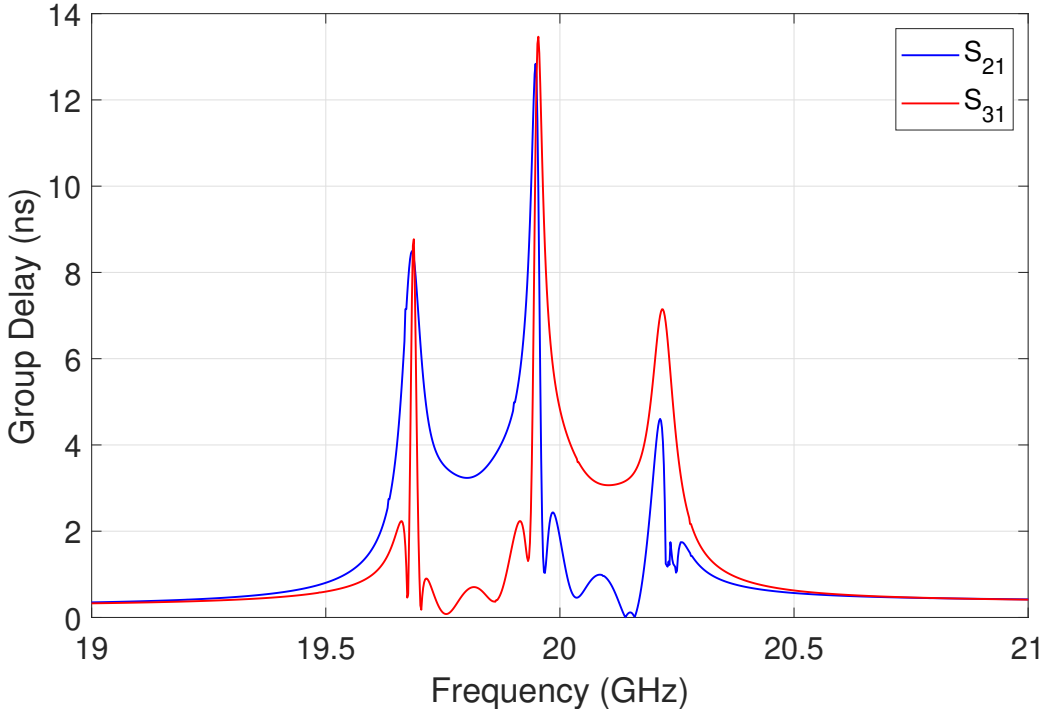

Figure 7.46: Group delay response of the diplexer.

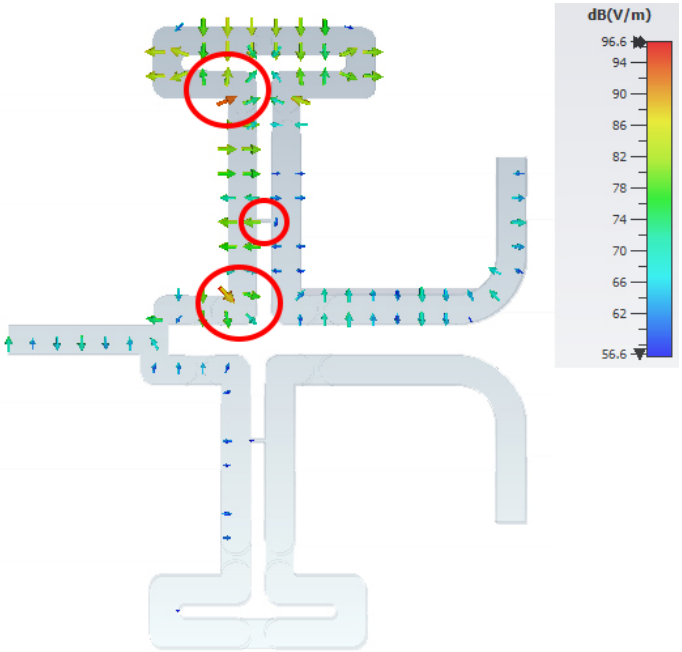

Figure 7.47: Representation of the E-field and the critical zones in the diplexer for 19.69 GHz.

The initial number of electrons and the multipactor criterion increase factor are typical values for multipactor analysis based on multiple past simulations.

The initial and maximum power of the analysis are usually defined by the requirements for the specific device under test. In particular, the diplexer we have designed is intended to be used as multiplexer in the satellite, with a maximum of 200 W of RF power in each channel.

After each simulation, we have recorded the values for which the multipactor effect can be produced. Fig. 7.48 shows the result of one simulation for the capacitive window.

The different lines in the graphic represent the evolution of the number of electrons in time for each different RF power level. When we have no discharges, the number of electron decreases. When the multipactor effect appears, the electron density increases in time. If the growth factor becomes greater than the multipactor growth criterion, we consider that a multipactor discharge has taken place.

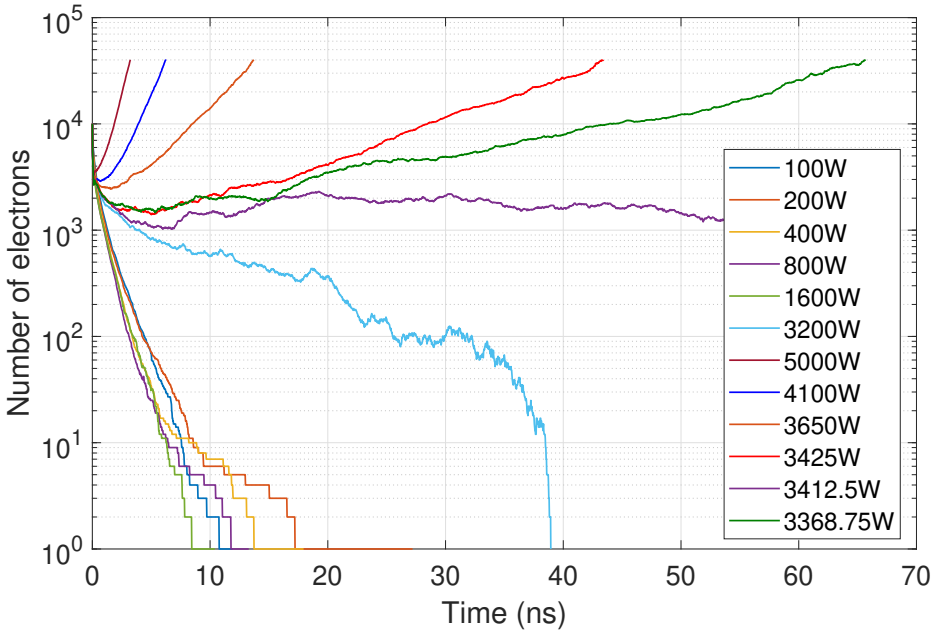

Figure 7.48: Multipactor simulation with discharges for the bottom capacitive window at 19.95 GHz.

Finally, Table 7.5 shows the power thresholds obtained with the different simulations, and the areas of the diplexer that are affected.

As expected, the multipactor effect has a lower power threshold at low frequency. In addition, the multipactor effect is first generated in the capacitive window of the bottom filter where the waveguide height is smaller (0.5 mm).

Furthermore, the simulations indicates that we do not have any multipactor effect in the corners of the cavity filters as far as the power is below $\approx$ 30000 W. From the simulated data we have collected, we can see that the lowest power threshold we have identified is 3300 W.

This power level is definitely far above any current requirement. The diplexer can therefore be safely considered to be multipactor-free. Additionally, the diplexer has low insertion losses and has been designed following the low PIM design guidelines discussed in [118].

To conclude this section, and in order to validate the results obtained, we have performed another multipactor discharge simulation with a different simulation tool, namely, CST Particle Studio (from Dassault Systèmes). This code uses time-domain simulations to predict the multipactor thresholds.

The results obtained are virtually coincident with the previous simulations and verify the data from SPARK3D, showing a multipactor discharge in the bottom capacitive aperture around 3500 W, and at about 6600 W for the top capacitive aperture at 19.95 GHz.

Table 7.5: Power threshold of multipactor effect (in Watts)

Structure	19.69 GHz	19.95 GHz	20.24 GHz
Capacitive aperture Top	7640	5810	>30000
Capacitive aperture Bottom	>30000	3300	5820
First corner Top	>30000	>30000	>30000
Second corner Top	27185	>30000	>30000
First corner Bottom	>30000	>30000	>30000
Second corner Bottom	>30000	28750	>30000

7.2.7 Measurements

Finally, in order to fully validate the diplexer structure, we have manufactured a prototype. The diplexer has been fabricated in aluminum with E-plane cut in order to reduce the insertion losses. The maximum error guaranteed by the manufacturer was less than 20 microns. Fig. 7.49 shows the inside of the two parts of the diplexer. The final dimensions of the diplexer are $104 \times 85 \times 24$ mm with a total mass of 432 g, thus satisfying the physical specifications. In Fig. 7.50 and Fig. 7.51 we show the breadboard of the diplexer, and the comparison between the measurements and the ideal response of the diplexer, respectively.

As we can see, the responses are practically coincident. We can, however, observe that there is a small frequency shift in the response towards lower frequencies.

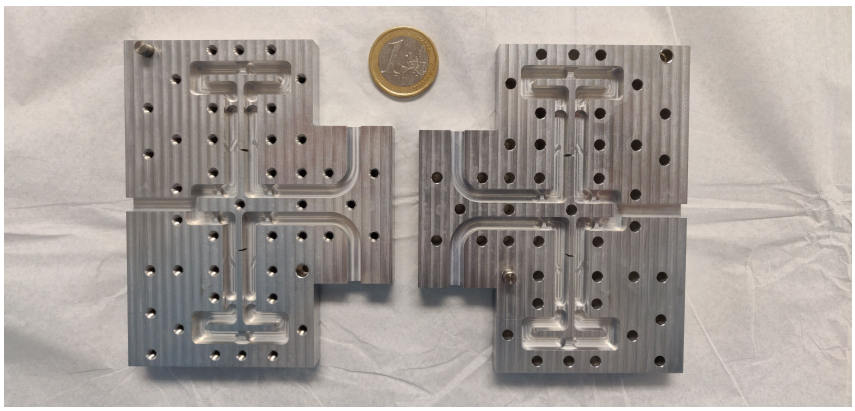

Figure 7.49: Fabricated prototype of the diplexer.

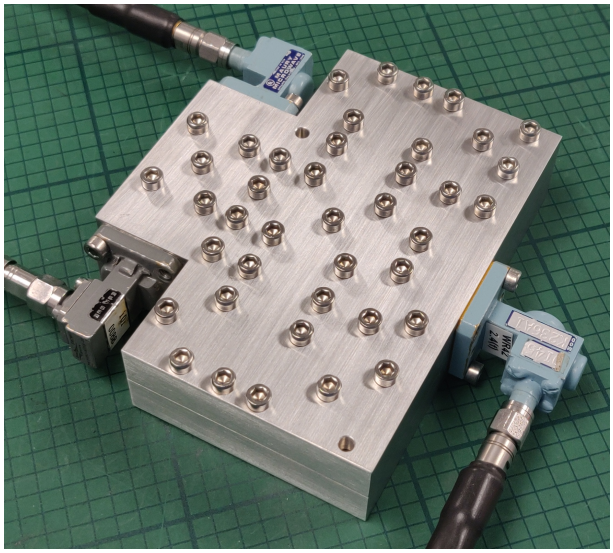

Figure 7.50: Diplexer breadboard.

To further understand this aspect, we have recovered by simulation the response that we have measured with the real hardware.

The results of this analysis indicates that there is a maximum error of 17 microns. This is indeed inside the declared tolerance of 20 microns. Moreover, as we can observe, the S_{11} is always below -20 dB in the whole in-band response of the diplexer, as required by the specifications. The measured insertion losses, on the other hand, are 0.389 dB and 0.374 dB for the lower and higher filter, respectively. These results are close to the required specifications but are not compliant. A compliant insertion loss can, however, be easily obtained by silver-plating the device.

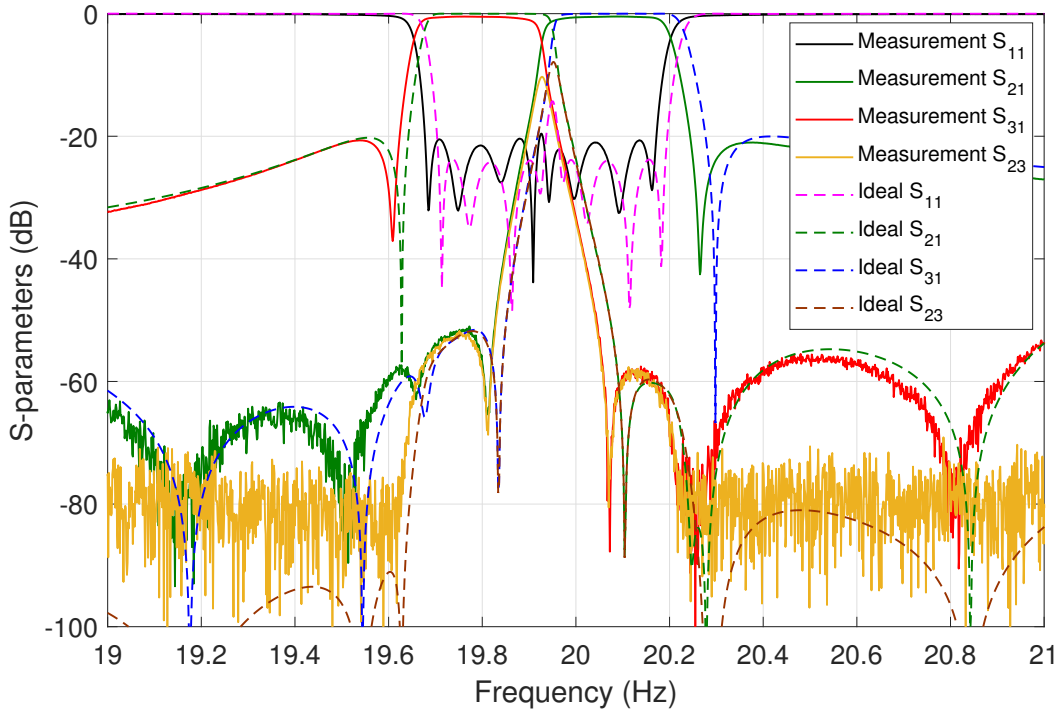

Figure 7.51: Comparison between measurement and ideal response.

7.2.8 Conclusions

In this section, we have discussed the detailed design procedure for a diplexer structure based on the use of an E-plane T-junction together with two rectangular waveguide quadruplet filters (the ones proposed in section 7.1.1). The structure allows to implement a number of TZs in the performance of the filters, thus resulting in a highly selective response. The final structure is simple and very easy to manufacture. In addition, a multipactor study of the device has been carried out, indicating no multipactor problems up to 3300 W.

Finally, the performance of the diplexer has been verified successfully with several commercial simulation tools of well known accuracy, and by measurements of a prototype manufactured in aluminum.

The results obtained are compliant with all of the initial specifications, except for the insertion losses (0.389/0.374 dB). However, this can be easily compensated by silver-plating the device. In conclusion, we have successfully proven that the diplexer structure we developed can be built to be fully compliant with the requirements of modern multi-beam satellite payloads.

7.3 Filter-switch

Modern communication systems for both ground and space applications require microwave hardware with ever increasing flexibility [65], [66]. A very common implementation of flexible input/output (I/O) networks for communication payloads is based on the use of microwave filters and waveguide switches [67]. Most switches are based on mechanical rotatory systems [147], or use semiconductor technology and Micro-Electro-Mechanical Systems (MEMS) [148]. Recently, in [149], a new approach to design waveguide switches was proposed. They were based on alternating short and open circuits in the signal path of a waveguide. The same concept was later on used in [150] and in [151] to design a single-pole six-throw (SP6T), and a single-pole twelve-throw (SP12T) waveguide switch.

In addition, in the last few years, a number of publications have also discussed devices that combine filtering and switching functions. In [152] and [153], waveguide switches based on switchable planar band-stop filters, and band-pass filters using RF MEMS switchable planar resonators, are presented respectively. This novel concept is used in [154] to implement waveguide filters that can perform channel aggregation. Other solutions can also be found in the technical literature. In [155], for example, a filtering switch based on coaxial resonators is proposed. Furthermore, in [156] a dual-function T/R switch, incorporating a Complementary Metal-Oxide-Semiconductor (CMOS) integrated band-pass filter as part of the switch circuitry, is also demonstrated.

In this context, therefore, the objective of this section is to propose an alternative solution to the problem of designing switching and filtering networks in communication payloads based on the use of separate filters and rotary switches. In particular, we describe a new simple device that integrates the waveguide filter and switch functions in a single component (F&S), thereby producing significant mass and volume reductions, and actuation power savings [157].

7.3.1 Filter & Switch

Fig. 7.52 shows one of the implementations of the basic F&S concept that we discuss in this section. The structure in Fig. 7.52 behaves at the same time as a 3-pole filter and as a one-pole triple-throw (1P3T) switch. The device has one input (P1) and three outputs (P2, P3 and P4).

Each branch is composed of rectangular waveguide resonators with inductive apertures connected to a common central square shape resonator. The input branch (P1) and the central cavity have conventional tuners that can be adjusted manually. The resonators of the other 3 branches (P2, P3 and P4) have in their centers the novel *modified tuning pin* (MTP) shown in Fig. 7.53.

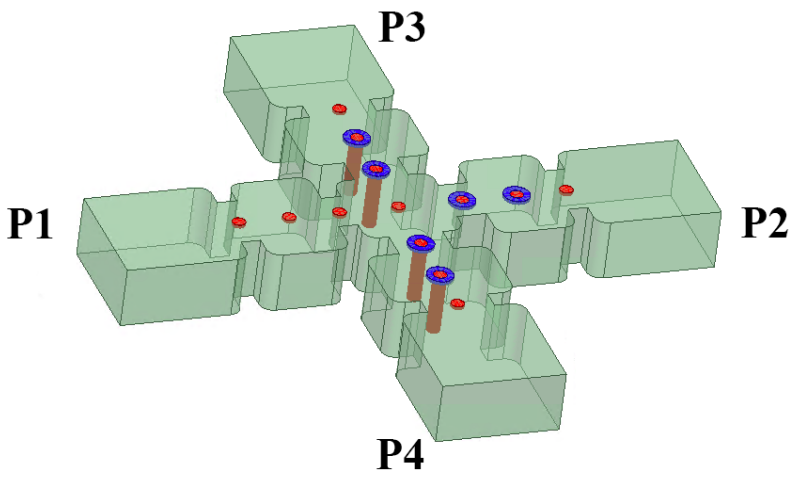

Figure 7.52: Possible implementation of the F&S. The device behaves at the same time as a 3-pole filter and as a 1P3T switch.

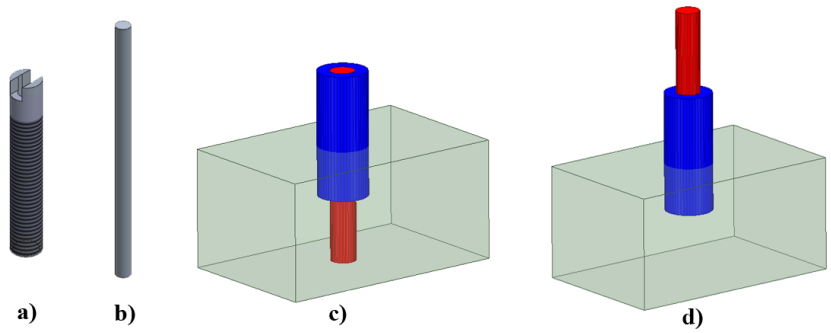

Figure 7.53: Modified Tuning Pin (MTP): (a) Hollow M4 screw (blue cylinder) that can be adjusted manually to tune each cavity or aperture; (b) Pin (red cylinder) that can be inserted in the center of the hollow M4 tuning screw to short circuit a cavity or an aperture; (c) MTP detuned state; (d) MTP tuned state.

The MTP allows two states: detuned and tuned state. In the detuned state (see Fig. 7.53c), the central pin (see Fig. 7.53b) is fully inserted in the waveguide until contact is made with the bottom wall of the waveguide. It is important to note, however, that it is not necessary to establish a good electric contact with the waveguide wall. The simple presence of the pin in the resonator, or in the apertures, is enough to fully detune the filter. In the tuned state (see Fig. 7.53d), the pin is extracted till the M4 screw (see Fig. 7.53a) that is hosting the pin is the only element that remains inside the waveguide. The penetration of the M4 tuning screw is carefully adjusted to obtain the desired filter performance. The pin is never fully removed from the hollow M4 screw so that no radiation can occur.

7.3.2 Design procedure

In the structure shown in Fig. 7.52, the branch P2 has its MTPs in the tuned position. The other two output branches (P3 and P4) have their MTPs in the detuned position. With this configuration, the behavior from port 1 to port 2 (the active path) is a standard 3-pole filter, whereas the paths from port 1 to port 3 and 4 are strongly attenuated.

The design of this structure has been performed using FEST3D (from AuroraSat, now with CST and Dassault Systèmes), and it is very simple, optimizing in all the steps only the physical dimensions of the structure:

1. The starting point is to design the 3-pole filter of Fig. 7.54, forcing the central cavity to be square. We included traditional M2 tuners in the first half of the filter and in the last aperture. In the third cavity and in the third window (T1 and T2 in Fig. 7.54) we included M4 MTPs. The structure is then optimized to obtain the desired filter response (see Fig. 7.55)

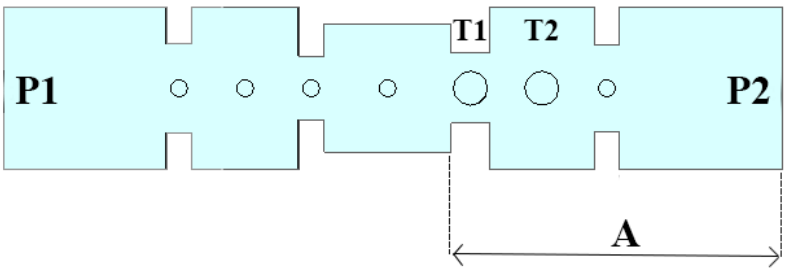

Figure 7.54: 3-pole filter. The central cavity must be square so that the perpendicular branches can be added later.

2. We next add the perpendicular branches (P3 and P4) using the same dimensions as in the P2 branch ('A' in Fig. 7.54). We then set the MTPs of branches P3 and P4 to the detuned state. We now re-optimize the branch P2 to take into account the effect of the newly added branches. Fig. 7.56 shows the F&S structure at this point. The black circles in the MTPs of branches P3 and P4 indicate that they are in the detuned state.
3. The next step is to set the MTPs of branch P2 into the detuned state and set the MTPs of branch P3 to the tuned state (as in Fig. 7.57). Re-optimize the branch P3 until the desired performance is recovered.

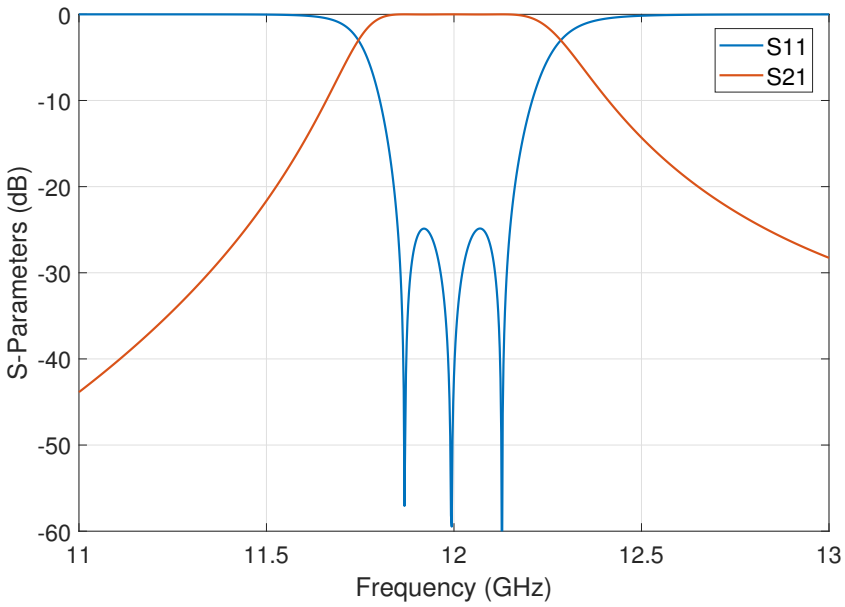

Figure 7.55: Response of the 3-pole filter. In this example, the filer is centered at 12 GHz, and has a bandwidth of 200 MHz.

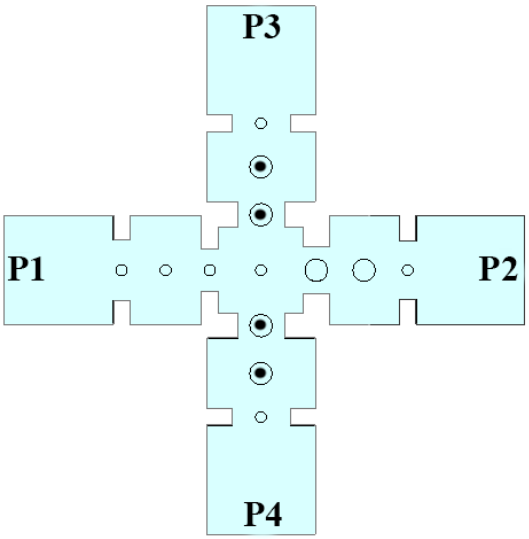

Figure 7.56: F&S device. The black circles in the MTPs of branches P3 and P4 indicate that they are in the detuned state.

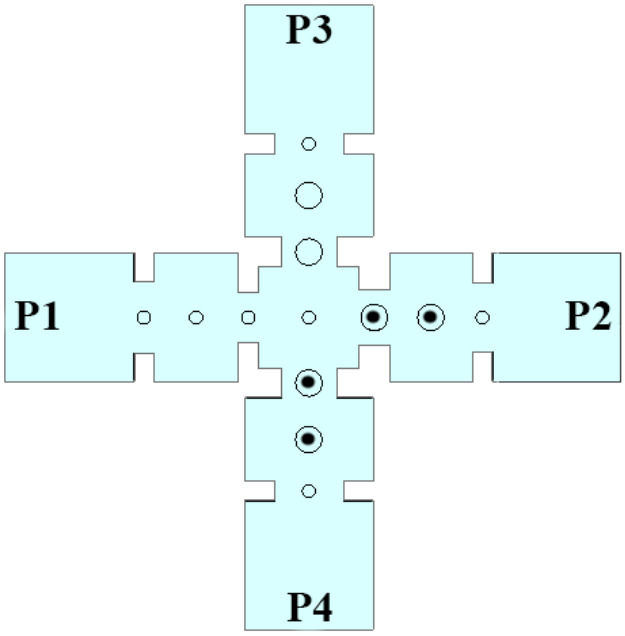

Figure 7.57: F&S device. The black circles in the MTPs of branches P2 and P4 indicate that they are in the detuned state.

4. Since the optimization of the parameters of P3 will affect the P1-P2 path, it is necessary to repeat steps 2 and 3 until an steady state is achieved. Two cycles of this iterative process are normally sufficient.

With this configuration, we obtain the simulated performance shown in Fig. 7.58. As we can see, the behavior from port 1 to port 2 is the same as a standard 3-pole filter. The power from port 1 to ports 3 and 4 undergoes more than 55 dB of attenuation. The power from port 3 to 4 (and vice versa) undergoes more than 115 dB of attenuation. Very similar results are obtained when the active path is chosen between P1 and P3 (see Fig. 7.58). Note that, if more attenuation is desired in any of the directions, additional MTPs could be used for each branch. Our simulations indicate that we can increase by approximately 20 dB the isolation for each extra MTP used. It is important to note that all cavities and the related apertures are tuned individually in order to obtain the desired performance. While one branch is being tuned, the other branches have their MTPs in the detuned position. The first and central cavity, on the other hand, are tuned only once.

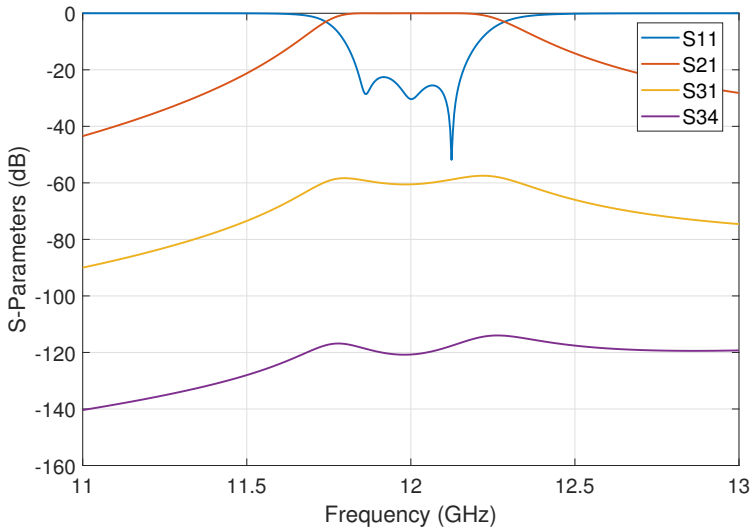

Figure 7.58: F&S response with the active path between P1 and P2. All MTPs in branches P3 and P4 are in the detuned state.

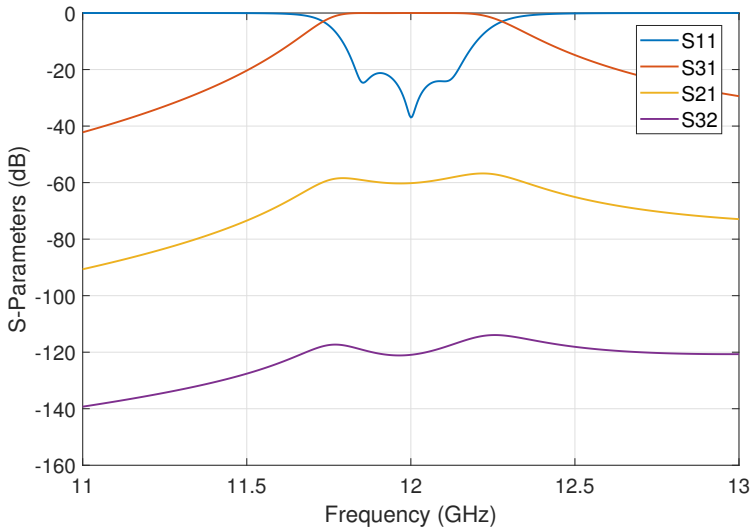

Figure 7.59: F&S response with the active path between P1 and P3. All MTPs in branches P2 and P4 are in the detuned state.

Up to this point, all simulations have been carried out considering sharp, 90 degree corners in all cavities. The last step in the design process is to consider the effect of rounded corners (as shown in Fig. 7.52) and the insertion losses due to the material. This last step is performed using the commercial simulator CST Microwave Studio (also with Dassault Systèmes) and the OS-ASM technique described in chapter 3.

It must be mentioned that, although the previous F&S example was based on a simple 3-pole filter, the same basic principle can also be used with higher order filters implementing filter-switch structures with a larger number of switching paths.

7.3.3 Experimental results

The assembled F&S device is shown in Fig. 7.60. The filters are centered at 12 GHz with 200 MHz of bandwidth. A standard TRL calibration with WR75 transitions and a vector network analyzer (VNA) E8363B from Keysight, have been used to perform the measurements. The tuning elements of branch P1 are regular tuners. The MTPs of branches P3 and P4 are set to the detuned state while the P2 MTPs are set to the tuned state. The measured results with this configuration are shown in Fig. 7.61. As expected, the filter is correctly tuned and the P1-P3 and P1-P4 paths are completely detuned. We obtain similar measured results for the P1-P3 active path, which are shown in Fig. 7.62 (the same results of the P1-P3 path are also measured for the P1-P4 case). As we can see, for all cases, there is a good agreement between the measured and simulated responses. Finally, the insertion losses obtained are 0.307 and 0.236 dB for the direct path (P1-P2) and the other two active paths (P1-P3 and P1-P4), respectively.

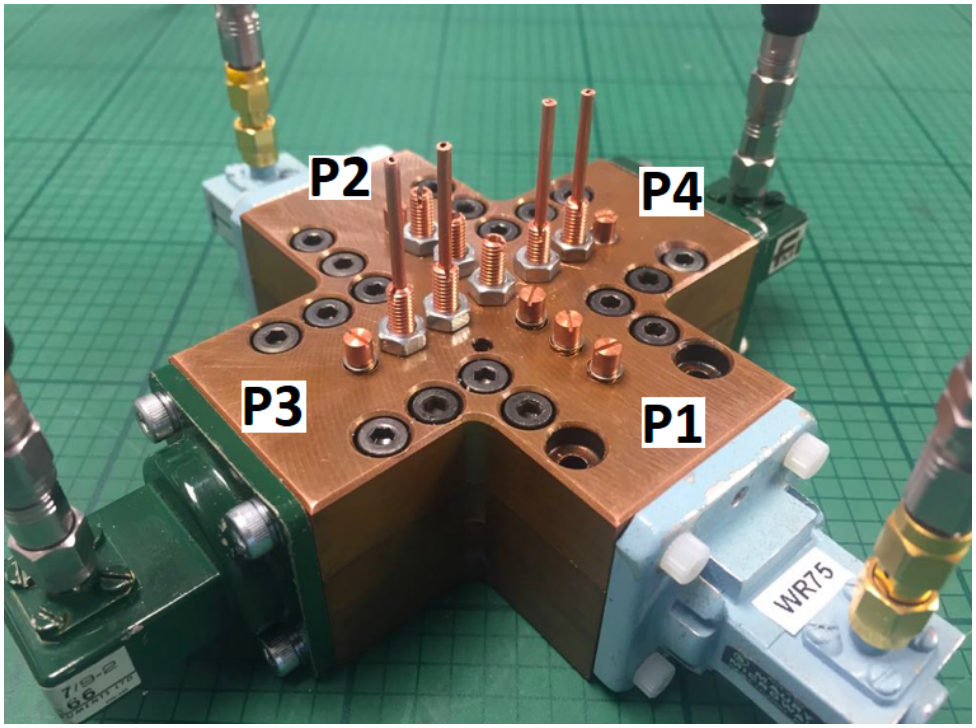

Figure 7.60: Assembled F&S with the active path between P1 and P2.

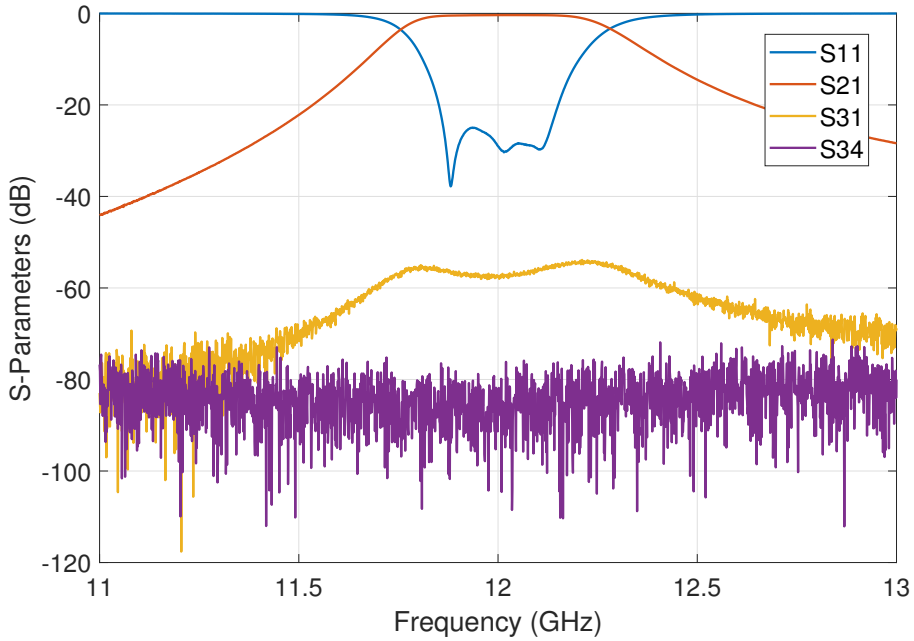

Figure 7.61: F&S response. Active path between P1 and P2. All MTPs in branches P3 and P4 are set to the detuned state.

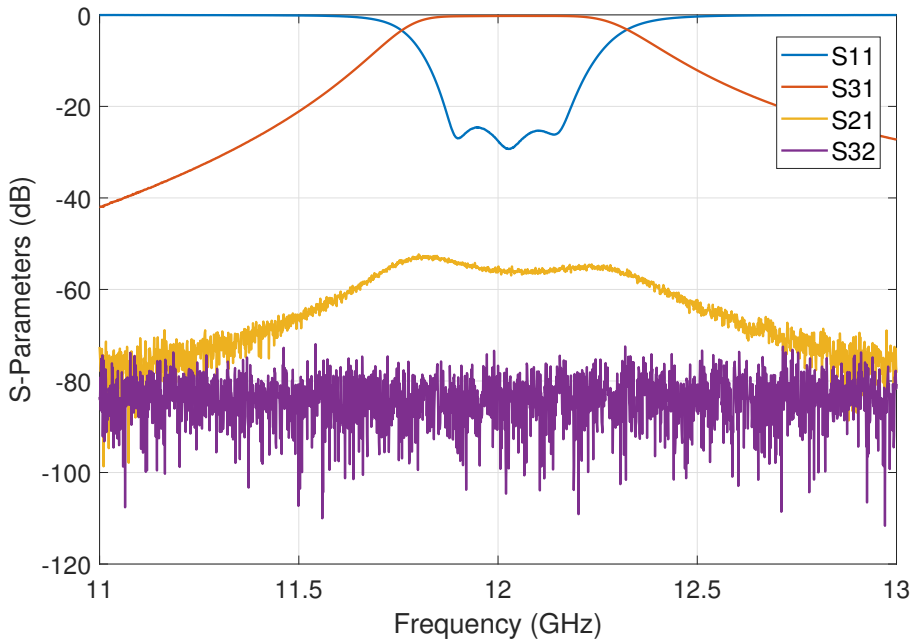

Figure 7.62: F&S response. Active path is between P1-P3. All MTPs in branches P2 and P4 are in the detuned state.

7.3.4 Remote control

One important feature of the MTP is that it allows for the remote operation of the F&S. The central pin of the MTP can, in fact, be easily lifted or lowered using a simple linear actuator. As a proof of concept, we have used low-cost linear actuators (VS-19 Pico linear servo, Fig. 7.63) to control the position of the pins. The pins are attached to the mobile shaft of the actuators (linear motors) with a soldered wire. The motors are placed vertically in a support structure that is attached to the filter (see Fig. 7.64).

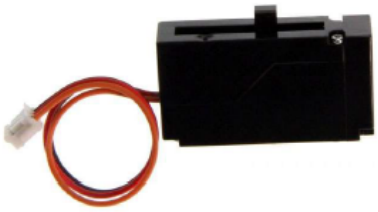

Figure 7.63: Linear actuator used to lift/lower the central pin of each MTP.

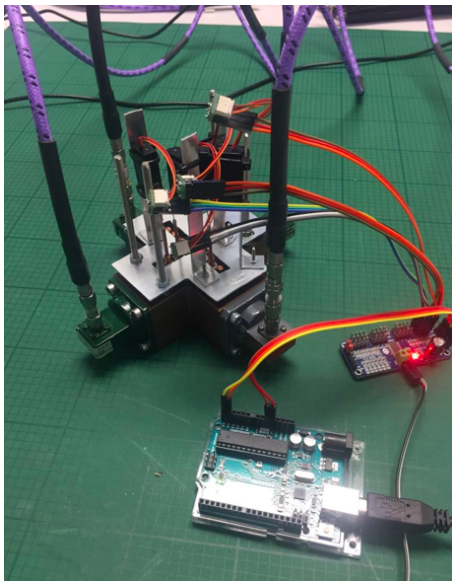

Figure 7.64: Assembled F&S. An Arduino board is used to control 6 servomotors.

The actuators are used to change the position of the metallic pins inside the MTPs between the two different states, namely, the detuned and tuned state. The actuators easily change the position of the pins from one state to the other in about 1-2 seconds. All the actuators can be controlled by a simple Arduino board. Since the actuators only move the central pin of each MTP, and not the threaded tuning part of the MTPs, the measured results using this setup are exactly the same as the ones shown in Fig. 7.61 and Fig. 7.62.

One important aspect is that the actuators do not need to position accurately the detuning pin, since their function is only to short circuit cavities or apertures. As previously described, when the device operates as a microwave filter, the detuning pins are removed from the inside of the filter structure and have no electromagnetic effect. This is indeed an important feature since, currently, microwave switches implemented in waveguide technology are based on high precision rotary components that need to be positioned very accurately. The result is that rotary waveguide switches are generally rather bulky and expensive.

A standard rotary switch in WR75 waveguide, for instance, may have a weight of approximately 500 g, a volume of approximately 325000 mm^3, consume about 250 mA at 28 Volts, and a cost of several thousand dollars. To perform the function of switch and filter, one would have to add the filter to the switch. With the solution that we propose, the weight of the F&S would be approximately 350 g, a volume of 165000 mm^3 (with 5 mm aluminum walls), plus 50 g and 21000 mm^3 for the actuators (including holders and the electronics). The power consumption would be approximately 150 mA at 3.7 Volts. It is therefore evident, that the proposed solution can result in mass and volume savings.

7.3.5 Conclusions

In this section, we have discussed a novel microwave passive component that can integrate the functions of filter and waveguide switch in a single component, the F&S. In addition, we also discuss a systematic design procedure that in a few simple steps leads to compliant hardware. In addition to theory, we also present measured results showing how simulations and measurements are in excellent agreement. Finally, the possibility of operating remotely the F&S using simple actuators and a basic micro-controller has also been demonstrated.

Chapter 8

Conclusions and future work

8.1 Conclusions

In this doctoral thesis, we have presented a number of advances in the area of microwave filters in rectangular waveguide technology, discussing new devices, design methodologies, and tunability features.

First, we have presented a novel design methodology based on the use of ASM, namely the OS-ASM. Our research indicates that, when two models are identical, the OS-ASM procedure can converge in just one step. As we have demonstrated with several examples, when both models are not identical but differ in small volumes, it is more efficient to use the identity mapping matrix than the classic update formula of ASM based on the Broyden update formula. This is a very interesting finding because it can very significantly reduce the time and cost required to obtain a filter design that can be actually manufactured.

Another advancement of the state-of-the-art that we have discussed is a modified cross-coupling iris, for classic circular waveguide dual-mode filters, that can effectively implement tunability properties. Using this iris, we have demonstrated that we can easily change the center frequency and channel bandwidth of the dual-mode filter.

However, we have also shown that the tunability is limited in frequency and that only near-by channels can be correctly tuned. For this reason, we have developed an alternative folded rectangular waveguide inductive filter with tuning screws that provides the same response with an extended tuning range.

The results clearly show that the folded rectangular waveguide implementation has a measured center frequency tuning performance ($\Delta BW_{rw} = \pm 763\%$) that is far superior to the one of the dual-mode circular waveguide implementation ($\Delta BW_{cw} = \pm 125\%$). Furthermore, the bandwidth tuning of the rectangular waveguide filter is also superior (92%) to the one of the circular waveguide dual-mode filter (42%).

One key finding of our research that has clearly emerged from the above results is that metallic tuning elements, although very effective in practice, can only be used for manual tuning and should not be used to implement remote tuning or reconfiguration of the devices.

For this reason we have explored, both theoretically and experimentally, the use of dielectric (Teflon and Sapphire) tuning rods. The results obtained show that, although the tuning range achieved (with Teflon) is smaller than the one achieved with metallic tuning elements, the tuning range can be equally significant. Moreover, our studies demonstrated that using Sapphire rods we can easily achieve the same tuning range as for metallic screws.

Besides, the dielectric tuning elements do not introduce significantly PIM products, and do not require good electric contact with the body of the filter in order to provide the desired EM response.

Finally, the dielectric tuning elements need to penetrate more inside the filter structure in order to provide the same performance obtained with metallic tuning elements. This is indeed a key finding, because it significantly reduces the position accuracy required to achieve the correct remote tuning response. The practical feasibility of this concept has also been demonstrated experimentally with an inductive rectangular waveguide filter using dielectric tuning elements driven by simple actuators.

An additional contribution in the area of filter tuning has also been provided demonstrating the feasibility of a computer controlled tuning system (robotuner). The results of our research show that, using Robotuner, it is, in fact, possible to perform economically the automatic tuning of a very large number of identical filters.

Finally, our research has also produced a number of practical, novel filtering waveguide devices specifically designed for advanced telecommunications satellites, namely:

- A waveguide quadruplet filter. A single-mode rectangular waveguide structure without tuning elements, that can generate two symmetric transmission zeros using the cross-coupling concept.
- A waveguide quadruplet diplexer. A diplexer structure based on the use of an E-plane T-junction, together with two rectangular waveguide filters based on the use of the previous waveguide quadruplets filters. The structure is simple and very easy to manufacture.

- A waveguide filter-switch (F&S). A novel passive microwave device that integrates the functions of filter and waveguide switch in a single component, and that can be easily operated remotely using simple actuators.

In conclusion, several investigations, devices and techniques have been presented in this document, that extends the state-of-the-art of the waveguide filter and contribute in the advance of the tunability remote configuration area. We are confident that the solutions presented are implementable in the actual communication satellite systems, and can be very helpful for the development of the next generation of advance communication satellites.

8.2 Future work

The results of this thesis can be used as the initial step for future investigations, or can be extended for their application to other multiple kind of waveguide filters. In the next paragraph we outline some of the possible future works that can be achieved the development of the results presented, that will also help to the progress of the satellites communication ecosystem:

- Reconfigurable devices. As demonstrated in chapter 4, some of the current filter structure devices can be modified in order to expand its tunability range. This idea can be extended to several different kind of classic waveguide filters (with irises, stubs, corrugated topologies or geometries...), and modify their structures to allow tunability through the use of tuning screws. Moreover, this concept can be applicable to other passive devices such as circulators, couplers, hybrids, to mention a few, and try to make them tunable modifying a key part of their classical configurations.
- New dielectrics for tunability. In the thesis we have focused on the use of Teflon and Sapphire as possible dielectric tuning rods materials. However, there exists a number of other potential dielectric materials that can be used for this function. A complete research about the use of ceramics or quartz in waveguide filters, are two examples of useful studies about alternatives to the materials presented in this thesis.
- A remotely tunable diplexer. The combination of tunable dielectrics rods and new tunable expanded filtering structures can contribute in the development of a new class of remotely tunable diplexers to be used in the transponders of future communications satellites. In this direction, for example, the diplexer presented in chapter 7, can be extended including tunable dielectric rods into its structure and lineal motors.

- Industrial grade robotuner. As initially demonstrated in chapter 6, a robotic arm in combination with advanced design techniques can be used for the automatic tunability of a large number of waveguide filters. The preliminary results demonstrated that the full automation of the process can be completed with the inclusion of a tool to control the Z-axis and a visual system (based on a camera or laser), in order to place the screwdriver correctly in the head of the different screws of the filter to be tuned.
- Advanced filtering and switching networks. The filter & switch concept in chapter 7 can be easily extended to create more complex filtering structures. Using the classic manifold configuration we will be able to combine different filter responses in the same component. Additionally, these filters can present a wider tuning range using dielectric materials (as proposed in chapter 5). Its potential combination with MTPs (Modified Tuning Pins of chapter 7), that would provide the requested short-circuits to isolate different paths, could be also studied.

To conclude, all the work presented in the doctoral thesis as well as the future work discussed in this chapter, can be completely integrated to create a new family of tunable filtering devices for satellite communications. The work and the lines proposed will provide the concepts for the design process, the tools for the extension of the tunability range, the techniques for the automatic measurement and tunability of the fabricated devices, and a simple way for the remote reconfiguration of the device after the integration in the transponder satellite.

Appendix A

Robotuner flow-chart and M-code

The automatic tuning algorithm executed by robotuner, and described in chapter 6, is based on the flow chart detailed next.

This algorithm also makes use of a standard Vector Network Analyzer (VNA), in order to get the required measurements, and of the specific control software of robotuner (as mentioned in chapter 6). In addition to the flow chart, its implementation in Matlab code (programmed and executed in a personal computer) is also detailed in this appendix.

Next, together with the corresponding Matlab codes, short descriptions of the main functions of the program developed are included.

A.1 Flow-chart

The flow-chart of the robotuner algorithm is presented in Fig. A.1.

A.2 Get Connection to VNA

This function (see Fig. A.2) has as an input a character with the IP of the VNA. The port is specified at the VNA as the port to send and receive Virtual Instrument Standard Architecture (VISA) commands. Then we need to create the VISA object and initialize the connection. The buffer span and timeout are defaults values for this kind of connection.

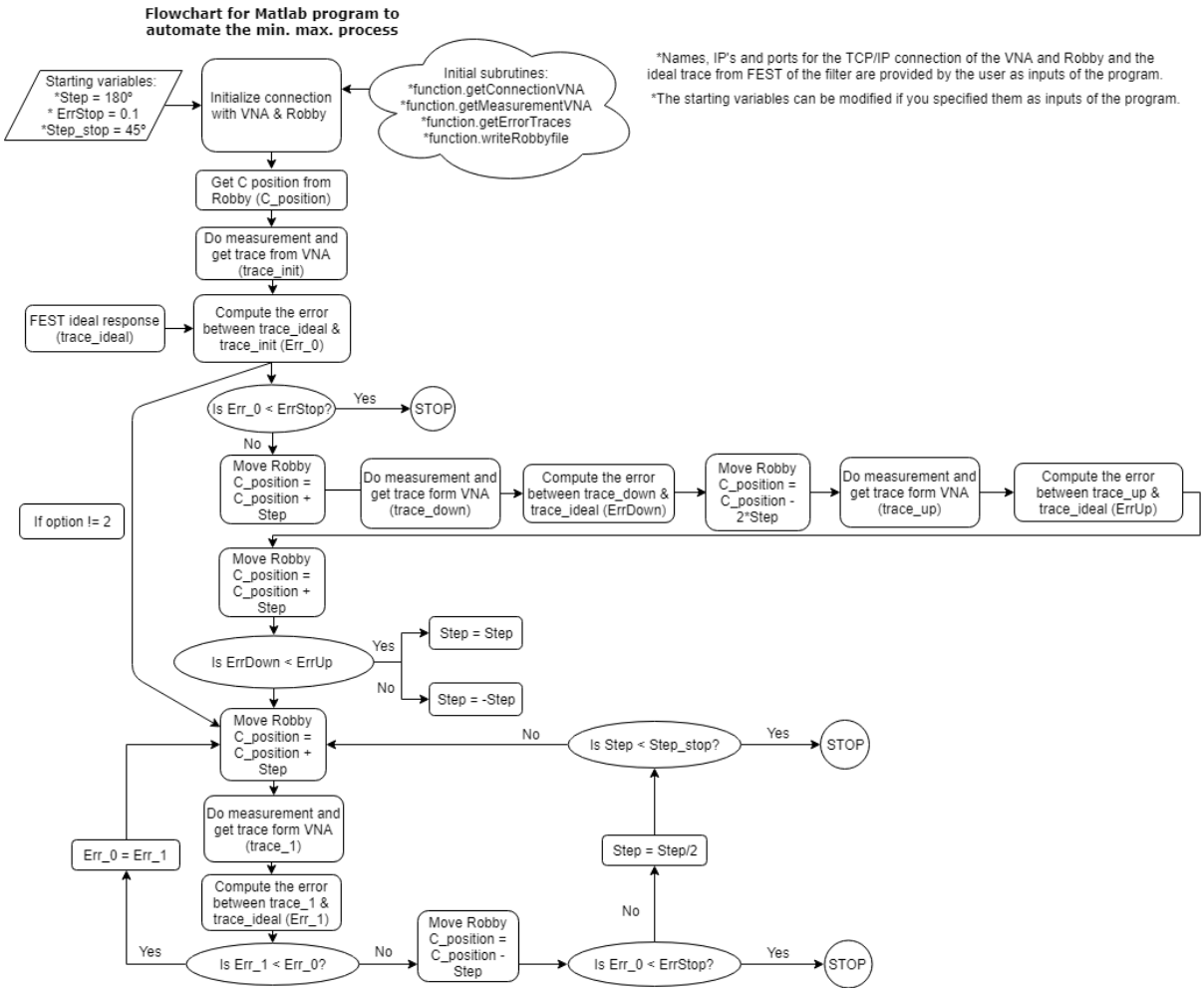

Figure A.1: Matlab code flow-chart for automatic tuning with robotuner.

```
function [vna] = getConnectionVNA(ip)
% This module set the connection between the computer and the VNA.

port_vna = 5025; % Default VNA TCP port connection.

% Inicialize the object TCP connection for VNA.
vna = tcpip(ip,port_vna);

% Configure interface VNA connection.
set(vna, 'InputBufferSize', 20000);
set(vna, 'Timeout', 300);


end
```

Figure A.2: Get connection M-code.

A.3 Write Robby File

This function (see Fig. A.3) has as input the name of the file to write the values of movement of the screw for the robotuner control software. These values are defined in turning degrees. The optional input from the main program specifies if it is a new screw, in order to set the initial position of robotuner.

```
function [] = writeRobbyfile(file,A,opt)

fid = fopen(file, 'w');

if(opt == 0)
    fprintf(fid,'home x\r\n');
    fprintf(fid,'home y\r\n');
    fprintf(fid,'home c\r\n');
end

fprintf(fid,'g0 c%d\r\n', A);

fclose(fid);
```

Figure A.3: Write Robby file M-code.

A.4 Get Error Traces

This function (see Fig. A.4) calculates the error between the ideal response and the measured response as defined in chapter 6. Finally, the program returns the total error value in order to be used by the proposed algorithm.

A.5 Get Measurements from VNA

This function (see Fig. A.5) obtains the VNA measurement of the filter. Later, the program stores the captured data as two different vectors with the information of the S_{11} and S_{21} parameters in dB.

```
function [err_s11,err_s12] =
getErrorTraces(dblimit,freq,min_s11_freq,max_s11_freq,min_s12_freq,max_s12_freq,trace
_real_s11,trace_real_s12)

format long;

pos_s11_min=find(freq==min_s11_freq);
pos_s11_max=find(freq==max_s11_freq);
pos_s12_min=find(freq==min_s12_freq);
pos_s12_max=find(freq==max_s12_freq);

i = pos_s11_min;
total = 0;

while(i<=pos_s11_max)
    if(trace_real_s11(i)<=dblimit)
        trace_real_s11(i)=0;
    else
        trace_real_s11(i)=trace_real_s11(i)-dblimit;
    end
    total = total + trace_real_s11(i);
    i = i + 1;
end

if(trace_real_s12(pos_s12_min)<=-30)
    trace_real_s12(pos_s12_min)=0;
else
    trace_real_s12(pos_s12_min)=trace_real_s12(pos_s12_min)+30;
end

if(trace_real_s12(pos_s12_max)<=-30)
    trace_real_s12(pos_s12_max)=0;
else
    trace_real_s12(pos_s12_max)=trace_real_s12(pos_s12_max)+30;
end

err_s11 = total/i;
err_s12 = sum(abs(trace_real_s12(pos_s12_min))+abs(trace_real_s12(pos_s12_max)))/2;

end
```

Figure A.4: Get error traces M-code.

A.6 Start Program

The initial part of the main program (see Fig. A.6) receives as inputs the ideal response of the filter that we want to tune, the filename to write the rotation values for the robotuner, and an option to specify if we want to move the tuner a certain direction or let the program to find out the best direction.

As we can see, the program starts defining all the parameter needed for the device to be tuned. The first part corresponds to the ideal filter specifications that we are working on, and to the movement restrictions for the screws (if there are any). The second part defines several variables related to the behavior of the robotuner, like for instance the initial turning value.

```
function [freq,S11,S12] = getMeasurementVNA(vna)
% This module gets the last measurement (.S2P) in the VNA and transform
% the data in three vectors with the frequency (GHz), the module of S11 (dB)
% and the module of S12 (dB). This module assumes the VNA is configured
% with the correct number of points and the start/stop frequency.

% Connect to VNA.
fopen(vna);

% Select the measurement.
fprintf(vna,'CALC:PAR:SEL "CH1_S11_1"');
localWaitForSystemReady(vna);

% Query selected measurement name.
meas = query(vna,'CALC:PAR:SEL?','%s\n','%s');
localWaitForSystemReady(vna);

% Set byte order to swapped (little-endian) format.
fprintf(vna,'FORM:BORD NORM');
localWaitForSystemReady(vna);

% Set data type to real 64 bit binary block.
fprintf(vna,'FORM REAL,64');
localWaitForSystemReady(vna);

% Read S2P data back from PNA. A S2P file will return number of points * 9
% data points back.
fprintf(vna,'CALC:DATA:SNP? 2');
localWaitForSystemReady(vna);
[data,count,msg] = binblockread(vna,'double');

% Disconnect VNA connection.
fclose(vna);

% Reshape data so it is split into columns.
data_r = reshape(data,[(length(data)/9),9]);
data_r = data_r';

% Read frequency data back from returned data.
freq = data_r(1,:);

% This assumes that the return format is in log mag, angle pairs in the
% .S2P file.

S11 = data_r(2,:);
S12 = data_r(6,:);

end
```

Figure A.5: Get Measurements M-code.

The next step is to obtain the initial filter measurements with the help of a VNA (according to the M-code of Fig. A.7).

Then, the program calculates the initial error (see Fig. A.8) and shows the responses on screen. Next, the program start the tuner movement (see Fig. A.9 and Fig. A.10). As indicated before, if there is not predefined direction, the program tries to find out the best one, first performing a measurement after applying the step to one direction and then to the opposite one.

After finding the best direction, the loop is executed multiples times uninterruptedly, until any of the stop conditions is satisfied. As we can see, this is performed in the last part of the M-code shown in Fig. A.11.

Finally, note that for each different set of filter specifications, we need to modify the corresponding values in the program.

```
function [] = StartMinMaxRobby(fest_i_trace,robby_file,updown)
%updown = 0 move screw down, = 1 move screw up, = 2 find the direction.
% Starting variables for a concrete filter:
dblimit = -25;
pos_s11_min = 17.572; % Min. freq. s11
pos_s11_max = 17.608; % Max. freq. s11
pos_s12_min = 17.55; % Min. freq. s12
pos_s12_max = 17.63; % Max. freq. s12

% Starting condition variables.
step = 180;
step_stop = 15;
err_stop = 0.01;
err_s11_1 = 10e8;
C_position_ini = 0;
ip='192.168.1.2'; % IP of the VNA.
```

Figure A.6: M-code of the initial part of the main program.

```
% Get initial measurement data from VNA.
vna = getConnectionVNA(ip);
[freq,real_s11,real_s12] = getMeasurementVNA(vna);

% Get  and display the ideal trace from FEST3D .out and
% get the error with the real trace.
data_import = importdata(fest_i_trace,' ',3);
ideal_data=data_import.data;
ideal_s11 = ideal_data(:,2);
ideal_s12 = ideal_data(:,5);
title='Ideal';
displayMeasurement(freq,ideal_s11,ideal_s12,title);
title='Real';
displayMeasurement(freq,real_s11,real_s12,title);
[err_s11,err_s12] =
getErrorTraces(dblimit,freq,pos_s11_min,pos_s11_max,pos_s12_min,pos_s12_max,real_s11,real_s12);
errors1=['Err_s11 = ',num2str(err_s11)];
errors2=['Err_s12 = ',num2str(err_s12)];
disp(errors1);
disp(errors2);
writeRobbyfile(robby_file,C_position_ini,0);
```

Figure A.7: M-code for obtaining the filters measurements from VNA.

```
if(updown==2)
    if (err_s11 <= err_stop)
        disp('Error Stop reached!\n');
    return
    else
        C_position = C_position_ini + step;
    end

    % Move Robby one step down.
    writeRobbyfile(robby_file,C_position,0);
    disp('Press ENTER when Robby stops to continue!')
    pause;

    % Get and display the down movement screw measurement
    [freq,s11_down,s12_down] = getMeasurementVNA(vna);
    title='Screw down';
    displayMeasurement(freq,s11_down,s12_down,title);
    [err_s11_down,err_s12_down] =
getErrorTraces(dblimit,freq,pos_s11_min,pos_s11_max,pos_s12_min,pos_s12_max,s11_down
,s12_down);
    errors1=['Err_s11_down = ',num2str(err_s11_down)];
    errors2=['Err_s12_down = ',num2str(err_s12_down)];
    disp(errors1);
    disp(errors2);

    % Move Robby file one step up from original position.
    C_position = C_position - 2*step;
    writeRobbyfile(robby_file,C_position,1);
    disp('Press ENTER when FEST stops to continue!')
    pause;

    % Get and display the up movement screw measurement
    [freq,s11_up,s12_up] = getMeasurementVNA(vna);
    title='Screw up';
    displayMeasurement(freq,s11_up,s12_up,title);
    [err_s11_up,err_s12_up] =
getErrorTraces(dblimit,freq,pos_s11_min,pos_s11_max,pos_s12_min,pos_s12_max,s11_up,s
12_up);
    errors1=['Err_s11_up = ',num2str(err_s11_up)];
    errors2=['Err_s12_up = ',num2str(err_s12_up)];
    disp(errors1);
    disp(errors2);
```

Figure A.8: M-code for processing data from measurements.

```
    % Move FEST to original position
    C_position = C_position_ini;
    writeRobbyfile(robby_file,C_position,1);

    % Set the correct step direction
    if (err_s11_down > err_s11_up)
        step = -step;
        step_stop = -step_stop;
        disp('Moving up');
    else
        disp('Moving down');
    end
else
    if(updown==1)
        step = -step;
        step_stop = -step_stop;
        disp('Moving up');
    else
        disp('Moving down');
    end
end
```

Figure A.9: M-code for setting up the movement of the robotuner.

```
% Starts min. max. loop
i=1;
C_position = C_position_ini;

while(err_s11_1 > err_stop)
    % Move Robby
    C_position = C_position + step;
    writeRobbyfile(robby_file,C_position,1);
    disp('Press ENTER when FEST stops to continue!')
    pause;

    % Get and display the new measurement
    [freq,s11_1,s12_1] = getMeasurementVNA(vna);
    title=['Loop ',num2str(i)];
    displayMeasurement(freq,s11_1,s12_1,title);

    % Get the new error
    [err_s11_1,err_s12_1] =
getErrorTraces(dblimit,freq,pos_s11_min,pos_s11_max,pos_s12_min,pos_s12_max,s11_1,
s12_1);
    errors1=['Err_s11_1 = ',num2str(err_s11_1)];
    errors2=['Err_s12_1 = ',num2str(err_s12_1)];
    disp(errors1);
    disp(errors2);

    % Compare errors
    if (err_s11_1 <= err_s11 && (err_s12_1-err_s12) <= 10)
        err_s11 = err_s11_1;
        err_s12 = err_s12_1;
    else
        % Move Robby to the previous step
        C_position = C_position - step;
        step=step/2;
        writeRobbyfile(robby_file,C_position,1);
        disp('Step reduced /2');
        disp('Back to the previous position');
        disp('Press ENTER when Robby stops to continue!')
        pause;
    end
```

Figure A.10: M-code for starting the optimization (min. max.) loop.

```
% Compare with error stop condition
    if (err_s11_1 <= err_stop)
        [freq,s11_min,s12_min] =
getMeasurementVNA(vna);
        title='Min. error simulation';

displayMeasurement(freq,s11_min,s12_min,title);
        disp('Error Stop reached!\n');
        disp('Program finished!\n');
        return
    end

    % Compare with step stop condition
    if (step <= step_stop && step_stop > 0)
        [freq,s11_min,s12_min] =
getMeasurementVNA(vna);
        title='Min. error simulation';

displayMeasurement(freq,s11_min,s12_min,title);
        disp('Step Stop reached!\n');
        disp('Program finished!\n');
        return
    end

    if (step >= step_stop && step_stop < 0)
        [freq,s11_min,s12_min] =
getMeasurementVNA(vna);
        title='Min. error simulation';

displayMeasurement(freq,s11_min,s12_min,title);
        disp('Step Stop reached!\n');
        disp('Program finished!\n');
        return
    end
```

Figure A.11: M-code for performing the optimization loop until one stop condition is reached.

Appendix B

Publications list

The main and novel results of this doctoral thesis have resulted into a total number of 8 scientific publications, which are distributed as 4 journal papers and 4 contributions to international conferences, as follows.

- B.1 Journal publications
  - J. Ossorio, J. Vague, V. E. Boria, and M. Guglielmi, "Exploring the tuning range of channel filters for satellite applications using electromagnetic-based computer aided design tools," *IEEE Transactions on Microwave Theory and Techniques,* vol. 66, no. 2, pp. 717-725, Feb. 2018.
  - J. Ossorio, J. C. Melgarejo, V. E. Boria, M. Guglielmi, and J. W. Bandler, "On the alignment of low-fidelity and high-fidelity simulation spaces for the design of microwave waveguide filters," *IEEE Transactions on Microwave Theory and Techniques,* vol. 66, no. 12, pp. 5183-5196, Dec. 2018.
  - J. Ossorio, J. C. Melgarejo, S. Cogollos, V. E. Boria and M. Guglielmi, "Waveguide Quadruplet Diplexer for Multi-Beam Satellite Applications," *in IEEE Access,* vol. 8, pp. 110116-110128, June 2020.
  - J. Ossorio, J. C. Melgarejo, V. E. Boria and M. Guglielmi, "On the Integration of Microwave Filters and Waveguide Switches," *in IEEE Microwave and Wireless Components Letters,* Dec. 2020.

- B.2 Conference publications
  - J. Ossorio, J. Vague, V. E. Boria, and M. Guglielmi, "Exploring the tunability range of classic circular waveguide dual mode filters using EM-based CAD," *in IEEE MTT-S International Conference on Numerical Electromagnetic and Multi-physics Modeling and Optimization for RF, Microwave, and Terahertz Applications,* pp. 332-334, May 2017.
  - J. Ossorio, J. Vague, V. E. Boria, and M. Guglielmi, "Eficient implementation of the aggressive space mapping technique for microwave filter design," *in 47th European Microwave Conference,*, pp. 644-647, Oct. 2017.
  - J. Ossorio, V. E. Boria, and M. Guglielmi, "Dielectric tuning screws for microwave filters applications," *in IEEE MTT-S International Microwave Symposium,* pp. 1253-1256, June 2018.
  - J. Ossorio, S. Cogollos, V. Boria, and M. Guglielmi, "Rectangular waveguide quadruplet filter for satellite applications," *in IEEE MTT-S International Microwave Symposium,* pp. 1359-1362, June 2019.

Bibliography

[1] European Space Agency (ESA), *Strategic Research Agenda*. European Space Technology Platform, July 2011.

[2] International Telecommunicacion Union (ITU), *Recommendation ITU-R P.676-12, Attenuation by atmospheric gases and related effects*. International Telecommunicacion Union, Aug. 2019.

[3] M. Yu, "Latest development of filter technology for space applications: Passive hardware for space applications," in *European Microwave Week Workshop*, Oct. 2011.

[4] European Space Agency (ESA), "Corona and passive intermodulation in space RF hardware," in *9th International Workshop on Multipactor, Corona and Passive Intermodulation*, Apr. 2017.

[5] G. Maral, M. Bousquet, and Z. Sun, *Satellite Communications Systems: Systems, Techniques and Technology*. Wiley, Aug. 2011.

[6] H. Fenech, S. Amos, A. Tomatis, and V. Soumpholphakdy, "High throughput satellite systems: an analytical approach," *IEEE Transactions on Aerospace and Electronic Systems*, vol. 51, no. 1, pp. 192–202, Jan. 2015.

[7] M. Dishal, "Alignment and adjustment of synchronously tuned multiple-resonant-circuit filters," *Proceedings of the IRE*, vol. 39, no. 11, pp. 1448–1455, Nov. 1951.

[8] G. Matthaei, L. Young, and E. Jones, *Microwave Filters, Impedance-matching Networks, and Coupling Structures*. Artech House Books, June 1980.

[9] M. Yu, "Power-handling capability for RF filters," *IEEE Microwave Magazine*, vol. 8, no. 5, pp. 88–97, Oct. 2007.

[10] J. W. Bandler, R. M. Biernacki, S. H. Chen, P. A. Grobelny, and R. H. Hemmers, "Space mapping technique for electromagnetic optimization," *IEEE Transactions on Microwave Theory and Techniques*, vol. 42, no. 12, pp. 2536–2544, Dec. 1994.

[11] J. W. Bandler, R. M. Biernacki, S. H. Chen, R. H. Hemmers, and K. Madsen, "Aggressive space mapping for electromagnetic design," in *IEEE MTT-S International Microwave Symposium Digest*, vol. 3, May 1995, pp. 1455–1458.

[12] J. W. Bandler, R. M. Biernacki, S. H. Chen, R. H. Hemmers, and K. Madsen, "Electromagnetic optimization exploiting aggressive space mapping," *IEEE Transactions on Microwave Theory and Techniques*, vol. 43, no. 12, pp. 2874–2882, Dec. 1995.

[13] S. Tirro, "Satelite communication systems - state of the art and develpment trends," in *7th European Microwave Conference*, Sept. 1977, pp. 275–280.

[14] D. Roddy, *Satellite Communications*. McGraw-Hill, March 2001.

[15] C. Kudsia, T. Stajcer, and M. Yu, "Evolution of microwave technologies for communications satellite systems," in *34th AIAA International Communications Satellite Systems Conference*, Oct. 2016.

[16] R. K. Gupta, "Communications satellite RF payload technologies evolution: A system perspective," in *Asia-Pacific Microwave Conference*, Dec. 2016, pp. 1–4.

[17] F. Connor, *Wave Transmission*. Edward Arnold Publishers, Feb. 1972.

[18] S. Choocadee and S. Akatimagool, "Design and implementation of band pass filters in waveguide using simulation tools," in *8th Electrical Engineering/ Electronics, Computer, Telecommunications and Information Technology Association of Thailand*, July 2011, pp. 248–251.

[19] B. Pratsiuk, Y. Prokopenko, and Y. Poplavko, "Tunable filters based on metal-dielectric resonators," in *18th International Conference on Microwaves, Radar and Wireless Communications*, June 2010, pp. 1–3.

[20] F. Huang and R. R. Mansour, "Tunable compact dielectric resonator filters," in *39th European Microwave Conference*, Oct. 2009, pp. 559–562.

[21] F. Teberio, I. Arnedo, J. M. Percaz, I. Arregui, T. Lopetegi, and M. A. G. Laso, "Accurate design of corrugated waveguide low-pass filters using exclusively closed-form expressions," in *47th European Microwave Conference*, Oct. 2017, pp. 632–635.

[22] F. Teberio, I. Arnedo, J. M. Percaz, I. Arregui, P. Martin-Iglesias, T. Lopetegi, and M. A. G. Laso, "Accurate design procedure for waffle-iron low-pass filter," in *IEEE MTT-S International Microwave Symposium*, June 2018, pp. 1238–1241.

[23] L. Chen, Q. Wang, and C. Wu, "A compact filter with resonating-irises and shorting stubs," in *China-Japan Joint Microwave Conference*, Apr. 2011, pp. 1–3.

[24] A. E. Williams and A. E. Atia, "Dual-mode canonical waveguide filters," *IEEE Transactions on Microwave Theory and Techniques*, vol. 25, no. 12, pp. 1021–1026, Dec. 1977.

[25] A. E. Williams, "A four-cavity elliptic waveguide filter," in *IEEE MTT-S International Microwave Symposium*, May 1970, pp. 90–93.

[26] A. E. Atia and A. E. Williams, "Narrow-bandpass waveguide filters," *IEEE Transactions on Microwave Theory and Techniques*, vol. 20, no. 4, pp. 258–265, Apr. 1972.

[27] C. Arnold, J. Parlebas, and T. Zwick, "Center frequency and bandwidth tunable waveguide bandpass filter with transmission zeros," in *45th European Microwave Conference*, Sept. 2015, pp. 1220–1223.

[28] L. Accattino, G. Macchiarella, and G. Bertin, "Modelling techniques for dual-mode reconfigurable filters used in satellite applications," in *IEEE MTT-S International Conference on Numerical Electromagnetic and Multiphysics Modeling and Optimization*, July 2016, pp. 1–2.

[29] J. Uher and W. J. R. Hoefer, "Tunable microwave and millimeter-wave band-pass filters," *IEEE Transactions on Microwave Theory and Techniques*, vol. 39, no. 4, pp. 643–653, Apr. 1991.

[30] B. Yassini, M. Yu, and B. Keats, "A Ka-band fully tunable cavity filter," *IEEE Transactions on Microwave Theory and Techniques*, vol. 60, no. 12, pp. 4002–4012, Nov. 2012.

[31] U. Rosenberg, R. Beyer, P. Kraus, T. Sieverding, A. Papanastasiou, M. Pueyo-Tolosa, P. M. Iglesias, and C. Ernst, "Reconfigurable doublet dual-mode cavity filter designs providing remote controlled center frequency and bandwidth re-allocation," in *46th European Microwave Conference*, Oct. 2016, pp. 532–535.

[32] C. Arnold, J. Parlebas, T. Zwick, and M. Schneider, "In-orbit reconfigurable waveguide filter," in *46th European Microwave Conference*, Oct. 2016, pp. 540–543.

[33] J. Ruiz-Cruz, C. Wang, and K. Zaki, "Advances in microwave filter design techniques," *Microwave Journal*, vol. 51, pp. 26–44, Nov. 2008.

[34] Q. Zhang, "Advances in modeling and optimization techniques for microwave design," in *IEEE MTT-S International Microwave Workshop Series on Millimeter Wave Wireless Technology and Applications*, Oct. 2012.

[35] P. Jarry, *Advanced Design Techniques and Realizations of Microwave and RF Filters*. Wiley-IEEE Press, Feb. 2008.

[36] V. E. Boria, P. Soto, and S. Cogollos, "Distributed models for filter synthesis," *IEEE Microwave Magazine*, vol. 12, no. 6, pp. 87–100, Oct. 2011.

[37] D. Baillargeat, S. Verdeyme, and P. Guillon, "Elliptic filter rigorous design and modelling applying the finite element method," in *IEEE MTT-S International Microwave Symposium Digest*, vol. 3, May 1995, pp. 1195–1198.

[38] M. Guglielmi, "Simple CAD procedure for microwave filters and multiplexers," *IEEE Transactions on Microwave Theory and Techniques*, vol. 42, no. 7, pp. 1347–1352, July 1994.

[39] J. A. Ruiz-Cruz, Y. Zhang, J. M. Rebollar, K. A. Zaki, J. R. Montejo-Garai, and A. J. Piloto, "TEM mode-matching analysis of multi-coupled strip-line filters," in *IEEE MTT-S International Microwave Symposium*, June 2007, pp. 541–544.

[40] T. Weiland, "A discretization method for the solution of Maxwell's equations for six-component fields," *Electronics and Communications*, vol. 31, no. 3, pp. 116–120, Sept. 1977.

[41] S. Bastioli and R. V. Snyder, "Design, modelling, and manufacturing of extremely selective waveguide filters using a multi-port optimization technique," in *IEEE MTT-S International Conference on Numerical Electromagnetic and Multiphysics Modeling and Optimization for RF, Microwave, and Terahertz Applications*, May 2017, pp. 338–340.

[42] J. Byun and I. Park, "Design of dielectric waveguide filters using topology optimization technique," *IEEE Transactions on Magnetics*, vol. 43, no. 4, pp. 1573–1576, Apr. 2007.

[43] C. G. Broyden, "A class of methods for solving nonlinear simultaneous equations," *Mathematics of Computation*, vol. 19, no. 92, pp. 577–593, Oct. 1965.

[44] J. W. Bandler, Q. S. Cheng, S. A. Dakroury, A. S. Mohamed, M. H. Bakr, K. Madsen, and J. Sondergaard, "Space mapping: the state of the art," *IEEE Transactions on Microwave Theory and Techniques*, vol. 52, no. 1, pp. 337–361, Jan. 2004.

[45] J. E. Rayas-Sanchez, "Power in simplicity with ASM: Tracing the aggressive space mapping algorithm over two decades of development and engineering applications," *IEEE Microwave Magazine*, vol. 17, no. 4, pp. 64–76, Apr. 2016.

[46] J. W. Bandler, R. M. Biernacki, S. H. Chen, and D. Omeragic, "Space mapping optimization of waveguide filters using finite element and mode-matching electromagnetic simulators," in *IEEE MTT-S International Microwave Symposium Digest*, vol. 2, June 1997, pp. 635–638.

[47] M. A. Ismail, D. Smith, A. Panariello, Y. Wang, and M. Yu, "EM based design of large-scale dielectric resonator multiplexers by space mapping," in *IEEE MTT-S International Microwave Symposium Digest*, vol. 1, June 2003, pp. 291–294.

[48] R. Lehmensiek and P. Meyer, "An efficient adaptive frequency sampling algorithm for model-based parameter estimation as applied to aggressive space mapping," *Microwave and Optical Technology Letters*, vol. 24, no. 1, pp. 71–78, Jan. 2000.

[49] M. A. Ismail, K. G. Engel, and M. Yu, "Multiple space mapping for RF T-switch design," in *IEEE MTT-S International Microwave Symposium Digest*, vol. 3, June 2004, pp. 1569–1572.

[50] J. V. Morro, P. Soto, H. Esteban, V. E. Boria, C. Bachiller, M. Taronger, S. Cogollos, and B. Gimeno, "Fast automated design of waveguide filters using aggressive space mapping with a new segmentation strategy and a hybrid optimization algorithm," *IEEE Transactions on Microwave Theory and Techniques*, vol. 53, no. 4, pp. 1130–1142, Apr. 2005.

[51] E. Diaz Caballero, J. V. Morro, A. Belenguer, H. Esteban, and V. E. Boria, "CAD technique for designing H-plane waveguide filters considering rounded corners," in *IEEE MTT-S International Microwave Symposium*, June 2013, pp. 1–3.

[52] M. Brumos, V. E. Boria, M. Guglielmi, and S. Cogollos, "Correction of manufacturing deviations in circular-waveguide dual-mode filters using aggressive space mapping," in *44th European Microwave Conference*, Oct. 2014, pp. 624–627.

[53] G. Crevecoeur, L. Dupre, L. Vandenbossche, and R. Van de Walle, "Reconstruction of local magnetic properties of steel sheets by needle probe methods using space mapping techniques," *Journal of Applied Physics*, vol. 99, no. 8, pp. 08H905 1–3, Apr. 2006.

[54] J. Wu, Y. Dong, J. He, and J. Deng, "An ameliorated aggressive space mapping based on responses error," in *International Workshop on Microwave and Millimeter Wave Circuits and System Technology*, Apr. 2012, pp. 1–4.

[55] J. Xu, X. Luo, L. Z. Cao, and R. S. Chen, "Optimization of coaxial dielectric resonator filter with aggressive space mapping," in *Asia Pacific Microwave Conference*, Dec. 2012, pp. 229–231.

[56] Q. Deng, T. Fan, and S. Lu, "The design of ka band filter with active space mapping algorithm," in *Proceedings of 3rd Asia-Pacific Conference on Antennas and Propagation*, July 2014, pp. 1140–1143.

[57] A. Rodriguez, J. V. Morro, J. Selga, M. Sans, J. Ossorio, M. Guglielmi, F. Martín, and V. E. Boria, "Robust optimization and tuning of microwave filters and artificial transmission lines using aggressive space mapping techniques," in *IEEE MTT-S International Microwave Symposium*, June 2017, pp. 1501–1504.

[58] J. Ossorio, J. Vague, V. E. Boria, and M. Guglielmi, "Efficient implementation of the aggressive space mapping technique for microwave filter design," in *47th European Microwave Conference*, Oct. 2017, pp. 644–647.

[59] J. Ossorio, J. C. Melgarejo, V. E. Boria, M. Guglielmi, and J. W. Bandler, "On the alignment of low-fidelity and high- fidelity simulation spaces for the design of microwave waveguide filters," *IEEE Transactions on Microwave Theory and Techniques*, vol. 66, no. 12, pp. 5183–5196, Dec. 2018.

[60] M. Guglielmi, R. Sorrentino, and G. Conciauro, *Advanced Modal Analysis: CAD Techniques for Waveguide Components and Filter*, 1st ed. USA: John Wiley &. Sons, Inc., Sept. 1999.

[61] A. Cunliffe and L. E. S. Mathias, "Some perturbation effects in cavity resonators," *Proceedings of the IEE - Part III: Radio and Communication Engineering*, vol. 97, no. 49, pp. 367–376, Sept. 1950.

[62] M. Guglielmi and A. A. Melcon, "Novel design procedure for microwave filters," in *23rd European Microwave Conference*, Sept. 1993, pp. 212–213.

[63] J. Ossorio, J. Vague, V. E. Boria, and M. Guglielmi, "Exploring the tunability range of classic circular waveguide dual mode filters using em-based cad," in *IEEE MTT-S International Conference on Numerical Electromagnetic and Multiphysics Modeling and Optimization for RF, Microwave, and Terahertz Applications*, May 2017, pp. 332–334.

[64] J. Ossorio, J. Vague, V. E. Boria, and M. Guglielmi, "Exploring the tuning range of channel filters for satellite applications using electromagnetic-based computer aided design tools," *IEEE Transactions on Microwave Theory and Techniques*, vol. 66, no. 2, pp. 717–725, Feb. 2018.

[65] R. Heinen and S. Wunderlich, "High dynamic range RF frontends from multiband multistandard to cognitive radio," in *Semiconductor Conference Dresden*, Sept. 2011, pp. 1–8.

[66] H. Maune, M. Nikfalazar, C. Schuster, T. Franke, W. Hu, M. Nickel, D. Kienemund, A. Prasetiadi, C. Weickhmann, M. Jost, A. Wiens, and R. Jakoby, "Tunable microwave component technologies for satcom-platforms," in *German Microwave Conference*, March 2016, pp. 23–26.

[67] R. Cameron, R. Mansour, and C. Kudsia, *Microwave Filters for Communication Systems: Fundamentals, Design and Applications*. Wiley, July 2007.

[68] M. Guglielmi, R. C. Molina, and A. A. Melcon, "Dual-mode circular waveguide filters without tuning screws," *IEEE Microwave and Guided Wave Letters*, vol. 2, no. 11, pp. 457–458, Nov. 1992.

[69] R. Beyer and F. Arndt, "Field-theory design of circular waveguide dual-mode filters by a combined mode-matching finite element method," in *24th European Microwave Conference*, vol. 1, Sept. 1994, pp. 294–303.

[70] S. Moretti, F. Alessandri, and R. Sorrentino, "Field theory design of a novel circular waveguide dual-mode filter," in *25th European Microwave Conference*, vol. 2, Sept. 1995, pp. 779–783.

[71] J. R. Montejo-Garai and J. Zapata, "Full-wave design and realization of multicoupled dual-mode circular waveguide filters," *IEEE Transactions on Microwave Theory and Techniques*, vol. 43, no. 6, pp. 1290–1297, June 1995.

[72] W. Schroeder and M. Guglielmi, "Boundary integral equation approach to multimode Y-matrix characterization of multi-ridged sections in circular waveguide," in *IEEE MTT-S International Microwave Symposium Digest*, vol. 3, June 1996, pp. 1849–1852.

[73] P. Mezzanotte, F. Alimenti, L. Roselli, and S. Sordi, "Design and realization of a dual-mode circular waveguide filter for digital audio broadcasting (DAB) applications," in *27th European Microwave Conference*, vol. 2, Sept. 1997, pp. 773–778.

[74] V. E. Boria, M. Guglielmi, and P. Arcioni, "Accurate CAD for dual mode filters in circular waveguide including tuning elements," in *IEEE MTT-S International Microwave Symposium Digest*, vol. 3, June 1997, pp. 1575–1578.

[75] K.-L. Wu, "An optimal circular-waveguide dual-mode filter without tuning screws," *IEEE Transactions on Microwave Theory and Techniques*, vol. 47, no. 3, pp. 271–276, March 1999.

[76] K.-L. Wu, M. Yu, and A. Sivadas, "Novel modal analysis of a circular-to-rectangular waveguide T-junction and its application to design of circular waveguide dual-mode filters," *IEEE Transactions on Microwave Theory and Techniques*, vol. 50, no. 2, pp. 465–473, Feb. 2002.

[77] W. Steyn and P. Meyer, "A shorted waveguide-stub coupling mechanism for narrow-band multimode coupled resonator filters," *IEEE Transactions on Microwave Theory and Techniques*, vol. 52, no. 6, pp. 1622–1625, June 2004.

[78] M. Taroncher, A. Vidal, V. E. Boria-Esbert, S. Marini, S. Cogollos, J. Gil, and B. Gimeno, "CAD of complex passive devices composed of arbitrarily shaped waveguides using Nyström and BI-RME methods," *IEEE Transactions on Microwave Theory and Techniques*, vol. 53, no. 6, pp. 2153–2163, June 2005.

[79] J. Zheng and M. Yu, "Rigorous mode-matching method of circular to off-center rectangular side-coupled waveguide junctions for filter applications," *IEEE Transactions on Microwave Theory and Techniques*, vol. 55, no. 11, pp. 2365–2373, Nov. 2007.

[80] H. Hu and K.-L. Wu, "An automated design technique for asynchronously-tuned circular waveguide dual-mode filters," in *Asia-Pacific Microwave Conference*, Dec. 2010, pp. 1970–1973.

[81] H. Hu, K.-L. Wu, and R. J. Cameron, "Stepped circular waveguide dual-mode filters for broadband contiguous multiplexers," *IEEE Transactions on Microwave Theory and Techniques*, vol. 61, no. 1, pp. 139–145, Jan. 2013.

[82] S. Cogollos, M. Brumos, V. E. Boria, C. Vicente, J. Gil, B. Gimeno, and M. Guglielmi, "A systematic design procedure of classical dual-mode circular waveguide filters using an equivalent distributed model," *IEEE Transactions on Microwave Theory and Techniques*, vol. 60, no. 4, pp. 1006–1017, Apr. 2012.

[83] W. Han, Q. Wang, Y. Chen, and Y. Tan, "Design of a narrow-band dual-mode circular waveguide filter," in *International Workshop on Microwave and Millimeter Wave Circuits and System Technology*, Apr. 2012, pp. 1–3.

[84] H. Hu and K.-L. Wu, "A deterministic EM design technique for general waveguide dual-mode bandpass filters," *IEEE Transactions on Microwave Theory and Techniques*, vol. 61, no. 2, pp. 800–807, Feb. 2013.

[85] C. Tomassoni, M. Dionigi, and R. Sorrentino, "Strategies for the improvement of the out of band behavior of TM dual-mode filters," in *IEEE 1st International Forum on Research and Technologies for Society and Industry Leveraging a better tomorrow*, Sept. 2015, pp. 90–93.

[86] X.-P. Liang, K. A. Zaki, and A. E. Atia, "Dual mode coupling by square corner cut in resonators and filters," in *IEEE MTT-S International Microwave Symposium Digest*, vol. 3, June 1992, pp. 1327–1330.

[87] J.-F. Liang, X.-P. Liang, K. A. Zaki, and A. E. Atia, "Dual-mode dielectric or air-filled rectangular waveguide filters," *IEEE Transactions on Microwave Theory and Techniques*, vol. 42, no. 7, pp. 1330–1336, July 1994.

[88] M. Guglielmi, P. Jarry, E. Kerherve, O. Roquebrun, and D. Schmitt, "A new family of all-inductive dual-mode filters," *IEEE Transactions on Microwave Theory and Techniques*, vol. 49, no. 10, pp. 1764–1769, Oct. 2001.

[89] J. A. Ruiz-Cruz, Y. Zhang, J. R. Montejo-Garai, J. M. Rebollar, and K. A. Zaki, "Longitudinal dual-mode filters in rectangular waveguide," in *IEEE MTT-S International Microwave Symposium*, June 2008, pp. 631–634.

[90] M. M. Darwish, A. M. El-Tager, H. N. Ahmed, and H. S. El-Hennawy, "Design of in-line dual-mode rectangular waveguide bandpass filters using multiple inductive circular posts," in *38th European Microwave Conference*, Oct. 2008, pp. 500–503.

[91] R. Sorrentino, L. Pelliccia, and S. Bastioli, "Recent progress in miniaturized and reconfigurable filters for advanced communications and space applications," in *Microwaves, Radar and Remote Sensing Symposium*, Aug. 2011, pp. 20–23.

[92] Z. Zheng, J. Hu, S. Liu, and Y. Zhang, "WR-1.5 band waveguide bandpass dual-mode filter on silicon micromachining technique," in *IEEE International Conference on Communication Problem-Solving*, Oct. 2015, pp. 112–114.

[93] S. Liu, J. Hu, Z. Xuan, Y. Zhang, and R. Xu, "Micromachined WR-1.0 waveguide band-pass filter," in *IEEE International Conference on Microwave and Millimeter Wave Technology*, vol. 2, June 2016, pp. 949–951.

[94] C. Kelleci and A. Atalar, "An analytical approach to the design of multiple mode rectangular cavity waveguide filters," *IEEE Transactions on Microwave Theory and Techniques*, vol. 65, no. 8, pp. 2857–2865, Aug. 2017.

[95] W. Junlin, Z. Binzhen, W. Xin, D. Junping, and W. Wanjun, "Dual-mode band-pass filters made by SU-8 micromachining technology for terahertz region," *Electronics Letters*, vol. 53, no. 11, pp. 730–732, May 2017.

[96] L. Accatino, G. Bertin, and G. Macchiarella, "A compact waveguide filtering structure with transmission zeros for multi-beam satellites," in *IEEE MTT-S International Microwave Symposium*, June 2017, pp. 737–740.

[97] H. Leblond, J. F. Villemazet, J. L. Cazaux, D. Pacaud, J. J. Herren, L. Rigaudeau, L. Lapierre, D. Baillargeat, P. Blondy, S. Bila, S. Verdeyme, C. Delage, C. Quendo, J. F. Favennec, B. Potelon, E. Rius, F. Seyfert, and S. Pacchini, "When new needs for satellite payloads meet with new filters architecture and technologies," in *39th European Microwave Conference*, Sept. 2009, pp. 1712–1715.

[98] L. Accattino, G. Macchiarella, and G. Bertin, "Modelling techniques for dual-mode reconfigurable filters used in satellite applications," in *IEEE MTT-S International Conference on Numerical Electromagnetic and Multiphysics Modeling and Optimization*, July 2016, pp. 1–2.

[99] M. H. N. Potok, "Capacitive-iris-type mechanically tunable waveguide filters for the X-band," *Proceedings of the IEEE - Part B: Electronic and Communication Engineering*, vol. 109, no. 48, pp. 505–510, Nov. 1962.

[100] M. Lamming, "Tunable irises for waveguide channel filters," in *Proceedings of the ESA Workshop on Advanced CAD for Microwave Filters and Passive Devices*, March 1995, pp. 301–315.

[101] P. Mader, H. Dillenbourg, C. Labourdette, P. Lepeltier, J. Sinigaglia, J. Smits, J. Puech, F. Gizard, J. M. E. Lopez, D. Anderson, M. Lisak, E. I. Rakova, and V. E. Semenov, "Experimental validation of fringing field effects for the multipactor phenomenon," in *15th International Symposium on Antenna Technology and Applied Electromagnetics*, June 2012, pp. 1–5.

[102] C. Arnold, J. Parlebas, and T. Zwick, "Reconfigurable waveguide filter with variable bandwidth and center frequency," *IEEE Transactions on Microwave Theory and Techniques*, vol. 62, no. 8, pp. 1663–1670, Oct. 2014.

[103] C. Arnold, J. Parlebas, R. Meiser, and T. Zwick, "Fully reconfigurable manifold multiplexer," *IEEE Transactions on Microwave Theory and Techniques*, vol. 65, no. 10, pp. 3885–3891, Apr. 2017.

[104] F. Alessandri, M. Comparini, and F. Vitulli, "Low-loss filters in rectangular waveguide with rigorous control of spurious responses through a smart modal filter," in *IEEE MTT-S International Microwave Sympsoium Digest*, vol. 3, May 2001, pp. 1615–1617.

[105] A. Morini, G. Venanzoni, M. Farina, and T. Rozzi, "Modified adaptive prototype inclusive of the external couplings for the design of coaxial filters," *IEEE Transactions on Microwave Theory and Techniques*, vol. 55, no. 9, pp. 1905–1911, Sept. 2007.

[106] W. Meng and K.-L. Wu, "Analytical diagnosis and tuning of narrowband multicoupled resonator filters," *IEEE Transactions on Microwave Theory and Techniques*, vol. 54, no. 10, pp. 3765–3771, Oct. 2006.

[107] V. Boria, M. Guglielmi, and P. Arcioni, "Computer-aided design of inductively coupled rectangular waveguide filters including tuning elements," *International Journal of RF and Microwave Computer-Aided Engineering*, vol. 8, no. 3, pp. 226–235, Dec. 1998.

[108] G. Craven and R. Skedd, *Evanescent Mode Microwave Components*, ser. Microwave Library. Artech House, March 1987.

[109] V. E. Boria, M. Guglielmi, and P. Arcioni, "Accurate CAD for dual mode filters in circular waveguide including tuning elements," in *IEEE MTT-S International Microwave Symposium Digest*, vol. 3, June 1997, pp. 1575–1578.

[110] W. Hauth, D. Schmitt, and M. Guglielmi, "Accurate modelling of narrow-band filters for satellite communications," in *IEEE MTT-S International Microwave Symposium Digest*, vol. 3, June 2000, pp. 1767–1770.

[111] V. E. Boria, G. Gerini, and M. Guglielmi, "Computer aided design of reentrant coaxial filters including coaxial excitation," in *IEEE MTT-S International Microwave Symposium Digest*, vol. 3, June 1999, pp. 1131–1134.

[112] K.-L. Wu, "An optimal circular-waveguide dual-mode filter without tuning screws," *IEEE Transactions on Microwave Theory and Techniques*, vol. 47, no. 3, pp. 271–276, March 1999.

[113] S. B. Cohn, "Microwave bandpass filters containing high-Q dielectric resonators," *IEEE Transactions on Microwave Theory and Techniques*, vol. 16, no. 4, pp. 218–227, Apr. 1968.

[114] S. J. Fiedziuszko, I. C. Hunter, T. Itoh, Y. Kobayashi, T. Nishikawa, S. N. Stitzer, and K. Wakino, "Dielectric materials, devices, and circuits," *IEEE Transactions on Microwave Theory and Techniques*, vol. 50, no. 3, pp. 706–720, March 2002.

[115] J. Ossorio, V. E. Boria, and M. Guglielmi, "Dielectric tuning screws for microwave filters applications," in *IEEE MTT-S International Microwave Symposium*, June 2018, pp. 1253–1256.

[116] M. Yu and A. E. Atia, "Introduction to high power issues of microwave filter design and realization," *in IEEE MTT-S International Microwave Symposium Workshop*, June 2007.

[117] C. Vicente and H. L. Hartnagel, "Passive-intermodulation analysis between rough rectangular waveguide flanges," *IEEE Transactions on Microwave Theory and Techniques*, vol. 53, no. 8, pp. 2515–2525, Aug. 2005.

[118] D. Smacchia, P. Soto, V. E. Boria, M. Guglielmi, C. Carceller, J. Ruiz Garnica, J. Galdeano, and D. Raboso, "Advanced compact setups for passive intermodulation measurements of satellite hardware," *IEEE Transactions on Microwave Theory and Techniques*, vol. 66, no. 2, pp. 700–710, Feb. 2018.

[119] R. V. Snyder, "Practical aspects of microwave filter development," *IEEE Microwave Magazine*, vol. 8, no. 2, pp. 42–54, Apr. 2007.

[120] A. Lindner and E. Biebl, "A manual tuning method for coupled cavity filters," in *36th European Microwave Conference*, Sept. 2006, pp. 1340–1342.

[121] A. R. Mirzai, C. F. N. Cowan, and T. M. Crawford, "Intelligent alignment of waveguide filters using a machine learning approach," *IEEE Transactions on Microwave Theory and Techniques*, vol. 37, no. 1, pp. 166–173, Jan 1989.

[122] J. Zhou and J. Huang, "Intelligent tuning for microwave filters based on multi-kernel machine learning model," in *IEEE International Symposium on Microwave, Antenna, Propagation and EMC Technologies for Wireless Communications*, Oct. 2013, pp. 259–266.

[123] V. Miraftab and R. R. Mansour, "Computer-aided tuning of microwave filters using fuzzy logic," in *IEEE MTT-S International Microwave Symposium Digest*, vol. 2, June 2002, pp. 1117–1120.

[124] J. C. Melgarejo, J. Ossorio, S. Cogollos, M. Guglielmi, V. E. Boria, and J. W. Bandler, "On space mapping techniques for microwave filter tuning," *IEEE Transactions on Microwave Theory and Techniques*, vol. 67, no. 12, pp. 4860–4870, Dec. 2019.

[125] S. K. Rao, "Advanced antenna technologies for satellite communications payloads," *IEEE Transactions on Antennas and Propagation*, vol. 63, no. 4, pp. 1205–1217, Apr. 2015.

[126] L. Accatino, G. Bertin, and G. Macchiarella, "A compact waveguide filtering structure with transmission zeros for multi-beam satellites," in *IEEE MTT-S International Microwave Symposium Digest*, June 2017, pp. 737–740.

[127] C. Kudsia, R. Cameron, and W. C. Tang, "Innovations in microwave filters and multiplexing networks for communications satellite systems," *IEEE Transactions on Microwave Theory and Techniques*, vol. 40, no. 6, pp. 1133–1149, June 1992.

[128] L. Accatino, G. Bertin, and M. Mongiardo, "A four-pole dual mode elliptic filter realized in circular cavity without screws," *IEEE Transactions on Microwave Theory and Techniques*, vol. 44, no. 12, pp. 2680–2687, Dec. 1996.

[129] P. Savi, D. Trinchero, R. Tascone, and R. Orta, "A new approach to the design of dual-mode rectangular waveguide filters with distributed coupling," *IEEE Transactions on Microwave Theory and Techniques*, vol. 45, no. 2, pp. 221–228, Feb. 1997.

[130] J. Ossorio, S. Cogollos, V. E. Boria, and M. Guglielmi, "Rectangular waveguide quadruplet filter for satellite applications," in *IEEE MTT-S International Microwave Symposium*, June 2019, pp. 1359–1362.

[131] ARTES 5.1, "Lightweight and compact diplexer for multibeam payloads," in *ESA-ESTEC Document AO/1-7447/13/NL/EM (ITT)*, March 2013.

[132] J. Uher, J. Bornemann, and U. Rosenberg, *Waveguide Components for Antenna Feed Systems: Theory and CAD*. Artech House Antennas and Propagation Library. Artech House, Dec. 1993.

[133] A. Morini and T. Rozzi, "Analysis of compact E-plane diplexers in rectangular waveguide," *IEEE Transactions on Microwave Theory and Techniques*, vol. 43, no. 8, pp. 1834–1839, Aug. 1995.

[134] Y. Rong, H-W. Yao, K. A. Zaki, and T. G. Dolan, "Millimeter-wave ka-band H-plane diplexers and multiplexers," *IEEE Transactions on Microwave Theory and Techniques*, vol. 47, no. 12, pp. 2325–2330, Dec. 1999.

[135] J. M. Rebollar, J. R. Montejo-Garai, and A. Oñoro, "Asymmetric H-plane T-junction for broadband diplexer applications," in *IEEE Antennas and Propagation Society International Symposium Digest*, vol. 4, July 2000, pp. 2032–2035.

[136] T. Shen, K. A. Zaki, and T. G. Dolan, "Rectangular waveguide diplexers with a circular waveguide common port," *IEEE Transactions on Microwave Theory and Techniques*, vol. 51, no. 2, pp. 578–582, Feb. 2003.

[137] E. Ofli, R. Vahldieck, and S. Amari, "Novel E-plane filters and diplexers with elliptic response for millimeter-wave applications," *IEEE Transactions on Microwave Theory and Techniques*, vol. 53, no. 3, pp. 843–851, March 2005.

[138] S. Bastioli, L. Marcaccioli, and R. Sorrentino, "An original resonant Y-junction for compact waveguide diplexers," in *IEEE MTT-S International Microwave Symposium Digest*, June 2009, pp. 1233–1236.

[139] L. Zhu, R. R. Mansour, and M. Yu, "A compact waveguide diplexer employing dual-band resonators," in *IEEE MTT-S International Microwave Symposium*, June 2014, pp. 1–4.

[140] F. Teberio, I. Arregui, M. Guglielmi, A. Gomez-Torrent, P. Soto, M. A. G. Laso, and V. E. Boria, "Compact broadband waveguide diplexer for satellite applications," in *IEEE MTT-S International Microwave Symposium*, May 2016, pp. 1–4.

[141] U. Rosenberg, M. Knipp, and S. Amari, "Compact diplexer design using different E-plane triplets to serve contiguous passbands with high interband selectivity," in *36th European Microwave Conference*, Sept. 2006, pp. 133–136.

[142] J. Ossorio, J. C. Melgarejo, S. Cogollos, V. E. Boria, and M. Guglielmi, "Waveguide quadruplet diplexer for multi-beam satellite applications," *IEEE Access*, vol. 8, pp. 110 116–110 128, June 2020.

[143] C. Carceller, P. Soto, V. Boria, and M. Guglielmi, "Capacitive obstacle realizing multiple transmission zeros for in-line rectangular waveguide filters," *IEEE Microwave and Wireless Components Letters*, vol. 26, no. 10, pp. 795–797, Oct. 2016.

[144] N. Marcuvitz, *Waveguide Handbook*. IEE Electromagnetic Waves series. McGraw-Hill, March 1951.

[145] J. R. M. Vaughan, "Multipactor," *IEEE Transactions on Electron Devices*, vol. 35, no. 7, pp. 1172–1180, July 1988.

[146] ECCS-20-01A, *Multipacting Design and Test*. European Space Agency (ESA), May 2003.

[147] COMDEV, now with Honeywell Aerospace, *COMDEV Space Group*. Canada: Cambridge [Online], May 2010. Available at: https://aerospace.honeywell.com/en/learn/products/space/mechanical-switches.

[148] M. Daneshmand and R. R. Mansour, "RF MEMS satellite switch matrices," *IEEE Microwave Magazine*, vol. 12, no. 5, pp. 92–109, Aug. 2011.

[149] J. A. Ruiz-Cruz, M. M. Fahmi, and R. R. Mansour, "Compact four-port rectangular waveguide switches based on simple short circuit loads," in *IEEE MTT-S International Microwave Symposium*, June 2011, pp. 1–4.

[150] J. A. Ruiz-Cruz, M. M. Fahmi, and R. R. Mansour, "Single-pole six-throw waveguide switch embedded in a seven port loaded junction," in *IEEE MTT-S International Microwave Symposium*, June 2013, pp. 1–4.

[151] J. A. Ruiz-Cruz, M. M. Fahmi, and R. R. Mansour, "Single-pole multiple-throw waveguide switch for twelve output ports (SP12T)," in *44th European Microwave Conference*, Oct. 2014, pp. 468–471.

[152] K.Y. Chan, R. Ramer, R.R. Mansour, and R. Sorrentino, "Design of waveguide switches using switchable planar bandstop filters," *IEEE Microwave and Wireless Components Letters*, vol. 26, no. 10, pp. 798–800, Oct. 2016.

[153] K.Y. Chan, R. Ramer, and R.R. Mansour, "A switchable iris bandpass filter using RF MEMS switchable planar resonators," *IEEE Microwave and Wireless Components Letters*, vol. 27, no. 1, pp. 34–36, Jan. 2017.

[154] K.Y. Chan, R. Ramer, and R.R. Mansour, "Ku-band channel aggregation waveguide filters by RF MEMS-based detuning," *IEEE Transactions on Microwave Theory and Techniques*, vol. 68, no. 2, pp. 750–761, Feb. 2020.

[155] H. Li, J. Xu, X. Y. Zhang, and X. Zhao, "Low-loss narrowband filtering switch based on coaxial resonators," *IEEE Access*, vol. 6, pp. 47 717–47 722, Aug. 2018.

[156] Y. Um, M. Hsiao, and C. Nguyen, "Design of a Ka/V-band CMOS T/R filter-switch," in *IEEE MTT-S Latin America Microwave Conference*, Dec. 2018, pp. 1–2.

[157] J. Ossorio, J. C. Melgarejo, V. E. Boria, and M. Guglielmi, "On the integration of microwave filters and waveguide switches," *IEEE Microwave and Wireless Components Letters*, Dec. 2020.